UNIVERSITY OF CALIFORNIA, SAN DIEGO

Electromagnetic Exploration of the Exmouth and Vøring Rifted Margins

A dissertation submitted in partial satisfaction of the requirements for the degree of Doctor of Philosophy

in

Earth Sciences

by

David Gerard Myer

Committee in charge:

Steven Constable, Chair
C. Fred Driscoll
Kerry Key
David Sandwell
Lisa Tauxe

2012

The Dissertation of David Gerard Myer is approved, and it is acceptable in quality and form for publication on microfilm and electronically:

_____

_____

_____

_____

_____

Chair

University of California, San Diego

2012

DEDICATION

Dedicated to my lovely wife, Debbie, who told me to stop talking about going back to school and do it, and then had the courage to stick by that conviction for the ensuing fourteen years it took to finish. “There’s no remedy…”

Also dedicated to my two wonderful kids, now launched into lives of their own. Surely it must have been unsatisfying to complain about your homework when dad was also complaining about his own. I hope that you have seen from me that life is an adventure which you should throw yourself into. I am proud of the adults both of you have become. Remember to choose the risky option. Even if you fail, you'll still have great stories to tell.

EPIGRAPH

The Six Stages of a PhD:

Year 1

The mind is not a vessel to be filled,
but a fire to be lighted.
– Plutarch

Year 2

Opportunity is missed by most people
because it is dressed in overalls
and looks like work.
– Thomas Edison

Year 3

Far and away the best prize that life offers
is the chance to work hard
at work worth doing.
– Teddy Roosevelt

Year 4

The only thing you can do easily is be wrong.
And that's hardly worth the effort.
– Norton Jester, *The Phantom Tollbooth*

Year 5

Electricity is actually made up of extremely tiny particles called electrons,
that you cannot see with the naked eye unless you have been drinking.
– Dave Barry

Year 6

Exit, pursued by a bear.
– William Shakespeare

TABLE OF CONTENTS

LIST OF FIGURES

LIST OF TABLES

ACKNOWLEDGEMENTS

Many thanks to Professor Steven Constable, my committee chair, for working tirelessly to provide data so early in and throughout my studies, for his direction, and for his patience and hands-off approach as I went down a series of alleyways to see which ones were blind. Thanks as well for pushing at the right times and reining me in when the horizons became too broad.

Many thanks also to Kerry Key for his tutelage in my early years and the stimulating discussions throughout. Thank you for always being willing to take the time to explain, even for the umpteenth time and with the pressures of your own research time-line looming.

Thanks to Professor David Sandwell for giving me the opportunity to extend a homework assignment into exploration of Kilauea with InSAR and GPS and for pointing me in the right directions for surface deformation modeling. Every opportunity to publish is worth the time. Thanks also to Professors Lisa Tauxe and Fred Driscoll for taking the time to serve on my committee and provide direction.

I give special thanks to Jacques Lemire, John Souders, Cambria Berger, Chris Armerding, and Jake Perez for working so tirelessly to prepare and execute each cruise and for working extra carefully to make sure all the details are handled well. It is always a pleasure sailing with you and working side-by-side at hard work that is worth doing. You made it fun!

Funding for the Exmouth Plateau expedition was provided by BHP Billiton Petroleum. Shell, Esso Australia, and Chevron provided ingress permissions. Fugro Development and Production Company funded the Vøring Plateau expedition. The

Seafloor Electromagnetic Methods Consortium funded the bulk of the processing and inversion of both datasets. We thank them all. Without their commitment to science, this work would not have been possible.

Chapter 2, in full, is a reprint of material as it appears in the Geophysical Journal International, Myer D., Constable S., and Key K., Blackwell Publishing Ltd., 2011. The dissertation author was the primary investigator and author of this paper.

Chapter 3, in full, has been submitted for publication of the material as it may appear in Geophysics, Myer D., Constable S., Key K., Glinsky M. E., and Liu G. The dissertation author was the primary investigator and author of this paper.

Chapter 4, in full, has been submitted for publication of the material as it may appear in Geophysics, Myer D., Constable S., and Key K. The dissertation author was the primary investigator and author of this paper. Steven Constable provided text and figures for the section on pseudo-imaging.

Chapter 5, in full or in part, is currently being prepared for submission for publication, D. Myer, Constable S., and Key K. The dissertation author was the primary investigator and author of this paper.

VITA

2005	Bachelor of Science, University of California, San Diego Physics (Astrophysics), minor in Earth Sciences
2005-2011	Research Assistant, University of California, San Diego
2012	Doctor of Philosophy, University of California, San Diego Earth Sciences, Scripps Institution of Oceanography

PUBLICATIONS

2008, Myer, D., D. Sandwell, B. Brooks, J. Foster, and M. Shimada, *Inflation along Kilauea's Southwest Rift Zone in 2006*, Journal of Volcanology and Geothermal Research, 177(2), 418-424.

2008, Sandwell, D., D. Myer, R. Mellors, M. Shimada, B. Brooks, and J. Foster, *Accuracy and Resolution of ALOS Interferometry: Vector Deformation Maps of the Father's Day Intrusion at Kilauea*, IEEE Transactions on Geoscience and Remote Sensing, 46(11), 3524-3534.

2008, Brooks, B. A., J. Foster, D. Sandwell, C. J. Wolfe, P. Okubo, M. Poland, and D. Myer, *Magmatically Triggered Slow Slip at Kilauea Volcano, Hawaii*, Science, 321(5893), 1177.

2010, Myer, D., S. Constable, K. Key, *A marine EM survey of the Scarborough gas field, Northwest Shelf of Australia*, First Break, 28(5), 77-82.

2011, Myer, D., S. Constable, K. Key, *Broad-band waveforms and robust processing for marine CSEM surveys*, Geophysical Journal International, 184(2), 689-698.

ABSTRACT OF THE DISSERTATION

Electromagnetic Exploration of the Exmouth and Vøring Rifted Margins

by

David Gerard Myer

Doctor of Philosophy in Earth Sciences

University of California, San Diego, 2012

Professor Steven Constable, Chair

In this work, we present improvements to and the use of two marine electromagnetic exploration methods at the Exmouth and Vøring Plateaus. First we discuss the marine controlled-source electromagnetic method (CSEM), specifically the formation and characteristics of custom binary and ternary waveforms as well as improvements to time-series processing which allow derivation of noise estimates.

We then apply these improvements to the study of the Scarborough gas reservoir beneath the Exmouth Plateau off the northwest shelf of Australia, over which we collected the world's largest academic CSEM dataset. Using these data we (1) discuss

methods for determining uncertainties in CSEM, (2) investigate the resolution of CSEM in an environment where multiple resistive geologic layers lie in close repose, (3) develop the prejudiced minimum norm as a regularization method in 1D CSEM inversion, discussing its strengths and limitations, and (4) develop the 1D/2D and 1D/3D inversion methods in which the forward model is 1D but the regularization is 2D or 3D. All of the new inversion methods derive more realistic results than 1D smooth inversion alone and may form a good starting point for higher dimensional inversion.

Finally we target the deep structure of the Exmouth Plateau with marine magnetotellurics and compare the results to the Vøring Plateau off the northwest shelf of Norway. Magnetotelluric data reveal that both plateaus host a body of unexpectedly low resistivity (≤ 0.1 Ωm) at ~10 km depth. We show that the depth of each body is consistent with known sills and theorize that the low resistivity is due to magnetite cumulates precipitated as layers in mafic-ultramafic sills. Both plateaus exhibit the features of volcanic passive margins in which the final continental rifting event was relatively quick and accompanied by voluminous volcanism. Our data are consistent with this explanation and suggest that a large volume of mafic material was injected into the crust forming a relatively interconnected network of conductive minerals.

1 Introduction

In 2009 we carried out a survey of the Scarborough super-giant gas field on the Exmouth Plateau using two marine electromagnetic methods: magnetotellurics (MT) and controlled-source electromagnetics (CSEM). The Exmouth Plateau is part of the passive margin formed by the break-up of Gondwanaland into Australia and Greater India. In 2010, we augmented the Exmouth survey results with an MT survey on the Vøring Plateau, which is also a passive margin, formed by the breakup of northern Europe and Greenland.

A margin is the transition between two different geological regimes. Plate tectonic boundaries are "active" margins because deformation is currently taking place: California is being sheared by the San Andreas Fault, new oceanic crust is being formed at spreading ridges, etc. A "passive" margin is the transition between continental and oceanic crust left-over from the breakup of a continental landmass by the formation of what eventually becomes a mid-ocean ridge. As the ridge moves away, it leaves behind a transition zone of varying width in which blocks of continental crust may be interspersed with and intruded by rift-related volcanics. In some cases volcanism is wide-spread and extensive (volcanic passive margins) and in other cases there is almost no volcanism (non-volcanic passive margins) (Coffin and Eldholm, 1992; White, 1992; White and McKenzie, 1989).

Before breakup, the region of the continent where rifting will be established is stretched and thinned. Continental crust which may have begun as 40+ km thick can be fractured and stretched to a fraction of its original thickness. There may be many

episodes of thinning before the eventual separation of the continent, leaving the edges as highly deformed and complex environments. In some cases, early spreading episodes leave deep interior sub-basins which fill with thick sequences of sediments. Some of these sub-basins are rich in hydrocarbons as a result of the complex sedimentary history.

Both the Exmouth and Vøring Plateaus are volcanic passive margins which jut out several hundred kilometers from the surrounding continental shelf making wide, complex margins. Both plateaus have experienced early spreading episodes, contain deep interior sub-basins, and are rich in hydrocarbons. Away from the sub-basins, both plateaus are relatively sediment starved, which has made them preferential targets for scientific ocean drilling aimed at studying passive margin formation. Combined with the economic interest in the hydrocarbon deposits, this has led to the collection of extensive volumes of geophysical data at both plateaus. A brief review of the pertinent geologic history of each plateau is given in Chapter 5 of this dissertation in relation to the discussion of the MT data and results, where it is most relevant.

The two marine electromagnetic exploration methods used in this work are frequency domain techniques which occupy complementary portions of the electromagnetic spectrum. MT relies on time-variations in Earth's electromagnetic field to produce an inductive response in the ground (Figure 1.1). Because the source region for these variations is high above the surface of Earth, the electromagnetic equations are simplified by the assumption that the source field is horizontally polarized and vertically propagating. Faraday's law of induction can then be reduced to a relationship between horizontal components of the electric and magnetic field vectors in the form of a 2x2

complex impedance tensor. The electric and magnetic fields each contain both source and response effects, so it is necessary to form a ratio between the two fields. By recording

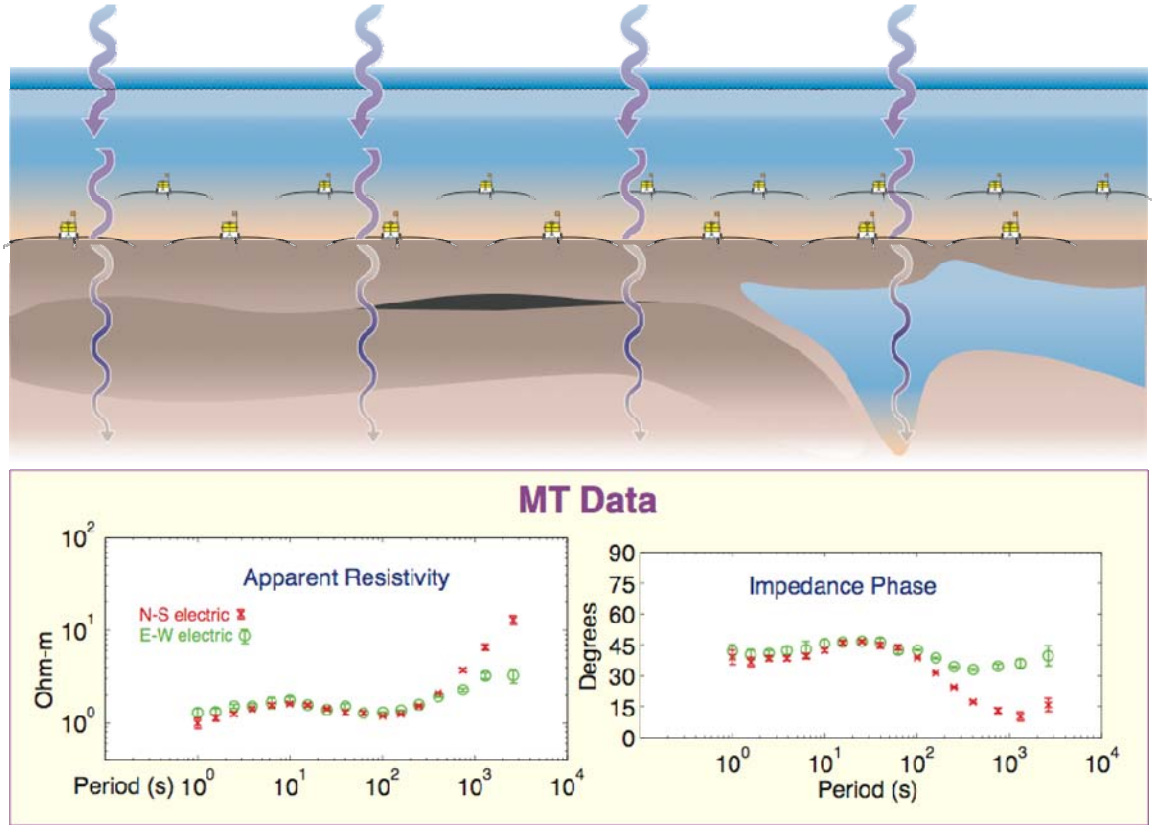

Figure 1.1. Conceptual drawing of an MT survey
Variations in Earth's electromagnetic field propagate through the atmosphere, ocean, and seafloor. Instruments placed along the seafloor record both the source field and the inductive response of the underlying earth. The bottom panels illustrate the types of data derived from the complex impedances: apparent resistivity (from amplitude) and phase, both as a function of frequency.

the horizontal electric and magnetic fields using instruments placed across the seafloor and applying suitable time-series processing and spectral estimation techniques, one can form the impedance tensor which is a function of conductivity and frequency. As an inductive technique, MT is characterized by a diffusion equation, the attenuative effects of which are frequency-dependent with the result that lower frequencies sense deeper Earth structure than higher frequencies. The frequencies covered by marine MT are

approximately 10^{-4} – 10^{0} Hz. Reviews of the MT technique may be found in Constable (2007); Simpson and Bahr (2005); Key (2003); Constable (1990); Ward and Hohmann (1987); and Cagniard (1953).

CSEM relies on a dipolar man-made source field which is deep-towed near the recording instruments laid out on the seafloor (Figure 1.2). Unlike MT, the source field is known, which means that a transfer function between input and output signals may be formed directly. However, the source has a complicated 3D configuration and its location is constantly changing. The frequencies used in CSEM are typically higher than 0.1 Hz but it is also a diffusion equation technique. The deepest Earth structure sensed typically overlaps with the shallowest section of an MT survey, making these two

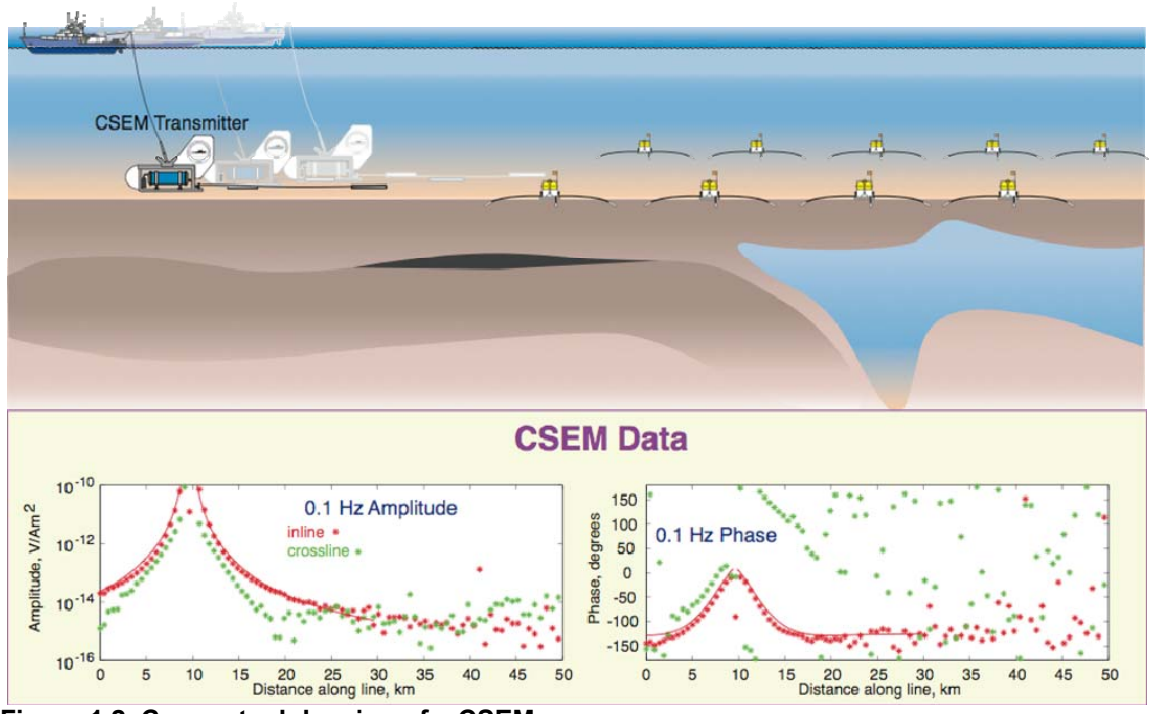

Figure 1.2. Conceptual drawing of a CSEM survey.

In CSEM, an artificial electric current dipole is deep-towed near a collection of seafloor receivers which measure the known source field as it attenuates through the seabed. Time series data are transformed into the frequency domain at the discrete frequencies prescribed by the transmitter waveform. The bottom panels illustrate the types of data derived by CSEM: signal amplitude and phase, both as a function of range and frequency.

techniques complementary. A review and in-depth compilation of reference material regarding the development and current state of CSEM is contained in Key (2011).

Although both the MT and CSEM techniques are a function of resistivity, neither type of data yields resistivity structure directly. Both must be "inverted" to achieve a model of resistivity. In the case of known resistivity structure, the data one would observe can be calculated from the known physics. This is called the "forward problem" and can be quite complicated to calculate accurately. The "inverse problem" involves deducing from the data the resistivity structure that might have generated it. This is typically more complicated than the forward problem for a variety of reasons, such as uncertainties in the data, non-linearities in the physics, etc. Geophysical inversion is its own field of study with a rich literature (e.g. Zhdanov, 2002; Parker, 1994). For the purposes of this dissertation, it is only important to note that the inverse problem is both unstable and non-unique, such that an additional constraint is required beyond just fitting the data within their uncertainties. In the case of diffusive electromagnetics techniques, this is usually in the form of a "roughness" penalty on the resistivity model space. In other words, the inversion is constrained to pick the smoothest model which fits the data. The roughness penalty is not the only constraint available to inversion; others are investigated in Chapter 4 in the context of CSEM.

The roughness penalty tends to produce resistivity models that are diffuse and "blobby", which is entirely appropriate given that both MT and CSEM are diffusion techniques with resolution that is limited compared to a wave-propagation technique. Figure 1.3 is an example of MT inversion and illustrates the type of resolution possible. The top panel shows a sample geologic model. This model was run "forward" to generate

the MT data that would be observed at the sites (diamonds) placed along the seabed. The data were then inverted to the best-fitting smooth model, shown in the bottom panel. Though the basic features of the forward model are present, the details of the conductive feature between 8-10 km depth are blurred. This is a typical MT inversion result.

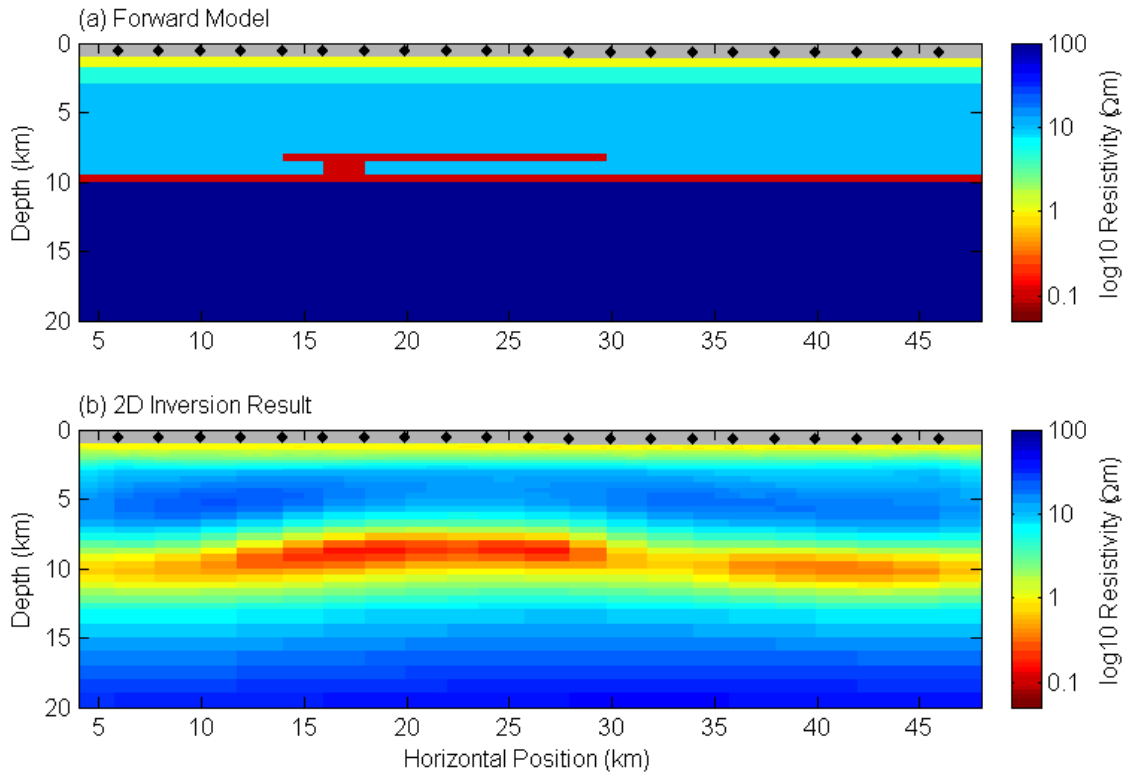

Figure 1.3 Example of MT Inversion
(a) A sample resistivity model used to generate synthetic data at a collection of sites (diamonds). (b) The model resulting from inversion of the synthetic data.

In Chapter 2 of this work, we discuss classes of CSEM waveforms and a method for deriving an optimal waveform for given criteria. We also present an improved method of transforming time-series data into the frequency domain which decreases spectral contamination from MT. We discuss a method for deriving noise estimates in stacked frequency domain data which also takes into account biases introduced by the non-stationarity of the source.

In Chapter 3, we present a review of the design, collection, and processing of the Scarborough CSEM survey dataset from the Exmouth Plateau. We give a detailed analysis of the sources of uncertainty in this survey and translate them into a minimum error structure suitable for inversion. Additionally, we validate the uncertainty estimates with analysis of data from a unique repeat tow.

In Chapter 4, we present pseudo-imaging of the Scarborough CSEM electric and magnetic field values and draw a few broad conclusions concerning various field components. In the context of 1D inversion, we compare the performance of two common methods for collecting data along a tow track. We also develop the prejudiced minimum norm as a replacement for the typical roughness constraint used for inversion regularization. Finally, we develop the 1D/2D and 1D/3D inversion techniques which extend 1D inversion into higher dimensions through modified regularization, providing a new tool for quick characterization of a dataset.

In Chapter 5 of this work, we use the MT method to explore the deep structure of the Exmouth and Vøring Plateaus. We show that both plateaus contain bodies of unusually low resistivity at approximately the same depth. Through a series of modified inversions, we constrain the dimensions of these bodies and discuss possible interpretations within their geologic contexts.

References

Cagniard, L., 1953. Basic Theory of the Magneto-telluric method of Geophysical Prospecting, *Geophysics,* 18**,** 605-635.

Coffin, M.F. & Eldholm, O., 1992. Volcanism and continental break-up: a global compilation of large igneous provinces, *Geological Society, London, Special Publications,* 68**,** 17-30.

Constable, S., 1990. Marine Electromagnetic Induction Studies, *Surveys in Geophysics,* 11**,** 303-327.

Constable, S., 2007. 7 Geomagnetic Induction Studies. *in Treatise on Geophysics: Geomagnetism*, pp. 237-276, eds. Shubert, G. & Kono, M. Elsevier.

Key, K., 2003. Application of Broadband Marine Magnetotelluric Exploration to a 3D Salt Structure and a Fast-Spreading Ridge, PhD Thesis, University of California, San Diego, La Jolla.

Key, K., 2011. Marine Electromagnetic Studies of Seafloor Resources and Tectonics, *Surveys in Geophysics***,** 1-33.

Parker, R.L., 1994. *Geophysical Inverse Theory,* edn, Vol., Princeton University Press.

Simpson, F. & Bahr, K., 2005. *Practical magnetotellurics,* edn, Vol., Cambridge University Press.

Ward, S.H. & Hohmann, G.W., 1987. 4 Electromagnetic Theory for Geophysical Applications. *in Electromagnetic Methods in Applied Geophysics*, ed. Nabighian, M. N. SEG, Tulsa.

White, R.S., 1992. Magmatism during and after continental break-up, *Geological Society, London, Special Publications,* 68**,** 1-16.

White, R.S. & McKenzie, D., 1989. Magmatism at Rift Zones: The Generation of Volcanic Continental Margins and Flood Basalts, *J. Geophys. Res.,* 94**,** 7685-7729.

Zhdanov, M.S., 2002. *Geophysical Inverse Theory and Regularization Problems,* edn, Vol., Elsevier Science.

2 Broad-band waveforms and robust processing for marine CSEM surveys

Abstract

In the marine controlled-source electromagnetic method, the earth response varies in frequency; therefore, using a wide range of frequencies may better constrain geologic structure than using a single frequency or only a few closely spaced frequencies. Binary waveforms, such as the square wave, provide a number of frequencies, though many are limited in usefulness because of the rapid decline of amplitude with frequency. Binary waveform design can be improved by recognizing that the class of doubly symmetric waveforms has special properties: they are compact, have controlled phase, are never polarizing, and can be described by a simple closed-form mathematical solution. Using this solution, we discovered a compact waveform in which the amplitudes of the 3rd and 7th harmonics are maximized and which has a signal-to-noise advantage at higher frequencies over several other common waveforms.

Compact waveforms make possible improved methods for time series processing. Using short time windows and a first-difference pre-whitener lessens spectral contamination from magnetotelluric signal and oceanographic noise; robust stacking reduces bias from time series noise transients; and accurate variance estimates may be derived from averages of waveform-length Fourier transform windows of the time series.

2.1 Introduction

In the frequency-domain marine controlled source electromagnetic (CSEM) method, an electromagnetic dipole is used to create a source field which is measured at receivers placed across the seabed (Edwards, 2005; MacGregor *et al.*, 2001; Constable and Cox, 1996; Cox *et al.*, 1986). This source dipole field couples with surrounding materials and the measured field is treated as a linear convolution of the source with an attenuative, diffusive earth (Loseth *et al.*, 2006; Ward and Hohmann, 1987). The frequency response of the earth transfer function varies according to conductivity, source-receiver range, and a variety of other (chiefly geometric) factors, with the result that the CSEM method is sensitive to thin resistive bodies embedded in conductive sediments. This has led to its increasing use in hydrocarbon and gas-hydrate exploration (e.g. Constable and Srnka, 2007; Weitemeyer *et al.*, 2006; Eidesmo *et al.*, 2002; Ellingsrud *et al.*, 2002).

Because the peak frequency sensitivity of an exploration target is not well known a priori, it is common to transmit a source waveform which allows for simultaneous broadcast of multiple frequencies. The classic example of such a waveform is the square wave, which provides a spread of frequencies at the odd harmonics of the fundamental transmission frequency. However, the square wave is not ideal for the CSEM method because the amplitude of its harmonics falls off as 1/n, where n is the harmonic number. For an inductive method like CSEM in which fields attenuate exponentially as a function of range and frequency, many of the square wave's harmonics have too little power to be detected to useful ranges.

The signal-to-noise ratio of the measured CSEM signal is directly related to the source dipole moment (SDM) of the transmitter. Since the SDM is composed of three factors, this suggests that there are three modifications to a transmitter which may increase the signal-to-noise ratio: increase the output current, lengthen the transmitter dipole, and modify the waveform. Existing transmitters output up to 1000 amps. Increasing this value is technically difficult, increases the danger and complexity of ship-board operations, and may eventually run into environmental concerns. Transmitter dipole lengths up to 300 meters are common, but because of the complexity of deep-towing a streaming antenna near the seabed, longer dipoles are impractical. In contrast, customizing the waveform is a relatively easy way to increase the SDM at particular frequencies.

Specialized waveforms have been presented by Constable and Cox (1996) and patented by ExxonMobil (Lu and Srnka, 2005). Mittet and Schaug-Pettersen (2008) present a collection of waveforms discovered using a Monte-Carlo approach for finding waveforms that fit a given criterion. In this paper, we discuss classes of waveforms, develop an analytical method for finding the optimal second-order symmetric waveform for any given criterion, and compare the bandwidth of an example waveform so derived with those mentioned above. We also discuss techniques for time series processing which take advantage of compact waveforms to reduce spectral contamination and provide accurate variance estimates. We show examples from a recent academic CSEM survey over a gas prospect on the northwestern Australian shelf.

2.2 Waveform Classes

CSEM waveforms are usually either binary (alternating polarity between constant positive and negative output current) or ternary (positive and negative separated by "off" states). Ternary waveforms are sometimes intentional (e.g. Constable and Cox, 1996) and sometimes required due to hardware limitations (e.g. Mittet and Schaug-Pettersen, 2008; Sinha *et al.*, 1990). Regardless of the reason, we note that introducing time in a waveform in which the transmitter is off decreases the integrated output current and therefore the cumulative signal-to-noise ratio. Thus we primarily consider binary waveforms in this work. However, the mathematical development presented here applies equally well to ternary waveforms with one small addition, which we note after the main development.

The family of binary waveforms may be divided into three classes based on symmetry: asymmetric, singly symmetric, and doubly symmetric. In a singly symmetric waveform, the second half of the waveform is either the mirror image of the first half or the mirror image with reversed polarity. (Note that to avoid confusion we refer to these as "mirror" and "rotational" symmetry respectively and restrict the use of the classical terms "even" and "odd" to the discussion of harmonic numbers.) In a doubly symmetric waveform, each half of the waveform is itself composed of two symmetric halves. For the waveform to be doubly symmetric, the quarter symmetry must be opposite in sense to the half symmetry; i.e. if the waveform is rotationally symmetric about its center, then the quarters must have mirror symmetry. The square wave is an example of a doubly symmetric waveform with rotational half symmetry and mirror quarter symmetry. Figure 2.1 shows examples of the three classes. Note that doubly symmetric waveforms

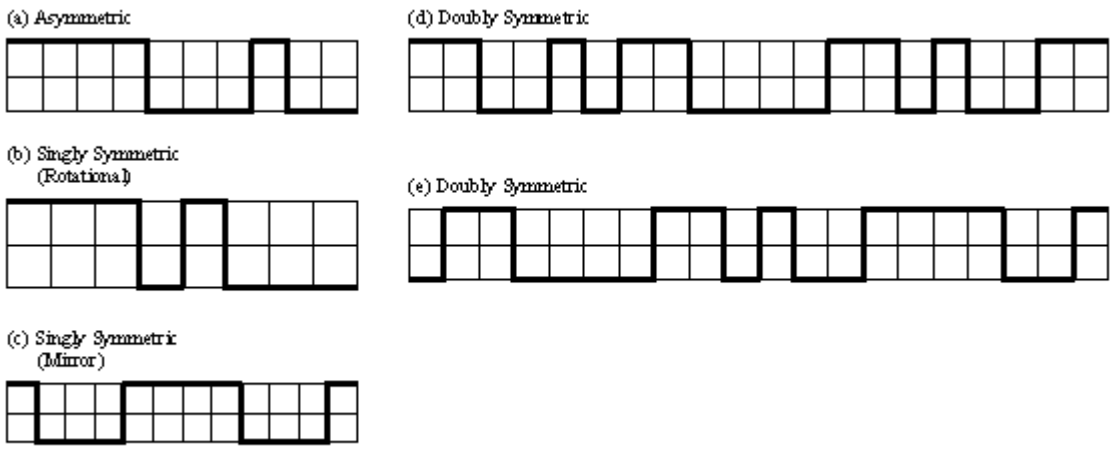

Figure 2.1 Waveform classes.
Examples of the three classes of waveforms: (a) asymmetric, (b) singly symmetric with rotational symmetry, (c) singly symmetric with mirror symmetry, and (d) and (e) doubly symmetric. Note that waveform (e) is merely waveform (d) shifted 90 degrees. This is the waveform currently in use by our group.

are constructed of an asymmetric segment which is repeated four times with alternating symmetry: rotational, mirror, rotational; or mirror, rotational, mirror. The slight change in ordering corresponds to a 90 degree shift of the waveform as is shown in plots (d) and (e) of Figure 2.1.

To evaluate the usefulness of a particular class of waveforms for CSEM and other frequency domain exploration techniques, we examine the familiar Fourier series expansion given by equations 2.1 to 2.4:

$$f(t) = a_0 + \sum_{n=1}^{\infty} a_n \cos(2\pi nt/T) + \sum_{n=1}^{\infty} b_n \sin(2\pi nt/T) \tag{2.1}$$

where $a_0 = \frac{1}{T}\int_{-T/2}^{T/2} f(t)\, dt$ (2.2)

$$a_n = \frac{2}{T}\int_{-T/2}^{T/2} f(t) \cos(2\pi nt/T)\, dt \tag{2.3}$$

$$b_n = \frac{2}{T}\int_{-T/2}^{T/2} f(t) \sin(2\pi nt/T)\, dt\,. \tag{2.4}$$

Here *f(t)* is the time domain representation of a waveform, *T* is the time length of one full wave, *t* is time, and *n* is the harmonic number. Equation 2.1 is a statement of the Fourier theorem, namely that any waveform can be decomposed into parts with mirror and rotational symmetry about *t=0*. Equation 2.2 is the mean of the waveform (i.e. its DC component). Equations 2.3 and 2.4 are the frequency domain amplitude coefficients of the *n*th harmonics and correspond respectively to sinusoidal components with mirror symmetry about *t=0* and rotational symmetry about *t=0*.

Equation 2.2 is zero unless the waveform has a non-zero mean. In practice, a non-zero mean has several undesirable side effects which should be avoided. First, it indicates a polarizing waveform which, in a marine environment, accelerates the destruction of the current carrying electrodes through ablation. Second, a non-zero mean indicates that some of the total power of the waveform is in the DC component. Since total power is finite and conserved, a non-zero DC component indicates that the frequency domain components have less overall power and thus lower signal-to-noise ratio (SNR). Though one might surmise that the non-zero mean produced by a polarizing waveform could be useful as a proxy for DC measurements, it will be confounded by various sources of self-potential across the receiver electrodes and, therefore, likely useless.

In equations 2.3 and 2.4, when *f(t)* has rotationally symmetric halves $a_n = 0$, and when *f(t)* has mirror symmetric halves $b_n = 0$, for all *n*. If the waveform is doubly symmetric, the even values of *n* cancel, leaving only odd harmonics (as is the case for the square wave).

When *f(t)* is binary or ternary, the integrals in equations 2.3 and 2.4 are trivial to solve because *f(t)* has only the values -1, 1, or 0. Equation 2.3 becomes a sum of sine

terms and equation 2.4 a sum of cosine terms. The coefficients a_n and b_n interact through the oscillatory terms in equation 2.1 to determine the amplitude and phase of the frequency domain harmonics of the waveform. Thus when either a_n or b_n is zero, the output phase will be 0, 90, 180, or 270 degrees.

For an asymmetric waveform, equations 2.2 – 2.4 may all be non-zero, yielding both even and odd harmonics of a variety of magnitudes and phases and in some cases a polarizing non-zero mean. This forms the largest class of waveforms and includes many subclasses such as: pseudo-random binary sequences, which attempt to provide a white signal spectrum; chirps, which sweep through a range of frequencies; and sequential waveforms, in which multiple waveforms of different fundamental frequencies are transmitted sequentially. We experimented with sequential waveforms and found them to produce overly complicated data with the inductive decay from one fundamental frequency contaminating the time series of the next fundamental. Users of any waveform searching technique will want to discard a large number of sequential and polarizing waveforms in the search for a solution.

Singly symmetric waveforms have either non-zero a_n or non-zero b_n for all n, so the phase of each harmonic is a well-controlled multiple of $\pi/2$. Even and odd harmonics may both exist, giving densely spaced frequencies. However, some mirror symmetric waveforms are polarizing.

Doubly symmetric waveforms also have either non-zero a_n or b_n for all n, but due to cancellation are limited to odd harmonics only. They have the desirable quality that it is impossible for doubly symmetric waveforms to be polarizing since they are constructed from a short time segment which is repeated twice in each polarity. Further, they have a

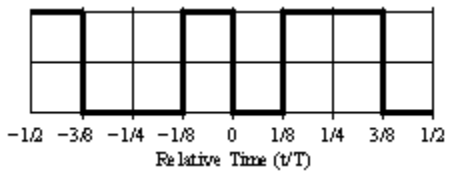

Figure 2.2 Sample doubly-symmetric waveform.
Simple, doubly-symmetric waveform with rotational symmetry in the center and mirror symmetry at the quarters. Its Fourier coefficients are given by Equation 2.5.

discrete mathematical form which makes it simple to search all possible waveforms to find the one which best fits a given set of criteria.

2.3 Finding the Optimal Waveform

To develop the mathematical form we need, we begin with the simple, doubly-symmetric waveform in Figure 2.2. This waveform has rotational symmetry in the center, so all a_n are zero. The solution of equation 2.4 is given by:

$$b_n = \frac{4}{\pi n}\left[\frac{1}{2}\cos(2\pi n\frac{4}{8}) - \cos(2\pi n\frac{3}{8}) + \cos(2\pi n\frac{1}{8}) - \frac{1}{2}\right] \tag{2.5}$$

where we have not simplified the fractions introduced by t to emphasize that each term comes from a specific polarity transition in the waveform. Because $cos(-t) = cos(t)$ and the sign of the polarity change at t is the same as at $-t$, cosine terms from the latter half of the waveform reinforce those in the former half. Thus the equation contains four terms: one for the end, one for the middle, and one for each transition inside the half waveform. This pattern holds true for any doubly symmetric waveform with rotationally symmetric halves. The expansion for the waveform in Figure 2.1(e), for example, has six terms because there are four transitions in the half wave. The expansion of the standard square wave has only the terms for the end and the center because there are no transitions in the half wave. Note in equation 2.5 that when n is even, the terms interfere destructively in pairs, effectively eliminating all even harmonics. If there were an odd number of

transitions in the half wave, then a term would be left unpaired and there would be even harmonics. However, in a doubly-symmetric waveform, the repetition of the quarter wave ensures that there are always an even number of transitions and thus only odd harmonics.

A pattern similar to equation 2.5 can be derived from equation 2.3 in doubly-symmetric waveforms with mirror symmetric halves. However, since a mere shift of 90 degrees changes these to rotationally symmetric halves, we ignore this solution as trivially redundant.

We note that a ternary waveform has the same class of solutions as a binary waveform. The difference is that the off state during each polarity change splits every term in equation 2.5 into two terms with half amplitudes. So, for example, $\cos(2\pi n\ 3/8)$ becomes $\frac{1}{2}\cos(2\pi n\ [3/8 - \delta]) + \frac{1}{2}\cos(2\pi n\ [3/8 + \delta])$, where δ is one half of the off time. The split cosine terms interact destructively, decreasing the amplitude at each frequency. When both n and δ are small, the difference between a ternary and binary waveform is small. However, as either n or δ increases, the decrease in amplitude becomes quite large and results in frequencies with very little usable range. Also, as δ increases, the SNR of the entire waveform decreases because the total output current is diminished. Thus, a binary waveform transmitter is preferred to a ternary waveform transmitter.

The importance of the example given in equation 2.5 is that doubly symmetric waveforms have a simple mathematical form. When searching for new waveforms, there is no need to construct a time series for each possibility and Fourier transform it to get the amplitude of the frequency components. Instead, the spectrum is determined by the time of each transition in the waveform. This suggests that a compact general form may be derived in which the number of cosine terms is a function of the number of transitions.

However, we first note that singly symmetric waveforms have the same solution form as the example in equation 2.5. Because single symmetry allows polarized waveforms, we must take an additional step in order to exclude them from our solution set. This is easily solved by recognizing that in double symmetry the transition times in the second quarter of the waveform are a function of the times in the first quarter. Thus we have a general solution which is parameterized in terms of the number and times of the polarity transitions in the first quarter of the waveform:

$$b_n = \frac{4}{\pi n}\left[\frac{1}{2}\cos(\pi n) - \frac{1}{2} + \sum_{j=1}^{\tau}(-1)^j\left[\cos(2\pi n\, t_j) - \cos\left(2\pi n\left\{\frac{T}{2} + t_j\right\}\right)\right]\right] \tag{2.6}$$

where T is the total length of the waveform in time, τ is the number of transitions in the first quarter, and t_j is the time of each transition in that quarter expressed as a function of T.

While transitions can theoretically be placed infinitely close to one another, in reality, digitally controlled hardware involved in both the transmitter and receiver imposes limitations on switching and sampling rates. Most importantly, the waveform transitions are discretized by the switching frequency of the transmitter. Our present transmitter, for example, runs at 400 Hz, so any waveform it produces must have polarity transitions which are an integer multiple of 2.5 ms apart. Further, to be robustly sampled, a waveform must have transitions that are far enough apart in time (the "minimum time") that they meet certain criteria. First, the minimum time must be long enough to allow the transmitter to reach full output power after switching. This time is highly dependent on the electronic components of the transmitter and the inductance of the antenna and must

be experimentally determined. Second, according to the sampling theorem, the minimum time must be long enough to allow the receiver to sample a transition.

With these limitations, the number of possible waveforms decreases from infinity to a reasonable number. For example, for a 1 second waveform, a transmitter able to switch at 400 Hz, a receiver sampling at 50 Hz, and requiring a minimum of 2 receiver samples of minimum time, there are 60,331 possible doubly-symmetric waveforms. A simple MATLAB program using equation 2.6 to inspect every possible waveform for one that matches a given criterion (e.g. the highest amplitude of the sum of the 3^{rd} & 7^{th} harmonics) takes about 12 seconds on an ordinary laptop.

There are cases where there are too many possible waveforms to make searching the entire set practical. (For example, for an 8 second waveform with the same criteria as above, there are well over 10^{17} doubly symmetric waveforms!) In this situation, it is advisable to combine our analytic formulation with a stochastic search method such as Monte Carlo in order to find a suitable waveform in a reasonable amount of time. While such a method cannot be said to find the one optimal waveform fitting the criterion, it may certainly find one suitable for exploration purposes.

2.4 The Waveform in Practice

Since in the CSEM method higher frequencies attenuate more rapidly and are limited to sensing shallower structure, choice of frequency is important. Model studies of 1D synthetic data show that having two widely spaced frequencies improves the resolution of inversion results (Key, 2009). Key also shows that for synthetic modeling, there is no benefit to having a dense collection of frequencies because the earth transfer

function varies smoothly in frequency. We note, however, that while a forward model of a target survey area may identify a preferred frequency, unexpected geologic conditions may interfere and shift the peak response. There may also be enough uncertainty regarding the earth structure to be explored that an optimal frequency cannot be determined a priori. Additionally, noise encountered in the marine environment is commonly band limited and may adversely affect one or more target frequencies. It is often difficult to predict the frequency of such noise ahead of time, so having a broad spectrum of frequencies is desirable to mitigate these effects. While using a square wave provides one decade of frequencies with harmonic amplitudes above 10% of the peak current, most of the signal is concentrated in the fundamental with the next frequency available (the third harmonic) at only 42% amplitude.

We used the process described in the preceding section to search for a waveform with maximum amplitude in the third and seventh harmonics. Setting the target frequency as the third harmonic rather than the fundamental allows for the lowest frequency to establish background structure or to provide a safeguard if the estimated optimal frequency is too high. Also, increasing power in the seventh harmonic ensures higher amplitude across at least one half decade of frequency.

Table 2.1 The harmonic amplitudes and phases of the doubly-symmetric waveform shown in Figure 2.1(d) and compared with other commonly used waveforms in Figures 2.3 and 2.4. Only harmonics with an amplitude > 0.10 are shown.

Harmonic Number	Amplitude	Phase	Harmonic Number	Amplitude	Phase
1	0.35	0	13	0.40	0
3	0.88	0	17	0.16	180
5	0.25	0	23	0.12	0
7	0.74	180	27	0.19	180
9	0.24	0	33	0.16	0
11	0.20	180	47	0.11	180

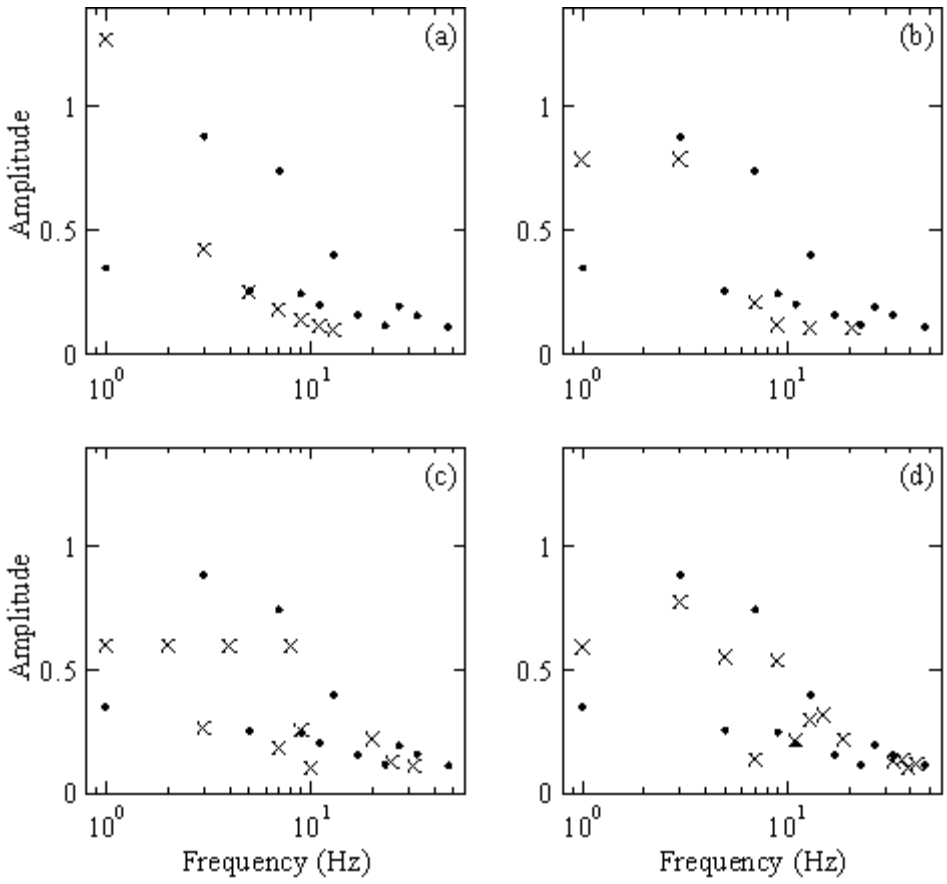

Figure 2.3 Waveform amplitude comparisons.

Comparison of the amplitudes of the waveform D (filled circles) with several other waveforms in use (crosses). Frequencies whose amplitudes are below 0.1 of peak current have been excluded. Comparison waveforms are from (a) a square wave, (b) the Cox waveform, (c) the LS waveform, and (d) the MSP waveform. The x-axis is log10 frequency. The fundamental for each waveform is set to 1 Hz and the peak output current to 1.0. All harmonics are odd integers with the exception of the LS waveform, which is asymmetric and thus has some even harmonics.

We discovered the waveform shown in Figure 2.1(d) (hereinafter referred to as "D") and whose output amplitudes are listed in Table 2.1. In Figure 2.3(a), we compare waveform D to a square wave. The amplitude of the fundamental is 0.35, which is low. However, the power has been spread to higher frequencies so that the 1/n fall-off observed in the higher harmonics of the square wave is mimicked but at higher amplitude. The highest harmonic above 10% amplitude is the 47^{th} harmonic and the total spread of frequencies above 10% covers nearly two decades.

Figure 2.3(b) compares waveform D with the doubly-symmetric ternary waveform presented by Constable and Cox (1996) (hereinafter referred to as "Cox"). The Cox waveform has amplitude concentrated in the first and third harmonics with each at about 78%. Most other harmonics are low, with total coverage above 10% just passing a decade in frequency. We note that for this ternary waveform the output current is off for 31% of the time, significantly reducing the signal-to-noise ratio of all frequencies when compared with a binary waveform with the same peak-to-peak output current.

ExxonMobil have patented several waveforms with equal power in a series of pseudo-logarithmically spaced frequencies covering one decade (Lu and Srnka, 2005). These are asymmetric, polarizing waveforms. However, for comparison we show in Figure 2.3(c) the waveform with the broadest frequency range for which timing is provided in the patent filing (hereinafter referred to as "LS"). The LS waveform was designed to mimic a pseudo-random binary sequence in which the output amplitude is approximately 60% for the 1^{st}, 2^{nd}, 4^{th}, and 8^{th} harmonics. Because it is an asymmetric waveform, it has both even and odd harmonics and the total output power, which is conserved, is divided among more harmonics than a symmetric waveform. Many harmonics have close to zero amplitude and those above the 8^{th} harmonic fall off rapidly. Nevertheless, the total frequency coverage above 10% is almost 1.5 decades.

Mittet and Schaug-Pettersen (2008) presented three waveforms of which we compare the one with the broadest frequency range (hereinafter referred to as "MSP") in Figure 2.3(d). Since timings are not provided in their paper, we have approximated the waveform from their figure 4. The amplitudes of the 1^{st}, 5^{th}, and 9^{th} harmonics are almost

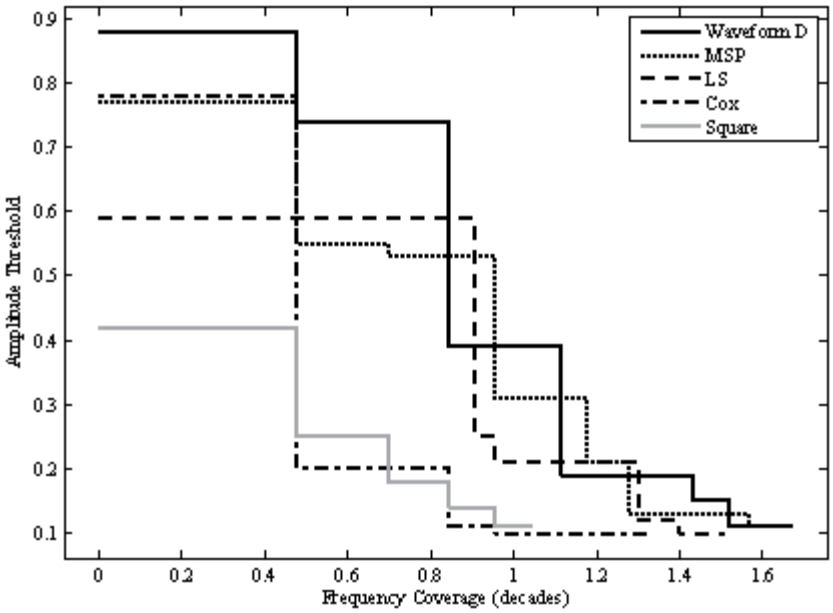

Figure 2.4 Waveform amplitude threshold versus frequency coverage.
Plot of amplitude threshold versus frequency coverage for the waveforms compared in Figure 2.3. For a given output amplitude threshold, the plot shows the number of decades of frequency between the fundamental and the highest harmonic above the threshold. The D and MSP waveforms have similarly broad frequency coverage, though waveform D has an advantage in the first decade. Total coverage is ~1.7 decades at an amplitude threshold of 0.1 (i.e. 10% output amplitude).

60% while the 3rd harmonic is about 70%. Higher harmonics fall off at a rate similar to waveform D.

Figure 2.4 is a comparison of the frequency coverage of the five waveforms discussed above. For each waveform, we plot the frequency coverage between the fundamental and the highest harmonic above a given output amplitude threshold, where the frequency coverage is defined as the difference of the $\log_{10}$ harmonic frequency and fundamental frequency. For example, for the Cox waveform, there is a little less than half a decade of frequency coverage provided by harmonics above a 0.3 amplitude threshold. Note that we use the fundamental as the low end of the frequency band regardless of its amplitude because it has a large skin depth compared to the harmonics and therefore the longest range detection, even when its amplitude is suppressed. Through the whole range

of cut-off thresholds, waveforms D and MSP perform similarly. However, waveform D has a slight signal-to-noise ratio advantage in the first decade.

In the waveforms shown in Figures 2.3 and 2.4, some effort has been made by the various authors to retain output power in the fundamental frequency; whereas we placed no constraint on the fundamental, sacrificing its amplitude for enhanced higher harmonics. We believe that this approach is beneficial for three reasons. First, lower frequencies have lower attenuation, thus propagating farther than higher frequencies even at reduced transmission amplitudes, so higher amplitude is not necessary. Second, one may want to scale the waveform so that the peak amplitude harmonic is the frequency that is most sensitive to the target structure, and yet still be able to bracket it with frequencies on both the high and low sides. Having at least one lower frequency provides either data to help resolve background structure or insurance in case the target frequency turns out to have been set too high. Last, because output power is conserved, decreased amplitude in the fundamental is associated with elevated amplitudes in higher harmonics. Waveforms like those shown in Figure 2.3, in which the amplitude of the fundamental is kept high, may be decreasing the effective range of the higher frequencies.

We have now used waveform D in three large surveys: in 2008 in the Gulf of Mexico to study hydrates (Weitemeyer and Constable, 2010), in 2009 off the coast of Australia to study the Scarborough hydrocarbon reservoir (Myer *et al.*, 2010), and in 2010 off the coast of Nicaragua to study a subduction zone. We have usually selected a fundamental of 0.25 Hz. Figure 2.5 is a plot of amplitude versus range from the Scarborough survey off the northwest shelf of Australia. The survey is in 1 km of water with several kilometers of conductive sediments overlaying a resistive basement (a

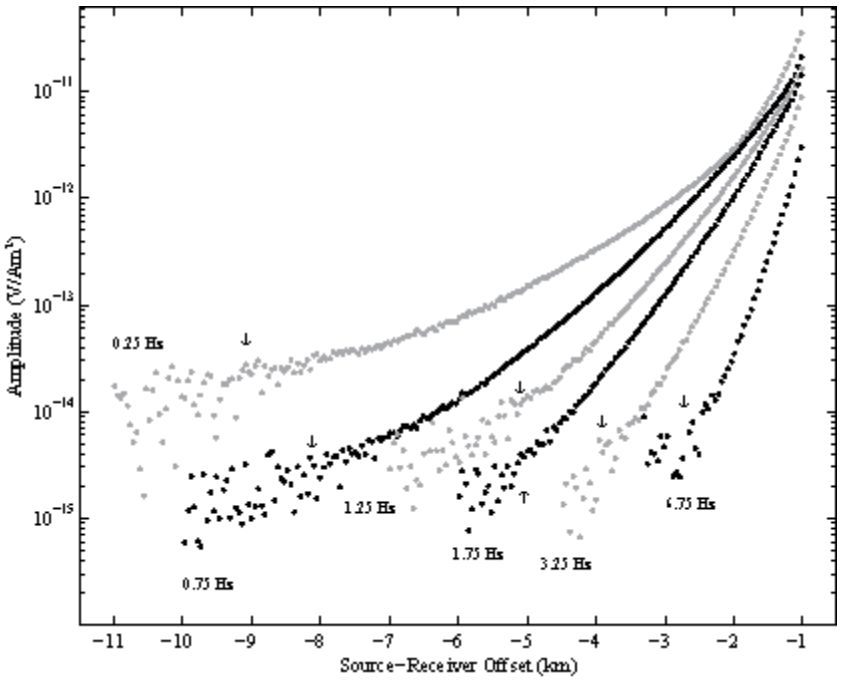

Figure 2.5 Waveform D amplitudes from a recent survey.
Inline horizontal electric field amplitude versus range data from a recent CSEM survey over the Scarborough hydrocarbon reservoir using waveform D. Arrows indicate the range at which each frequency's data reaches SNR=1. The augmented amplitude of the 3rd harmonic (0.75 Hz) has raised its SNR sufficiently that it is detected to ranges that are within 1-2 km of the fundamental. Though the lower amplitude of the fundamental has limited its detection range, this does not adversely impact its usefulness in multi-frequency inversion.

common hydrocarbon target scenario). From the amplitudes of the frequency components shown in Figure 2.3(a), one might expect that the 3rd harmonic, which has an amplitude of 0.88, should be detectable above the noise floor to farther ranges than the fundamental, whose amplitude is only 0.35. However, the data shown in Figure 2.5 indicate that this is not the case. This is due to the complicated manner in which the SNR is affected by amplitude and frequency.

The maximum detection range for the electric field, which we define as the range at which the SNR declines to less than 1, is a function of the field's exponential decay rate. The decay rate is frequency dependent, such that higher frequencies approach the noise floor at a much steeper angle with increasing range than lower frequencies. Thus,

even though changes in the amplitude of a source field frequency component affect its SNR linearly, the effect on maximum detection range is non-linear. As depicted in Figure 2.5, raising the amplitude of the 3rd harmonic raised its SNR sufficiently that it is detected to ranges that are within 1-2 km of the fundamental. Conversely, lowering the amplitude of the fundamental lowered its SNR and limited its detection range, though not adversely impacting its usefulness in multi-frequency inversion. Evidently, waveform D has achieved a good balance between these two frequencies in a common hydrocarbon target scenario. We note, however, that the rate of electric field decay is also related to conductivity structure, and in a more resistive environment (e.g. sub-basalt hydrocarbon targets, mid-ocean ridges, etc.) the higher harmonics will also decay slowly. Explorers in these environments may find benefit in designing a new waveform which augments harmonics that are over a decade above the fundamental. The mathematical process described in the previous section can easily accommodate this.

2.5 Time Series Processing

Compact waveforms such as those discussed above lend themselves to particular statistical methods in processing. In the frequency domain CSEM method, the data of interest are not the time series, but the transfer function estimates derived in the frequency domain. Workers in the CSEM method have not generally used the term "transfer function" because they have focused on the change in amplitude and phase at one particular frequency over range. However, the CSEM response function also varies in frequency. With the growing use of multi-frequency inversion, we prefer the term transfer function (TF). In a typical TF estimate, the cross-spectrum of the input with the

output signal is divided by the auto-spectrum of the input signal to derive the earth-system transfer function (Bendat and Piersol, 2000, Ch. 6). Since the CSEM input signal is known, auto- and cross-spectral techniques are not necessary. Instead, the Fourier transform of the receiver time series is simply divided by the complex Fourier components of the input signal (i.e. the output current measured at the transmitter). The result is then normalized by the source dipole length and corrected for the response function of the receiver. Because the whole process is linear, a number of statistical techniques may be applied to decrease spectral leakage, decrease the noise floor, and derive a variance estimate for each complex transfer function.

In general, TF estimates are not necessary for very short time windows since the CSEM response varies smoothly in time. Typical transmitter tow velocities are on the order of 0.5-1.0 m/s (1-2 knots), so one minute of time series represents less than a typical antenna length. Though the movement of the transmitter means that the data are not statistically stationary, they are assumed to be so and it is common practice to apply a FFT to time series windows that are one or more minutes long and ignore any bias which may be introduced (e.g. Behrens, 2005). In Figure 2.6, we quantify this bias using a simple three layer model and the 1D CSEM modeling code of Key (2009), which we have modified to support a finite dipole source rather than a point dipole. The model is composed of a 1 km thick, 0.3 Ωm seawater layer between half-spaces of air (10^{12} Ωm) and sediment (1 Ωm). The transmitter is 50 m above the seafloor and is given a dipole length of 250 m. We calculate the inline response at receiver positions spaced at every meter between 500 – 2500 m for 31 frequencies between 0.1 and 10 Hz. Assuming a transmitter velocity of 1 m/s, these data points are also spaced every second in time. We

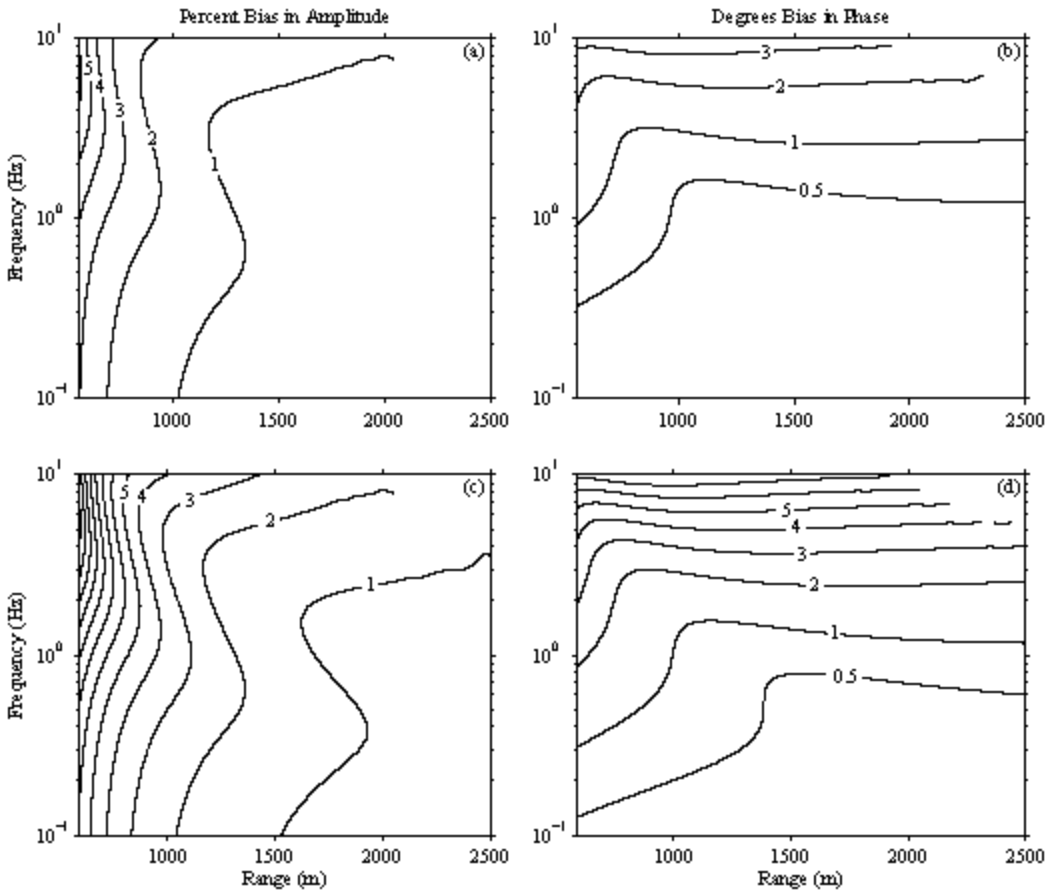

Figure 2.6 Stacking bias in amplitude and phase.

Percent bias in amplitude (a) and degrees bias in phase (b) due to non-stationarity of the CSEM source calculated for a two minute stack length using a 1D model described in the text. The amplitude bias decreases with range and increases with frequency as expected. The phase bias unexpectedly plateaus to a constant value for each frequency, indicating the complex nature in which the phase velocity is affected by the ocean-seafloor interface. Plots (c) and (d) are for a three minute stack length and illustrate the increase in bias as stack length is increased.

used window lengths of one to three minutes and calculated the percent bias by comparing the mean response of the complex field data within the time window to the response at the center point of the window. Bias is a measure of the curvature in the data being stacked and is therefore primarily a function of the change in the field gradient.

The contours in Figure 2.6 (a) and (b) are the percent bias in amplitude and the bias in phase in degrees, respectively, for a two minute stack length; (c) and (d) are for a three minute stack length. The bias for the one minute stack is insignificant (< 1%) for

range > 700 m and is not plotted. The bias increases with increasing stack window length, as expected. The rapid decline in amplitude bias with range reflects the exponential decay of the electric field and shows that even for the three minute window length, the assumption of stationarity is reasonable after about 1500 m range. However, the bias in phase behaves quite differently than the bias in amplitude, leveling out to a minimum bias per frequency. The sharp turn in the phase bias contours is a strong function of the seafloor resistivity and the leveling of the bias contours is due to the phase velocity in the seafloor being modulated by energy leaking up from the seafloor into the water column. At much farther ranges, where the electric field from the air dominates, the phase velocity will become relatively constant and the phase stacking bias will reduce to zero.

Another problem with using a long time window is contamination by magnetotelluric (MT) signal. The MT signal is a broad-bandwidth EM signal sourced in the ionosphere and impinging everywhere on Earth. It has a red spectrum and while in a marine environment the higher frequencies can be attenuated by the overlying ocean, frequencies below 0.1 Hz are typically measurable. A one minute FFT window in CSEM is subject to spectral leakage by MT signal which contaminates the TF estimate (McFadden and Constable, 1983). Additional similar sources of spectral leakage such as self-potential, electronic drift, and motional inductance may also be present and minimized by the process described below.

First difference pre-whitening is a simple method to reduce spectral contamination that can take advantage of the compact waveform. Without a pre-whitener, the TF estimate for a long time window (e.g. 60 s) is identical to the average of TF estimates for short time windows covering the same time (e.g. fifteen 4 s windows) when

the signal is periodic, so there is no advantage to using a shorter time window. However, with pre-whitening, which is not a linear operation, this no longer holds true. In terms of a red spectral contamination source like MT, first-difference pre-whitening is roughly analogous to a high-pass filter whose corner frequency is a function of the window length. The shorter the time window, the higher the corner. The reason for this is simple. For a given window length *T*, frequencies below about one quarter or one fifth of the lowest frequency that can be derived from the window (i.e. 1/T) will appear in the time series as a linear ramp and can be effectively removed by first difference pre-whitening. Shrinking the time window to the length of one source waveform maximizes the effect of the pre-whitener by moving the cut-off frequency close to the fundamental frequency of the source waveform. Thus if one desires long time window TF estimates (e.g. 60 seconds), it is better to use the shortest time window possible (i.e. one fundamental wavelength long) and average in the frequency domain. When pre-whitening is used, this will yield an improved TF estimate compared to a single, long time window TF estimate.

Equations 2.7 and 2.8 below are the first-difference pre-whitening and post-darkening equations, respectively, where lowercase variables *x* and *y* are samples in the time domain, uppercase variables *X* and *Y* are in the frequency domain, and *F* is the sampling frequency of the receiver (Shumway and Stoffer, 2000, Ch. 3).

$$y_j = x_{j+1} - x_j \tag{2.7}$$

$$X(f) = \frac{Y(f)}{e^{2\pi i f/F} - 1}. \tag{2.8}$$

The pre-whitener is applied in the time domain, the data are Fourier transformed into the frequency domain, then the post-darkener is applied to remove the amplitude and

frequency effects of the filter. First differencing is not as aggressive as some pre-whiteners such as auto-regressive filters; however, it has the advantage that the post-darkening step is analytical and complete; no residual amplitude or phase distortions remain on the data after post-darkening.

In the Scarborough survey data shown in Figure 2.5, we used waveform D with a fundamental frequency of 0.25 Hz. To derive the CSEM data at each receiver, we used an FFT with a 4 second window (i.e. one waveform in length). Each time series window was pre-whitened by first differencing to remove the effects of long-period MT noise. After transformation into the frequency domain, the data were post-darkened to remove the phase and amplitude effects of the pre-whitener. The TF estimates from the 4 s windows were then averaged to yield TF estimates for 60 s windows. With first-differencing, we observe a factor of 2 reduction in the noise floor compared to without differencing. Since we are using a short time window, polynomial noise reduction such as described by Pankratov and Geraskin (2010) is not necessary. Indeed, in a short time window, polynomial noise reduction could have the undesirable effect of partially removing the CSEM signal.

Another practical benefit of the use of the average of short time windows is that it allows derivation of a variance estimate for each stacked TF datum. For each set of data to be averaged, we calculate the variance of the mean using the complex amplitudes. To do this, we use the Bienaymé formula which states that the variance of the mean is the mean of the variances, where the variance of each datum is assumed to be equal (Loeve, 1978). When calculating this value, it is important to consider the decay in amplitude with increasing range. As with the case of stacking bias discussed above, the linear

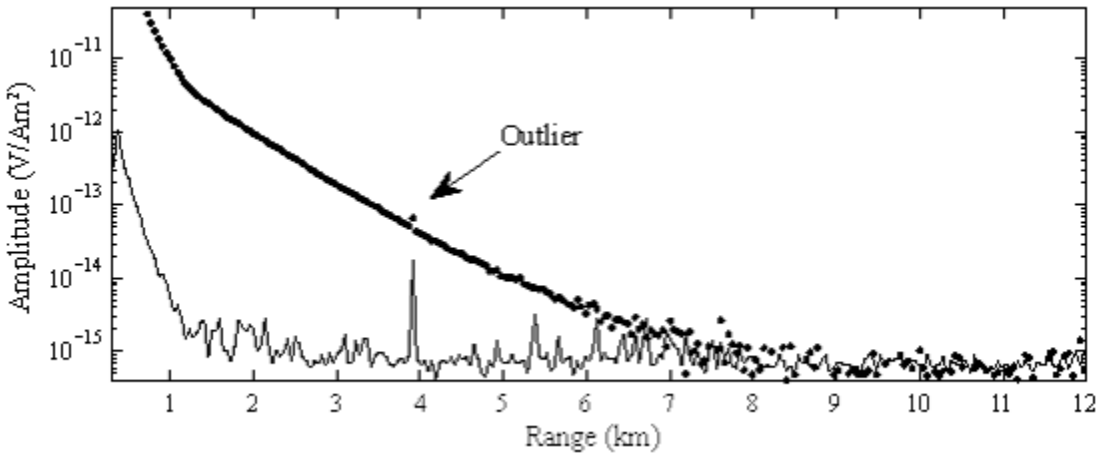

Figure 2.7 Sample 60s stacks with variance estimates and an outlier.
Sixty second 0.75 Hz electric-field transfer function amplitude estimates (filled circles) and variance estimates (line; plotted as standard deviation) from a site in the Scarborough survey. TF estimates are each the mean of fifteen 4 s estimates. Variance estimates are calculated using the procedure described in the text. At close range, the variance estimate is high due to bias from the curvature of the exponential decay. After about 1 km range, the variance settles to the noise floor, as verified by the long range TF data. The outlier identified in the plot is discussed in the text and shown in Figure 2.8.

component of this decay does not bias the use of averages – the average of the amplitudes and the average of the ranges define a point that lies on a linear trend of amplitude with range, and inclusion of the linear part of the decay in our estimation of variance will result in an overestimate. Rather, we remove a linear trend from the data and estimate the variance of the residuals, dividing by the number of data to get the variance in the mean.

Figure 2.7 shows 60 second TF amplitude estimates for 0.75 Hz derived in this way. The variance estimates (plotted as standard deviation) are shown by the thin line below the TF data. At close ranges the variance is inflated by the accentuated curvature of the exponentially decaying signal. This is the bias discussed above and modeled in Figure 2.6. Because it is relatively small (0.1% of signal amplitude or less), we make no attempt to remove it from the TF estimate. After a kilometer in range, the variance estimate settles to a constant value. Since the data also settle to this value at longer

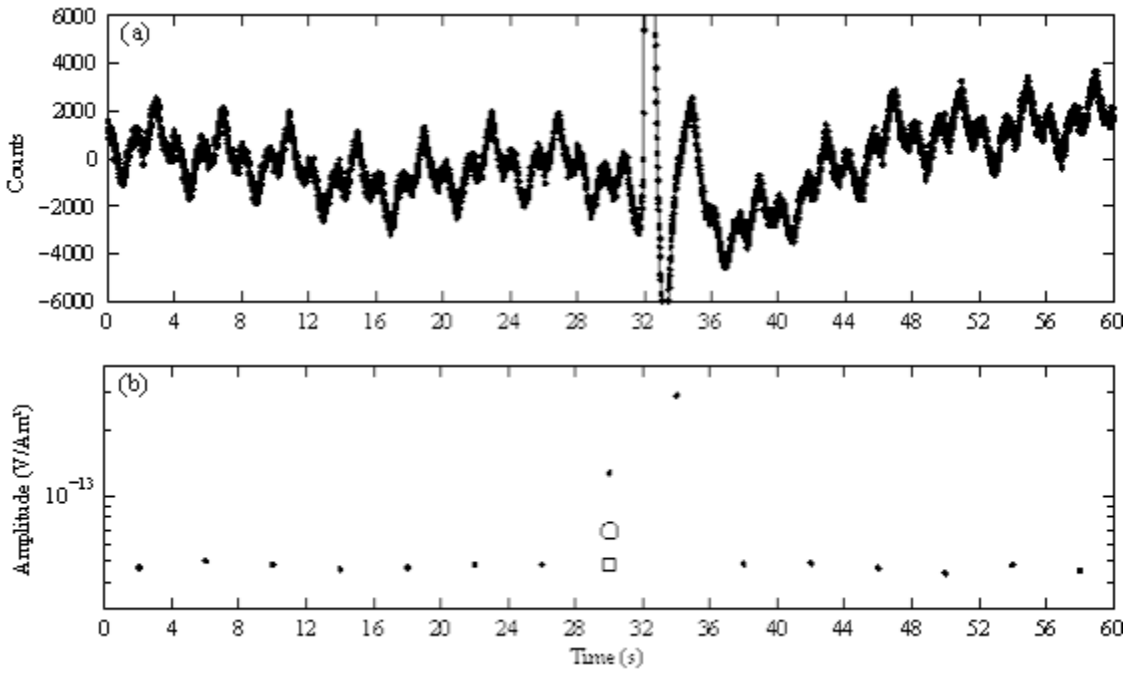

Figure 2.8 The effect of an outlier on stacking.
(a) Sixty seconds of time series from around the outlier shown in Figure 2.7 near 4 km range. The spike in the time series between 28 and 36 seconds is from the activation of an acoustic transponder. (b) The 4 second TF amplitude estimates for 0.75 Hz derived from the time series. Note the outlier values caused by the time series spike. The arithmetic mean of these data (circle) is ~40% higher than the median (square), which is more robust.

ranges, we take it to be the system noise floor and validation that our variance estimation procedure is correct.

Both the long time window and the average of short time windows are subject to bias from noise contamination of the time series as discussed earlier. Brief excursions of the variance from the noise floor in Figure 2.7 indicate points which are biased by noise transients in the time series. An advantage of using the short time window is that the averaging can be replaced with any of a variety of robust stacking techniques. Transient defects in the time series can be common in CSEM data and usually are of very short duration – less than one waveform in length. TF estimates for time windows containing these defects may be abnormally high and consequently can bias the statistical average, which is notoriously sensitive to outliers. In Figure 2.8 we show 60 s of time series from

the Scarborough survey with a short duration defect caused by activation of the receiver's acoustic transponder. Below the time series are the TF estimates for 0.75 Hz showing the outlier points caused by the electric field spike. The circle shows the average of the estimates and the square shows the median, which is less sensitive to outliers. The expected value should lie near and above the 4 s data which are slightly concave upwards because of exponential decay of the electric field. As expected, the median provides a better TF estimate than the mean, which in this example is biased ~40%. For noisier data, more complicated methods than the median may be used to identify outliers and exclude them from the stacking and variance calculations, thus also improving the variance estimation procedure.

It is important to note that the estimate from a long time window is identically sensitive to outliers, since the estimate from a long time window is identical to the average of estimates of short time windows. Had we used 60 s of time series to produce the TF estimate, we would have derived a biased estimate which would have to be discarded. In our procedure, in which we take advantage of the compactness of the waveform to derive short-time TF estimates, the effect of outliers can be reduced or eliminated from the long-time TF estimates, thus increasing the amount and quality of available data.

2.6 Conclusions

Binary and ternary waveform design can be improved by recognizing that the class of doubly-symmetric waveforms has special properties: they are compact, have controlled phase, are never polarizing, and can be described by a close-form solution

which makes searching the entire class tractable on a standard computer. We have searched the class for a waveform in which two of the middle harmonics (3^{rd} and 7^{th}) are maximized and shown with data from a survey off the coast of Australia that the resulting waveform is a reasonable choice for collecting multi-frequency data in hydrocarbon-related CSEM surveys.

The use of compact waveforms allows for more robust statistical methods to be introduced into CSEM time series processing. Using short, waveform-length, time windows and a simple first-difference pre-whitener lessens spectral contamination from magnetotelluric or other low frequency noise. The detailed data may then be robustly stacked to the more typical 60+ s time windows, while reducing bias from time series transients. Variance estimates may also be derived to accurately characterize the instrument noise floor and, at close ranges, the curvature bias from the rapid exponential decay.

Acknowledgements

The authors acknowledge funding support from BHP Billiton and the Seafloor Electromagnetic Methods Consortium at the Scripps Institution of Oceanography. We thank David Jabson for helpful discussion, and Rune Mittet and an anonymous reviewer for many useful suggestions. We thank Phillip K. Dick for inspiring the name of our waveform.

Chapter 2, in full, is a reprint of material as it appears in the Geophysical Journal International, D. Myer, Constable S., and Key K., Blackwell Publishing Ltd., 2011. The dissertation author was the primary investigator and author of this paper.

References

Behrens, J.P., 2005. The Detection of Electrical Anisotropy in 35 Ma Pacific Lithosphere, PhD Thesis, University of California, San Diego, La Jolla.

Bendat, J.S. & Piersol, A.G., 2000. *Random data : analysis and measurement procedures,* 3rd edn, Vol., Wiley, New York.

Constable, S. & Cox, C.S., 1996. Marine controlled-source electromagnetic sounding .2. The PEGASUS experiment, *J. Geophys. Res.-Solid Earth,* 101**,** 5519-5530.

Constable, S. & Srnka, L.J., 2007. An introduction to marine controlled-source electromagnetic methods for hydrocarbon exploration, *Geophysics,* 72**,** WA3-WA12.

Cox, C.S., Constable, S.C., Chave, A.D. & Webb, S.C., 1986. Controlled-source ElectroMagnetic sounding of the oceanic lithosphere, *Nature,* 320**,** 52-54.

Edwards, N., 2005. Marine controlled source electromagnetics: principles, methodologies, future commercial applications, *Surveys in Geophysics,* 26**,** 675-700.

Eidesmo, T., Ellingsrud, S., MacGregor, L.M., Constable, S., Sinha, M.C., Johansen, S., Kong, F.N. & Westerdahl, H., 2002. Sea Bed Logging (SBL), a new method for remote and direct identification of hydrocarbon filled layers in deepwater areas, *First Break,* 20**,** 144-152.

Ellingsrud, S., Eidesmo, T., Johansen, S., Sinha, M.C., MacGregor, L.M. & Constable, S., 2002. Remote sensing of hydrocarbon layers by seabed logging (SBL): Results from a cruise offshore Angola, *The Leading Edge,* 21**,** 972-982.

Key, K., 2009. 1D inversion of multicomponent, multifrequency marine CSEM data: Methodology and synthetic studies for resolving thin resistive layers, *Geophysics,* 74**,** F9-F20.

Loeve, M., 1978. *Probability Theory,* 4th edn, Vol. 45, Springer-Verlag, New York.

Loseth, L.O., Pedersen, H.M., Ursin, B., Amundsen, L. & Ellingsrud, S., 2006. Low-frequency electromagnetic fields in applied geophysics: Waves or diffusion?, *Geophysics,* 71**,** W29-W40.

Lu, X. & Srnka, L.J., 2005. Logarithmic spectrum transmitter waveform for controlled-source electromagnetic surveying: U. S. Patent WO 2005/117326A2.

MacGregor, L., Sinha, M. & Constable, S., 2001. Electrical resistivity structure of the Valu Fa Ridge, Lau Basin, from marine controlled-source electromagnetic sounding, *Geophys. J. Int.,* 146**,** 217-236.

McFadden, P.L. & Constable, S.C., 1983. The estimation and removal of a linear drift from stacked data, *Journal of Geophysics-Zeitschrift Fur Geophysik,* 53**,** 52-58.

Mittet, R. & Schaug-Pettersen, T., 2008. Shaping optimal transmitter waveforms for marine CSEM surveys, *Geophysics,* 73**,** F97-F104.

Myer, D., Constable, S. & Key, K., 2010. A marine EM survey of the Scarborough gas field, Northwest Shelf of Australia, *First Break,* 28**,** 77-82.

Pankratov, O.V. & Geraskin, A.I., 2010. On processing of Controlled Source Electromagnetic (CSEM) Data, *Geologica Acta,* 8**,** 31-49.

Shumway, R.H. & Stoffer, D.S., 2000. *Time series analysis and its applications,* 1st edn, Vol., Springer Verlag, New York.

Sinha, M.C., Patel, P.D., Unsworth, M.J., Owen, T.R.E. & Maccormack, M.R.G., 1990. An Active Source Electromagnetic Sounding System for Marine Use, *Mar. Geophys. Res.,* 12**,** 59-68.

Ward, S.H. & Hohmann, G.W., 1987. 4 Electromagnetic Theory for Geophysical Applications. *in Electromagnetic Methods in Applied Geophysics*, ed. Nabighian, M. N. SEG, Tulsa.

Weitemeyer, K. & Constable, S., 2010. Mapping shallow geology and gas hydrate with marine CSEM surveys, *First Break,* 28**,** 97-102.

Weitemeyer, K.A., Constable, S.C., Key, K.W. & Behrens, J.P., 2006. First results from a marine controlled-source electromagnetic survey to detect gas hydrates offshore Oregon, *Geophysical Research Letters,* 33.

3 Marine CSEM of the Scarborough Gas Field, Part 1: Experimental Design and Data Uncertainty

Abstract

In 2009 we carried out a comprehensive, month-long CSEM survey of the Scarborough gas field on the Exmouth plateau off the northwest coast of Australia. This survey consisted of 144 seafloor instrument deployments and 20 transmitter tow lines with a complex arrangement of in-line and broadside data. The purpose of this survey was to collect a high quality dataset over a known hydrocarbon prospect and use it to further the development of CSEM as a hydrocarbon mapping tool. Here we describe the planning, acquisition, and uncertainty analysis of this survey. We transmitted a complex binary waveform with highest power at 0.75 Hz, where 2D forward model studies showed the strongest sensitivity to the reservoir. Receivers were positioned along both a dense 2D profile crossing the center of the reservoir and in a complex 3D grid covering a more morphologically complex region.

Recent improvements in transmitter navigation and data processing techniques yielded high quality data, from which perturbation analysis of the calculated uncertainties in the transmitter parameters yielded predicted uncertainties in amplitude and phase of just a few percent at close ranges. The uncertainties from perturbation modeling may, however, be underestimated. More accurate uncertainties are calculated by comparing the data from a line of receivers towed twice in opposite directions. Comparing the residuals for each line yields a Gaussian distribution that is directly related to the aggregate uncertainty of the transmitter parameters. For Scarborough, this is 2.8% in amplitude and

2.4% (1.4°) in phase between 2-4 km range and grows at longer ranges due to the decrease in the signal-to-noise ratio. We further show that perturbation analysis of the repeat tow line data allows constraints to be placed on systematic error in the transmitter antenna dip and inline range. For this survey, these values are ±1° and ±5 m, respectively. Both methods show that uncertainties are not equal in amplitude and phase, suggesting that inversion of these data would be better suited in these components rather than in real and imaginary components.

1D inversion of synthetic data shows that the reservoir at 1 km below sea level and the confounding resistive siltstone layer which resides 200 m above it cannot be resolved when only a model smoothness constraint is used. When the constraint is modified to allow for jumps in resistivity at the two resistive layers and when resistivity prejudices are provided, the inversion performs better but still cannot completely resolve the two layers separately, indicating that this level of detail is beyond the single-site CSEM data. Further, when range-dependent error bars derived from Scarborough uncertainties are used, the resolution decreases at a shallower depth than when a fixed error level is used. Inversion of two sample sites from the survey confirms both these results. Additionally, comparison of the inversion models with the expected background derived from well logs suggests an anisotropy in the resistive siltstone layer of about a factor of 2.

3.1 Introduction

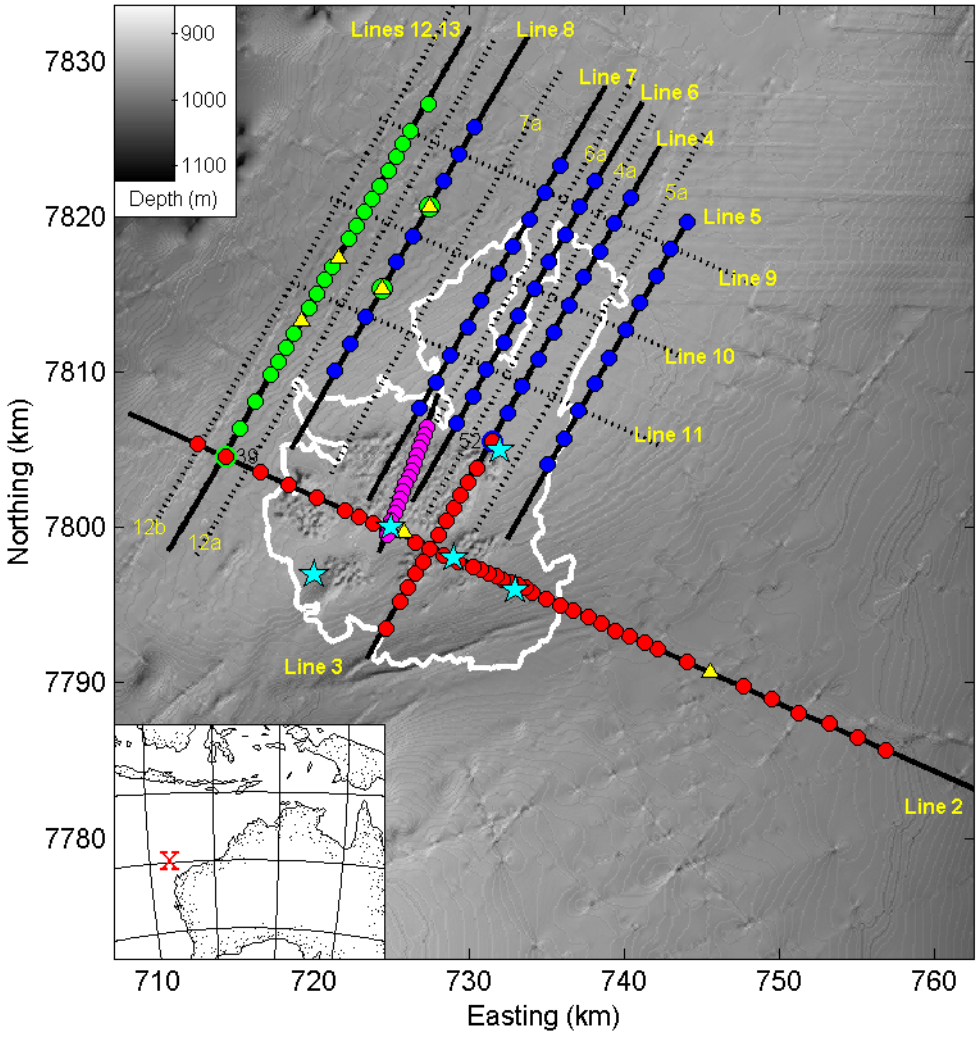

Figure 3.1 Map of the Scarborough Gas Field.
A bathymetric map overlain with the Scarborough instrument deployment locations (filled circles), predicted reservoir outline (white), exploration wells (stars), and tow lines (black lines). The inset shows the survey location off the west coast of Australia. LEMs are shown as yellow triangles. Phases 1-4 are colored red, blue, green, and magenta, respectively. Repeated deployments are shown with two colors. The two LEMs in phase 2 were replaced with OBEMs in phase 3. The primary tow lines are solid lines, secondary tow lines are dotted.

The marine controlled-source electromagnetic method (CSEM) uses an electric current dipole to create a source field that is measured at receivers placed across the seafloor. The electric field diffuses through the earth and contains information about the

electrical conductivity of the seabed. Electrical conductivity in sedimentary sections is largely controlled by the porosity and composition of pore fluids within the sediments. Though the resolution is not as fine-scaled as the wave-propagation of seismics, CSEM surveying is more detailed than a potential method like gravity (Edwards, 2005; MacGregor *et al.*, 2001; Constable and Cox, 1996; Cox *et al.*, 1986). Over the past decade, there has been increasing interest in the use of CSEM for hydrocarbon exploration because of its sensitivity to thin resistive layers embedded in conductive strata. (For recent reviews, see Key (2011), Constable (2010), and Zhdanov (2010).) The race to commercialization has often been leveraged by the use of academically designed equipment such as the Scripps ocean bottom electromagnetic instrument (OBEM) (Constable *et al.*, 1998; Webb *et al.*, 1985) and the Southampton deep-towed active source instrument (Sinha *et al.*, 1990). Although some limited data has been made available to academic researchers (e.g. Newman *et al.*, 2010), the research community has lacked general access to a data set with which to further our understanding of the method. We had the opportunity to remedy this situation by carrying out a comprehensive electromagnetic survey in 2009 over the Scarborough gas reservoir on the Exmouth Plateau, off the northwest shelf of Australia (Figure 3.1).

The Scarborough survey was designed to cover a wide range of geometries and data types in order to demonstrate the effectiveness of marine EM methods for hydrocarbon exploration and to allow for the development and testing of more complex interpretation methods. It was specifically designed to (a) obtain a calibration dataset over a known structure, with control from five wells and excellent 3D seismic data coverage, in order to develop our ability to interpret data with 1D, 2D, and 3D forward

and inverse modeling tools; (b) collect a dataset suitable for joint magnetotelluric, CSEM, and seismic interpretation; (c) investigate the effect of shallow, confounding resistors; (d) understand how to optimize the density and geometry of CSEM receivers and transmitter tows; (e) examine how well CSEM data can differentiate between various reservoir thicknesses and saturations; and (f) examine noise and repeatability in CSEM data collection.

This survey also provided the opportunity to test a considerable number of instrument developments that had been made since our first hydrocarbon survey carried out in 2000 and reported by Ellingsrud *et al.* (2002). The receivers themselves were considerably improved over the 4 channel, 16-bit instrument described by Constable *et al.* (1998). All included 24-bit digitization and 80% of the receivers used a more modern logging system with up to 8 channels of data, allowing the installation of vertical electric field sensors in addition to the standard horizontal electric and magnetic field sensors. The smaller least count allowed us to reduce the gain from 1,000,000 to 10,000, reducing the effects of saturation when the transmitter was near the receivers. The large, front-end coupling capacitors were removed from the electric field amplifiers, which allowed more precise calibrations to be made. Orientations were recorded using external electronic compasses that were mounted as far from the distorting effects of magnetometers and batteries as possible. The seafloor receivers were supplemented by two instruments having twin 100 m antennas configured as gradiometers, to provide increased sensitivity and direct measurements of apparent phase velocity. A 3-axis electric field instrument was towed at a fixed offset of a few hundred meters behind the transmitter to record near-surface variations in conductivity. Our newly developed transmitter was powered by a

400 Hz source in which every cycle was locked to GPS time, producing highly accurate phase data, and included a number of improvements to aid in navigation. The most innovative of these was an inverted long-baseline acoustic ranging system that used transponders towed behind the research vessel. The transmitted waveform had a usable bandwidth that was considerably larger than the traditional square wave, yet remained compact enough to carry out signal processing and noise estimation using recently developed pre-whitening and stacking algorithms. The performance of many of these improvements are discussed in more detail below.

In this paper, we present a review of the design, collection, and processing of this dataset as well as a detailed error analysis, arranged into the following sections. First, we present an overview of the survey area along with pre-survey 1D modeling to highlight some of the challenges. This is followed by a review of the collection and processing of the CSEM data and a qualitative comparison of the data pseudosections with the expected results from modeling. In section 3, we give a detailed analysis of the sources of uncertainty and translate them into a minimum error structure suitable for inversion.

3.2 Survey Design

3.2.1 Scarborough gas field description

The Exmouth plateau (Figure 3.1) is a passive margin between continental and oceanic crust left over from the break-up of Australia and India, and is surrounded on three sides by oceanic crust at abyssal depths. The plateau, which is ~400x600 km, is bounded to the northeast and southwest by transform faults. The transition between continental and oceanic crust to the northwest is thought to be bounded by a sub-

horizontal detachment fault which undercuts the plateau at about 10 km depth, dipping towards the Australian continent (Driscoll and Karner, 1998). Since the Mesozoic era, the plateau has undergone a complex sequence of fracture, extension, uplift, truncation, and subsidence (Lorenzo *et al.*, 1991; Mutter and Larson, 1989; Exon *et al.*, 1982). The result is that the plateau is covered by a number of mostly horizontal sedimentary layers of resistivities varying between 1-10 Ωm.

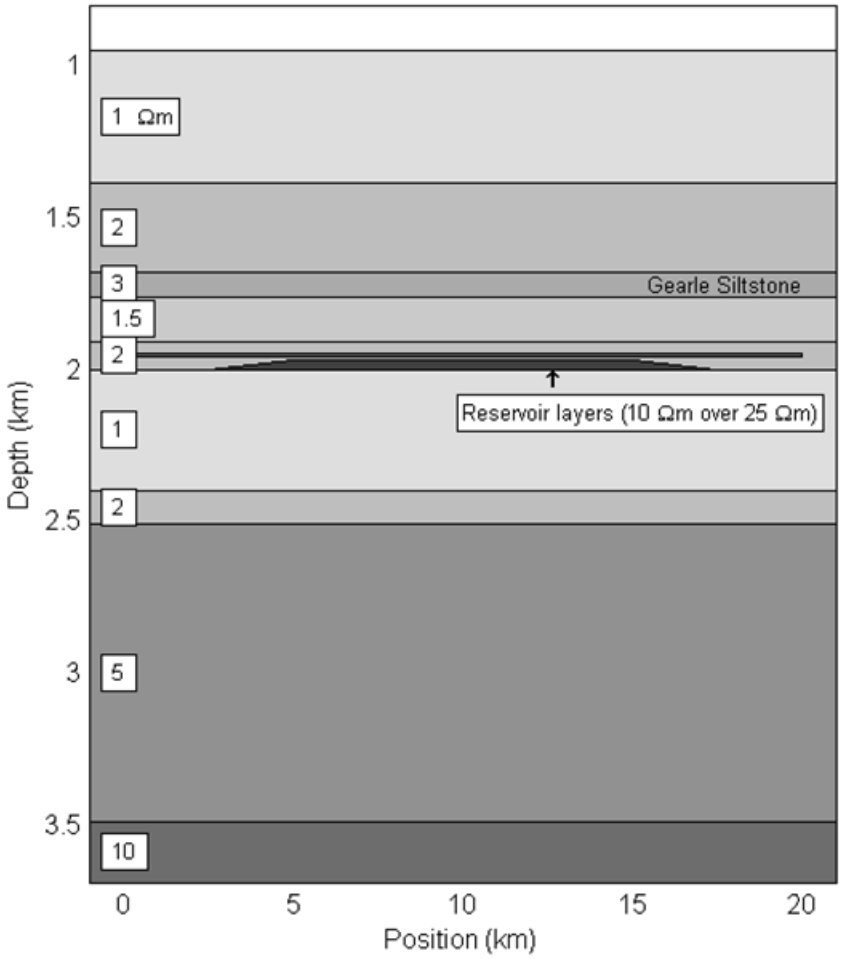

Figure 3.2. Scarborough depth structure.
A section view of the expected geologic background with resistivities for each layer. The reservoir is not a monolithic body, but a stack of thin traps ranging from 6 to 10 Ωm on top of larger body of varying thickness and ~25 Ωm.

Five exploration wells have been drilled in the Scarborough gas field and their data, combined with 3D seismic coverage, were used to define the areal extent and section profile of the reservoir. The white contour in Figure 3.1 is the expected edge of the reservoir – the boundary within which the concentration of gas is expected to be higher than the concentration of water. The reservoir itself (Figure 3.2) is a 20-30 m layer residing between 1900 and 2000 m below sea level (mbsl) in about 900-950 m of water. It has a moderate resistivity of 25 Ωm and is overlain by several thin layers of lower gas saturation with resistivities of 5-10 Ωm. To first order, CSEM is more sensitive to the resistivity-thickness product (*T)* than resistivity alone (Key, 2011; Constable and Weiss, 2006). For the reservoir stack, T is ~1000 Ωm^2, which is less than a factor of 10 above the background value of about 150-200 Ωm^2. In general, T for hydrocarbon saturated reservoirs varies between 10^2-10^5 Ωm^2 and therefore the Scarborough reservoir is a relatively small target. Since it is considered economically viable, it is important to establish the conditions under which CSEM can distinguish a low contrast body such as is found here from the background.

Scarborough presents an additional challenge to CSEM in the form of a confounding resistive layer in the overburden. The Gearle siltstone formation lies a few hundred meters above the reservoir, between 1650-1750 mbsl (Veevers and Johnstone, 1974). Its resistivity-thickness product (300 Ωm^2) is between the background and reservoir, and we expect the heightened electric field transmission through this layer to provide a modicum of shielding to the sensitivity of the reservoir below.

3.2.2 Pre-survey modeling

To characterize the size of the anomaly we expect from Scarborough and to find a suitable frequency range for transmission, we modeled the predicted geology in 2D with and without the reservoir using the finite element code of Key and Ovall (2011). This code uses a parallel, goal-oriented adaptive method to iteratively refine the finite-element mesh, producing electromagnetic responses accurate to a user-specified error tolerance. Here we set a tolerance of 1%. The model without the reservoir is the set of 1D layers shown in Figure 3.2. The reservoir model added a 30 m thick trapezoid with a top width of 10 km, a bottom width of 15 km and 25 Ωm resistivity, overlain by a 10 m x 15 km prism of 10 Ωm separated from the main reservoir by 10 m.

Figure 3.3 shows the difference at multiple frequencies between the two models for a site in the middle of the reservoir. The data for each frequency is excluded when either the range reaches 10 km (i.e. the edge of the reservoir) or the amplitude falls below the typical instrument noise floor of 1e-15 V/Am^2. It has been common practice in CSEM hydrocarbon exploration since the initial survey off Angola to choose 0.25 Hz as the fundamental frequency (Ellingsrud *et al.*, 2002). Our model predicts that this frequency is not particularly sensitive to the configuration of the Scarborough reservoir, producing less than a 20% anomaly in amplitude and 20° in phase. The sensitivity to the reservoir increases with frequency, producing large anomalies at the higher frequencies of 0.75 Hz and 1.75 Hz. However, the maximum acquisition ranges for these frequencies are more constrained due to the increase in attenuation with frequency. Thus, to acquire useful CSEM data, peak output current of the transmitter should be around 1 Hz.

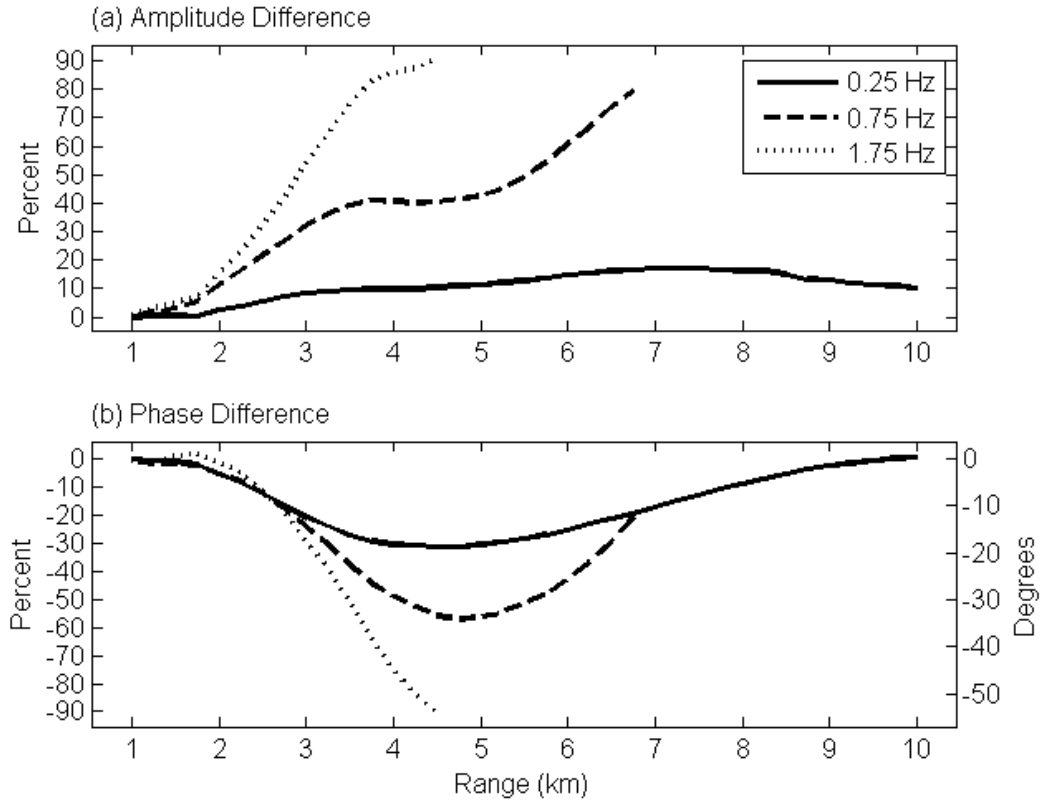

Figure 3.3 On- and off-reservoir model response.
Difference between 2D models of the electric field (a) amplitudes and (b) phases with and without the Scarborough reservoir. The model without the reservoir is the set of 1D layers shown in Figure 3.2. The reservoir model adds a 30 m thick trapezoid with a top width of 10 km, a bottom width of 15 km and 25 Ωm resistivity, overlain by a 10 m x 15 km prism of 10 Ωm separated from the main reservoir by 10 m.

To investigate the level of accuracy required in order to resolve the reservoir, we inverted the forward model data using a variety of realizations of Gaussian noise and the 1D Occam inversion code of Key (2009) specifying a first-difference regularization constraint (i.e. "smooth" inversion). Figure 3.4(a) shows the resulting inversion models. Between 10-15% noise, the reservoir anomaly disappears, leaving just the signal from the confounding Gearle siltstone and relatively little sensitivity to the layers between it and the resistive basement. At the 5% noise level, there is increased resolution to the bottom of the reservoir, but the signals of the Gearle layer and the reservoir are not

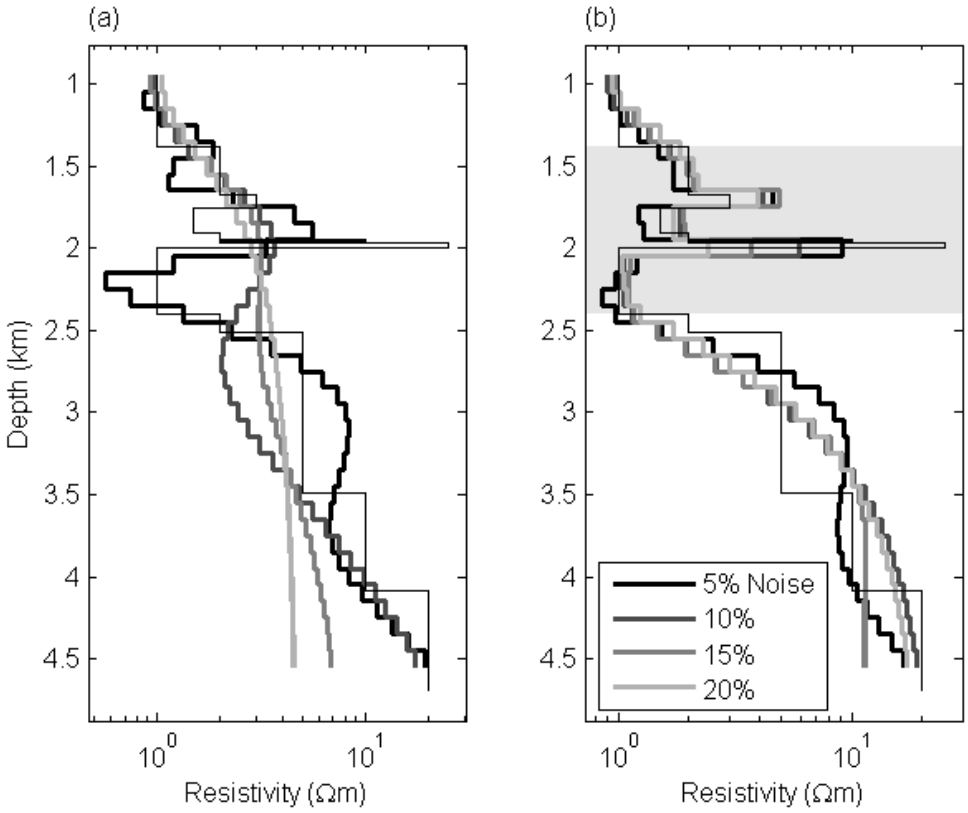

Figure 3.4 Inversion sensitivity tests.

(a) Models resulting from the 1D inversion of the 2D forward model on-reservoir data described in Figure 3.3 with different levels of Gaussian noise added. The thin black line is the forward model. The Gearle and reservoir layers cannot be distinguished separately with a smooth inversion and one needs less than 10% noise to image bottom of Gearle-reservoir complex. (b) Models resulting from 1D inversion in which the roughness penalty has been removed above and below the Gearle and reservoir layers. To stabilize the inversions, a prejudice penalty for deviating from values of 2, 3, 1.5, 2, 1 Ωm is set for the five layers starting with the one above the Gearle, going to the one below the reservoir (demarcated by the grey area on the plot). Though the Gearle and reservoir can now be separated, the resistivity of the Gearle is always overestimated even though there is a penalty for doing so.

distinguishable. Decreasing the noise level to 1% (not shown) produces no significant change over the 5% model.

The scale of structures that can be resolved by the inversion are limited by the smoothness constraint. We tested whether this is responsible for the ambiguity in resolving the reservoir separately from the Gearle by removing the penalty above and below the model layers positioned at the depths of these two geologic layers. To counter

the destabilization this introduces into the inversion, a preference penalty was added to the Gearle and reservoir layers for deviating from 3 and 2 Ωm respectively. This, however, was insufficient guidance to allow separation of the two layers. Instead, the inversion created a large resistive layer between the Gearle and reservoir. So, we increased the guidance given to the inversion by adding preference resistivities of 2, 1.5, and 1 Ωm for the geologic layers above the Gearle, between the Gearle and reservoir, and below the reservoir, respectively. We show in Figure 3.4(b) that with guidance constraints from the regional geology, the presence of separate layers can be determined even up to 20% noise, but that the magnitude of the reservoir declines with rising noise such that it might not be interpreted as a reservoir by the 15% noise level. Curiously, the Gearle layer is over-estimated at all noise levels even though there is a penalty imposed whenever it varies from 3 Ωm. It is likely that the ~200 m spacing between the Gearle and Scarborough reservoir is too small for the diffusive CSEM method to resolve them separately. We expect that any inversion of the Scarborough dataset will have a similar problem.

3.3 Data

3.3.1 Data Collection

We carried out the survey of the Scarborough gas field from 22 May through 23 June, 2009 from the UNOLS research vessel Roger Revelle. Using a fleet of 54 broadband EM receivers, we occupied 144 seafloor sites in four phases. In phase 1, we deployed 40 sites SE to NW across the wide southern portion of the reservoir with site spacing varying from 2 km at the ends to 500 m in the middle. We also deployed a

perpendicular line of 12 sites with a site spacing of 1-2 km. Forty of the instruments measured horizontal magnetic fields and three axes of electric fields, and ten measured only horizontal magnetic and electric fields. The remaining two sites were each deployed as single axis, long-wire EM (LEM) receivers (Webb *et al.*, 1985) configured as gradiometers: two 100 m electrode pairs deployed in series. Sites in phase 1 remained on the seafloor between 5 and 7 days, three days of which were devoted to towing our electric dipole source, the Scripps undersea electromagnetic source instrument (SUESI). On the remaining days, the instruments collected magnetotelluric data which will be reported in a separate publication (Myer, *et al.*, manuscript in prep). The goal of phase 1 was to collect CSEM data over an area of essentially 1D structure.

SUESI was configured with a 250 m electric current dipole which was deep-towed 60 m above the seafloor at an average speed of 0.75 m/s (1.5 knots). It output 300 amps using the binary, broad-spectrum waveform "D" described in Myer *et al.* (2011). Because waveform D puts more power in the 3rd, 7th, and 13th harmonics than the fundamental, we used a 0.25 Hz waveform with peak output in the response frequencies of the reservoir: 0.75, 1.75 and 3.25 Hz. This also allowed us to test the prediction that 0.25 Hz would be relatively insensitive to the reservoir.

We towed the source over the long line twice and refer to these separate tows as lines 1 and 2, though they cover the same receivers. The tow over the perpendicular line is referred to as line 3. During the line 1 tow, we configured and tested a new inverted long-baseline (iLBL) navigation system which uses acoustic ranging from a pair of surface-towed paravanes to triangulate the horizontal location of the transmitter vehicle (Key and Constable, manuscript in prep). Unfortunately, the iLBL system was not fully

functional until after tow line 1, so iLBL navigation solutions are only available for lines 2 and later. Since line 2 is a re-tow of line 1 in the opposite direction, we did not lose any data coverage of the reservoir.

SUESI is equipped with a Kongsberg Simrad 1007 altimeter and a Valeport Midas SVX2 CTDV (conductivity, temperature, depth, and sound velocity) sensor. These sensors provide, among other things, depth and altitude data which are accurate to the centimeter scale. The altimeter readout is continually monitored and digitally recorded so that the depth of the transmitter can be adjusted in real time to ensure that the desired tow height is maintained. A Paroscientific Inc. pressure sensor attached to the far electrode is used in the calculation of antenna dip. Additionally, we deployed an acoustic relay at the end of the antenna to be used in conjunction with the iLBL system to provide navigation of the antenna tail, but a fault in the relay transponder prevented it from functioning. The azimuth of the antenna will be discussed in more detail below.

We recovered all 52 instruments from phase 1 and redeployed 51 of them in phase 2 in a grid pattern of five lines over the northern portion of the reservoir (Figure 3.1). Spacing along the lines is 2 km and between the lines varies between 2 and 6 km. Two sites (51 and 52) from phase 1 were redeployed at the same locations for phase 2 to test the repeatability of CSEM results. Sites were deployed for between 9 and 18 days, with longer deployments corresponding to sites which remained on the seafloor during phase 3. The transmitter was towed continuously for 6.5 days in twelve lines during this phase. Tow lines 4-8 are directly over the lines of receivers. Tow lines 4a-7a run between the lines of receivers and tow lines 9-11 run perpendicular. The goal of this phase was to collect a 3D dataset with a large volume of broadside data and crossing lines over a

morphologically complex body. The geologic model as reflected in the outline in Figure 3.1, indicates that the reservoir, which resides in the distal end of a turbidite fan (Boyd *et al.*, 1992; Haq *et al.*, 1992), splits into two parallel lobes like rabbit ears.

For phase 3, we recovered and redeployed the two LEMs and 23 of the OBEMs from the eastern portion of phase 2. Site 39 from phase 1 was re-occupied and the sites of the two LEMs from phase 2 line 8 were redeployed with OBEMs. The bulk of the instruments were deployed in a single line with 1 or 2 km spacing and the line was towed four times: once in each direction (lines 12 & 13), and broadside on either side (12a & 12b). Instruments were deployed for ~5 days with 2.5 days occupied by towing of the source. At the end of phase 3, all instruments were recovered.

Phase 4 targeted an area of possible hydrates located in the main body of the reservoir and denoted by pock-marks in the bathymetry. Since hydrates are generally shallow, the deep penetration of lower frequencies was not desired, so the fundamental frequency of the transmitter was moved upward to 0.5 Hz and the source dipole was shortened to 50 m. Also, the recording frequency of the receivers was increased from 62.5 Hz to 250 Hz. Sixteen instruments were deployed for less than a day each on a site spacing of 500 m and line 14 was towed directly over them. All equipment was recovered successfully.

For all four phases of this survey, an experimental 3-axis towed electric-field receiver (Vulcan) was tethered 250 m beyond the end of the far electrode of the transmitter (Myer *et al.*, 2010). For phases 1-3, this placed the Vulcan 390 m from the center of the transmitter dipole. In phase 4, in which a shorter dipole was used, a second

Vulcan was added 250 m beyond the first. They were 280 m and 530 m from the center of the transmitter dipole, respectively.

3.3.2 Time Series Processing

Time series data were processed into the frequency domain using the procedure detailed in Myer *et al.* (2011) and summarized here. Data were fast Fourier transformed (FFT) into the frequency domain using a non-overlapping time window which is exactly one waveform long and synchronized with the receiver's minute mark. Since the source waveform is also synchronized with the minute mark and both clocks are independently synchronized to GPS time – the transmitter continuously during transmission and the receiver at the beginning and end of deployment – we expect that the receiver phase will be well controlled and near zero at close approach of the transmitter. (The phase is primarily a measure of signal delay and at close range the delay is nearly zero or 180 degrees, depending on the specific field component.)

To suppress spectral leakage due to the red spectrum caused by time variations in Earth's electromagnetic fields, data are pre-whitened by first-differencing prior to the FFT, then post-darkened in the frequency domain to remove the effects of the first difference operation (Shumway and Stoffer, 2000; Keisler and Rhyne, 1976). Instrument specific calibrations are applied in the frequency domain and electric field data are normalized by the receiver dipole length. All data are presented in the phase "lead" convention (i.e. phase becomes more negative with increasing attenuation).

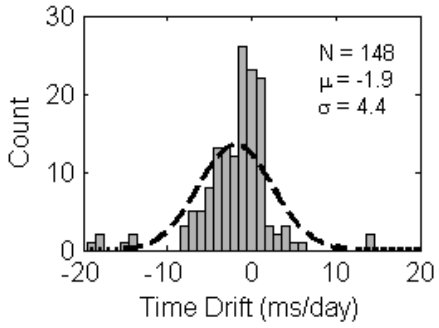

Figure 3.5 Receiver time drift.
Histogram of the time drift calculated for all receiver deployments. The outliers (> ±10 ms/day) are due to an operator error during the startup of the receiver instruments. The dashed line is an ideal Gaussian which has the same mean, standard deviation, and sample size.

Receiver time drift is determined by time synchronization with a GPS clock. Figure 3.5 shows a histogram of time drift values for all receivers in the Scarborough survey. The distribution is steeper than Gaussian with 50% of the deployments having drift rates between ±1.5 ms/day and 79% having rates within the instrument clock specification of ±4.3 ms/day. The time drift introduces a frequency dependent phase shift which we correct in the frequency domain under the assumption that the drift is linear over the course of each deployment.

To calculate the CSEM transfer function, we divide the receiver data by the transmitted source dipole moment (SDM). The SDM varies somewhat throughout the tows, being affected by ablation of the current-carrying electrodes and occasional manual changes in the output current. We continuously record the output current and build a piecewise linear model of the current over time. The receiver field data are divided by this model and by the length of the transmitter dipole to yield final units of V/Am^2 for the electric field transfer functions and nT/Am for the magnetics. The standard deviation of the current measurements from the linear models is 2%, but this is artificially high. We record the RMS of instantaneous current measurements taken over a three second interval

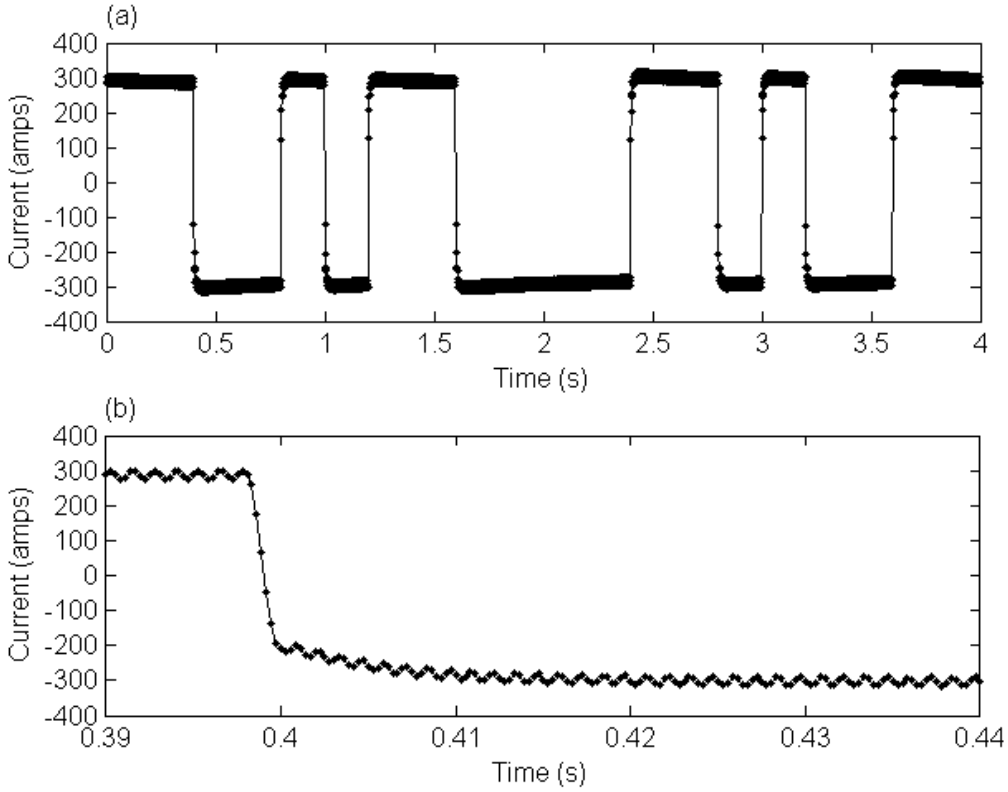

Figure 3.6 Waveform snapshots.
(a) Measurement taken at 600 Hz of the electric current forming the waveform that we used in this experiment. The waveform is scaled to four seconds so that the fundamental is 0.25 Hz. (b) One transition in the waveform sampled at 3600 Hz. The transition takes 1.7 ms with a further 10 ms to settle to its full value. The receivers are recording a data point every 16 ms, so the entire transition occurs in one sample datum. Also visible is the 800 Hz ripple caused by the rectified 400 Hz power source. Most of the ripple has already been smoothed out by the inductance of the antenna during transmission.

and this includes a varying number of polarity transitions. Though the transitions are brief, they represent outliers to which the RMS calculation is especially sensitive. The actual uncertainty in the SDM as estimated from high frequency snapshots of the waveform is probably less than 0.5%.

The next step in processing is to correct for the frequency-dependent scaling of the source waveform. Waveform D has a closed-form mathematical solution for its complex scaling coefficients. However, the theoretical model requires that the switching

in the binary waveform occur in zero time, a feat which is not obtainable with actual electronics. To quantify the effect of finite-time switching, we periodically recorded high frequency snapshots of the waveform measured by an on-board current clamp at the output of the transmitter. Figure 3.6a shows one such snapshot recorded at 600 Hz. SUESI uses fast-switching insulated-gate bipolar transistors which enable it to switch polarity in the waveform without stopping at zero output current (as previous EM transmitters, see for example Constable and Cox, 1996; Sinha *et al.*, 1990). Figure 3.6b shows one transition sampled at 3600 Hz. The polarity change occurs in 1.7 ms and takes an additional 10 ms to settle to its full value. The transmitter creates the output waveform from a rectified 400 Hz power source. This introduces an 800 Hz ripple into the instantaneous output current, visible in the figure, which has been smoothed out by the inductance of the antenna. Further attenuation of the 800 Hz ripple occurs in the seawater associated with the ~10 m skin depth at this frequency.

Multiple snapshots were taken throughout towing and show that the theoretical and practical waveform differ by less than 1%. Furthermore, the waveform changed less than 0.3% over 6.5 days of continuous transmission, even as the transmitter electrodes ablated. We used complex coefficients calculated from the median of the snapshots to scale the transfer functions.

The transfer function data were then phase corrected for linear drift calculated for each receiver's clock and stacked up to one data point per minute using an arithmetic mean. Variances were calculated using the Bienaymé formula on the differences between the amplitudes of the data and a linear trend through them. To first order, this allows the variance to account for actual scatter in the data without being biased by exponential

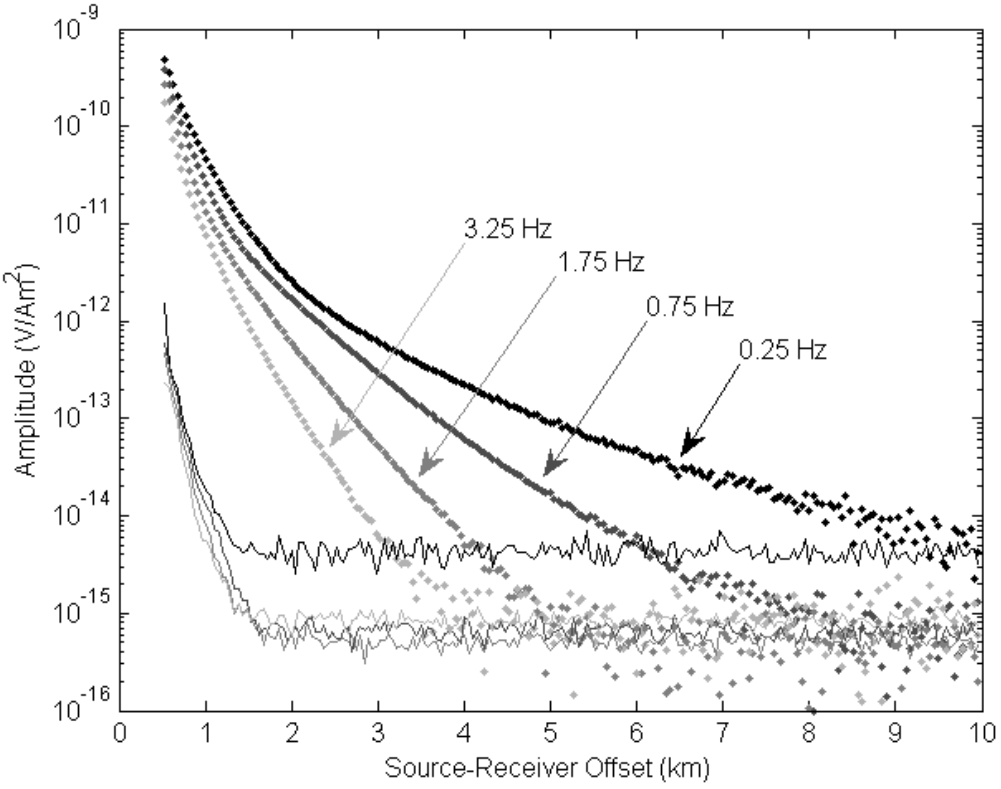

Figure 3.7 Example instrument amplitudes and stacking variances.
Site 1 amplitudes (points) and standard deviations (lines) for the 60 second stacks of the four strongest harmonics: 0.25, 0.75, 1.75, 3.25 Hz. The ramp in the standard deviation at close ranges is due to biases from the finite dipole and stacking.

decay. We find that for ranges greater than ~1.5 km, this variance accurately reflects the noise floor of the instrument at each frequency (Figure 3.7). At closer ranges, the variance shows the increasing bias from both the finite length of the dipole and the changing range of the transmitter.

3.3.3 Pseudosections

Pseudosections of the normalized amplitude data provide a qualitative observation of the performance of each frequency in the detection of the Scarborough reservoir and are a useful approach for rapidly identifying lateral variations in the data. Inline electric field amplitudes for the pseudosections are normalized by the 1D model response of the

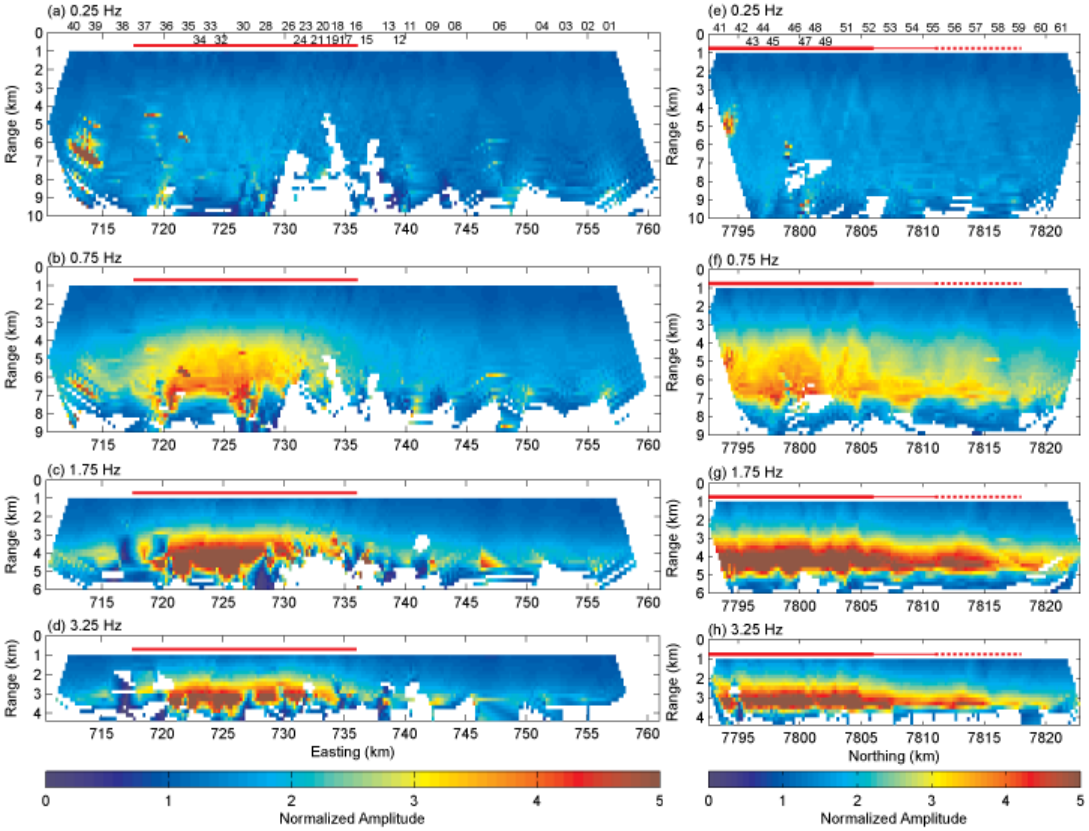

Figure 3.8 Amplitude pseudosections.

(a-d) Amplitude pseudosections for line 2 projected into UTM easting and (e-h) lines 3+4 projected into northing. All pseudosections are normalized by the 1D off reservoir background in Figure 3.2. In line 2, the thick red line marks the expected extent of the reservoir; in lines 3+4, the line thins where the reservoir narrows, and is dotted where the reservoir splits into the "rabbit ears". All figures have 1.5x vertical exaggeration. Data below a signal-to-noise ratio of 2 have been cut out. As predicted by forward modeling, the sensitivity to the reservoir increases with increasing frequency.

off-reservoir Scarborough geology and placed in 200x200 m bins. Each bin is centered at the x-axis location corresponding to the midpoint between the transmitter and receiver and the y-axis location corresponding to the range (source-receiver offset). A gridding algorithm averages the bins and fills empty neighbors with linear interpolants. Data with a signal-to-noise ratio less than 2 are not shown.

Figure 3.8 shows the pseudosections for line 2 and lines 3+4, projected onto easting and northing lines, respectively. The scale is the ratio of the observed amplitudes to the normalizing 1D background, such that a value of 2 indicates a 100% anomaly.

Because CSEM is volume sampling, anomalies tend to get stronger with range as more of the anomalously resistive body enters the volume being sampled by each datum.

The pseudosections agree with our prediction that the 0.25 Hz frequency is relatively insensitive to the reservoir compared to the other frequencies. They also show an anomaly which is clearly stronger with increasing frequency as predicted, even though the usable range is declining. The line 2 pseudosections (a-d) place the reservoir anomaly between 718 and 734 km easting which agrees quite well with the geologic prediction. The higher frequencies, however, continue a 60-80% anomaly across the line. This anomaly may indicate that the geologic background model underestimates the resistivity of some layers, particularly the resistive Gearle siltstone. On the other hand, the reservoir outline in Figure 3.1 is not the precise edge of the reservoir, merely the boundary inside which gas saturation is expected to be above 50%. It may be that the CSEM data are sensitive to the lower gas saturated volume outside the outline. If we had used the common industry practice of normalizing pseudosections by "off-target" sites, this portion of the anomaly would have been normalized out of the pseudosections and the main body of the gas field would have been associated with a smaller anomaly.

The line 3+4 pseudosections (e-h) strike northeast across the body of the reservoir and along the easternmost of the "rabbit ears". The anomaly decreases starting at 7806 km northing, corresponding to a narrowing of the reservoir body about 5 km before the "ears" begin. It is likely that the saturation or thickness of the reservoir begins to decline here, though according to the two highest frequencies, this is a step, not a gradual change towards the edge, indicating the possible location of a structural control on the migration and trapping potential of the reservoir or variations in the deeper source region.

3.4 Error Analysis

3.4.1 Location Uncertainties

The most significant sources of uncertainty in CSEM data are typically the errors in the position and orientation of the receivers and transmitter. Positions are determined by acoustic ranging using a sound velocity profile of the water column. Changes in the water column may alter the sound velocity, so it is important to use local measurements in order to reduce location errors. The Valeport Midas SVX2 instrument mounted on the body of our transmitter continuously measures sound velocity, pressure, temperature, and conductivity. Though the bulk of this time is spent near the seafloor, the transmitter was raised into the water column for every turn and traversed the entire column at the beginning and end of each phase. We found that the sound velocity profile was similar throughout the survey, varying by about 1 m/s at a given depth. A composite sound velocity profile was created from these measurements by binning the data in 10 m bins from 0 - 500 m depth, where the thermocline gives rise to a sharp gradient, then 100 m bins below that. The resulting profile is constructed from the median of each bin and the upper 500 m is smoothed. The final sound velocity profile is shown in Figure 3.9 along with a conductivity profile that is constructed using the same procedure. Smoothing is required on the conductivity profile in order to match the shape of the 24 expendable bathy-thermograph (XBT) casts taken during the survey, and so we apply it to the sound velocity profile as well.

Receiver locations were determined by long base-line acoustic ranging from the ship. For each instrument, there are 40 – 200 range data points acquired from a variety of

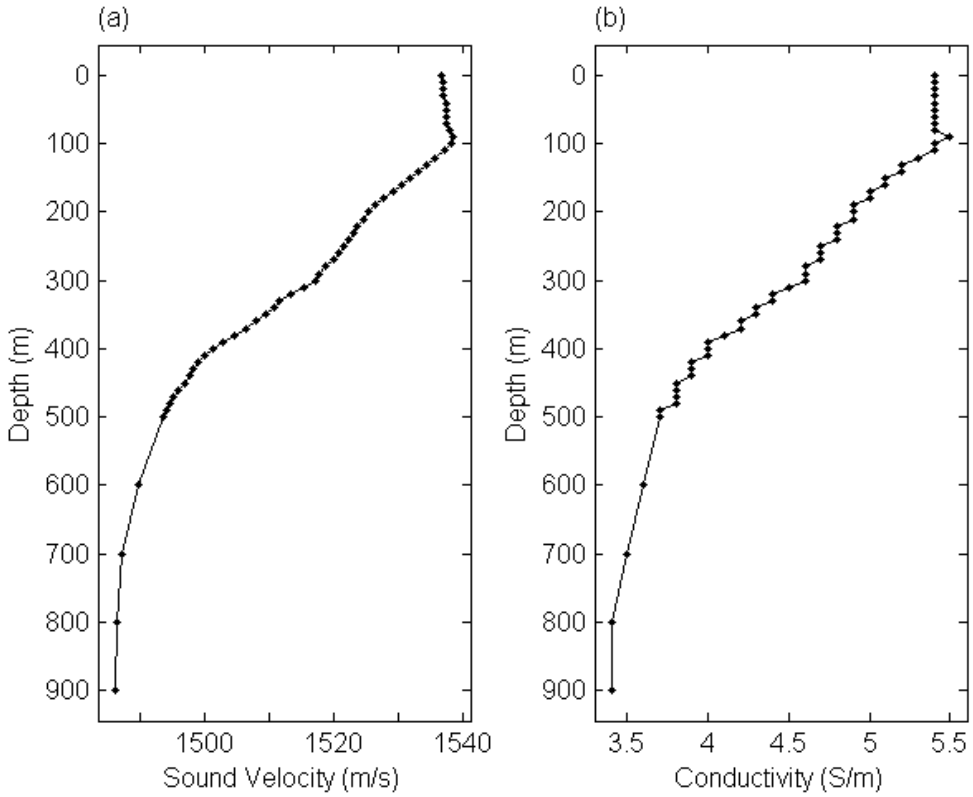

Figure 3.9 Depth profiles.
Composite (a) sound and (b) conductivity profiles for the ocean overlying the Scarborough gas field, created as described in the text.

ship positions. These data points along with GPS ship positions (referenced to WGS-84) were then used in a Levenberg-Marquardt ray-path inversion to solve for the best fitting receiver location. The covariance matrix from this inversion yields 2σ uncertainties on 95% of the site locations of 7 m horizontally and 2 m vertically (Figure 3.10a). The northing and easting components have similar distributions. The vertical component is more tightly constrained because of the steepness of the acoustic ray-paths.

In general during the 950 m free-fall through the water column, half of the receivers drifted horizontally more than 100 m from their drop locations (Figure 3.10b), which indicates the presence of strong currents. Industry practice is to reject any deployment that is farther than 50 m from the planned location. To accomplish this, the

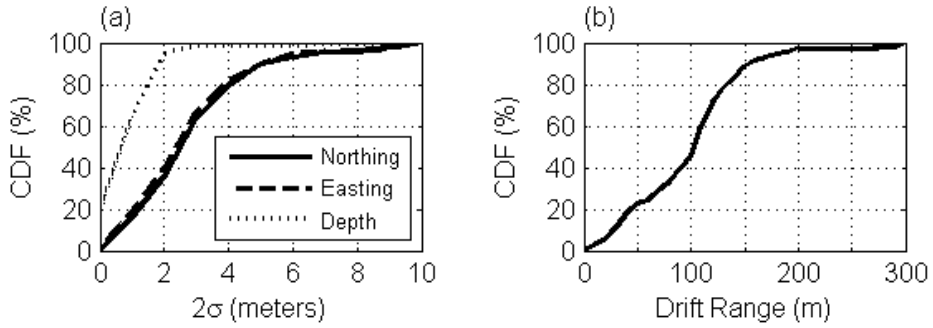

Figure 3.10 Receiver navigation uncertainties and drift.
(a) The cumulative distribution functions for the 2σ errors on receiver positions determined by a Levenburg-Marquardt ray-path inversion. (b) Cumulative distribution function of the drift in range between drop location and landing location for each receiver.

ship must stand-by and wait for a receiver to reach the seafloor, navigate it, then offset the ship position for the next deployment to account for the observed drift. Since drift varies over time, the drift "forecast" must be updated sequentially and receivers which land outside the tolerance zone must be recovered and redeployed. For a large survey such as Scarborough, this adds several days of ship time, at considerable cost. For this project, such deployment accuracy is not required; in-line field components will not be biased by instrument drift since the navigated locations are so well known, and modeling shows that 100 m of cross-line set has a small effect on in-line field components (< 0.5%).

Receiver orientations were measured directly with a compass mounted in a separate pressure case high on the instrument frame where it is less likely to be influenced by the receiver electronics. We performed an independent verification of the compass orientations using the orthogonal Procrustes rotation analysis (OPRA) method described in Key and Lockwood (2010). This method works by simultaneously inverting for the seafloor conductivity and the optimal rotation matrix between the observed data and the data predicted by the conductivity model. This approach allows the OPRA

method to find the orientation of both inline and offline receivers and does not require any a priori assumptions about component polarizations. Here we applied the method to the 0.25 and 0.75 Hz data at ranges of 1-4 km, including both in- and out-tow data. In general, the inversion was able to find the orientations within only a few iterations and most data could be fit to RMS 1.0. Comparing the OPRA-derived orientations with those measured by the compasses (Figure 3.11), we estimate the 2σ orientation error to be 6.6°. For in-line field components, this equates to less than 0.7% uncertainty.

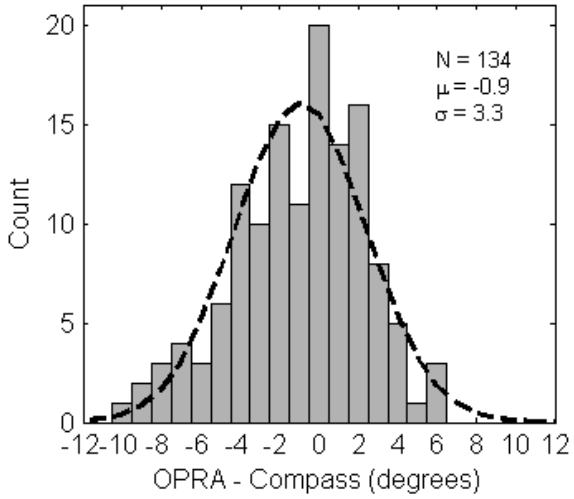

Figure 3.11 External compass validation.
A histogram of the differences between the receiver orientations measured with an in situ magnetic compass and those derived from the OPRA method. The dashed line is an ideal Gaussian which has the same mean, standard deviation, and sample size.

Transmitter locations were determined with the iLBL system. Individual point solutions were then smoothed into a transmitter track and the uncertainties of the in-line and cross-line locations were taken to be the standard deviation of the point solutions from the smoothed track.

The iLBL system uses acoustic ranging to solve for the location of the acoustic unit on the tow vehicle, but not the center of the dipole antenna trailing behind it. The

center of the dipole is the more pertinent value for modeling and inversion, so we estimate its location using the following procedure. For this survey, the near electrode of the dipole began 11 m behind the acoustic unit and consisted of 100 ft of soft copper pipe rigged with syntactic foam to be approximately neutrally buoyant. The far electrode began 261 m behind the acoustic unit and was identical to the near electrode. We calculated the location of the center of the antenna to be 151 m behind the tow vehicle along a straight horizontal line extending from the ship through the transmitter. For phase 4, which targets an area of suspected hydrates, the distance to the far electrode was shortened to 61 m and the copper electrodes were cut down to 10 m, so that the center of the dipole was 41 m behind the transmitter.

The dipole is given a dip corresponding to the difference in depth measurements derived from pressure gauges mounted on the transmitter and at the beginning of the far electrode. We convert pressure to depth using the procedure outlined in Leroy and Parthiot (1998). We measured dip in phases 2 and 3 (Figure 3.12) and found it to be remarkably stable: -5.5+/-0.7 and -5.2+/-0.9 degrees respectively, where negative dip indicates that the far electrode is deeper than the near. We attribute the stability to the flat bathymetry. Though we were towing to achieve a constant altitude, we were able to keep changes of the transmitter depth to a minimum, thus allowing the dipole assembly to trail unperturbed through the water. For phases 2 and 3, we use the dip time series. However, for phases 1 and 4 where we do not have dip measurements, we use a fixed dip value of -5.4 degrees. Additionally, we observe in phases 2 and 3 that it takes about 8 to 10 minutes for the antenna to settle after the transmitter has reached the target depth, so

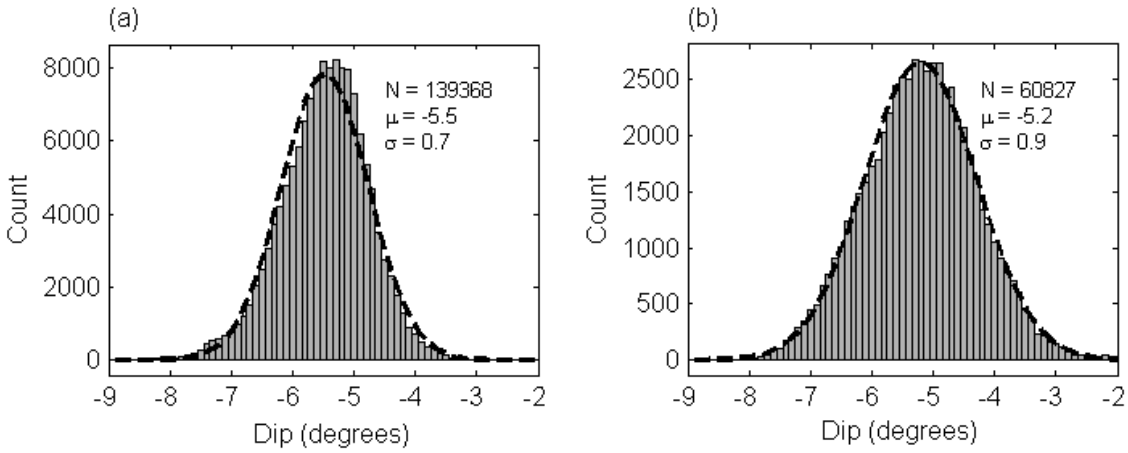

Figure 3.12 Distribution of dip values.
Histograms of dip calculations for (a) phase 2 and (b) phase 3 overlain with an ideal Gaussian (dashed line) which has the same mean, standard deviation, and sample size. Dip calculations are based on the difference between pressure gauges mounted at the transmitter body and the beginning of the far electrode. For both phases, the standard deviation in dip is less than one degree and the average is more than -5°, where negative indicates the head is above the tail.

there may be up to 15 degrees of error in dip in the first 10 minutes of tow for phases 1 and 4 which is not accounted for by the fixed value.

In the absence of acoustic positioning, we assume that the azimuth of the transmitter dipole lies along a line between the transmitter and the ship. On average, 1600 m of 0.680" deep-tow cable was deployed and this corresponds to a sail of ~28 m^2 being pulled sideways through the water. Friction with the water should keep the azimuth of the transmitter equal to the direction of motion; however, the iLBL navigation revealed significant lateral variation in the location of the transmitter with respect to the track line of the ship, so there is some ambiguity in the azimuth of the antenna dipole. Figure 3.13 shows that the cross-line variation of the transmitter position with respect to tow line 2 is up to 100 m. The other lines have similar variations. The tides measured at Broome, West Australia, 1000 km east of the survey area are overlaid in the figure and show that these variations are almost certainly related to tidal action. Since the insulated cables carrying

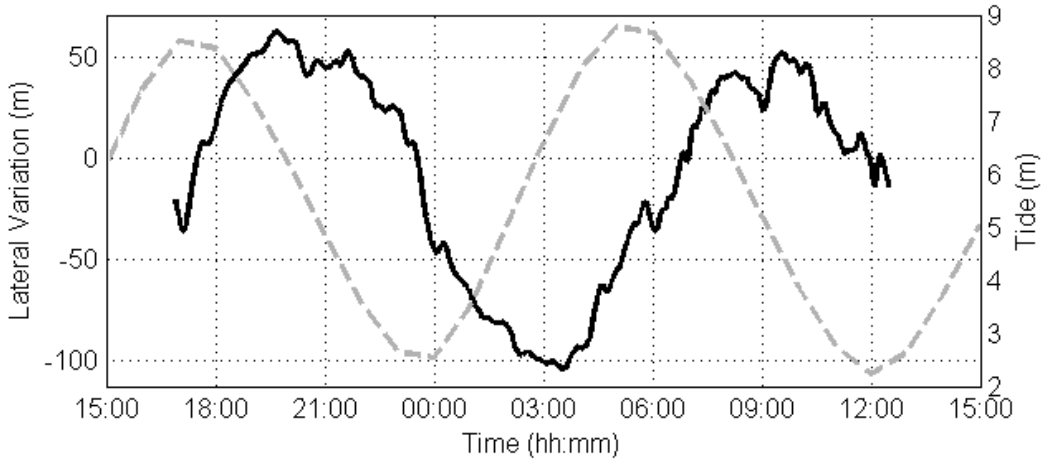

Figure 3.13 Lateral variation of the transmitter body.
Lateral variation of the transmitter with respect to the ship's track line for line 2 (black) superimposed with tides (grey, dashed) for Broome, WA ~1000 km east of Scarborough. The X axis is shown in time so that tidal nature of the lateral variation is more evident. (Tide data from the Australian Baseline Sea Level Monitoring Project at http://www.bom.gov.au/oceanography/projects/abslmp/data/index.shtml).

electric current to the electrodes have a large cross-section, presenting an additional ~15 m^2 to orthogonal currents, it seems likely that deep currents are responsible for the lateral variation. Accordingly, we assume the uncertainty in the transmitter azimuth to be approximately equal to the difference between the transmitter azimuth and line azimuth. The standard deviation of the difference between all line and antenna azimuths is 3.2 degrees. Using the law of cosines, this is a 8.4 m cross-line variation and a negligible in-line variation.

Table 3.1 summarizes the transmitter uncertainties for each tow line. We have projected the uncertainty in azimuth into the cross-line direction and the uncertainty in dip into depth. Uncertainty in depth from the pressure gauges is at the centimeter scale and therefore ignored. For total cross-line uncertainty, we add the uncertainties from the iLBL solutions and the azimuth (projected into cross-line) in quadrature.

Table 3.1 Transmitter uncertainties for each tow line.

Standard deviation in dip and azimuth measurements are projected into depth and cross-line set, respectively. The variation calculations for dip exclude the first 10 minutes of tow when the antenna is settling. Dip was not measured in phases 1 or 4, but the variation is expected to be less than 1 degree like the other tow lines. We expect the depth uncertainty in phase 4 due to dip to be negligible because it uses a much shorter dipole. Total cross-line uncertainty is calculated from the quadrature of the iLBL and azimuth uncertainties. Error in depth from the pressure gauge is negligible for all phases as is the inline error from dip and azimuth variations.

	Dip		iLBL		Azimuth		Total
Line	σ (degrees)	Depth (m)	Inline (m)	Cross (m)	σ (degrees)	Cross (m)	Cross (m)
Phase 1							
1	-	-	-	-	-	-	-
2	-	-	2.7	8.2	2.6	6.8	10.7
3	-	-	3.2	6.8	1.2	3.2	7.5
Phase 2							
4	0.6	1.6	2.8	5.7	2.6	6.9	8.9
4a	0.7	1.8	2.0	3.8	3.5	9.1	9.9
5	0.5	1.3	2.7	5.6	3.2	8.5	10.2
5a	0.5	1.3	2.1	4.5	1.8	4.8	6.6
6	0.7	1.8	3.2	7.1	2.1	5.6	9.0
6a	0.7	1.8	1.6	3.7	1.6	4.3	5.7
7	0.6	1.6	3.4	5.9	2.2	5.8	8.3
7a	0.5	1.3	3.6	4.0	3.7	9.8	10.6
8	0.8	2.1	2.8	7.1	2.8	7.2	10.1
9	0.4	1.1	2.8	5.4	1.7	4.4	7.0
10	0.5	1.3	2.4	5.5	2.5	6.5	8.5
11	0.6	1.6	2.6	5.9	2.5	6.7	8.9
Phase 3							
12	0.9	2.4	2.2	6.5	1.7	4.4	7.8
12a	0.6	1.6	3.2	6.0	2.4	6.4	8.8
12b	0.8	2.1	2.2	6.5	1.4	3.8	7.5
13	0.9	2.4	4.1	6.6	1.2	3.3	7.4
Phase 4							
14	-	-	2.8	4.3	0.9	0.6	4.3

3.4.2 Environmental Noise

In phases 1 – 3, we deployed LEMs with 100 m dipoles, which are ten times longer than the dipoles on the OBEMs. If the dominant source of noise is from the electrodes and amplifiers, or other instrumental voltage sources, then one would expect

an improvement in SNR that is proportional to antenna length. Since the LEMs and OBEMs use the same electronics, the longer dipole on the LEM should provide a factor of ten improvement in the noise floor at all frequencies. However, we find that the noise floor of the LEMs is lower than the OBEMs by a factor which is less than the expected value of 10 and increases with frequency. Table 3.2 shows the noise floor for LEM 2 (which has a slightly lower noise floor than LEM 1) and a low-noise OBEM chosen from each phase, as well as the ratio of the two. While the OBEM noise floors varied between 30-70% across the three phases of deployments, the LEM noise floors varied much more widely and were significantly lower in phase 1. This suggests that the LEM data are limited by environmental noise rather than electronic noise. The low variability in OBEM noise floors at the higher CSEM frequencies (> 0.75 Hz) may indicate that the noise source is at or below the noise floor of these frequencies and that their data are mostly limited by electronics.

At frequencies below the CSEM range, spectrograms of the OBEM data show a periodic increase in noise at intervals which match the tidal cycle (Figure 3.14a) and die off as the tide amplitudes decrease, lending support to the idea that environmental noise is present. This pattern is common to many of the receivers and leads us to recommend that marine CSEM and MT surveys be planned for times of lower tidal amplitude. On the spectrogram for LEM1 (Figure 3.14b), these noise intervals are only faintly observed indicating that for the OBEMs some of the noise is motional. Additionally, we observe occasional noise bursts on some OBEMs which raise the noise floor by a factor of 10 or more for a few hours. Curiously, two such events are captured simultaneously at sites 14

Table 3.2 Noise floors & noise floor ratios for LEM 2 and OBEMs from phases 1-3. LEM 2, which has a consistently lower noise floor than LEM 1, is compared with representative sites from phases 1 – 3 (sites 1, 96, and 110, respectively). The ratio should be 10 since the LEM dipoles are ten times longer. Variation with frequency and deployment indicates that the instrument noise floors are limited by environmental noise, not equipment. The noise floor is from the mean of the stacking variance on in-tow data at ranges greater than 2 km.

Frequency	Instrument	Line 2	Line 8	Line 12	Maximum Variation
0.25 Hz	OBEM	4.2e-15	5.4e-15	3.1e-15	74%
	LEM 2	1.9e-15	3.1e-15	2.4e-15	63%
	ratio	2.2	1.7	1.3	
0.75 Hz	OBEM	6.6e-16	7.1e-16	4.7e-16	51%
	LEM 2	2.0e-16	3.6e-16	4.1e-16	105%
	ratio	3.3	2.0	1.1	
1.75 Hz	OBEM	5.1e-16	5.6e-16	4.1e-16	37%
	LEM 2	0.74e-16	1.8e-16	2.1e-16	184%
	ratio	6.9	3.1	2.0	
3.25 Hz	OBEM	8.4e-16	9.5e-16	7.0e-16	34%
	LEM 2	1.0e-16	1.9e-16	2.3e-16	130%
	ratio	8.4	5.0	3.0	

and 15, which are spaced 1 km apart in line 2. While noise on a single site might be attributed to the electronics, contemporaneous noise must be environmental.

We suggest that the source of environmental noise is related to the movement of localized currents in the ocean, e.g. internal waves induced by tidal flow over bathymetry (Van Gastel *et al.*, 2009; Lim *et al.*, 2008). Usually in CSEM this takes the form of shaking of the instruments by the water moving over them. Though the noise on the OBEMs might be attributable to this, the LEM noise is unlikely to be motional. Unlike the OBEM electrodes which are housed in weighted, semi-rigid poles and may move when the instrument body is moved, the LEM electrodes are attached to loose, negatively buoyant cables. Motion on the LEM body does not translate down the cable, so shaking the electrodes requires that they be lifted out of the mud at the seafloor. If the LEM noise, the low-frequency tidal noise, and the burst noise all come from the same

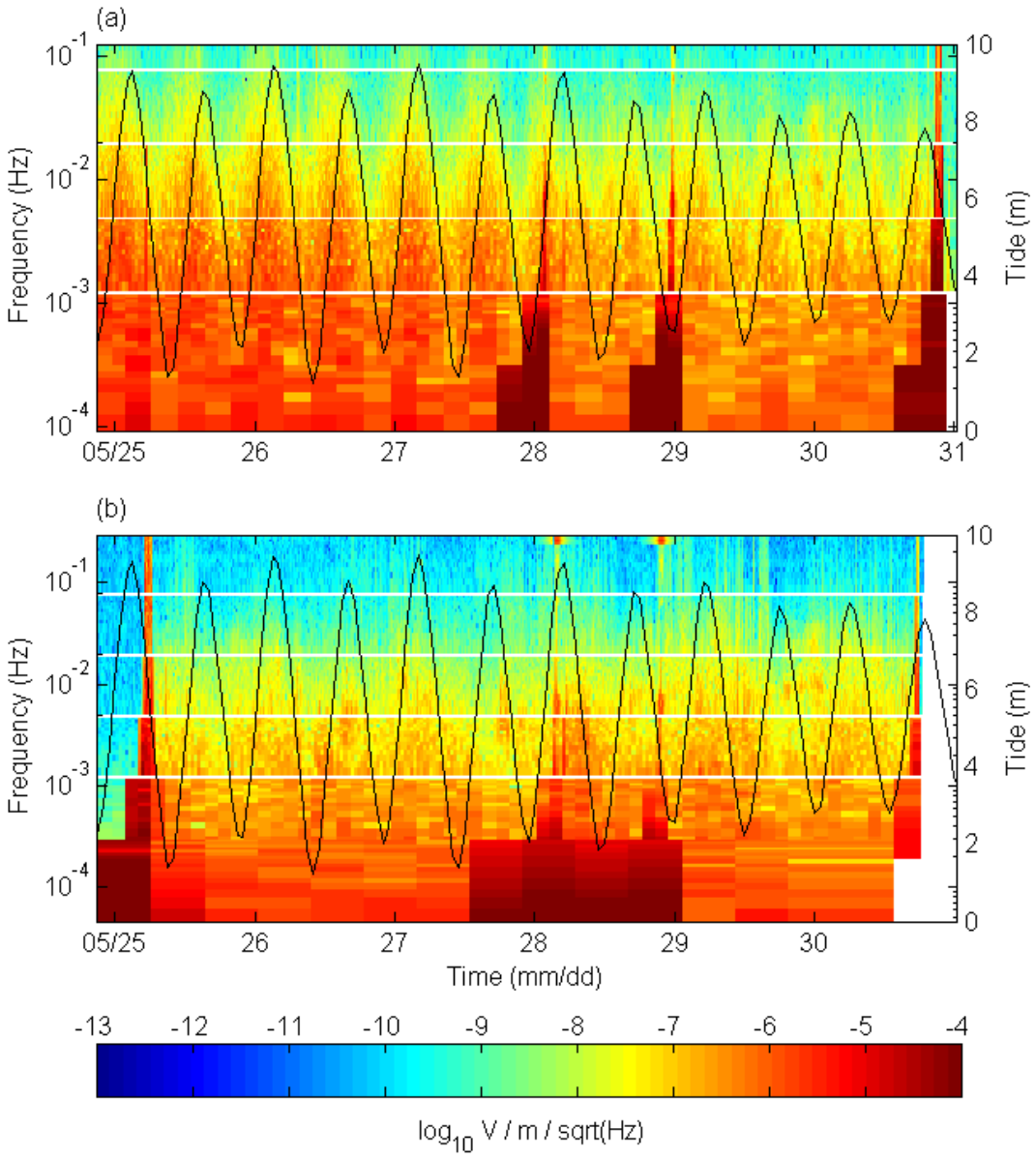

Figure 3.14 Receiver spectrograms.

Spectrograms from phase 1 of (a) the Ex channel from site 11, and (b) one of the channels from LEM1 at site 7 overlain with the tides observed at Broome, 1000 km to the east in West Australia. The regularly occurring increase in the power in the spectrum is an increase in noise which is correlated with the tides. The electric field noise decays in strength as the magnitude of the tides lessens. This noise source is less clear in the LEM indicating that the OBEM noise involves instrument motion. The saturated segments of the spectrogram near midnight on the 28th and 29th of May are passes by the transmitter. Saturated segments at the beginning and end are from the receiver traversing the water column.

source, which seems logical, it is unlikely to be limited to motion of the instruments. Possible additional sources are induction from the ocean moving across the instruments and microseisms (Webb and Constable, 1986; Webb and Cox, 1986; Webb and Cox, 1984).

3.4.3 Data Repeatability

We performed two tests in the Scarborough survey on the repeatability of data acquisition which provide important information on the level of random noise in the data and the aggregate effect of the position uncertainties. In the simpler of the two tests, we towed a line of sites in opposing directions – lines 12 and 13. Since the receivers remained in the same locations for this test, any difference in the out-tow of one line with respect to the in-tow of the other line will be due almost entirely to random noise and the uncertainty in the transmitter position, azimuth, and dip. This allows us to quantify the average effect of these uncertainties. There may be an additional effect due to the heterogeneity of the near-surface strata because the corresponding in-tow and out-tow positions are not over exactly the same portion of seafloor. However, the difference in positions is only on the order of a few tens of meters which will produce an insignificant effect when the range is over about one kilometer. We constrain the test data to ranges greater than 2 km to avoid bias from the finite dipole and the motion of the transmitter. We also impose a maximum range of 6 km and a minimum signal-to-noise ratio of 10. We carried out the comparison outlined below with several frequencies and found that 0.25 and 0.75 Hz yield similar results while higher frequencies do not have high enough

signal-to-noise ratios at intermediate ranges to produce relevant statistics. Here we discuss the results for 0.25 Hz.

Data from two tows cannot be compared directly because of small changes in transmitter altitude, dip, azimuth, and cross-line position. For example, if the antenna dip is 5° for both lines 12 and 13, then because these lines are in opposite directions, there is a 10° difference in dip between a datum from line 12 and its corresponding datum in line 13. A comparison of the data would result in large variations which are due to the value of the transmitter parameters, not their uncertainties. To remove these effects, we calculate the percent difference between each line's data and a reference 1D model in which the estimated transmitter position and orientation are used. By differencing the variation of the two tow lines from the model, we derive a comparison of the two datasets which is a function of the uncertainties of the transmitter parameters while being independent of the specific values of the parameters. If, for example, the two lines have identical data, then their variation from the model will be identical and the difference between them will be zero. If one line is one percent lower than the model and the other line is one percent higher than the model, then the difference in the two datasets is two percent, independent of the transmitter orientations in the model.

Because the CSEM data are complex, there are two components for each datum; real and imaginary, or amplitude and phase. It is typical to assume an equal error distribution between the components. For noise, this is mathematically correct because the Fourier transform is a linear operation. However, errors from position and orientation do not map equally in amplitude and phase. Error in transmitter dip, for example, has twice the effect on amplitude as on phase at intermediate ranges. So for completeness we

use our procedure to evaluate both amplitude and phase, and for the sake of comparison we convert degrees difference to percent difference.

We note that many workers prefer to use real and imaginary in order to avoid the problem of "phase wrapping"; i.e. the data value is 356° but the model value is 1° which appears to be a difference of 355° but is in fact merely 5°. Since transmitter uncertainties do not map equally in amplitude and phase, using them in real and imaginary requires the use of a full covariance matrix. We remind the reader that real and imaginary are simply a cartesian projection of the more natural components of amplitude and phase, which are in polar coordinates. It is simpler to use amplitude and phase with distinct uncertainties and apply the few lines of code required to account for phase wrapping than to implement a full covariance matrix for real and imaginary components. This is the approach we take in this and the companion work.

Figure 3.15(a-b) show histograms of the amplitude and phase differences for 2-4 km range. Each histogram is overlain by an ideal Gaussian curve with the same mean, standard deviation, and sample size. At these short ranges, the signal-to-noise ratio is well over 100, so the effects of random noise are small. The standard deviation, and therefore the joint error from the transmitter uncertainties and random noise, is 2.8% in amplitude and 2.4% (1.4°) in phase. Additionally, there is a bias of 0.3% and 1.3% (0.7°), respectively, which may indicate a systematic error in one or more transmitter parameters. This bias is not surprising since a smoothing function is used on the iLBL point-to-point solutions and one of the drawbacks of a smoothing function is that while suppressing randomness it may introduce a systematic bias. The small size of the bias we measure indicates that the smoothing step may not be a significant source of error.

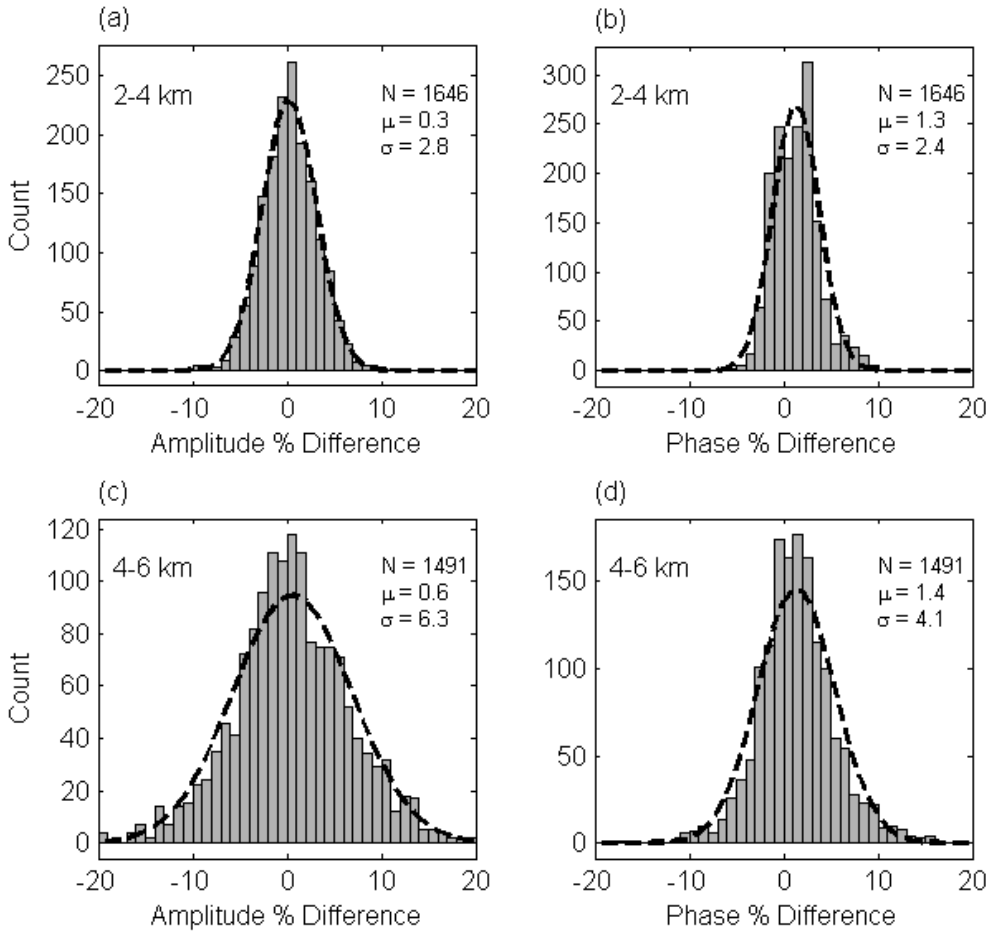

Figure 3.15 Comparison of lines 12 and 13.
Histograms of the amplitude and phase differences between lines 12 and 13 for (a-b) 2-4 km, (c-d) 4-6 km. Each is overlain by an ideal Gaussian (dashed line) with the same mean, standard deviation, and sample size. The effect of the estimated transmitter orientation has been removed, leaving just the errors in transmitter parameters and random noise. For data in ranges 2-4 km, the signal-to-noise ratio is > 80, so the scatter is primarily from the transmitter navigation errors. The increase in scatter with increasing range is due to the growing influence in random noise.

The effects of random noise may be seen in the longer ranges. Figure 3.15(c-d) show the same comparison but for 4-6 km ranges where the signal-to-noise ratio declines from about 80 to 10. The bias has not grown significantly in either amplitude or phase, but due to the increase in random noise, the standard deviation is approximately double.

The differences in the amplitude and phase uncertainties may provide some clue as to systematic errors in transmitter parameters. We investigate this by perturbing the

transmitter parameters then comparing lines 12 and 13 again, constraining the range to 2-4 km to minimize the influence of random noise.

Replacing the calculated transmitter azimuth with the tow line azimuth increases the amplitude bias by 0.3% without affecting the other errors, indicating that the data prefer the azimuth to be along a line between the ship and transmitter, not along the ship track.

Perturbing the transmitter altitude of both lines has no effect on the comparison since the electric field variations are symmetrical. However, an asymmetric perturbation, in which the altitude for line 13 is lowered by 1 m but line 12 is not changed, reduces the amplitude bias to 0.1% and the phase bias to 1.0%. This may explain a small portion of the difference in bias behavior between amplitude and phase, but cannot explain all of it.

Cross-line perturbations have only a slight effect for large variations (0.3% over 100 m) and cannot be reasonably constrained by this test. However, perturbations of dip and inline distance have a large effect on the error structure, producing a bi-modal distribution due to large asymmetry in the in-tow and out-tow portions of each site's data. Since our original comparisons are not bi-modal, we can use the appearance of two lobes in the perturbed distributions to place outer limits on the systematic errors in the dip and inline distance.

Using this procedure, we find that the dip is the most tightly constrained parameter. A perturbation of +1° (i.e. raising the far electrode with respect to the near electrode) raises the amplitude difference from 2.8% to 4.6% while a perturbation of -3° raises it to 6.3%, both due to the introduction of two lobes into the distributions. Interestingly, a perturbation of -1° lowers the amplitude difference slightly to 2.5% while

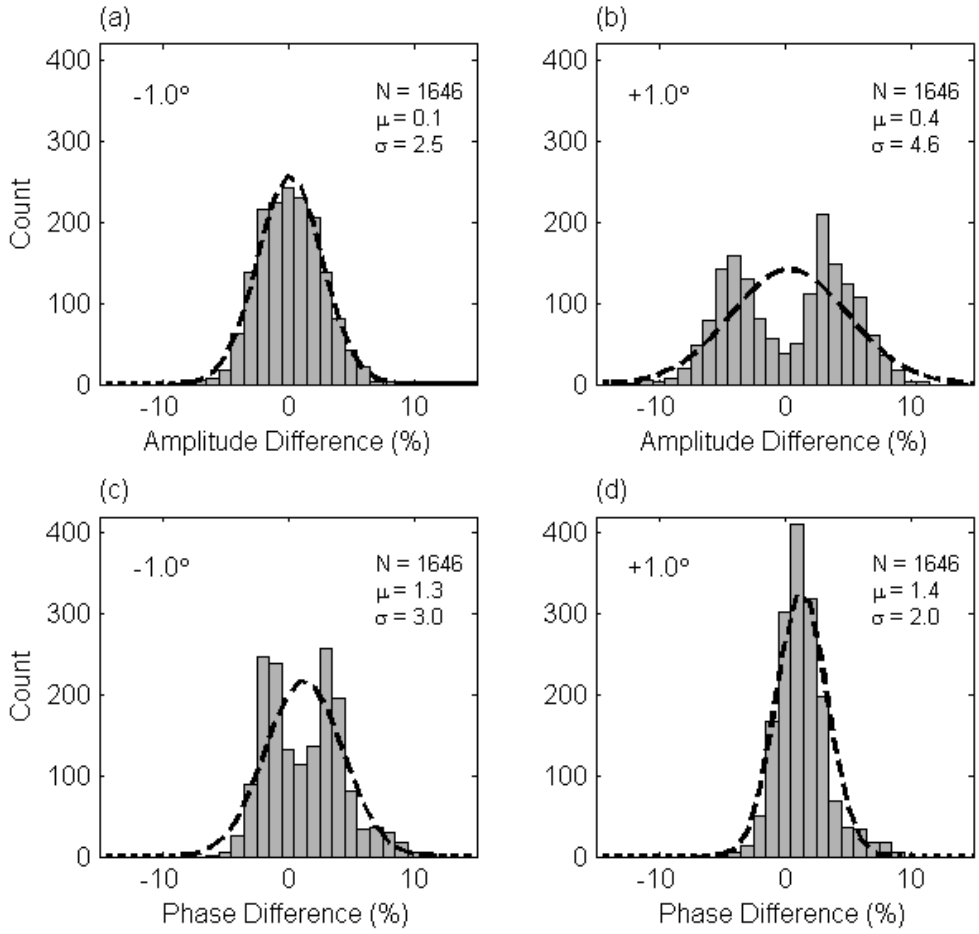

Figure 3.16 Phase perturbations in the comparison of lines 12 and 13.
Histograms of the line 12-13 comparison in amplitude and phase when dip is perturbed by -1 degree (a and c) and +1 degree (b and d). Each is overlain by an ideal Gaussian (dashed line) with the same mean, standard deviation, and sample size. The development of two lobes in the distribution identifies the maximum systematic error in dip as +/- 1 degree.

also lowering the bias from 0.3% to 0.1%. This may seem to indicate that this is a preferred configuration. However, the effect on phase is different; increasing the phase difference to 3.0% and creating a bi-modal distribution. A +1° perturbation decreases the phase difference to 2.0%, but at +1°, the amplitude distribution is distinctly bi-modal. Thus the systematic error in dip is constrained to +/- 1° (Figure 3.16). This is likely a pessimistic estimate in view of the 0.9° standard deviation found for the entire set of

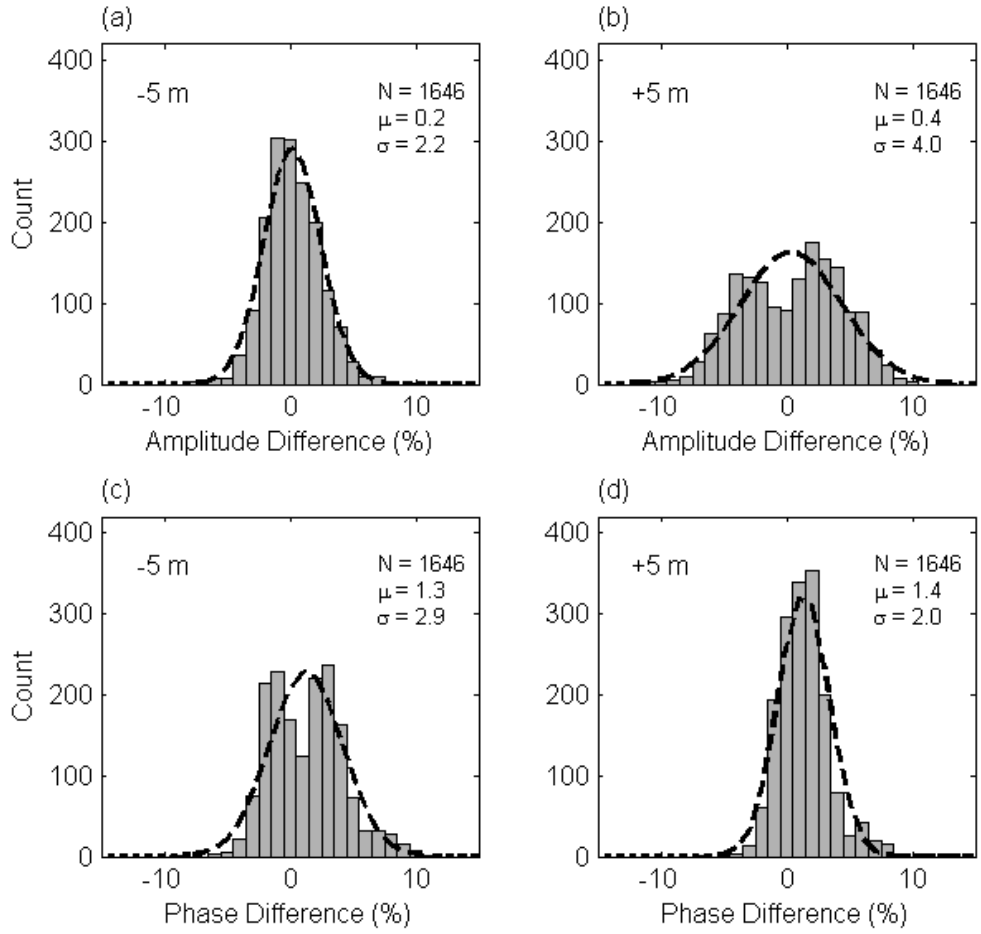

Figure 3.17 Inline range perturbations in the comparison of lines 12 and 13. Histograms of the line 12-13 comparison in amplitude and phase when inline range is perturbed by -5 meters (a and c) and +5 meters (b and d). Each is overlain by an ideal Gaussian (dashed line) with the same mean, standard deviation, and sample size. The development of two lobes in the distribution identifies the maximum systematic error in inline range as +/-5 m.

phase 3 data (Figure 3.9b). When the perturbation is +/- 0.5°, the distributions are still somewhat bi-modal, though not as clearly as at +/- 1°.

Inline range may be similarly constrained. The bi-modal distribution develops more slowly than for dip but is observed in phase at a -5 m perturbation and in amplitude at +5 m (Figure 3.17), where negative indicates moving the transmitter closer to the ship. The amplitude difference between lines 12 and 13 is lowest when the perturbation is

-5 m, but the phase difference is lowest when the perturbation is +10 m. Yet these two minima trade-off error in the other component, so we constrain the systematic error in inline range to +/-5 m.

We carried out a second, more complicated test of data repeatability by redeploying and re-towing instruments at two sites. Site 52 from phase 1 line 3 was redeployed with the same instrument in phase 2 line 4 and towed in the same direction. In addition to the random noise and transmitter position errors discussed above, differences in this redeployment should also contain the effects of errors in receiver location and orientation. Site 39 from phase 1 line 2 is more complicated since it was redeployed with a different instrument in phase 3 and towed in an orthogonal line. Differences at this redeployment will include the effects of variation in instrument calibration as well as heterogeneities in geologic structure along the orthogonal lines. Site 39 is 4 km off the projected edge of the reservoir, so we expect geologic heterogeneities to affect the 4-6 km range data but not closer ranges.

We applied the model-difference analysis to sites 52 and 39. For site 52, we have used only the in-tow data since during the out-tow there were changes in the line 3 transmitter altitude significant enough to cause changes in the antenna dip, and the dip in tow line 3 is unknown. For site 39, we compare the deployment of two different instruments in line 2 and line 12 which were towed in orthogonal directions. The difference for each redeployment is summarized in Table 3.3 along with the results from lines 12 & 13 for comparison.

Table 3.3 Summary of redeployment uncertainties.

Phase uncertainties are expressed in percent for comparison. Lines 12 and 13 are tows of the same deployment of 23 instruments but in opposite directions. Differences should include only the effects of uncertainty in the transmitter parameters. Site 52 is a redeployment of the same instrument and its differences should also include uncertainty in instrument rotation and location. Site 39 is the reoccupation of a site by a different receiver, which was towed in an orthogonal direction. Differences for this site add the effects of differences in receiver calibration as well as geologic heterogeneities.

		Amplitude		Phase	
	Range	% Bias	% Difference	% Bias	% Difference
Lines 12 & 13	2-4 km	0.3	2.8	1.3	2.4
	4-6 km	0.6	6.3	1.4	4.1
Site 52	2-4 km	-3.2	1.4	1.3	2.7
	4-6 km	-1.6	4.7	0.5	5.1
Site 39	2-4 km	-2.9	2.4	-0.4	3.2
	4-6 km	-2.6	5.6	0.4	7.1

The decline in bias with range observed at both sites may indicate that the bias is due to position error since rotation errors introduce a bias which is generally range independent. Presumably this effect is not observed in the line 12-13 comparison because the errors are random site-by-site and cancel in the comparison of those 23 sites. The single site redeployment differences are similar to those observed in the line comparison. Apparently, errors in instrument navigation and orientation introduce very little additional scatter in the data and only a few percent bias, which declines with range. Site 39, which might be reasonably expected to have larger differences due to one of its orthogonal tow lines being partially over the reservoir, is remarkably similar to the other comparisons. The higher values for its phase difference are probably due to the reservoir.

Over all, the differences in repeat tows and deployments give us a minimum error level of 3-6%, depending on range. Uncertainty from systematic navigational errors can be limited to +/- 1° in dip and +/- 5 m in range for systems which use iLBL navigation. We expect values similar to these to apply to any well-run survey and to be of guidance

for users designing and participating in time-lapse surveys to monitor the evolution of a hydrocarbon field during exploitation (e.g. Orange *et al.*, 2009). It is unlikely that changes in a target that produce less than a 3-6% change in the anomaly will be detectable unless additional measures are taken to constrain location errors.

3.5 Composite Uncertainty Model

We can reconcile the observed amplitude and phase variations with the estimated uncertainties in the transmitter parameters by forward modeling. We compare electric field amplitudes and phases computed from a 1D model of the reservoir, with fields generated on the same model but with one transmitter parameter perturbed by the uncertainties we have estimated from the Scarborough data. The base model uses the water conductivity profile from Figure 3.9 with the seafloor at 950 m, the transmitter 50 m above the seafloor, and -5.6° of dip. We modified the 1D code of Key (2009) to support a finite dipole source and calculate all models with a 250 m dipole. The finite length dipole was computed by Gauss quadrature integration of point dipole fields along the true dipole length, where a quadrature order of 10 was found to be sufficient for the ranges considered here. For location perturbations, we use the uncertainties outlined in Table 3.4, which we have derived from the values in Table 3.1 and the discussion in the previous sections. We have also calculated the difference between the finite and point dipoles and included it in our analysis since many modeling codes use a point dipole and there is a range-dependent bias introduced by the dipole length. Note that in the Scarborough data, we use a sixty second stacking window which covers ~45 m of transmitter motion. Since this is much smaller than the dipole length, we ignore it in our

calculations below, which are representative for phases 1-3. However, in phase 4 the dipole and stacking biases are comparable, so the stacking bias should not be ignored.

Table 3.4 Estimated transmitter uncertainties.
Perturbations used to calculate the effects of uncertainties on the amplitude and phase of electric fields in Figure 3.18. These values produce phase uncertainties which are lower than calculated from the line 12/13 comparison. Doubling the altitude perturbation produces values more in line with observations.

Parameter	Perturbation
Receiver Orientation	5°
Transmitter Dip	1°
Transmitter Azimuth	4°
Transmitter Altitude	3 m
Inline Distance	5 m
Crossline Distance	10 m
Finite Dipole	250 m

In Figure 3.18, we show the error that would be introduced in the 0.25 Hz amplitude and phase by each type of uncertainty, along with a composite curve in which all the components have been added arithmetically. We do not add them in quadrature because they are not independent. The effect of cross-line distance is nearly zero at all ranges so has been left off the plot for clarity but is included in the composite curve. Also note that we show positive bias produced by the finite dipole, but do not add it into the composite curve. Because of the transmitter dip included in all models, there is a slight asymmetry between the in-tow and out-tow portions of the dipole bias and transmitter dip components. We show only the out-tow where the uncertainties are slightly larger.

Close range uncertainties are dominated by the dipole bias. After about 2 km range, the amplitude uncertainty is due mostly to dipping of the source dipole, which mixes the stronger horizontal fields with the weaker vertical fields, suppressing the amplitudes observed at the receivers. Phase uncertainty, however, is due mostly to altitude. In electromagnetic diffusion, phase is a proxy for propagation velocity, so small

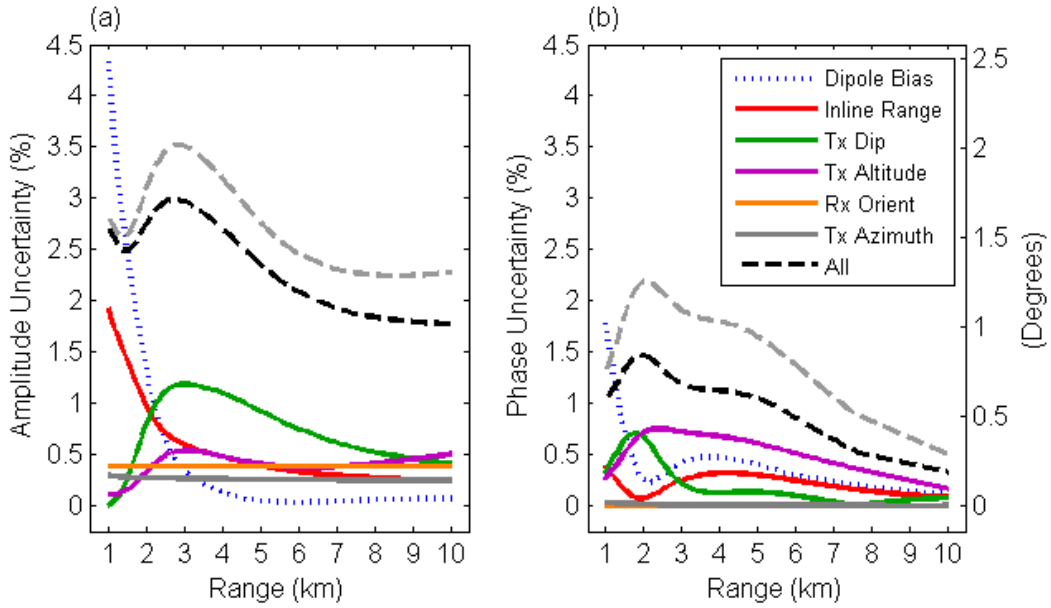

Figure 3.18 Uncertainty in amplitude and phase as a function of range.
Uncertainty curves in (a) amplitude and (b) phase calculated by comparing a 1D model of the Scarborough reservoir with a model in which one transmitter parameter is perturbed by the values in Table 3.4. The dashed black line is a composite uncertainty curve created from all the components added together except the dipole bias (dotted line), which is plotted for reference only. The dashed grey line is the composite uncertainty curve when the uncertainty in altitude is doubled. This more closely matches the phase differences observed in the line 12 and 13 comparison, but slightly over-estimates the amplitude error.

changes in the volume of water between the dipole and seabed translate into increased or decreased phase delay for all ranges because of the propagation velocity contrast between the ocean and seafloor. The minimum in the dipole bias and inline distance curves observed near 2 km is due to the -5.6° dip of the dipole. If the dipole were level, these minima would not appear.

Comparing the modeled uncertainties to the differences actually observed, we find that our estimates of transmitter parameter uncertainties are approximately correct in amplitude but too low in phase. In the 2-4 km range where the observed differences in lines 12 and 13 are from location errors and not random noise, we observe a 2.8% difference in amplitude and a 2.4% (1.4°) difference in phase. We calculate ~2.9%

uncertainty in amplitude but only ~1.2% (0.7°) in phase, approximately half what we observe.

Of the components of uncertainty shown, altitude produces some of the largest effects in phase. We based altitude uncertainty on the dip uncertainty since the altitude of the transmitter body is known to centimeter accuracy and the altitude of the center of the dipole is based on its dip. However, this assumes that the seafloor is perfectly flat over the horizontal distance between the altimeter and the center of the dipole. Since the seafloor is not flat, it is possible that the altitude uncertainty is larger than the 3 m we calculated from dip alone.

Since we do not know the magnitude of altitude uncertainty due to bathymetry, we make a rough calculation by simply doubling the contribution calculated from dip. The gray dashed curves shown in Figure 3.18 are the resulting composite uncertainties if the altitude uncertainty is six meters instead of three. In the 2-4 km range, the amplitude uncertainty is now ~3.3% and the phase uncertainty ~2% (1.1°). Since both values are within a half percent of the observed values, we prefer this increased value of altitude uncertainty and use it in calculations in the remainder of this work.

We repeated this modeling for the four primary frequencies in the survey and show in Figure 3.19 composite uncertainty curves calculated from the modeled uncertainties added arithmetically, then added in quadrature with instrument noise floors. We have added the finite dipole calculation to the model so that the shortest ranges reflect the influence of the dipole bias. For the noise floors, we used the median signal-to-noise ratios of all sites in line 13, but this is merely illustrative. Noise varies with instrument, so composite uncertainty curves should be constructed for each instrument

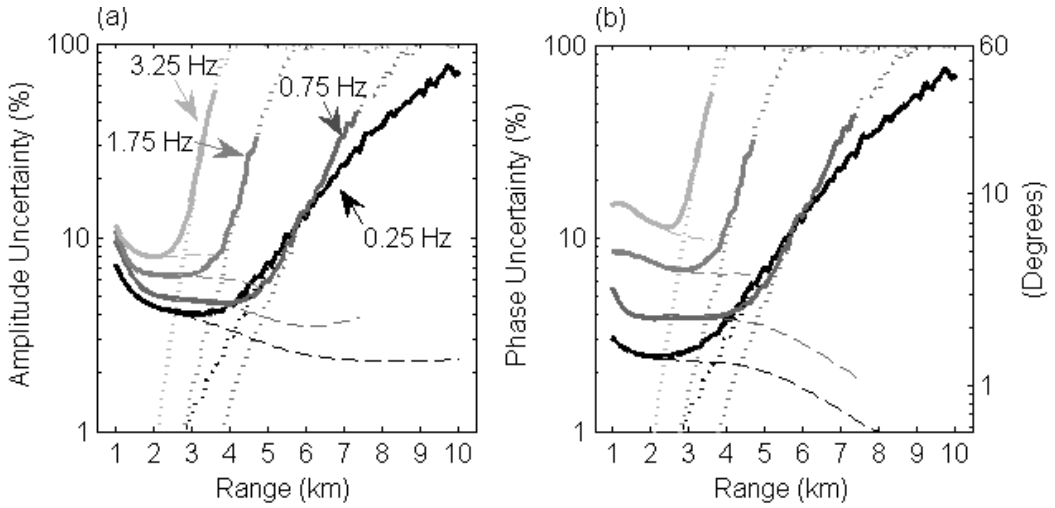

Figure 3.19 Minimum uncertainties in amplitude and phase as a function of range. **Minimum uncertainty (solid) in (a) amplitude and (b) phase from models and stacking variances added in quadrature. The models (dashed lines) are calculated using a 1D model of the Scarborough reservoir and perturbations in Table 3.4, but with altitude uncertainties doubled as discussed in the text. Dotted lines are from the median signal-to-noise levels of all sites in line 13 and are illustrative of noise levels which should in practice be derived for each site from its data variance. For a given range and frequency, the solid curve is the minimum uncertainty to use when fitting the data, e.g. in an inversion.**

using the variances calculated from its data. In the 4-6 km range, the noise from the declining signal-to-noise ratio agrees with the variation we observe in the line 12/13 evaluation (Figure 3.15c), validating our repeat-tow comparison procedure. We suggest that composite uncertainty curves calculated in this way provide the minimum uncertainty as a function of frequency and range for the Scarborough dataset.

We evaluated whether these uncertainties are small enough to allow separate resolution of the gas reservoir and overlying Gearle layer by repeating the pre-survey inversion study. In Figure 3.20, we show the models that result from a standard smooth inversion and a constrained inversion with stabilizing prejudice penalties and breaks in the regularization penalty as described earlier in the text. For both inversions, we used synthetic data in which we applied Gaussian random noise scaled by the curves given in

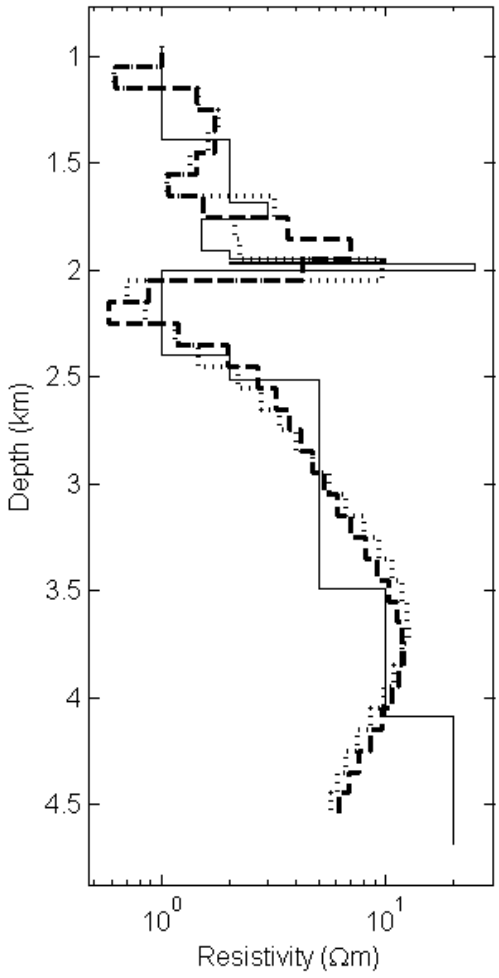

Figure 3.20 1D inversion of synthetic data with new error structure.
1D inversion results for the 2D synthetic model data of the Scarborough reservoir (solid line), with uncertainties and Gaussian random noise scaled by the curves in Figure 3.19. The roughness penalty of the standard Occam inversion (dashed line) smooths the Gearle and reservoir signals together. When preferences and breaks in the roughness penalty as described in Figure 3.4b are introduced (dotted line), the inversion resolves separate resistive layers of approximately correct resistivity thickness product.

Figure 3.19. As in the pre-survey study, the smooth inversion is unable to separate the signals of the two resistive layers, whereas the constrained inversion is.

There are two differences between these inversions and the fixed-noise-level inversions of the pre-model study. First, the resolution to the basement is decreased. All of the pre-survey inversion models show an increase in resistivity in accordance with the

basement layers. However, those inversions used a fixed noise level at all ranges. As our analysis shows, in real data the noise increases dramatically with range and in practice this limits the depth-sensitivity of CSEM to shallower depths than a pre-survey model study might otherwise indicate. We estimate that the Scarborough CSEM data will not be sensitive to structures over 3 km below the seafloor (4 km bsl).

Second, the resistivity of the Gearle siltstone layer is overestimated in the cut inversions of the pre-survey study, but properly estimated here. This suggests that when a fixed error structure is used, the penalty for deviating from the true model is approximately equal across depth. However, when a more realistic error structure is used in which uncertainty increases with frequency and range, the penalty for deviating from the true model is greater for shallower structure. Resolution decreases with depth faster than idealistic model studies otherwise indicate.

Though 1D inversion of this dataset is discussed in detail in the companion paper (Myer *et al.*, manuscript submitted), for completeness we present inversion of two sites from line 2. Site 9 is ~11 km outside of the reservoir boundary and represents the "off reservoir" response, while site 32 is in the middle of the reservoir near where the phase 4 hydrate line crosses line 2. For each site, we inverted the amplitude and phase of the inline data between ±8 km range for four frequencies and using uncertainty curves constructed like those shown in Figure 3.19 but with the variances calculated for each site. As in the synthetic study, roughness penalties are removed above and below the Gearle and reservoir layers and the inversion is stabilized with resistivity prejudices between 1400 and 2500 m depth.

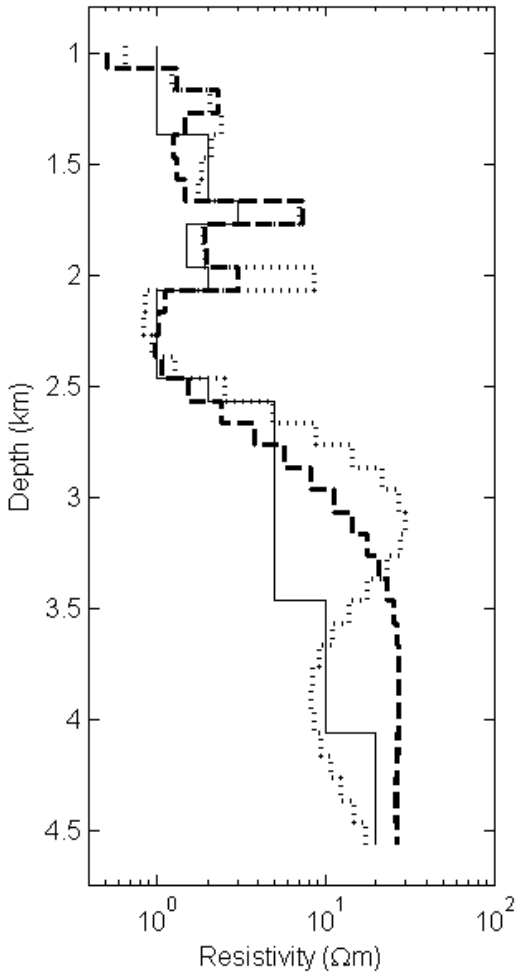

Figure 3.21 1D inversion of sample sites.

1D inversion results for two sites on line 2. Site 9 (dashed line) is 11 km outside the reservoir boundary and site 32 (dotted line) is near the center of it. The black line is the off-reservoir geologic background model. For both inversions, cuts and prejudices were applied as described in Figure 3.4b. Both the off and on reservoir require resistivities above the background model. The resistivity-thickness product for the top 1.5 km of each site is 611 and 1332 Ωm^2, respectively. The difference is equivalent to a 29 m x 25 Ωm resistor, which is the approximate dimension of the main body of the reservoir.

Both sites show enhanced resistivity compared to the off-reservoir geologic background, especially at the Gearle layer (Figure 3.21). Site 9 is far enough outside the reservoir that the enhanced resistivity is unlikely to be low gas saturation and more likely to be resistivity variations in the shallow layers. Site 32 has additional enhanced

resistivity from the Gearle down to the gas reservoir layer. The resistivity-thickness product for the top 1.5 km of the model for each site is 611 and 1332 Ωm^2, respectively. The difference is equivalent to a 29 m x 25 Ωm resistor, which is the approximate dimension of the main body of the reservoir, and is concentrated primarily at the depth of the reservoir layer. The synthetic results predicted that the inversion would be unable to completely concentrate the anomaly at the reservoir layer, which does seem to be the case for these two sites.

These two inversions are fit to RMS 1.3 and 1.7, respectively, and a large portion of this misfit is from the disparity between the in-tow and out-tow data. This is typical of variations in geology along the tow line. If the data are separately inverted as in-tow only and out-tow only, then RMS 1.0 is easily reached in each case and the resulting models are only slightly different from the models in Figure 3.21.

It is interesting to note that both the on- and off-reservoir sites have overestimated the resistivity of the Gearle siltstone layer by the same amount. Although from synthetic models we expect some "cross-talk" between the Gearle and reservoir layers (c.f. Figure 3.4b), it is surprising that it occurs to such a degree in the off-reservoir site in which there is no reservoir. This raises the possibility of significant anisotropy in the Gearle layer. The estimates of resistivity shown in Figure 3.2 are derived from well logs, which measure horizontal resistivity, but as a siltstone, the Gearle is likely to have increased vertical resistivity compared to its horizontal resistivity. The CSEM inversion, which is sensitive to both vertical and horizontal resistivity, is indicating an increased vertical resistivity over our background model (7 Ωm compared to 3 Ωm).

3.6 Conclusions

We have discussed the 2009 CSEM survey over the Scarborough gas field and shown that recent improvements in transmitter navigation and data processing techniques yield high quality data with predicted uncertainties of just a few percent at close ranges. Forward modeling of the predicted uncertainties in the transmitter parameters along with bias in the finite dipole size yields an error estimate that is not equal in amplitude and phase, suggesting that inversion in this basis is more desirable than in the complex basis (i.e. real and imaginary). Also, we show that uncertainties calculated this way can at times be too conservative.

We demonstrate that more accurate uncertainties can be calculated by towing the same line of receivers twice in opposite directions. Comparing the residuals for each line yields a Gaussian distribution that is directly related to the aggregate uncertainty of the transmitter parameters. For Scarborough, this is 2.8% in amplitude and 2.4% (1.4°) in phase between 2-4 km range and grows at longer ranges due to the decrease in the signal-to-noise ratio. We further show that perturbation analysis of the repeat tow line data allows constraints to be placed on systematic error in the transmitter inline location and dip. For this survey, these values are ±5 m and ±1°, respectively.

Initial 1D inversions with the improved error model are in good agreement with the resistivity profile determined by well logs. However, there is an indication that the vertical resistivity of the Gearle siltstone may be at least a factor of 2 above the measured horizontal resistivity.

Acknowledgements

The authors are grateful to BHP Billiton Petroleum for funding this project in its entirety and for providing the background information we needed for the experimental design phase. The captain, crew, and scientific party of the R/V Roger Revelle worked hard to make this project a success, and we thank them all. We thank Brent Wheelock for his improvements to the instrument calibrations which have helped us to obtain such high accuracy in our data. We also thank BHP Billiton, Shell, Esso Australia, and Chevron for providing ingress permissions for this survey. More information and data can be found at http://marineemlab.ucsd.edu/Projects/Scarborough.

Chapter 3, in full, has been submitted for publication of the material as it may appear in Geophysics, Myer D., Constable S., Key K., Glinsky M. E., and Liu G. The dissertation author was the primary investigator and author of this paper.

References

Boyd, R., Williamson, P.E. & Haq, B.U., 1992. Seismic stratigraphy and passive margin evolution of the southern Exmouth Plateau. *in Proceedings of the ODP, Science Results*, pp. 39-59, eds. Von Rad, U. & Haq, B. U. Ocean Drilling Program, College Station, TX.

Constable, S., 2010. Ten years of marine CSEM for hydrocarbon exploration, *Geophysics,* 75**,** 75A67-75A81.

Constable, S. & Cox, C.S., 1996. Marine controlled-source electromagnetic sounding .2. The PEGASUS experiment, *J. Geophys. Res.-Solid Earth,* 101**,** 5519-5530.

Constable, S., Orange, A.S., Hoversten, G.M. & Morrison, H.F., 1998. Marine magnetotellurics for petroleum exploration Part I: A sea-floor equipment system, *Geophysics,* 63**,** 816-825.

Constable, S. & Weiss, C.J., 2006. Mapping thin resistors and hydrocarbons with marine EM methods: Insights from 1D modeling, *Geophysics,* 71**,** G43-G51.

Cox, C.S., Constable, S.C., Chave, A.D. & Webb, S.C., 1986. Controlled-source ElectroMagnetic sounding of the oceanic lithosphere, *Nature,* 320**,** 52-54.

Driscoll, N.W. & Karner, G.D., 1998. Lower crustal extension across the Northern Carnarvon basin, Australia: Evidence for an eastward dipping detachment, *J. Geophys. Res.-Solid Earth,* 103**,** 4975-4991.

Edwards, N., 2005. Marine controlled source electromagnetics: principles, methodologies, future commercial applications, *Surveys in Geophysics,* 26**,** 675-700.

Ellingsrud, S., Eidesmo, T., Johansen, S., Sinha, M.C., MacGregor, L.M. & Constable, S., 2002. Remote sensing of hydrocarbon layers by seabed logging (SBL): Results from a cruise offshore Angola, *The Leading Edge,* 21**,** 972-982.

Exon, N.F., Von Rad, U. & Von Stackelberg, U., 1982. The geological development of the passive margins of the Exmouth Plateau off northwest Australia, *Marine Geology,* 47**,** 131-152.

Haq, B.U., Boyd, R.L., Exon, N.F. & von Rad, U., 1992. Evolution of the central Exmouth Plateau; a post-drilling perspective. *in Proceedings of the ODP, Science Results*, pp. 801-816, eds. Von Rad, U., Haq, B. U. & et al. Ocean Drilling Program, College Station, TX.

Keisler, S.R. & Rhyne, R.H., 1976. An Assessment of Prewhitening in Estimating Power Spectra of Atmospheric Turbulence at Long Wavelengths, pp. 1-55NASA Langley Research Center, Washington, D. C.

Key, K., 2009. 1D inversion of multicomponent, multifrequency marine CSEM data: Methodology and synthetic studies for resolving thin resistive layers, *Geophysics,* 74**,** F9-F20.

Key, K., 2011. Marine Electromagnetic Studies of Seafloor Resources and Tectonics, *Surveys in Geophysics***,** 1-33.

Key, K. & Lockwood, A., 2010. Determining the orientation of marine CSEM receivers using orthogonal Procrustes rotation analysis, *Geophysics,* 75**,** F63-F70.

Key, K. & Ovall, J., 2011. A parallel goal-oriented adaptive finite element method for 2.5-D electromagnetic modelling, *Geophys. J. Int.,* 186**,** 137-154.

Leroy, C.C. & Parthiot, F., 1998. Depth-pressure relationships in the oceans and seas, *The Journal of the Acoustical Society of America,* 103**,** 1346.

Lim, K., Ivey, G. & Nokes, R., 2008. The generation of internal waves by tidal flow over continental shelf/slope topography, *Environmental Fluid Mechanics,* 8**,** 511-526.

Lorenzo, J.M., Mutter, J.C. & Larson, R.L., 1991. Development of the Continent-Ocean Transform Boundary of the Southern Exmouth Plateau, *Geology,* 19**,** 843-846.

MacGregor, L., Sinha, M. & Constable, S., 2001. Electrical resistivity structure of the Valu Fa Ridge, Lau Basin, from marine controlled-source electromagnetic sounding, *Geophys. J. Int.,* 146**,** 217-236.

Mutter, J.C. & Larson, R.L., 1989. Extension of the Exmouth Plateau, offshore northwestern Australia: Deep seismic reflection/refraction evidence for simple and pure shear mechanisms, *Geology,* 17**,** 15-18.

Myer, D., Constable, S. & Key, K., 2010. A marine EM survey of the Scarborough gas field, Northwest Shelf of Australia, *First Break,* 28**,** 77-82.

Myer, D., Constable, S. & Key, K., 2011. Broad-band waveforms and robust processing for marine CSEM surveys, *Geophys. J. Int.,* 184**,** 689-698.

Newman, G.A., Commer, M. & Carazzone, J.J., 2010. Imaging CSEM data in the presence of electrical anisotropy, *Geophysics,* 75**,** F51-F61.

Orange, A., Key, K. & Constable, S., 2009. The feasibility of reservoir monitoring using time-lapse marine CSEM, *Geophysics,* 74**,** F21-F29.

Shumway, R.H. & Stoffer, D.S., 2000. *Time series analysis and its applications,* 1st edn, Vol., Springer Verlag, New York.

Sinha, M.C., Patel, P.D., Unsworth, M.J., Owen, T.R.E. & Maccormack, M.R.G., 1990. An Active Source Electromagnetic Sounding System for Marine Use, *Mar. Geophys. Res.,* 12**,** 59-68.

Van Gastel, P., Ivey, G.N., Meuleners, M.J., Antenucci, J.P. & Fringer, O., 2009. The variability of the large-amplitude internal wave field on the Australian North West Shelf, *Continental Shelf Research,* 29**,** 1373-1383.

Veevers, J.J. & Johnstone, M.H., 1974. Comparative stratigraphy and structure of the western Australian margin and the adjacent deep ocean floor, *Init. Repts. DSDP,* 27**,** 571-585.

Webb, S. & Cox, C.S., 1984. Pressure and Electric Fluctuations on the Deep Seafloor: Background Noise for Seismic Detection, *Geophysical Research Letters,* 11**,** 967-970.

Webb, S.C. & Constable, S.C., 1986. Microseism propagation between 2 sites on the deep sea-floor, *Bulletin of the Seismological Society of America,* 76**,** 1433-1445.

Webb, S.C., Constable, S.C., Cox, C.S. & Deaton, T.K., 1985. A sea-floor electric-field instrument, *Journal of Geomagnetism and Geoelectricity,* 37**,** 1115-1129.

Webb, S.C. & Cox, C.S., 1986. Observations and Modeling of Seafloor Microseisms, *JGR,* 91**,** 7343-7358.

Zhdanov, M.S., 2010. Electromagnetic geophysics: Notes from the past and the road ahead, *Geophysics,* 75**,** 75A49-75A66.

4 Marine CSEM of the Scarborough gas field, Part 2: Pseudo-imaging and 1D Inversion

Abstract

In 2009, we collected 144 sites of marine CSEM over the Scarborough gas field off the northwest coast of Australia, described in a previous publication. In this sequel, we discuss three tools for quick evaluation and inversion of marine CSEM data sets using Scarborough as a case study. Pseudo-imaging is a method of presenting the lateral variations in complex electric and magnetic field data in plan view without normalization. For the Scarborough gas field survey, we demonstrate with pseudo-imaging that the magnetic field is well predicted by the electric field. Since Scarborough contains both morphologically simple and complex geology, this result may indicate that magnetic fields are of low value in CSEM, though more study is required on this point. Also, we demonstrate that in systems with high-quality timing control, the phase of the electric field is less noisy than the amplitude. Finally, the vertical electric field exhibits site-to-site amplitude variations while the phase varies smoothly, partly due to the presence of small near-surface galvanic scattering and partly due to transmitter dip. This sensitivity may impact the usefulness of vertical field amplitude in CSEM surveys targeting deeper structures.

In the context of 1D inversion, we discuss the prejudiced minimum norm (PMN) regularization in which model parameters are penalized for deviating from an a priori model. This regularization does not penalize jumps in resistivity from layer to layer and, unlike a smoothness constraint, prefers the thin layers which are more common in

hydrocarbon exploration environments. For stitched 1D inversion, in which separate 1D inversions along a tow track are plotted side-by-side to show variations in geology, we show that the common midpoint gather is able to accurately reproduce along-tow changes in geology while the separate inversion of in-tow and out-tow for each site exhibits large lateral jumps between adjacent 1D models.

We use the PMN inversion on the Scarborough data and show that the resulting models agree reasonably well with the reservoir boundary defined by other geophysical methods and that they are more regular and more easily interpreted than individual 1D smooth inversions of the same data. However, there are some indications that higher dimensional inversion is required in the more complicated northern portion of the reservoir.

We extend 1D inversion into higher dimensions by inverting multiple 1D data sets simultaneously and applying horizontal roughness penalties across layers at the same depth in side-by-side common mid-point gathers. This “1D/2D” smooth inversion produces a more geologically plausible result than both the 1D smooth and 1D PMN stitched inversions. The addition of lateral roughness constraints creates more laterally uniform conductivity variations than found in the stitched 1D smooth inversions, alleviates the need for an instructive (and possibly restrictive) background as in PMN, and shows a progression of geologic structure that can be matched to previous academic seismic studies. This is a striking result for an inversion based on a 1D forward code. Though some of the changes in geologic structure shown in a 1D/2D inversion disappear in a 1D/3D inversion, the resistivity-thickness resolution is close to that expected for the gas field. That this code can be run on an average laptop rather than the more usual

server-farm required by large-scale 3D codes, should be a boon to many complex CSEM surveys as it allows for quick characterization of a dataset and provides a reasonable starting model for 3D inversions.

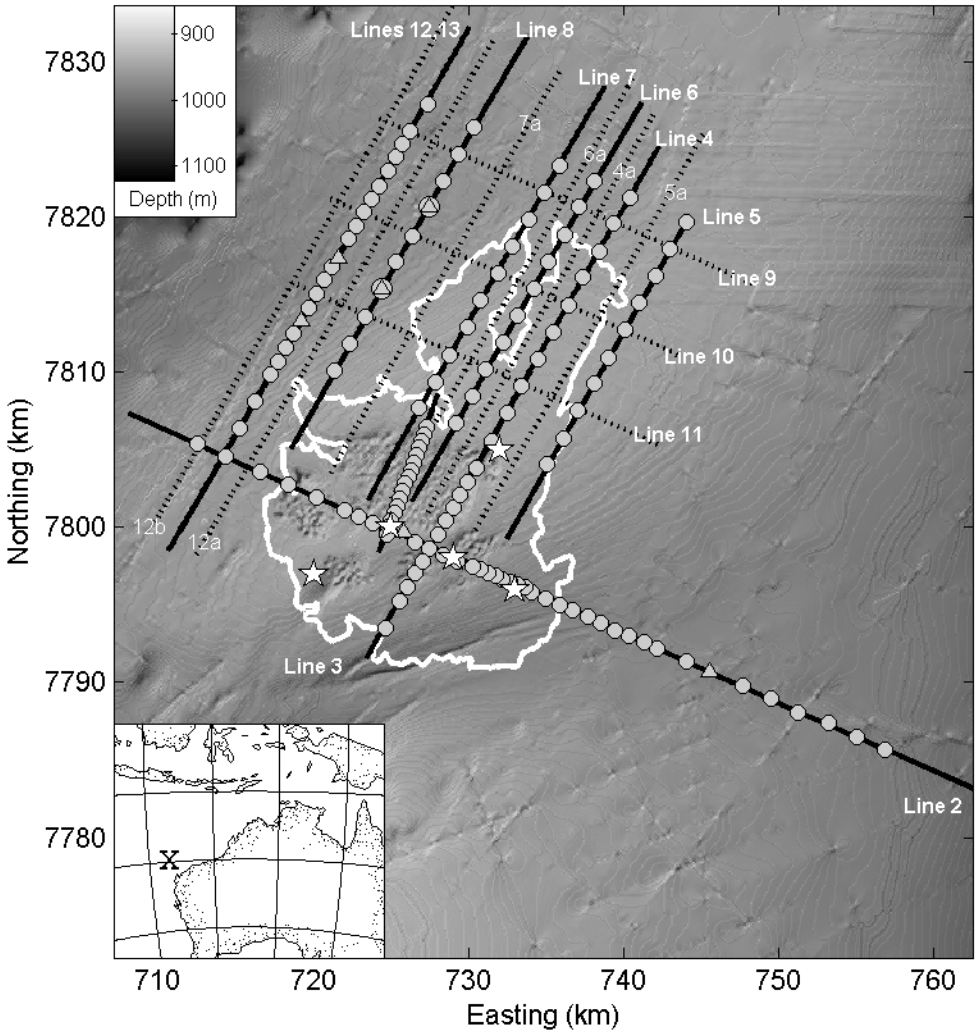

Figure 4.1 Scarborough Survey Map

A bathymetric map overlain with the Scarborough instrument deployment locations (filled circles), predicted reservoir outline (white), exploration wells (stars), and tow lines (black lines). The inset shows the survey location off the west coast of Australia. LEMs are shown as triangles. The primary tow lines are solid lines, secondary tow lines are dotted.

4.1 Introduction

In the companion paper (Myer *et al.* submitted, hereafter referred to as "Part 1"), we described a marine controlled-source electromagnetic (CSEM) survey over the Scarborough gas field, on the northwest shelf of Australia (Figure 4.1). Part 1 describes the data acquisition, processing, and quality, with particular attention to the uncertainties. In this paper, we examine the dataset in more detail and carry out interpretation using 1D regularized inversion.

The Scarborough gas reservoir is located near the middle of the Exmouth plateau where the local geology is comprised primarily of horizontal sedimentary layers of large extent. The average depth of the seabed is 950 m with ~50 m of bathymetric relief over the survey area. The reservoir consists of stacked channel sands located just above 2 km below sea level (Figure 4.2). Of particular concern to CSEM exploration is the presence of confounding resistive layer (the Gearle siltstone) approximately 200-300 m above the reservoir. The relatively horizontal repose of the entire sedimentary section and the large horizontal extent of the reservoir raises the possibility that data collected in the area can be suitably interpreted with 1D tools, rather than the more computationally demanding 2D and 3D tools.

This paper is divided into the following sections. First, we provide a qualitative examination of the various components of data using pseudo-imaging. Next, building on observations from Part 1, we develop and discuss the prejudiced minimum norm regularization and using synthetic data compare it with the standard first difference penalty. Since we are inverting data along tow lines with a series of 1D inversions, we also compare the common mid-point inversion with inversion of separate in-tow and out-

tow data. Applying the new regularization in a series of 1D common mid-point inversions for seven lines over and around the gas field, we compare the results with those from smooth inversion. Finally, we extend 1D inversion into two and three dimensions by the application of horizontal smoothness constraints on simultaneous side-by-side 1D inversions.

4.2 Data Pseudo-imaging

The Scarborough survey consisted of 144 seafloor deployments and 20 CSEM transmitter tows. All instruments collected horizontal electric and magnetic field data,

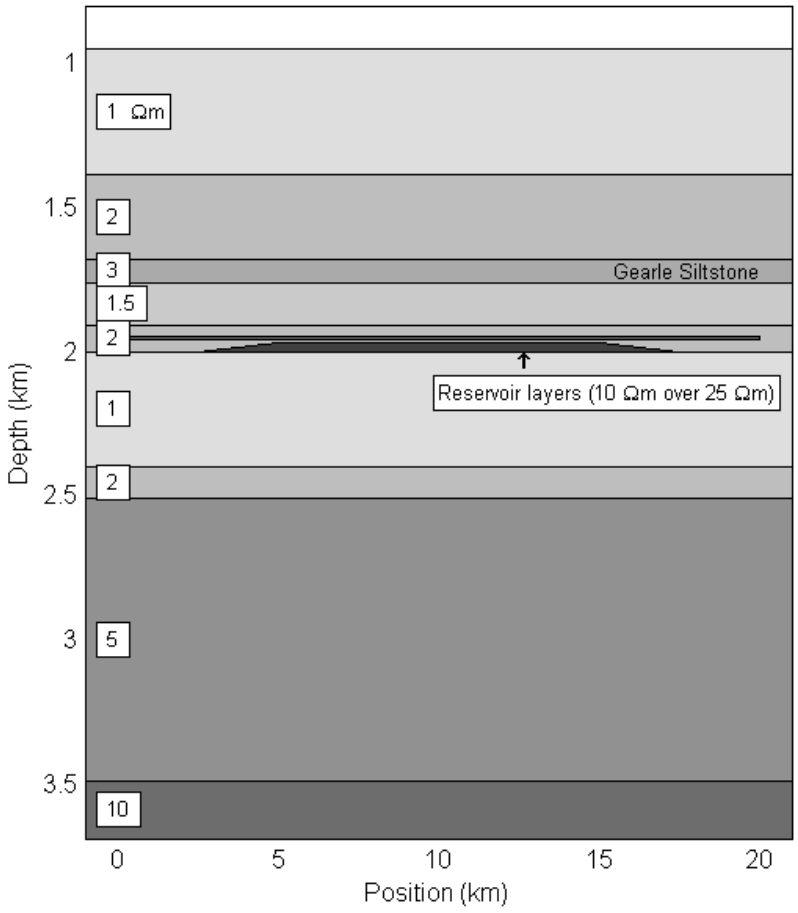

Figure 4.2 Reservoir Model
A section view of the expected geologic background with resistivities for each layer. The reservoir is not a monolithic body, but a stack of thin traps ranging from 6 to 10 Ωm on top of larger body of varying thickness and ~25 Ωm.

and 120 deployments collected vertical electric field data as well. We processed the four strongest harmonics of our custom waveform "D" described in Myer *et al.* (2011) – 0.25, 0.75, 1.75, and 3.25 Hz – and stacked the data in 60-second windows as described in Part 1. In the conductive sedimentary environment around Scarborough, this yielded data above the noise floor out to ~10 km range for the strongest harmonic.

It is insightful to present various components of the data in map form, using a similar approach to the one introduced by Ellingsrud *et al.* (2002) and which they called "pseudo-imaging". The highly non-uniform lateral distribution of somewhat noisy data requires that some form of averaging and interpolation be used. The plotting algorithm used by Ellingsrud *et al.* (2002) employed an objective mapping approach popular in oceanography and similar to the one described by Kim *et al.* (2007). A feature of this algorithm is that in the absence of data the image tends toward a uniform, mean background value, rather than a smooth surface, introducing artificial structure in the map. Here we use a more straightforward regularized approach, a linear version of the Occam algorithm of Constable *et al.* (1987), which produces a maximally smooth map (in a first derivative sense) that fits the data to a specified sum-squared measure X^2. We create a model (m) which is a 2D matrix whose size has the same dimensions as the surface to be mapped. The measure of the roughness of the map is found by multiplying m with a sparse matrix ∂ which is populated with ones and minus ones to difference the adjacent values of m in both the vertical and horizontal directions. We then minimize the functional

$$U = \|\partial m\|^2 + \mu^{-1}\left\{\|W(d - Gm)\|^2 - X^2\right\}, \quad (4.1)$$

which balances the 2-norm of the roughness (the first term) with the data misfit (the second term) through a Lagrange multiplier μ. The matrix W is a diagonal matrix of reciprocal data uncertainties and the matrix G performs a linear interpolation which samples the map at the locations of the actual data. The model is then given by

$$m = \left[\mu\,\partial^T\partial + (WG)^T WG\right]^{-1}(WG)^T Wd\,, \quad (4.2)$$

where μ is chosen to achieve the desired misfit X^2 by interpolation of the function $X^2(\log_{10}\mu)$. We have implemented this algorithm using the sparse matrix arithmetic within MATLAB and the 50x50 maps presented here each take 20-30 seconds to evaluate on an average laptop.

In the maps we present below, all combinations of transmitter tow and receiver were searched for data at a specific source-receiver range, regardless of the azimuth (θ) between the transmitter orientation and the vector from the transmitter location to the receiver location (i.e. both on-line and off-line data were sampled). Although we accepted any data within 200 m of the target range, the transmitter moves only about 46 m during the 60-second stacking window so in practice almost all the data are within ±23 m of the target range. The data were screened for a signal-to-noise ratio (SNR) of at least 10 and then assigned a uniform uncertainty so that all data had equal weight. Amplitudes were parameterized in log10 and phase in degrees (where negative indicates phase lag).

Data were rotated into pure radial and azimuthal modes and scaled using the cylindrical decomposition equations

$$E_\rho = \frac{\cos(\alpha)}{\cos(\theta)} E_{x'} + \frac{\sin(\alpha)}{\cos(\theta)} E_{y'}, \tag{4.3}$$

$$E_\phi = -\frac{\sin(\alpha)}{\sin(\theta)} E_{x'} + \frac{\cos(\alpha)}{\sin(\theta)} E_{y'}, \text{ and} \tag{4.4}$$

$$E_z = \frac{E_{z'}}{\cos(\theta)}, \tag{4.5}$$

where $E_{x'}$, $E_{y'}$, and $E_{z'}$ are the electric fields measured in the instrument frame of reference, E_ρ, E_ϕ, and E_z are the radial, azimuthal, and vertical field components, respectively, and α is the angle measured clockwise from north which rotates $E_{x'}$ into the radial direction. Transmitter dip, not included in these equations, affects the vertical and radial components by a few percent and has no effect on the azimuthal component. For inline geometry $\theta = 0°$ and the inline field is purely radial; similarly for broadside geometry $\theta = 90°$ and the broadside field is purely azimuthal. We can recover the equivalent of the inline and broadside fields from data at arbitrary θ simply by applying the decomposition equations above as long as we exclude data associated with small trigonometric terms. Here we selected data within 60° of the ideal geometries, so the sine and cosine terms never fall below 0.5. Although we present only a small fraction of the data collected by our survey, the figures below are representative. We show different frequencies and ranges from figure to figure to demonstrate that the results are generally consistent across all ranges and frequencies.

Figure 4.3 shows the amplitude and phase of E_r as a function of target range at a frequency of 1.75 Hz. Note that unlike the pseudosections presented in Part 1, where the

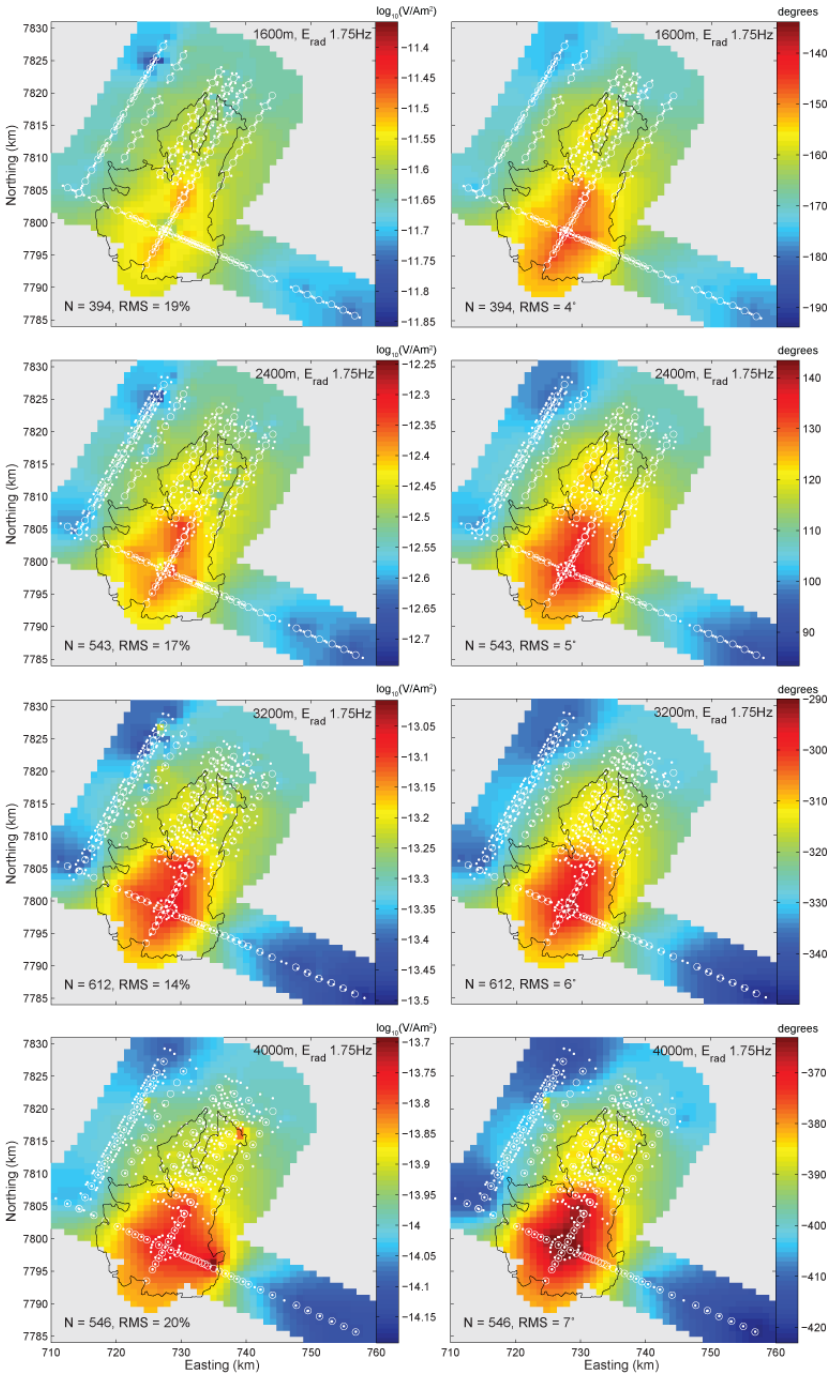

Figure 4.3 Pseudo-images by Range

Amplitude (left column) and phase (right column) of E_r at four source-receiver ranges and a fixed frequency of 1.75 Hz. White circles show locations of the seafloor instruments and white dots show the locations of the source-receiver midpoints contributing data to the maps. The approximate outline of the reservoir is shown by the black line. The number of data contributing to each map is shown in the panels, along with the RMS fit of the map to the data. The scales have been fixed to ±30° in phase and ±0.25 decades in amplitude around the median values for each map.

data needed normalization to remove the large effect of range on amplitude, these maps represent actual field values, with the only manipulation of the data being a degree of smoothing. We show 1.75 Hz because it is particularly sensitive to the reservoir and also has good SNR out to 4 km range. As expected, the signal from the reservoir increases with range, reaching about half a decade in amplitude and 60° in frequency at the longer ranges. There is a suggestion that the western "rabbit ear" of the reservoir is expressed at shorter ranges than the eastern "rabbit ear". The outline of the expected reservoir extent is well recovered by the data amplitudes and phases, except at the southern boundary where we have no data.

The square root of the mean squared misfit (RMS) is presented for each of the maps, showing that the amplitudes are fit to 14-20% and the phases to 8-14% (4-7°). The proportionally greater error in amplitude versus phase is similar to that derived in the error analysis in Part 1, and it can be seen in the maps that there is more scatter and noise in the amplitude data, particularly at shorter ranges.

In Figure 4.4 we compare the radial electric field component E_r to the azimuthal component E_ϕ at a range of 4 km and a frequency of 0.75 Hz. In CSEM the amplitude of the azimuthal component has much less sensitivity to sub-horizontal thin resistors than the radial component (e.g. Constable and Weiss, 2006), as demonstrated in the figure. Note, however, that this does not apply to the phase of the azimuthal component which shows correlation with the reservoir boundary that is similar to that of the radial components, though somewhat reduced. This is as expected, considering the 1D synthetic results of Key (2009) wherein inversion of broadside data alone is able to recover a thin

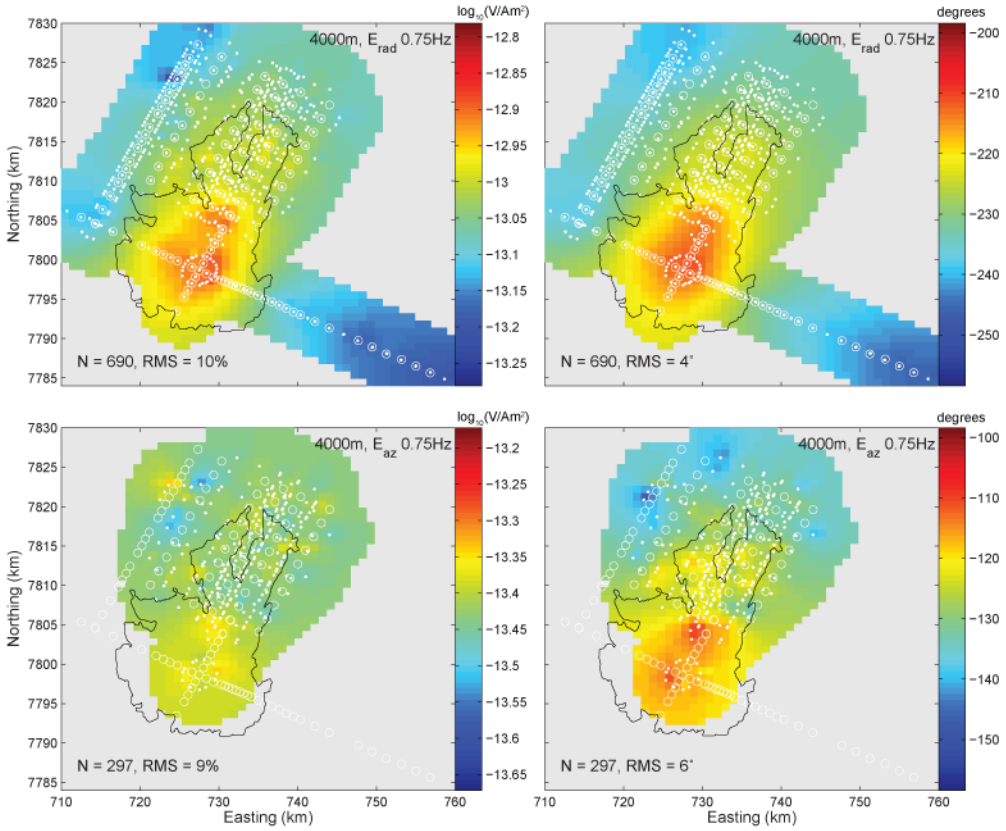

Figure 4.4 Pseudo-images of Radial and Azimuthal Components
The radial electric field component E_r (top panels) compared with the azimuthal component E_ϕ (bottom panels) at a range of 4 km and a frequency of 0.75 Hz. All other aspects of the figure are as described in Figure 4.3.

resistive body. We note that this is evidently because of the information contained in the phase, not the amplitude.

In Figure 4.5 we demonstrate the increased sensitivity of E_r to the reservoir with increasing frequency. Here we have shown only phase since the amplitude data show the same progression and are slightly noisier. As discussed in Part 1, the lowest frequency (0.25 Hz) has little sensitivity to the target, little more than 15° in phase and virtually at the noise level in amplitude (not shown). At 3.25 Hz the signal is strongest, but 3 km is the longest range at which data at this frequency meets our SNR threshold of 10 (note the drop in the number of data involved in each map).

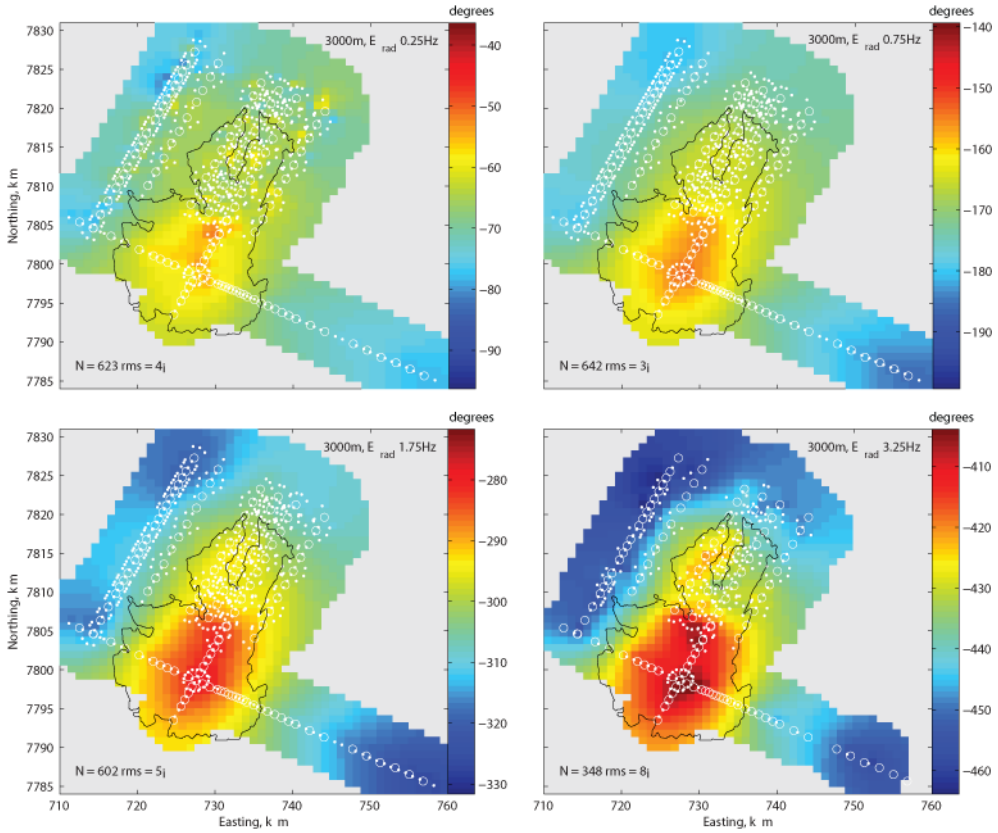

Figure 4.5 Pseudo-images by Frequency
Phase of E_r at four frequencies and a source-receiver range of 3 km. All other aspects of the figure are as described in Figure 4.3.

Finally, in Figure 4.6 we compare the radial electric field E_r to the azimuthal magnetic field B_ϕ and vertical electric field E_z. The azimuthal magnetic field (which is actually collected in the inline geometry like E_r) is extremely similar to E_r in both amplitude and phase, except for a slightly higher noise level (manifest here as 359 data versus 642 data). The magnetic field is well predicted by the electric field at all ranges and frequencies and seems to provide little additional information. This might not always be the case such as in the presence of near-surface structure creating a galvanic effect on magnetic field amplitudes. Indeed, the magnetic amplitudes appear slightly more noisy than the electric amplitudes, which may be attributable to some near-surface conductivity fluctuations at Scarborough.

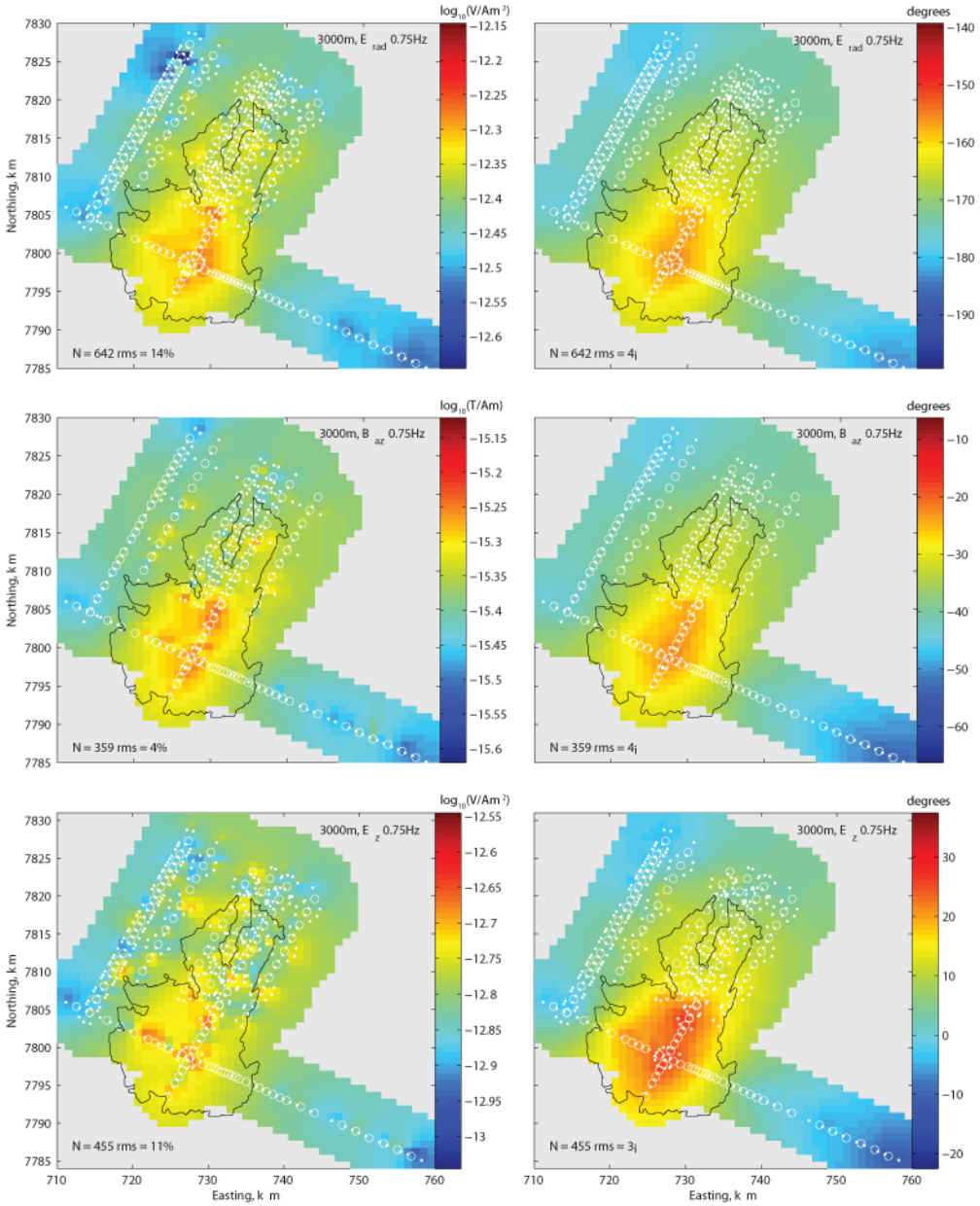

Figure 4.6 Pseudo-images of radial E, azimuthal B, and vertical E. Amplitude and phase of E_r (top panels), the azimuthal magnetic field B_ϕ (middle panels), and the vertical electric field E_z (bottom panels) at a source-receiver range of 3 km and a frequency of 0.75 Hz. All other aspects of the figure are as described in Figure 4.3.

The vertical electric field, which is sometimes collected but rarely interpreted, is thought to be sensitive to lateral structural boundaries (Constable and Weiss, 2006). Here the E_z amplitudes are noisy and lack any obvious structure. This is due to two effects. First, the dip of the antenna causes a few percent difference between the data in front of

the transmitter and the data behind the transmitter. If we separate these two data sets, the E_z amplitude pseudo-image becomes a little smoother, but not completely. The second cause of fluctuations is small galvanic effects at the seafloor where the continuity of vertical electric current expressed in Ohm's law implies that the change in conductivity between the seawater and seabed yields a change in the vertical electric field. Therefore, a 5% variation in amplitude implies a lateral variation of up to 5% in the seafloor conductivity. This type of variation apparently has a smaller effect on B_ϕ than on E_z.

It is debatable whether E_z amplitude will be useful, given this high sensitivity to things other than the deep target. The phase, however, does appear to carry a strong response to the reservoir of about 30° above the background, compared to 15° for the radial phase, and may be a useful addition to higher dimensional inversions. It is localized over the center of the target rather than the boundaries because of a paucity of vertical data in the center and because the data are placed at midpoints rather than transmitter positions.

What is particularly apparent in these figures is the value in collecting high quality phase data and a broad spectrum of frequencies. In the pseudo-imaging maps for Scarborough, the phase is fit to a lower RMS than the corresponding amplitude. We attribute this to lower random noise in phase resulting from excellent timing control in both our receivers and transmitter as discussed in Part 1, and larger amplitude fluctuations resulting from near surface conductivity variations. The differing levels of noise in phase versus amplitude lends further weight to our argument in Part 1 that CSEM data are better inverted in amplitude and phase than in real and imaginary. Also important, but not quite as obvious, is the value of processing off-line data to extract the

radial component. The number of data and the areal coverage of the maps was greatly increased by including data from instruments in several lines on either side of the tow line.

4.3 Inversion Regularization

In this and the following sections, we proceed beyond the pseudo-imaging visualization tool to a more quantitative analysis of the data using 1D inversion. We utilize the Occam inversion procedure discussed in the previous section, but in its usual context of data inversion where in the functional

$$U = \|\partial m\|^2 + \mu^{-1}\left\{\|W(d - F(m))\|^2 - X^2\right\}, \tag{4.6}$$

we have replaced *Gm* with the non-linear operator *F(m)* which is the synthetic data produced from the geologic model *m* by an electromagnetic modeling code. In this case, we use the 1D modeling code of Key (2009). In a 1D smooth inversion, ∂ is a first-difference operator, and the regularization penalty balancing the misfit is a measure of the roughness of the model. In this scheme, the inversion seeks to find the smoothest model which fits the data to some target misfit. A target misfit of RMS 1.0 indicates that on average the model responses fit the data within the specified uncertainties.

As we showed in Part 1, the smoothness constraint of this type of inversion does not permit separate resolution of the resistive gas reservoir and the overlying resistive Gearle siltstone. There are other possible choices for the operator ∂ which can drive the inversion in different directions in order to find a model which fits the data to the requested tolerance. For the Scarborough dataset, we prefer an operator which allows for

jumps in resistivity between layers while still providing the stabilization that regularization introduces into the inversion.

The minimum norm operator (i.e. ∂ is the identity matrix) is one such operator. It penalizes the sum of the squares of the model parameters, driving the inversion to seek the model with the lowest overall resistivity. Since resistivity values span many orders of magnitude, it is common practice to invert for the log10 of model resistivities, with the result that in minimum norm regularization the inversion will seek the model whose resistivities are closest to 1 Ωm (i.e. $\log_{10}(1) = 0$). Because there are no constraints between layers, the inversion is free to vary the resistivities. In practice the removal of layer-to-layer penalties unfortunately allows the inversion to create alternating layers with large variations in resistivity (e.g. ten orders of magnitude). Often infinities are introduced and the inversion breaks down. Imposing narrow limits on allowed resistivity values is required to stabilize the inversion. We find that the lower limit is the more sensitive of the two. If it is too low, the inversion can sometimes place a shallow, slightly too conductive body and compensate for it with a deep, very resistive body. Since in hydrocarbon environments we are looking for resistive bodies, we wish to minimize this effect so place the lower bound at or near 1 Ωm, a typical value for marine sediments.

A further modification may be made by recognizing that the minimum norm term is similar to the prejudice term which is a common addition to this formula (c.f. Key, 2009; deGroot-Hedlin and Constable, 1993):

$$U = \left\| P\left(m - m_p\right) \right\|^2 + \left\| \partial m \right\|^2 + \mu^{-1} \left\{ \left\| W\left(d - F\left(m\right)\right) \right\|^2 - \mathrm{X}^2 \right\}. \quad (4.7)$$

The prejudice term allows for the calculation of a penalty for deviation from a preferred model (m_p) where P is a set of penalty weights. The prejudice term is simply a minimum norm constraint whose preferred model is not 1 Ωm, but some potentially complicated a priori model created from other geophysical constraints. We refer to this as the prejudiced minimum norm (PMN) inversion and in it we set P to the identity matrix, m_p to an a priori model, and ∂ to zero.

Unlike the smooth inversion whose results are always biased towards thick, less-resistive layers, the bias in the PMN inversion is influenced by the domain of the model resistivity parameter values. If the model values are in the linear domain, then there is a bias toward thick layers. In the log10 domain, there is a bias toward thin layers. Consider, for example, two theoretical 2-layer models each penalized against a 1 Ωm half-space prejudice: the first model has a 49 Ωm layer and a 1 Ωm layer; the second has two 25 Ωm layers. In both models, the layers are relatively thin and embedded in a half-space. To first order, CSEM is T-equivalent (Constable and Weiss, 2006), so since the two models have identical resistivity-thickness products (T), they should produce the same electric field response, and an inversion of either set of data will consequently produce the same model. Whether that resulting model has a thick layer or a thin layer will be determined by the regularization penalty. In the linear domain, the minimum norm penalties calculated for the two models are 2304 and 1152, respectively, showing a bias toward the thick, less-resistive model. In the log10 domain, however, the situation is reversed: the penalties are 2.9 and 3.9, respectively, yielding a bias toward thin, more-resistive layers.

Geologic interpretation of minimum norm model results must take this bias into account. In some exploration environments, thin resistive layers are the preferred interpretation and so the PMN inversion provides a benefit over the smooth inversion. Hydrocarbon exploration is one example.

We compare the performance of the smooth inversion with the minimum norm inversion using synthetic data from models of the on and off-reservoir resistivity structure for Scarborough that are shown in Figure 4.2. We structured the two synthetic datasets to mimic the conditions under which we intend to invert the real data, calculating inline electric field amplitude and phase with a transmitter spacing of 150 m for our four target frequencies (0.25, 0.75, 1.75, and 3.25 Hz) at ranges between 1.5 and 8 km. We excluded any synthetic data whose amplitude falls below 1e-15 V/Am^2. We added Gaussian noise scaled by the range and frequency dependent error structure calculated for Scarborough in Part 1 of this study and then inverted each dataset with four different roughness constraints: smooth, smooth with prejudices (i.e. equation 4.7), minimum norm, and PMN.

For the prejudices, we use the off-reservoir model, even when a reservoir response is included in the synthetic data. Using the off-reservoir model as a prejudice has the advantage that any reservoir response added by the inversion will be penalized and thus can be considered a minimum value, i.e. the smallest variation from the background model required to fit the data.

Figure 4.7 shows the models resulting from the suite of inversions. The model layers have a uniform thickness of 100 m, and therefore do not exactly line up with the layer depths of the forward models, as might occur in the inversion of real data where

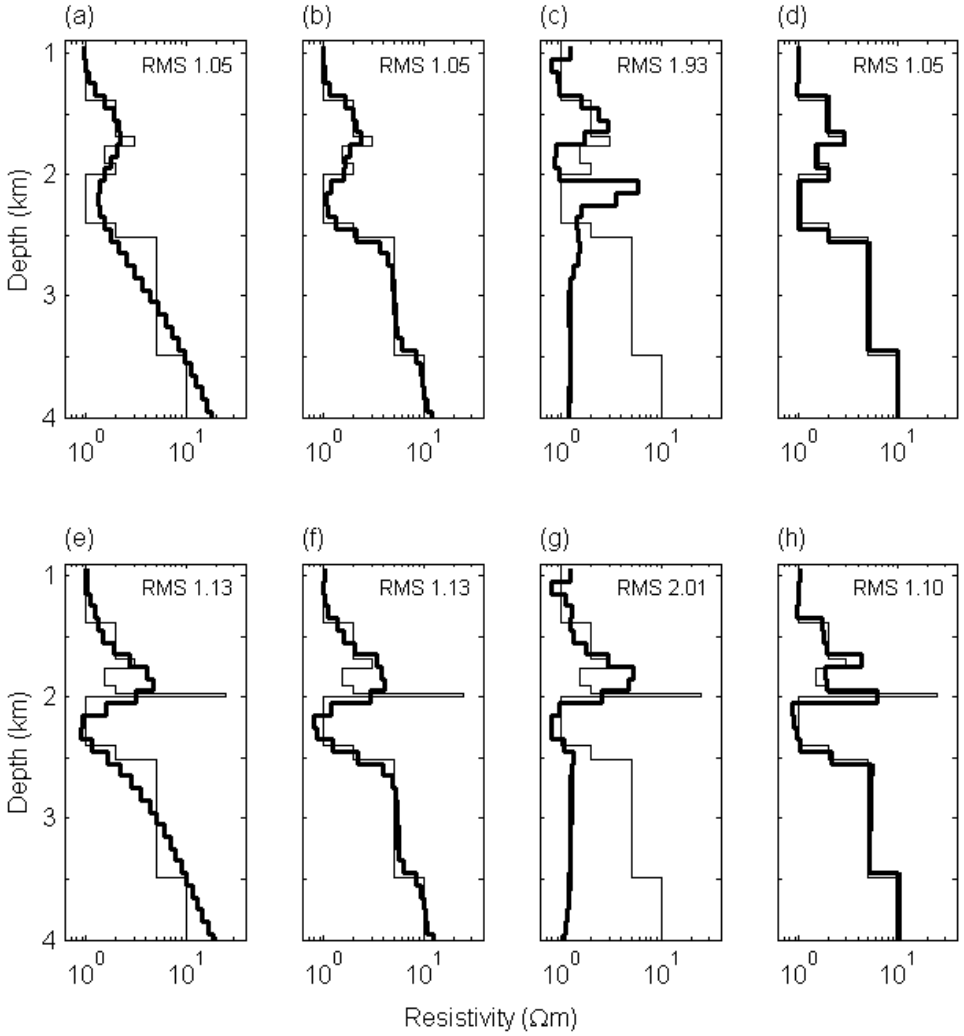

Figure 4.7 Synthetic tests of various 1D regularizations.
Models from inversion (thick lines) of synthetic data (thin lines) for Scarborough off-reservoir structure: (a) smooth inversion, (b) smooth inversion plus a prejudice penalty, (c) minimum norm inversion, and (d) prejudiced minimum norm (PMN) inversion. Plots (e)-(h) are for on-reservoir structure. The prejudice penalty is always the off-reservoir structure. Only the PMN inversion is able to distinguish between the reservoir and Gearle layers.

layer depths are not known precisely or vary across the survey line. The top row of plots (a-d) are for the off-reservoir synthetic data and the bottom row (e-h) are for on-reservoir. The smooth inversions (a & e) yield essentially a four layer model and give an approximate depth for a resistive complex between 1500 and 2000 m. Adding prejudices

to the smooth inversions (b & f) does not significantly improve the results other than to sharpen the basement response. The minimum norm inversions (c & g) drive the models toward 1 Ωm as expected and result in poor fits to the data. The RMS misfit for these two models is over 1.9, reflecting their poor performance compared to the other inversions, whose misfits are ~1.1. The model most closely resembling the synthetic model is from the PMN inversion (d & h). The on-reservoir inversion is of interest in that it shows that this type of inversion is able to separate the Gearle and reservoir layers, though not completely.

For each model, the resistivity-thickness product for the depth range covering the reservoir and Gearle (1450-2050 m) is close to the true product from the forward models. The off-reservoir value is 1155 Ωm^2 and the four inversions (a-d) yield values of 1158, 1148, 964, and 1168 Ωm^2, respectively. Similarly, the on-reservoir value is 1845 Ωm^2 and the four inversions (e-h) yield values of 1810, 1779, 1854, and 1799 Ωm^2. For a general characterization of on- versus off-reservoir, any of these regularization penalty schemes will apparently suffice. The primary difference is in the fine scale resolution determined by each.

CSEM is governed by electromagnetic diffusion physics, so the resolution contained in the data is inherently limited. By providing a geologically-informed prejudice to an inversion, we are introducing extra information into the process that may affect the resolution. If the prejudice is poor, the inversion may produce an unsatisfactory result (e.g. Figure 4.7c). It is not obvious, however, how the PMN inversion will perform when the prejudice is only approximately correct. To examine this, we inverted the on-reservoir synthetic data again with three different prejudice models. In Figure 4.8a, the

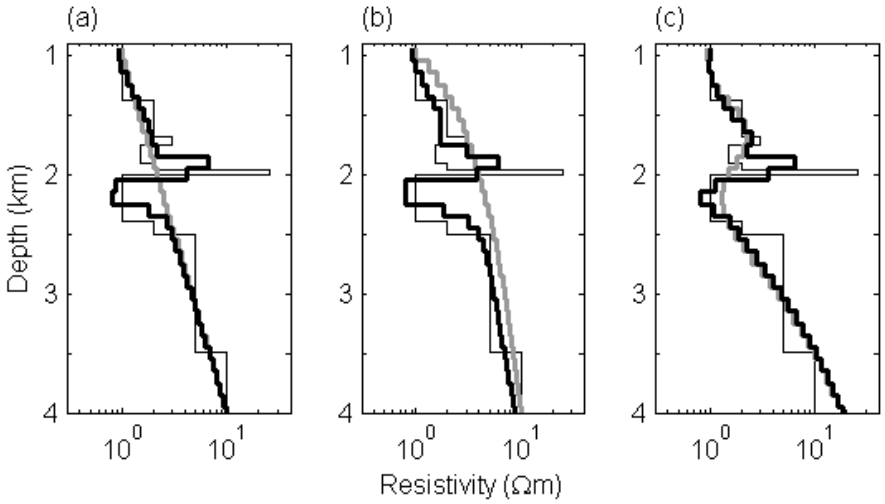

Figure 4.8 Synthetic test of PMN with approximate prejudice models.
Models (thick black lines) from PMN inversion of synthetic on-reservoir data (thin black lines). The prejudice model (grey) is (a) equal steps from 1 to 10 Ωm in log10, (b) equal steps in linear space, or (c) the model resulting from smooth inversion of the off-reservoir synthetic data (i.e. Figure 4.7a). This latter prejudice is to mimic survey conditions in which no a priori geologic information is known and a background is derived from the data. The resulting models for all three cases are remarkably similar.

prejudice increases uniformly in log10 from 1 to 10 Ωm over 3000 m of depth, while in Figure 4.8b, the prejudice increases uniformly in linear space. In Figure 4.8c, we mimic survey conditions in which there is no a priori geologic information and use the model from the smooth inversion of off-reservoir data (i.e. Figure 4.7a) as the prejudice. All three inversions yield remarkably similar models whose values for T of 1838, 1787, and 1841 Ωm^2, respectively, compare favorably with the true value of 1845 Ωm^2.

Though these results are not as fine-scaled as when a priori geology is used, they do show a concentration of resistivity in a much thinner layer than the smooth inversion. The roughness penalty of the smooth inversion evidently suppresses some resolution information in the data, compared to the PMN inversion. While one would certainly not be able to distinguish the reservoir from the overlying Gearle layer, the depth and T of the reservoir are approximately correct. In the Scarborough survey, we have the benefit of a

background which is informed by seismic surveys and logs from exploratory wells, so we expect the PMN inversion to perform well under these conditions.

4.4 1D Stitched Inversion

There are several ways to gather data for 1D inversions from a line of CSEM sites. In each procedure, groups of data are inverted separately and the model results are displayed side-by-side along the tow track, usually as vertical stripes in a color plot, so that common features across the tow line may be identified. We refer to such a plot as a stitched 1D inversion, though in fact it is many separate 1D inversions merely displayed together. A simple way to gather data for a stitched inversion is to invert the in-tow and out-tow data for each site separately – hereafter referred to as single-site stitch (S3). However, when sites are closely spaced, there is overlap in the data such that each resulting model covers most of the same geologic structure as the models next to it, blurring the horizontal extent of geological features. Since the Scarborough sites are spaced 500 m to 2 km apart and we are inverting data out to 8 km range, using this selection procedure would yield inversions in which each site overlaps data with at least three of its neighboring sites. The S3 procedure would likely result in a stitched inversion in which features are extended to greater lateral distances than in the actual geology.

Another method for grouping data for stitched 1D inversion is by common mid-point (CMP). Data from all sites are located along the tow track according to the horizontal mid-point between the transmitter and receiver positions. The tow-track is then divided into segments of equal width and all data whose midpoints are within a segment are gathered and inverted together. The “aperture” of each segment is wider than the

segment itself since the position of the transmitter and receiver may be up to half the maximum range away from the center of the segment. So though the gathering procedure may focus the data, some degree of blurring in the resulting models is expected.

To compare the S3 and CMP procedures, we inverted the electric field responses from a 2D synthetic model. The model contains a 30 m x 5 km reservoir of 25 Ωm embedded in the Scarborough 1D background and at the approximate depth of the Scarborough reservoir (2 km below sea level). There are 10 sites on the seafloor spaced 1 km apart with two sites off either end of the reservoir. Using the 2D code of Key and Ovall (2011), we computed inline electric fields for our four target frequencies for transmitter locations spaced every 150 m along a 23 km track-line centered on the reservoir. Data for each site were trimmed down to those within 1.5 – 8 km range and with amplitudes above 1e-15 V/Am^2. For both the CMP and S3 inversions, we used the PMN regularization with the prejudice defined as the 1D background used in the synthetic model. We used the range-dependent uncertainties discussed in Part 1 in order to mimic the loss of resolution with range inherent in CSEM. For the CMP inversions, we gathered the data every 1 km along the tow track.

Figure 4.9 shows the model results for (a) CMP and (b) S3 stitched inversions. Each vertical stripe is the result of a separate inversion and shows the difference in resistivity between the inversion model result and the 1D background used in the synthetic model. We show the difference so that the color scale is not dominated by the steps in the background. The CMP models identify the extent of the reservoir with some decline in resistivity at the reservoir boundary due to either the transmitter or receiver being off the reservoir in some of the gathered data. The S3 results, by comparison, blur

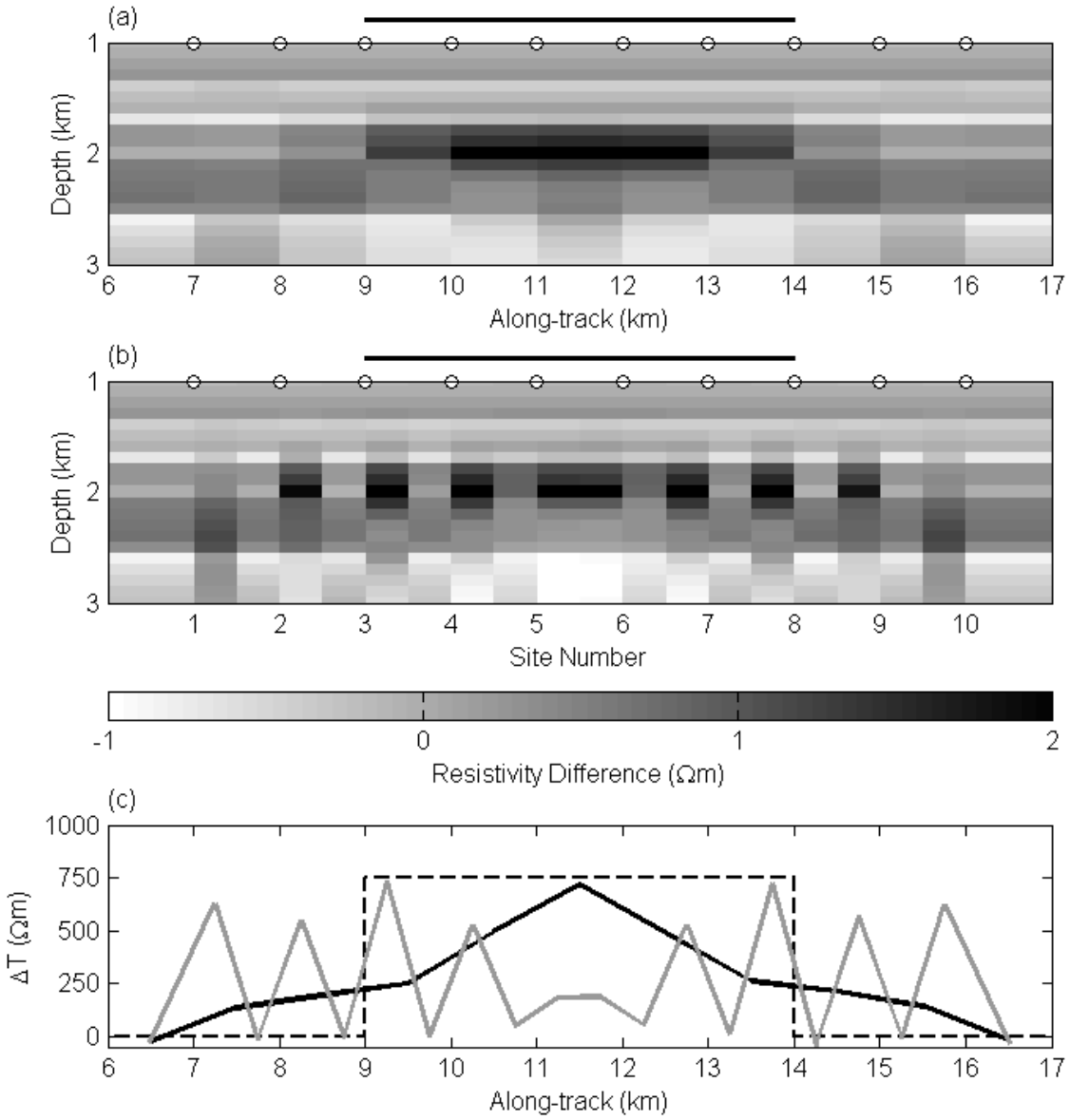

Figure 4.9 Synthetic test of CMP versus in-/out-tow data gathering procedures.

Model results from stitched 1D inversions of a synthetic 2D reservoir model using (a) common midpoint (CMP) and (b) separate in-tow and out-tow for each site (S3). The resistivity difference between the inversion model and off-reservoir background of the forward model is plotted for each individual 1D inversion. Site locations are denoted by the open circles and the location of the reservoir is indicated by the black line. (c) The difference in resistivity-thickness product between the model and background for the 1100 m centered on the reservoir depth. The dashed line is the true model, the black line is from the CMP inversions, and the gray line is from the S3 inversions.

the edges for several kilometers and feature an alternating on/off reservoir pattern which is related to the percentage of the data in the in- or out-tow segment that is on the reservoir.

Figure 4.9(c) shows the difference in resistivity-thickness between the inversion models and the background prejudice for top 2 km of the models. The CMP values peak at the expected 750 Ωm^2 and decline steadily towards the outermost gathers. The values of ΔT do not reach zero until the last gathers because there are still some data in these segments from transmitter or receiver positions over the reservoir. The S3 results are wildly oscillatory between on and off reservoir values. The center two inversions for S3 have suppressed ΔT because of the low resistivity values which occur at around 2.6 km bsl. The data in these inversions are approximately such that the near range data are on-reservoir and the far range data are off-reservoir. The inversion attempts to reconcile the disparity by placing a resistor over a conductor. Where this situation is reversed (i.e. to the right of site 1 and to the left of site 10), the inversion creates a deep, thick conductor to account for the far range data being on-reservoir. This comparison clearly shows that the CMP procedure is superior to the S3 procedure for stitched 1D inversions and a viable tool for use in simple 2D environments. However, we note that CMP places greater demands on the navigation accuracy. If there is an error in an individual receiver's position, for example, it may be easily accommodated by the S3 procedure since all of the in-tow or out-tow data, which will appear to have a bias, will be grouped together. In the CMP procedure, the biased data will be distributed through multiple bins, providing outliers which may drive many of the inversions in unexpected directions. So, care must be taken when using CMP to examine the residuals of each inversion.

4.5 Data Selection and Uncertainties

For inversion, we selected inline electric field data from the first three phases of the Scarborough survey. These data cover the body of the reservoir and even include off-reservoir control lines. We used the transmitter and receiver locations described in Part 1 and note that the transmitter antenna dip was not measured in phase 1, so a fixed value of -5.4 degrees is used for lines 2 and 3. We selected only the four strongest harmonics of our custom waveform "D" described in Myer *et al.* (2011): 0.25, 0.75, 1.75, and 3.25 Hz.

Though frequency domain data are available for time windows of a single waveform in length (4 seconds), we find it more useful to use the data which are stacked to sixty seconds. These data include a variance of the mean which can be used for signal-to-noise ratio (SNR) selection and minimum uncertainties. Because of the large volume of data available, we imposed a few selection criteria to automatically trim down the set to a manageable size before a final manual removal of extreme outliers. Data for each site were rotated with respect to the tow line to create inline and crossline components. We considered only every third inline data point and of those selected only data with SNR >= 10 and range between 1.5 and 8 km. Finally, we applied a frequency and range dependent error structure as described in Part 1, subject to a minimum defined by 2σ noise estimates from the stacking variances, and we invert the CSEM data in amplitude and phase.

We decimated the data because we observe that a high data density is not necessary to achieve good results in 1D. Our chosen decimation corresponds to one datum per frequency per receiver approximately every 150 m along the transmitter track. We also imposed a minimum range to constrain the effects of bias. There are two sources of bias present in the data which are quantifiable: stacking bias from the moving

transmitter, and the finite length of the transmitter dipole. The time series processing procedure we used in Part 1 assumes statistical stationarity of the data; however, the motion of the transmitter violates this assumption. For each sample measured in time, the range between the transmitter and receiver is slightly different, as is the attenuating volume. For short time windows or small changes in range relative to the total transmitter-receiver distance, the difference is negligible and can be ignored. However, for close range data and longer time windows it cannot. An additional bias is introduced by the finite length of the transmitter dipole. Viewed as the superposition of point dipoles along the length of the finite dipole, it is easily seen that this bias is equivalent to a stacking bias. For a 60 s stack frame, the stacking and finite dipole biases are large compared to other uncertainties below 1.5 km range and relatively inconsequential above that range. Since we invert with a point dipole formulation, we chose to leave out the biased data.

4.6 1D Inversion Results

We gathered data into common mid-point bins 2 km wide along the tow track and inverted the data in each bin separately. The seafloor must be flat in 1D inversion, so we adjusted the site depths in each midpoint group to be the same and altered the depth of each transmitter location to preserve its measured altitude above the seafloor. Since the portion of the Exmouth plateau above Scarborough has very little bathymetric relief, most adjustments were less than ten meters.

We ran a 1D PMN inversion for each bin of data, using the off-reservoir Scarborough structure as the prejudice. Each inversion was targeted for an RMS of 1.0

but many did not reach this. In these cases, we considered that an inversion had converged when its RMS changed by less than 0.01 over three iterations and at this point we reset the target misfit and allowed the inversion to begin minimizing the regularization penalty. The Occam inversion procedure has two phases, the first of which perturbs the model until it has converged to the target misfit. After convergence, the second phase perturbs the model until the regularization penalty is minimized, while keeping the misfit the same. This second phase is an important part of the Occam procedure especially in our PMN inversions where we are seeking the minimum variation from the off-reservoir model required to fit the data. When a particular inversion cannot reach the target misfit of 1.0, perhaps because of 2D or 3D effects in the data, stopping the inversion early does not allow the second phase of the Occam procedure to run and we cannot say with any certainty that the resulting model is the minimum variation from the background model for the given misfit. Therefore, we reset the misfit target to 1.1 times the misfit reached and continue the inversion so that it will converge and run the second phase to minimize the regularization penalty. There were 110 inversions in all, 83 of which converged to RMS values <= 2. Eighteen of these converged to 1.0 and are primarily from midpoint segments at the ends of the tow-lines where the 2D and 3D effects of the reservoir edges and resistivity variations are minimal.

Figure 4.10(a) shows the anomalous resistivity of the 1D inversion models for tow line 2 which crosses the main body of the reservoir and extends 24 km east of the gas-water-contact boundary. Each vertical stripe is a separate inversion and plots the difference in resistivity between the inversion model and the prejudice. The inversion has primarily concentrated the resistivity anomaly from the gas reservoir in the Gearle layer

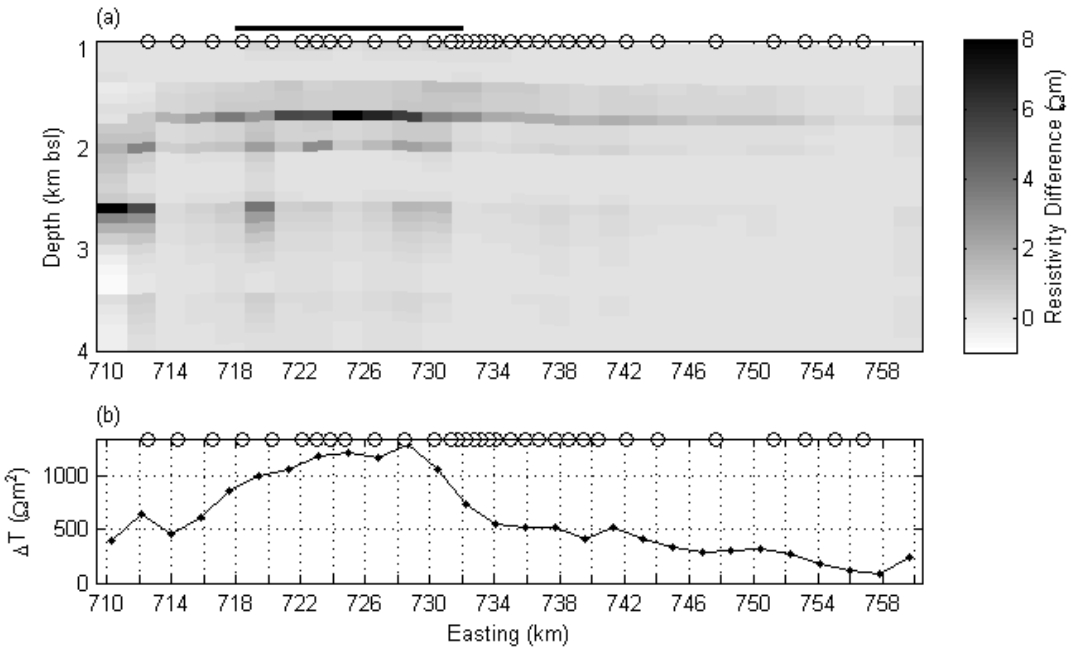

Figure 4.10 1D stitched PMN inversion results for line 2.
(a) Anomalous resistivity for the 1D inversion models for line 2. Each vertical stripe is a separate inversion and shows the difference between the inversion model and the prejudice. The vertical exaggeration is ~6. Circles are the locations of the receivers and the thick black line is the extent of the gas water contact outlining the reservoir. (b) The difference for depths 1450-2050 m in resistivity thickness product between the 1D inversion models and the off-reservoir prejudice used in the regularization penalty.

(~1.8 km bsl), with just a slight elevation of the resistivity at the expected reservoir depth (~2 km bsl). This is not entirely unexpected, given the ambiguity shown in the synthetic tests in Figure 4.7, but the small response at the reservoir depth compared to the synthetic tests may indicate that the a priori 1D background we have used is only approximately correct. It is also possible that the higher resistivity at the Gearle layer represents anisotropy, thickening of this layer, or even ponding of gas at this relatively impermeable siltstone. However, there is insufficient resolution to choose between these cases with any certainty.

Since the PMN inversion is penalized towards the minimum resistivity variation from the background, we take the resistivity-thickness product of the set of layers from

1450 – 2050 m below sea level as the minimum bounds on the resistive anomaly in the vicinity of the reservoir. Figure 4.10(b) shows ΔT calculated from the difference between the resistivity thickness product of the inversion models and the off-reservoir prejudice. The relatively large drop in ΔT near the reservoir boundary is spread over several inversions, then is followed by a steady decline. This pattern is completely consistent with the behavior of the CMP inversion of synthetic data as shown in Figure 4.9. We take the far eastern value of about 250 Ωm^2 to represent the difference between the idealized Scarborough background we used for a prejudice, and the in-situ background. If we subtract it from the value we calculate for the inversion in the center of the reservoir, then ΔT is 750-1000 Ωm^2, which is similar to the value of ~700 Ωm^2 in the idealized model.

Figure 4.11(a) is a plot of the anomalous resistivity of line 3+4 which runs orthogonal to line 2. The sites in this line are mostly within the reservoir boundary with line 3 crossing the main southern portion of the reservoir and line 4 extending up into the northern area where the reservoir appears to split into two lobes shaped much like rabbit ears. The reservoir narrows at about 7,806 km northing and splits at about 7,811 km northing. The value of ΔT (Figure 4.11b) shows a decline of ~30% northward of the narrowing of the reservoir but does not reach the low value found in the eastern end of line 2.

In our synthetic studies, we showed that the standard smoothness constraint would yield models too simple to be of value, even when prejudices are added. To verify this, we inverted the same groups of data with smooth inversion using the same convergence conditions we used in the PMN inversions. In order to obtain as much resolution as possible out of the smooth inversions, we also removed the smoothness constraint above

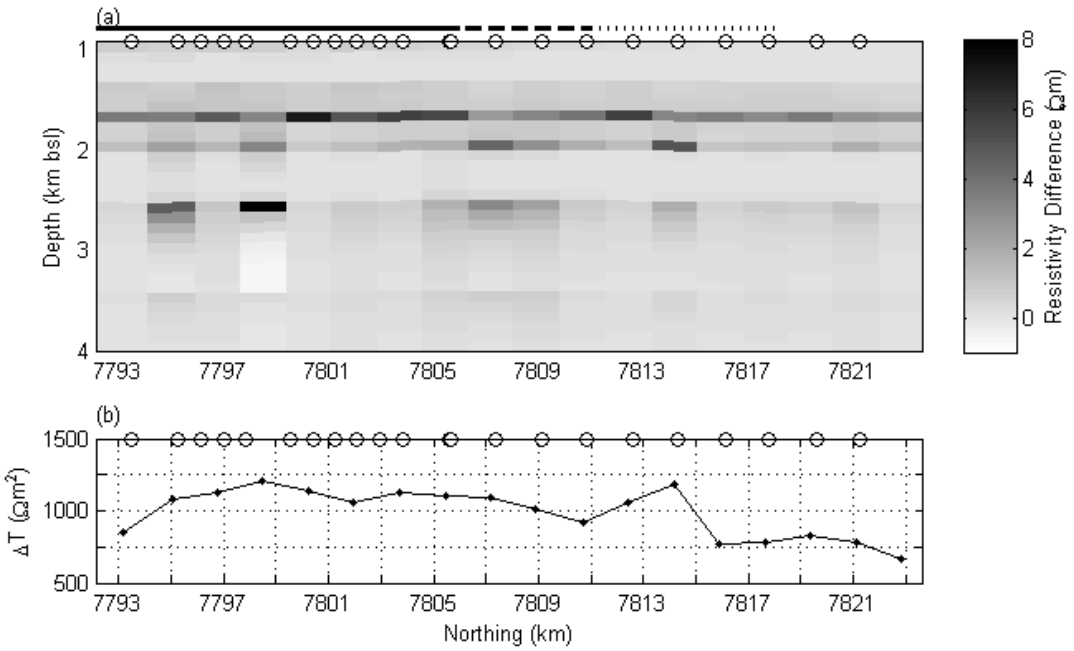

Figure 4.11 1D stitched PMN inversion results for line 3+4.
(a) Difference in resistivity of the PMN inversion models from the prejudice model for lines 3+4, which run orthogonal to line 2. Circles are the locations of the sites along the line, the black line is the extent of the reservoir: solid over the main body, dashed where it narrows, and dotted in the channels in the north. (b) The difference for depths 1450-2050 m in resistivity thickness product between the 1D inversion models and the off-reservoir prejudice used in the regularization penalty.

and below the model layers at the depths of the Gearle and reservoir to allow for jumps in resistivity and added prejudices to stabilize the inversion. Figure 4.12a shows the anomalous resistivity for line 2, which exhibits wide variation across the stitched profile with no apparent concentration of resistivity in either the Gearle or reservoir layers. Line 3+4, not shown, is similarly varied. These results are surprising considering that prejudices have been applied. From the smooth inversions, it is difficult to interpret either of these lines with any certainty and one might conclude based on these results alone that 1D is not appropriate for this target. If we consider ΔT (Figure 4.12b), the result is a little more regular; ΔT peaks in the reservoir then quickly levels off in the east to about 600 Ωm^2. This behavior is quite different from the PMN results, where ΔT continues to

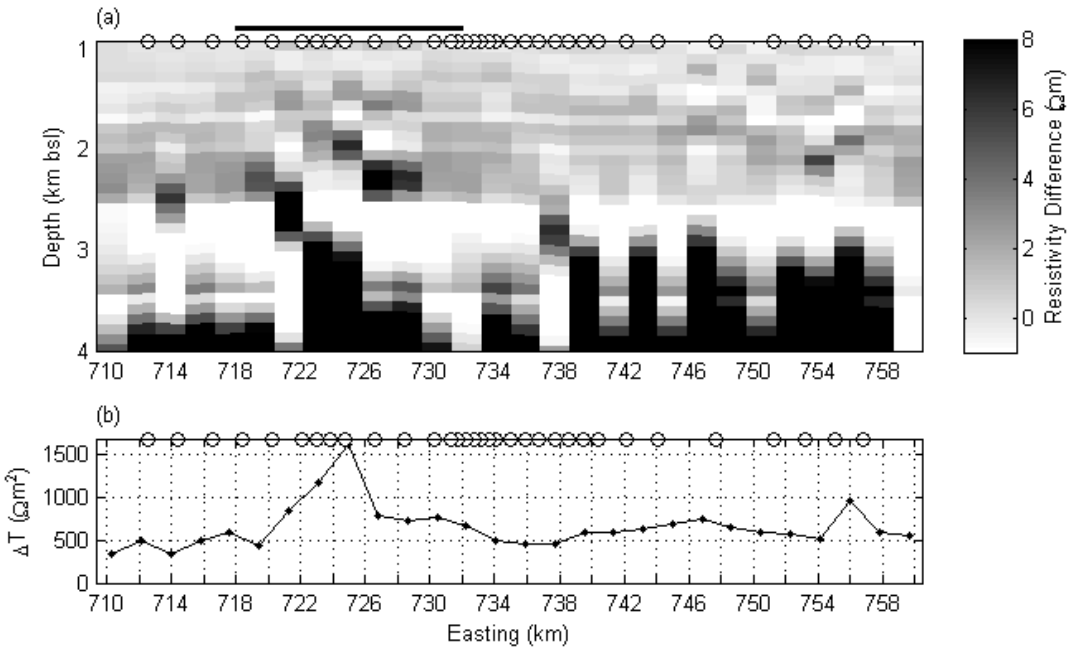

Figure 4.12 1D stitched smooth inversion results for line 2.
(a) Difference in resistivity of the smooth inversion models from the background model for line 2. To improve the smooth inversion results, we removed the roughness penalty above and below the Gearle and reservoir layers and added prejudices for all depths. The on/off reservoir signature is not readily apparent. (b) The difference in resistivity-thickness product for the inversion and background models shows a peak in the center of the reservoir, but does not define the extent of the reservoir well.

decline without leveling off. Our synthetic studies indicated that for gross on/off reservoir characterization, either regularization penalty would perform similarly. Inversions of the Scarborough data disagree, indicating that the PMN inversion is a better tool in this environment. Possibly the combination of higher dimensional effects in the data and the decreased resolution of the roughness penalty conspire to thwart the performance of the smooth inversion. We will show further below that this is no longer the case when lateral constraints are added to the smooth inversion.

In all, we inverted seven lines across the Scarborough reservoir with the PMN inversion. Figure 4.13 shows a plan-view of the anomalous resistivity-thicknesses from each inversion superimposed with an outline of the gas-water contact. The reservoir is

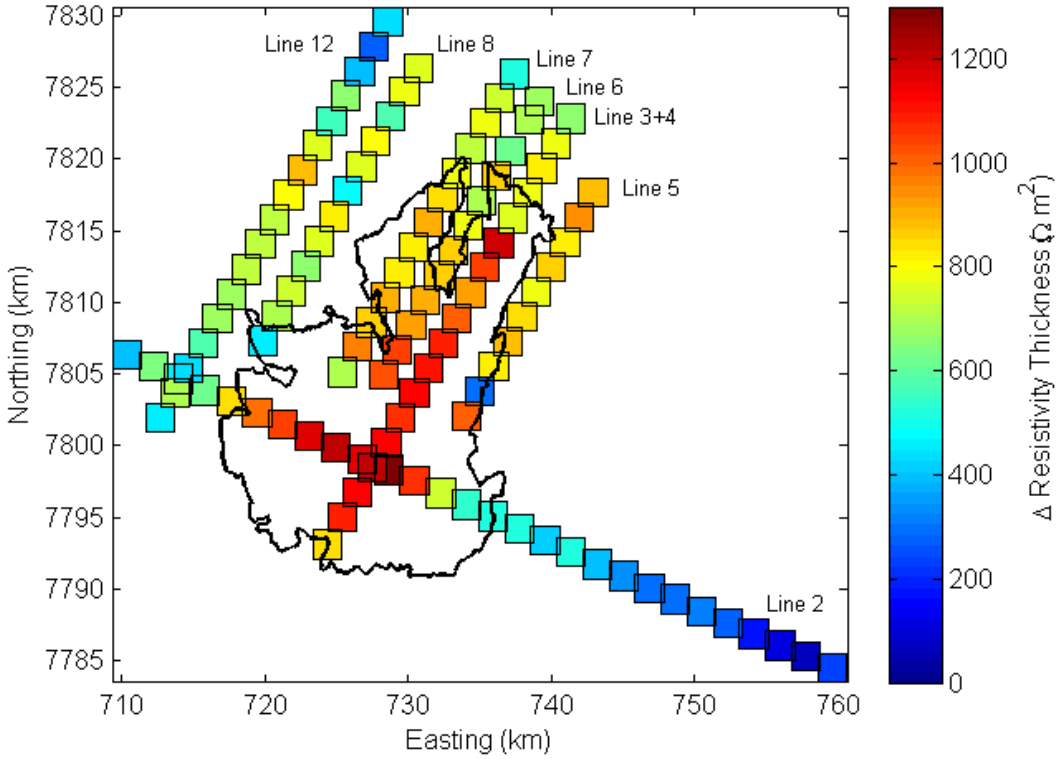

Figure 4.13 Anomalous resistivity thickness from 1D stitched PMN inversions. Map of the anomalous resistivity-thickness product for all the 1D inversions in the Scarborough survey. Each block is the resistivity-thickness above the background prejudice model. The black outline is the approximate gas-water contact outline for the reservoir.

clearly seen in the east-west trending line 2 and in the north-south trending lines 3+4, 6, and 7. These lines show that the strength of the reservoir signal weakens to the north, consistent with the expected narrowing and channelization exhibited by the "rabbit ear" structures.

Line 5, which runs 1 – 2 km outside the eastern edge of the reservoir, yields results similar to the lines on the reservoir, unexpectedly getting stronger in the north. While it is possible that the reservoir boundary is incorrect in this area and extends somewhat further east, this is not strictly required by the data. The CSEM method is volumetric, so there is some sensitivity to structure that is to the side of the direct path

between the transmitter and receiver (Constable, 2010). Since line 8, which is 4 km to the west of the reservoir, does not show the same enhanced resistivity-thickness as line 5, our data may indicate that the lateral sensitivity extends less than 4 km to the side of the tow line but at least 2 km. Only a higher dimensional inversion will be able to resolve this issue.

We suspect that the generally less well-defined resistivity boundary in the northern portion of the survey is due to higher dimensionality. For example, the gas concentration suggested by the ΔT does not decline to the expected value of 50% at the reservoir boundary in the north. If we subtract from ΔT the background value suggested by the eastern end of line 2 ($\Delta T = 250\ \Omega m^2$), we arrive at $\Delta T \sim 1000\ \Omega m^2$ for the central portion of the reservoir and $\Delta T \sim 700\ \Omega m^2$ for the northern portion of the reservoir. These values represent the anomalous resistivity introduced by the reservoir and since we have prejudiced the PMN inversion against anomalies, these values may be considered minimums. If we represent the reservoir as a 35 m thick monolithic layer, then we get resistivities declining from 30 to 20 Ωm. Archie's law (Archie, 1942) gives an empirical relationship between the measured resistivity of fluid saturated rock and its water content such that

$$\rho_m = \rho_w \phi^{-a} S_w^{-2}, \tag{4.8}$$

where ρ_m is the measured resistivity, ρ_w is the temperature-dependent resistivity of saline brines at depth, ϕ is the porosity of the host rock, S_w^{-2} is the water content as a fraction of pore fluids, and a the cementation factor. If we take a to be its usual value of 2 and ρ_m to be the resistivity values given above, we still need values for the brine resistivity and the rock porosity in order to calculate the hydrocarbon saturation ($S_H = 1 - S_w$). Brine

resistivity varies as a function of temperature (Von Herzen *et al.*, 1983) and estimates of the geothermal gradient vary across the Exmouth plateau. Using the work of Swift *et al.* (1992) as a guide, we select a temperature of 45C for the reservoir depth, yielding a value for ρ_w of 0.13 Ωm. If we assume $S_w = 1$ off the reservoir and use values of 1-2 Ωm for the off-target resistivity, we then have porosity of the host rock from 0.25 to 0.36. On-reservoir resistivity values then imply hydrocarbon saturation of 74-82% in the middle of the reservoir, declining slightly to 68-78% in the northern area. Well logs suggest that the reservoir is thinner than 35 m, which would increase the saturations we have calculated here. At 50% saturation, ΔT should be between 150 and 300 Ωm^2. While the east-west line appears to bound the gas-water contact appropriately, none of the north-south lines do.

There are several possible reasons for this. First, the CMP gather smears out boundaries, so we may have an insufficient number of sites extending off the northern end of the reservoir to allow these lines to decline to lower values. Second, the western end of line 2 as well as the off-reservoir lines in the northwest are at generally higher values of ΔT than the eastern end of line 2, which may indicate that the shallow background changes in this area (e.g. thickening of the Gearle siltstone). Finally, the northern area of the reservoir is generally not 1D. Higher dimensional inversion may provide a better interpretation of the data there.

4.7 1D Horizontally Constrained Inversions

It is possible to investigate the effects of higher dimensional inversion with a 1D code. We have modified the code of Key (2009) to simultaneously invert multiple data

sets while applying roughness penalties between neighboring model values. In this way, data from an entire line of CMP bins may be inverted simultaneously while the model parameters which are at the same depth along the line have roughness penalties applied across them horizontally. These penalties are in addition to the usual penalties between vertical layers. We refer to this as "1D/2D" inversion because the data for each CMP bin is isolated from the data in the other bins (i.e. no Jacobian is calculated between the data in one bin with respect to the model parameters in the other bins) and yet the roughness penalties are applied as for a 2D model space. We have extended this procedure to 3D as well, where a field of CMP bins is inverted together and roughness penalties are calculated between bins in two orthogonal, horizontal directions ("1D/3D" inversion). In both 1D/2D and 1D/3D inversion, the sensitivity matrix is not full as usual, but sparse, consisting of a series of rectangles of non-zero values with dimension M_i x N (where M_i is the number of data in bin i and N is the number of layers in the 1D model). The roughness matrix, on the other hand, is the usual sparse-banded structure for a 2D or 3D inversion.

We applied 1D/2D inversion to the Scarborough tow line 2 data where a single model involves twenty-five side-by-side CMP bins. These bins together encompass ~36,000 data and were inverted simultaneously. We inverted the data three times, each with a first difference roughness penalty in the horizontal direction and a different vertical regularization penalty. The PMN inversion (Figure 4.14a) finds enhanced resistivity within the lateral reservoir boundaries but places it primarily at the depth of the Gearle siltstone. There is also a slight enhancement in resistivity at the expected reservoir depth (2 km bsl) and in the resistive basement. These results are similar to those from the

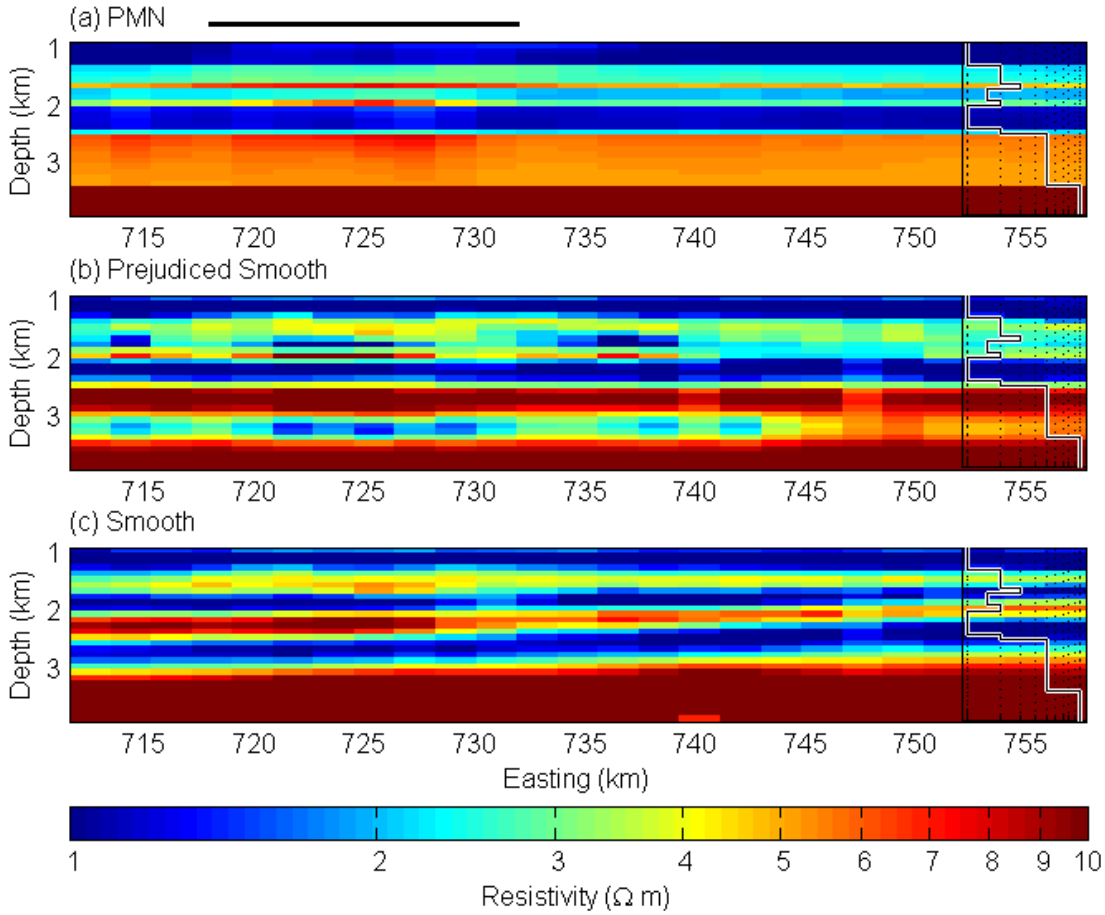

Figure 4.14 1D/2D inversion results with three different vertical regularizations. 1D/2D inversion models for CMP gathers of line 2 with a horizontal roughness constraint and (a) PMN, (b) smooth with prejudice, and (c) smooth without prejudice vertical constraint. The right side is overlain with the background model from Figure 4.2 which ranges from 1 to 10 Ωm in log scale. The line above the plot delineates the expected width of the reservoir. The inversion for the bottom panel did not use a background constraint.

1D stitched PMN inversion in that there is very little variation from the prejudicing a priori model. Surprisingly, the RMS misfit is 2.2 which is rather poor and may indicate that there are some higher dimensional effects unaccounted for. The distribution of residuals is nearly Gaussian and the RMS misfits calculated separately on the data of each of the four frequencies are approximately the same.

We inverted the data with a vertical roughness penalty both with and without a prejudice model (Figures 4.14b and c, respectively). These inversions both converged to

an RMS misfit of 1.5 which is significantly better than the PMN inversion, though still influenced by the higher dimensional structure not captured by the 1D algorithm used in the inversion. The addition of lateral constraints has significantly improved both results over the 1D smooth stitched inversions which were highly variable even though a prejudice was applied. It is not surprising that the addition of horizontal constraints has corrected this variability. However, what is surprising is the introduction in both smooth inversions of an additional conductive layer. Recall that CSEM is relatively insensitive to conductive layers sandwiched between resistors, and yet even when a prejudice is applied against it in the smooth inversion, this conductor appears. This conductor is not present in the PMN inversion and this is probably the reason that its misfit is higher.

In 1D stitched inversions, the PMN inversion produced a better result than the smooth inversions, but in the higher dimensional 1D/2D inversions, the reverse appears to be the case. The smooth inversions fit the data better apparently by introducing structure not reflected in the a priori background. The PMN inversion, whose only penalty is for deviation from this background, cannot account for this structure. This highlights one of the prime drawbacks of PMN regularization, namely its reliance upon the a priori prejudice. In individual 1D inversions, this reliance is beneficial, producing relatively consistent inversions along the tow line when the typical smooth inversion cannot. In higher dimensions, the inclusion of a prejudice is apparently unnecessary and perhaps even detrimental.

Regarding the basic question of reservoir extent, we show in Figure 4.15 the resistivity-thickness product of the first resistive layer (950-2050 mbsl) of each of the three 1D/2D models and show that the two prejudiced models yield similar results. The

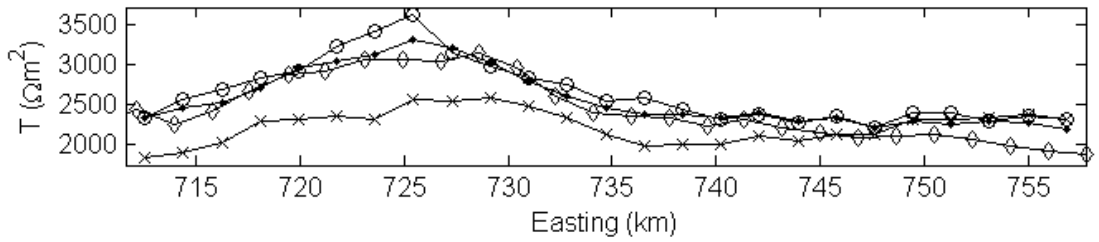

Figure 4.15 Resistivity-thickness for four different inversions of line 2. Resistivity-thickness product *T* for the top 1 km of the 1D/2D inversion models using PMN (dots), smooth with prejudices (circles), and smooth without prejudices (crosses). For comparison, *T* from the 1D stitched PMN inversions (diamonds) are also shown.

smooth, unprejudiced inversion yields values which are lower than the other inversions possibly because of cross-talk between the first and second resistive layers. For comparison, we have also included *T* from the 1D PMN stitched inversions and there is no appreciable difference between this result and the prejudiced 1D/2D inversions. So while PMN may not be necessary in higher dimensions, it is still useful as a quick 1D characterization tool. *T* peaks beneath the reservoir at about 500-700 Ωm^2 above the off-reservoir values which is a little less than the value of ~900 Ωm^2 expected based on well logs, but surprisingly consistent inversion to inversion.

For regional geology, we assume that the a priori background is not necessary in these 1D/2D inversions and may even be interfering with the results and consider only the unprejudiced model. The eastern end of the line has a structure whose depths are in good agreement with the background model (overlaid on the figure, though it was not used in the inversion). However, the bulk of the model has a basement depth which is approximately 400 m deeper than expected to make room for the additional conductive layer.

If we compare the 1D/2D results to the stratigraphic work of Boyd *et al.* (1992), we find that many of the resistive layers can be matched to structure identified from

seismic imaging. The resistive basement, for example, is most likely the Mungaroo Formation, a package of river delta and marine sediments which seismics shows is penetrated by widely-spaced high-angle normal faults and contains some small-throw horst and graben structures associated with limited block rotation. Seismic stratigraphy shows a shallowing trend eastward in the Scarborough area similar to what our inversion shows here.

The resistive layer just below 2 km bsl is not the reservoir itself, though the resistivity of this layer appears to be enhanced beneath the reservoir. The layer extends much farther beyond the reservoir boundary than the "smearing" inherent in CMP can account for. Also, this feature appears with generally equal or higher resistivity in the 1D/2D inversions of all of the orthogonal tow lines (discussed below), even line 12+13 which is many kilometers away from the reservoir. It is probably the Barrow Group, a complex depositional wedge of shales and sands whose original source was in the southeast of the Exmouth Plateau and which prograded to the northwest. The conductive layer beneath and separating it from the Mungaroo Formation is likely the Dingo claystones. The top of the Barrow Group is a major unconformity from around the time of the onset of rifting of the Exmouth Plateau.

The upper 1 km of the seabed is a complex assemblage of relatively thin layers of varying composition (e.g. marl, shale, sandstone). Boyd *et al.* (1992) note that the unconformities associated with some of these layers occasionally truncate underlying layers down to the Barrow Group due to the cycles of uplift and subsidence which occurred during and after the onset of rifting so some variation in layer thickness is expected across the line. The smooth inversion shows thickening of the top layers to the

west, which could be geological, but could just as easily be an artifact of the inversion. The roughness constraint tends to prefer thick, less-resistive layers over thin, more-resistive layers, so the deepening and thickening of the top two resistive layers in the west may simply be an expression of the enhanced resistivity caused by the reservoir.

We ran the smooth, unprejudiced 1D/2D inversion on the six NE-SW trending lines covering the "rabbit ear" portion of the reservoir. Each line converged to RMS 1.2 and recovered the six layer model shown in the western half of line 2. Figure 4.16 shows

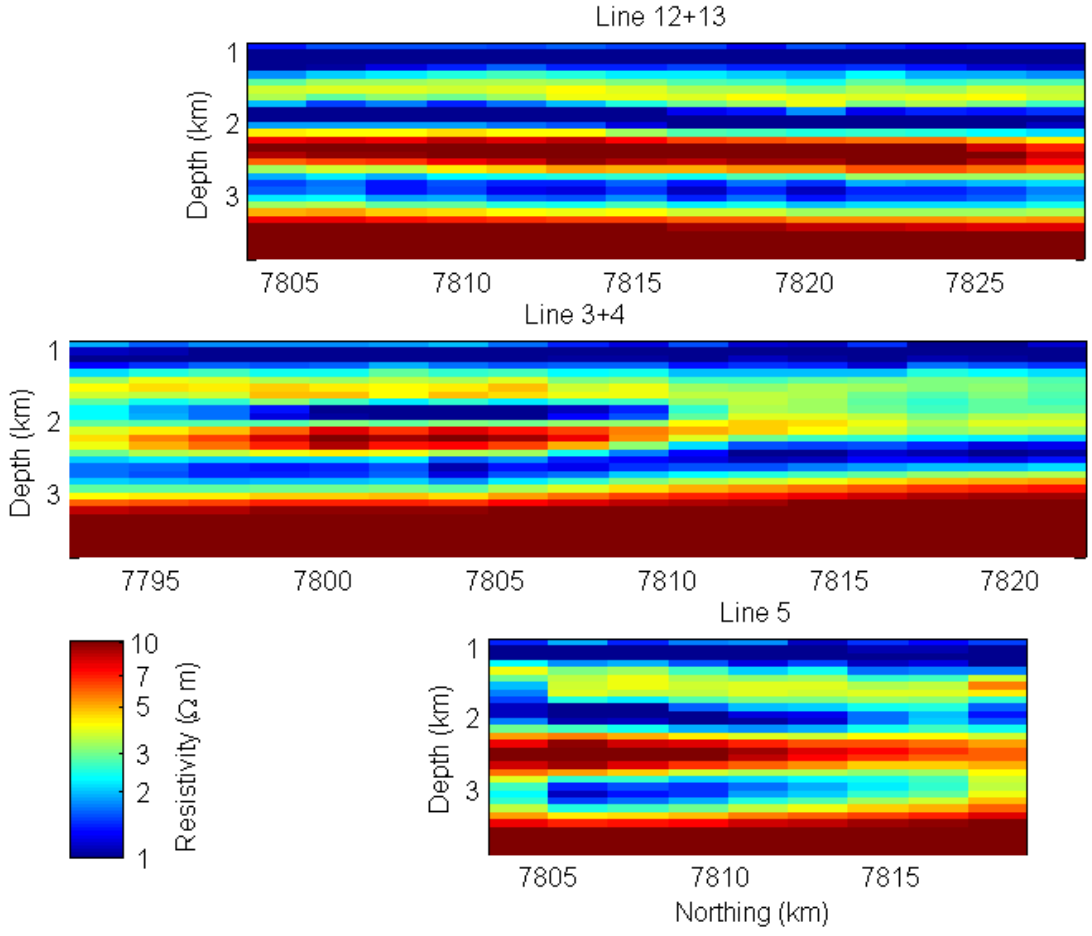

Figure 4.16 1D/2D inversion results for several N-S trending lines.
1D/2D inversion results for lines 12+13 which runs 9 km west of the reservoir, line 3+4 which crosses the main body and runs up the eastern "ear", and line 5 which is a few kilometers east of the reservoir. The plots are aligned to match the bins across the rabbit ear structures of the reservoir. Lines 6-8 are similar to these.

line 12+13, line 3+4, and line 5. We omit line 8, which is similar to line 5, and lines 6 and 7, which are similar to line 12+13. Comparing these model results, it is not easy to determine the reservoir extent. Even *T* calculated in the same way as for line 2 varies by only about 250 Ωm^2 from line to line. Evidently the 1D/2D inversion, which performs better than the stitched inversions for the long east-west line across the morphologically simpler body of the reservoir, performs no better over the more complicated rabbit ear area.

One of the biggest differences between the inversion models for the 1D/2D lines is a consistent shallowing of the Mungaroo basement and the Barrow Group in the side-by-side lines 6 and 3+4. Figure 4.17 shows the depth of the maximum resistivity of the second resistive layer. Shallower depths are found in the body of the reservoir and directly under the eastern rabbit ear. This shallowing is possibly the reason a channel was interpreted in the eastern ear as such an anticline may form a gas trapping structure if a seal is present. (Note that the gas reservoir is in a layer close to and overlaying the Barrow Group.)

We also inverted the entire rabbit ear region together in a 1D/3D inversion. For this inversion, we included all radial mode data between 1.5 and 8 km range which was within +/-60° of the ideal inline geometry. Data were selected for CMP bins centered on the ten northernmost sites from each of the six NE-SW trending lines so that a total of 60 bins were gathered. In all, over 183,000 data were inverted simultaneously with a full 3D roughness penalty. The inversion required about 3 Gb of memory and took nine hours on a typical laptop to run 37 iterations. In the end, the inversion converged to RMS 1.5 using

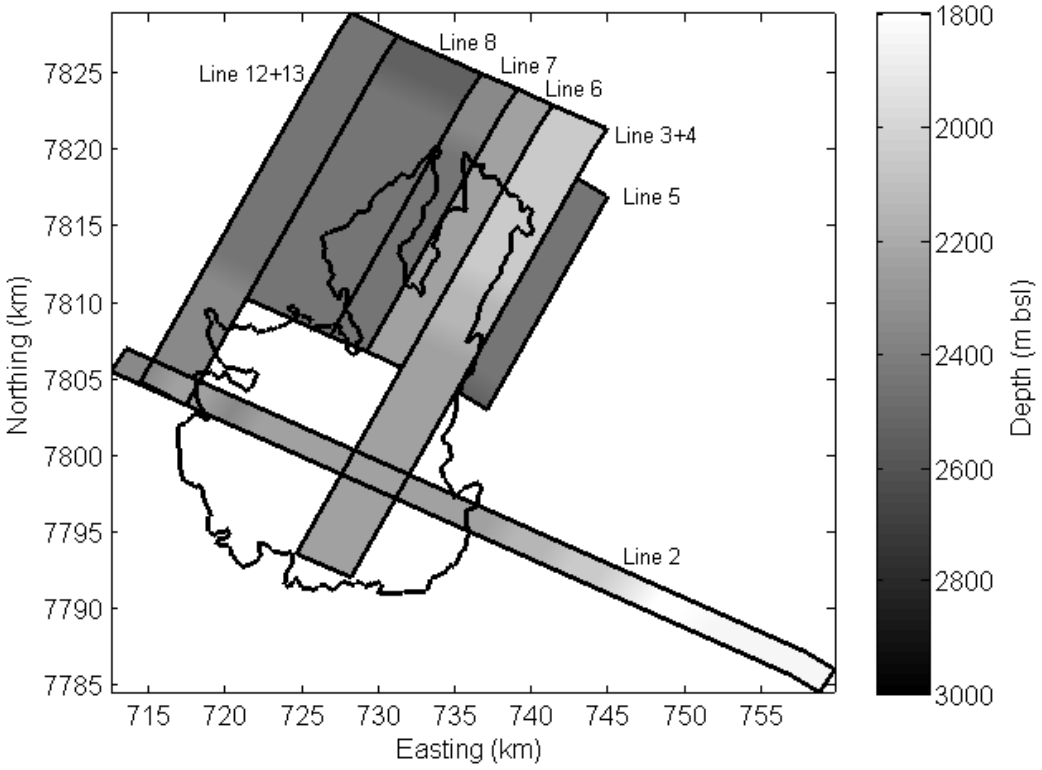

Figure 4.17 The depth of the maximum resistivity of the second resistive layer in the 1D/2D smooth inversions.

uncertainties calculated as described in Part 1 and the automatic convergence method described in a previous section of this work.

The resulting model shows six layers for all bins, which are very similar to one another. The thickness variations described for the 1D/2D inversion of line 3+4 disappears in the 1D/3D inversion, as does the shallowing of the second resistive layer and basement observed previously for lines 6 and 3+4. Quite possibly, the absence of cross-constraints between model spaces in the sensitivity matrix is being outweighed by the addition of the bi-directional horizontal roughness penalty and the inversion result is too smooth. However, the resistivity-thickness product of the first resistive layer now shows the reservoir more clearly (Figure 4.18a). The value around the reservoir boundary

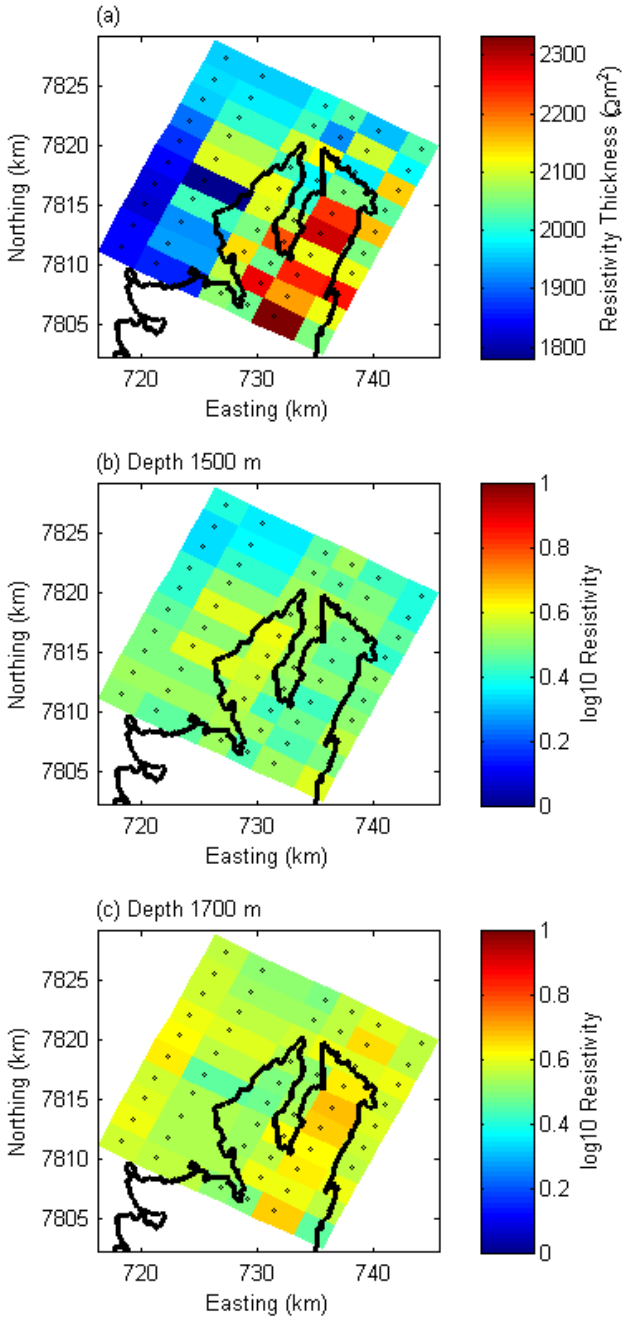

Figure 4.18 1D/3D inversion results.

(a) Resistivity-thickness product of the first resistive layer in the 1D/3D inversion for the northern portion of the reservoir. Circles show the locations of sites. Because of the varying distance between sites in the E-W direction, horizontal roughness penalties in this direction are scaled such that a distance of 2 km is a roughness penalty of 1. (b) Log10 resistivity of the layer centered on 1500 m depth or (c) 1700 m depth. The resistivity of the western ear expresses at a shallower depth than the eastern ear.

is about 300-400 Ωm^2 above the background in the west which is approximately what we expect for 50% gas saturation, as calculated earlier. Plots of the resistivity of the layers centered on 1500 and 1700 mbsl (Figure 4.18b and c), show that the resistivity of the western ear is expressed at a shallower depth than the eastern ear, in agreement with the pseudo-images in Figure 4.3. We suggest that the results from our 1D/3D inversion would make a good starting model for a true 3D inversion of these data.

4.8 Conclusions

We discuss three tools for quick evaluation and inversion of marine CSEM data sets. Pseudo-mapping is a method of presenting the lateral variations in complex electric and magnetic field data in plan view without normalization. For the Scarborough gas field survey, we demonstrate with pseudo-mapping that the magnetic field is well predicted by the electric field. Since Scarborough contains both morphologically simple and complex geology, this result may indicate that magnetic fields are of low value in CSEM, though more study is required on this point. Also, we demonstrate that in systems with high-quality timing control, the phase of the electric field is less noisy than the amplitude. Finally, the vertical electric field exhibits site-to-site amplitude variations while the phase varies smoothly, indicating the presence of small near-surface galvanic scattering. This sensitivity may impact the usefulness of vertical field amplitude data in CSEM surveys.

We have introduced the 1D PMN regularized inversion and shown that it has several properties which make it favorable in an exploration environment such as the Scarborough gas reservoir. First, unlike a smooth 1D inversion, it allows large jumps in

resistivity such as occur in actual geology. Second, it yields better fine-scale resolution than a smooth inversion, though this is most likely because (1) the roughness penalty of the smooth inversion is suppressing resolution information in the data and (2) the prejudice introduces additional resolution information into the PMN inversion. We show with synthetic data that the PMN inversion performs well, even when the prejudice is only approximately correct.

For stitched 1D inversion, in which separate 1D inversions along a tow track are plotted side-by-side to show variations in geology, we show with synthetic data that the common midpoint gather is able to accurately reproduce along-tow changes in geology while the separate inversion of in-tow and out-tow for each site is not. The use of common mid-point to gather data for prejudiced minimum norm inversions can make 1D inversion applicable to a higher dimensional environment.

We have used this combination on CSEM data collected over the Scarborough gas reservoir and show that the resulting models agree reasonably well with the gas-water contact boundary defined by other geophysical methods. However, there are some indications that higher dimensional inversion is required in the more complicated northern portion of the reservoir. Also, we show that even with the increased resolution afforded by the introduction of an a priori prejudice model into the inversion, it is not possible to fully resolve the resistive reservoir layer from the resistive Gearle siltstone layer which rests 200 m above it, though both are within 1 km of the seafloor.

In terms of resistivity-thickness equivalence, though synthetic modeling suggests that the PMN and smooth inversion should perform similarly, we find that the smooth inversion performs poorly, with little consistency along a stitched 1D inversion. This

suggests that the PMN inversion, which performed well on the same sets of data, is a more appropriate tool for individual 1D inversions of higher dimensional data.

We have extended 1D inversion into higher dimensions by inverting multiple 1D data sets simultaneously and applying horizontal roughness penalties across layers at the same depth in side-by-side CMP gathers. The 1D/2D smooth inversion has clearly produced a better result than both the 1D smooth and PMN stitched inversions. The addition of lateral roughness constraints has eliminated the randomness exhibited in the 1D smooth results, alleviated the need for an instructive (and possibly restrictive) background as in the PMN inversion, and shown a progression of geologic structure that can be matched to previous academic seismic studies. This is a striking result for an inversion based on a 1D forward code. Though some of the changes in geologic structure shown in a 1D/2D inversion disappear in a 1D/3D inversion, the resistivity-thickness resolution is reasonable. That this code can be run on an average laptop rather than the more usual server-farm required by large-scale 3D codes, should be a boon to many complex CSEM surveys as it allows for quick characterization of a dataset and provides a reasonable starting model for 3D inversion.

Acknowledgements

The authors are grateful to BHP Billiton Petroleum for funding this project, and Guimin Liu and Michael Glinsky of BHP for providing the background information we needed for the experimental design phase. We also thank the Seafloor Electromagnetic Methods Consortium for providing funding for the analysis and inversion phase of this project. The captain, crew, and scientific party of the Roger Revelle worked hard to make

this project a success, and we thank them all. We also thank BHPB, Shell, Esso Australia, and Chevron for providing ingress permissions for this survey.

Chapter 4, in full, has been submitted for publication of the material as it may appear in Geophysics, Myer D., Constable S., and Key K. The dissertation author was the primary investigator and author of this paper. Steven Constable provided text and figures for the section on pseudo-imaging.

References

Archie, G.E., 1942. The electrical resistivity log as an aid in determining some reservoir characteristics, *Transactions of the American Institute of Mining and Metallurgical Engineers,* 146**,** 54-61.

Boyd, R., Williamson, P.E. & Haq, B.U., 1992. Seismic stratigraphy and passive margin evolution of the southern Exmouth Plateau. *in Proceedings of the ODP, Science Results*, pp. 39-59, eds. Von Rad, U. & Haq, B. U. Ocean Drilling Program, College Station, TX.

Constable, S., 2010. Ten years of marine CSEM for hydrocarbon exploration, *Geophysics,* 75**,** 75A67-75A81.

Constable, S., Parker, R.L. & Constable, C.G., 1987. Occam's Inversion - A Practical algorithm for generating smooth models from electromagnetic sounding data, *Geophysics,* 52**,** 289-300.

Constable, S. & Weiss, C.J., 2006. Mapping thin resistors and hydrocarbons with marine EM methods: Insights from 1D modeling, *Geophysics,* 71**,** G43-G51.

deGroot-Hedlin, C. & Constable, S., 1993. Occams inversion and the North-American Central Plains electrical anomaly, *Journal of Geomagnetism and Geoelectricity,* 45**,** 985-999.

Ellingsrud, S., Eidesmo, T., Johansen, S., Sinha, M.C., MacGregor, L.M. & Constable, S., 2002. Remote sensing of hydrocarbon layers by seabed logging (SBL): Results from a cruise offshore Angola, *The Leading Edge,* 21**,** 972-982.

Key, K., 2009. 1D inversion of multicomponent, multifrequency marine CSEM data: Methodology and synthetic studies for resolving thin resistive layers, *Geophysics,* 74**,** F9-F20.

Key, K. & Ovall, J., 2011. A parallel goal-oriented adaptive finite element method for 2.5-D electromagnetic modelling, *Geophys. J. Int.,* 186**,** 137-154.

Kim, S.Y., Terrill, E. & Cornuelle, B., 2007. Objectively mapping HF radar-derived surface current data using measured and idealized data covariance matrices, *JGR,* 112**,** C06021.

Myer, D., Constable, S. & Key, K., 2011. Broad-band waveforms and robust processing for marine CSEM surveys, *Geophys. J. Int.,* 184**,** 689-698.

Swift, M.G., Boyd, R., O'Brien, D.K. & Lorenzo, J.M., 1992. Heat flow and thermal history of the Exmouth Plateau. *in Proceedings of the ODP, Science Results*, pp.

363-375, eds. Von Rad, U. & Haq, B. U. Ocean Drilling Program, College Station, TX.

Von Herzen, R.P., Francis, T.J.G. & Becker, K., 1983. In situ large-scale electrical resistivity of ocean crust, Hole 504B. *in CODEN: IDSDA6*, pp. 237-244, eds. Cann, J. R. & Langseth, M. G. Ocean Drilling Program, College Station, TX.

5 Very low resistivity beneath the Exmouth and Vøring rifted margins

Abstract

Magnetotelluric surveys at two volcanic passive margins have revealed a body of anomalously low resistivity (≤ 0.1 Ωm) at ~10 km depth. At the Vøring Plateau off the northwest shelf of Norway, 2D inversion of data from nine sites along a 54 km line resolve a body which is only a few km thick. At the Exmouth plateau off the northwest shelf of Australia, 2D inversion of data from 122 sites arranged in a dense grid and complementary long line finds a similar body, though insufficient long period data are available to resolve the bottom of it. Sensitivity tests show that it need not be more than a few hundred meters thick to fit the data. The Exmouth body is also shown to have long wavelength depth variations of 3-5 km height and 10-15 km width. Inversion of seventeen crossing lines confirms the existence of this structure and hypothesis testing places bounds on the depth variations of between 2 and 9 km. At both plateaus, the depth of the low resistivity body coincides with sills emplaced during continental breakup. We suggest that the low value is due to well-connected conductive cumulates (e.g. magnetite) precipitated in layered mafic intrusions.

5.1 Introduction

In 2009 we carried out an extensive electromagnetic survey of the Scarborough gas field on the Exmouth Plateau off the northwestern coast of Australia. As part of this survey we collected 122 sites of MT data. Inversion of the MT data in 2D yield a body at

~11 km depth which has an unusually high conductivity. This body was previously observed by Heinson *et al.* (2005) but in a survey whose wide site spacing (>60 km) made depth and structure determination ambiguous. Our close site spacing (0.5-2 km) and 3D site arrangement shows much greater detail on the body in question and provided new clues as to its origin.

Serendipitously, through a small test survey in 2010 we discovered a body of the same high conductivity and at the same approximate depth on the Vøring Plateau off the coast of Norway. The Vøring and Exmouth Plateaus are similar tectonic environments: they are large areas of thinned continental crust protruding into the transition zone between continental and oceanic crust remaining from the onset of rifting (i.e. "passive margins"). At both margins the rifting is thought to have had a quick onset and been accompanied by the formation of a large igneous province (White, 1992; White and McKenzie, 1989). The unexpected presence of an aerially extensive, mid-crustal conductive body in two plateaus with theorized similar formation histories may provide a clue as to the early processes involved.

In this paper, we address the processing and inversion of the plateaus separately. First we present the 9 site Vøring Plateau data which are of high quality with low noise and thus make an excellent introduction to our processing, quality control, and inversion processes. This is followed by the 122 site Exmouth Plateau survey for which we had to take special measures to minimize tide-related noise in the data. Finally we discuss possible interpretations of the conductive bodies.

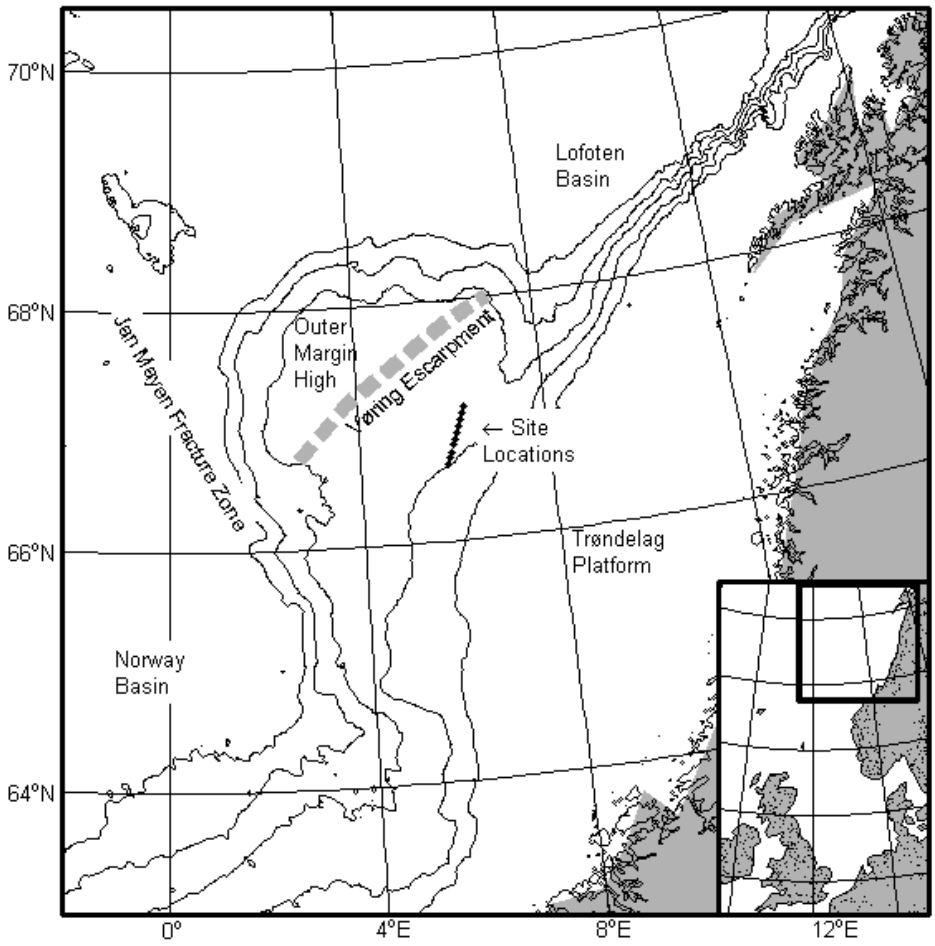

Figure 5.1. The Vøring Plateau.
A map of the Vøring plateau with bathymetry contours every 500 m to 2500 m depth. Deeper contours are omitted for clarity. The location of our MT survey is marked by the filled circles.

5.2 Vøring Plateau

5.2.1 Description of the plateau and survey

The Vøring Plateau (Figure 5.1) is a volcanic passive margin remaining from the breakup of Greenland and Norway during the opening of the North Atlantic. The bulk of the plateau is between 1-1.5 km water depth and is bounded to the east by the shallow Trøndelag platform leading up to the coast, to the southwest by the Jan Mayen Fracture Zone, and to the northwest and north by an outer margin high which dips steeply down to

abyssal depths. The outer margin high is comprised of a thin sedimentary cover over flood basalts interspersed with broken and dipping pieces of continental crust (Eldholm *et al.*, 1989a; Eldholm *et al.*, 1989b; Mutter, 1985; Mutter *et al.*, 1982). The plateau itself has undergone many episodes of extension since the Carboniferous period and is consequently only 15-20 km thick. There is no evidence for a continuous detachment zone cross-cutting the entire crust (Gernigon *et al.*, 2003), instead it is composed of many buried basins bounded by listric faults which are roughly perpendicular to the eventual spreading direction (Skogseid and Eldholm, 1989).

The sedimentary section contains a major unconformity of late Cretaceous - Paleocene age and a series of Eocene tuffs which date the breakup of this margin at about 57 Ma. The Cretaceous section is heavily cut by normal faults and intruded by numerous sills at depths from 2-10 km below the seafloor. These sills are ubiquitous across the plateau and have inhibited seismic resolution below them, requiring the use of ocean bottom seismometers for deeper imaging (Mjelde *et al.*, 1997). Many of these sills appear to have chimney structures leading to numerous small vent-like craters in the Eocene tuffs which appear as “eyes” in the seismic profiles (Skogseid *et al.*, 1992). The sills generally shallow in depth toward an escarpment which marks the boundary between the plateau and outer margin high where they appear to change from intrusive to extrusive in nature (Skogseid and Eldholm, 1989). The entire outer margin high and a portion of the plateau is underlain by a lower crustal high-velocity body which is interpreted as magmatic underplating when under the continental crust and thickened layer 3 when under the oceanic crust (Gernigon *et al.*, 2003)

In 2010, we deployed five broadband electromagnetic receivers (Constable *et al.*, 1998) on the Vøring Plateau as part of a test of the viability of carrying out a seafloor magnetotelluric survey during seismic operations. Each instrument was deployed twice for 8-9 days per deployment along a north-south trending line near the center of the plateau. The instruments were spaced 6 km apart for a total line length of 54 km, and all but one of the final deployments were recovered. The survey line is 9-40 km from four exploration wells (6605/1-1, 6605/8-1, 6605/8-2, 6706/11-1) whose logs show resistivities gradually increasing from 1 to 10 Ωm and a typical temperature gradient of ~30 C/km down to 4 km bsl (Norwegian Petroleum Directorate, unpublished data). There is a small area of heat flow anomaly north of our survey line on the plateau (75 versus 50 mW/m^2), but the plateau is generally homogeneous in this respect (Fernández *et al.*, 2004).

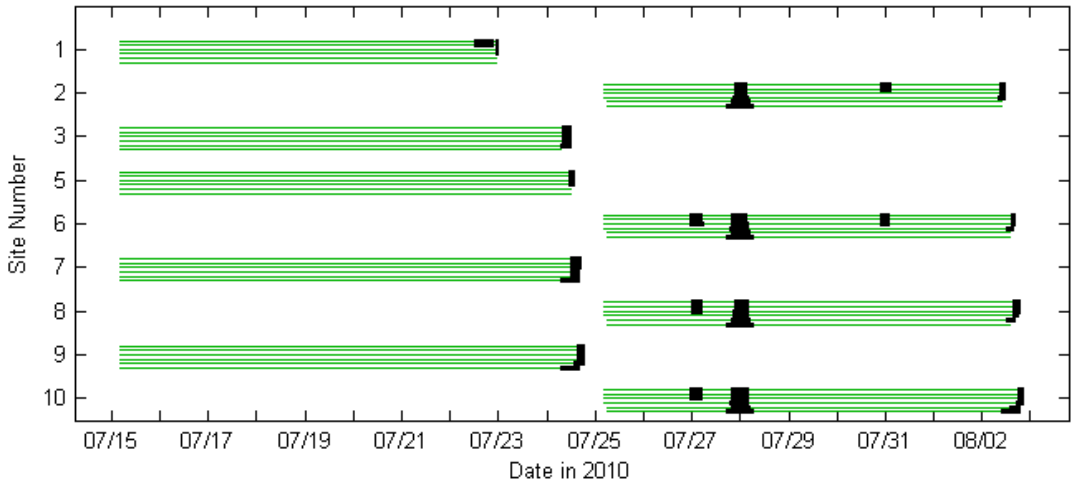

Figure 5.2. Available time series from the Vøring Plateau survey.
Green lines indicate Fourier coefficients that are available from each of the eight cascade decimation levels applied to the time series – higher frequencies are at the top of each group of lines. Black regions indicate data that have been excluded by eye from subsequent processing.

5.2.2 Calculation of MT impedances

Time series data were transformed into the frequency domain using the MT multi-station processing algorithm developed by Egbert (1997) and modified to support our data format and processing scheme. We configured the code to use a 250 point FFT window, which with our 62.5 Hz sampling rate yields a 4 second fundamental frequency. For each time window, the process applies a hamming window and a four term auto-regressive pre-whitening filter before transforming into the frequency domain. Time window overlap was set to 50% as appropriate for a Hamming window. Lower frequencies are calculated by cascade decimation. Eight successive passes are made over the time series, each decimating the data by 4 so that the fundamental periods for the successive passes are 4 s, 16 s, 64 s, etc…

Figure 5.2 shows a summary of the time series processed at each site per decimation level. Blacked out areas correspond to portions of the frequency domain data which were identified by inspection of a spectrogram as being overly noisy. A strong noise source was evident near midnight UTC between 27-28 July during the second deployment. These time periods were removed from the processing to reduce contamination. Clipped regions at the end of each site's deployment are for data that was collected as the receiver rose through the water column. The receiver deployed at site 4 was not recovered.

The second stage of the Egbert processing algorithm is the calculation of complex MT impedances from the Fourier coefficients. The cascade decimation of the time series yields eight sets of Fourier coefficients each with a different range of frequency coverage. The 250 point FFT window yields 124 unique frequencies, most of which we discard

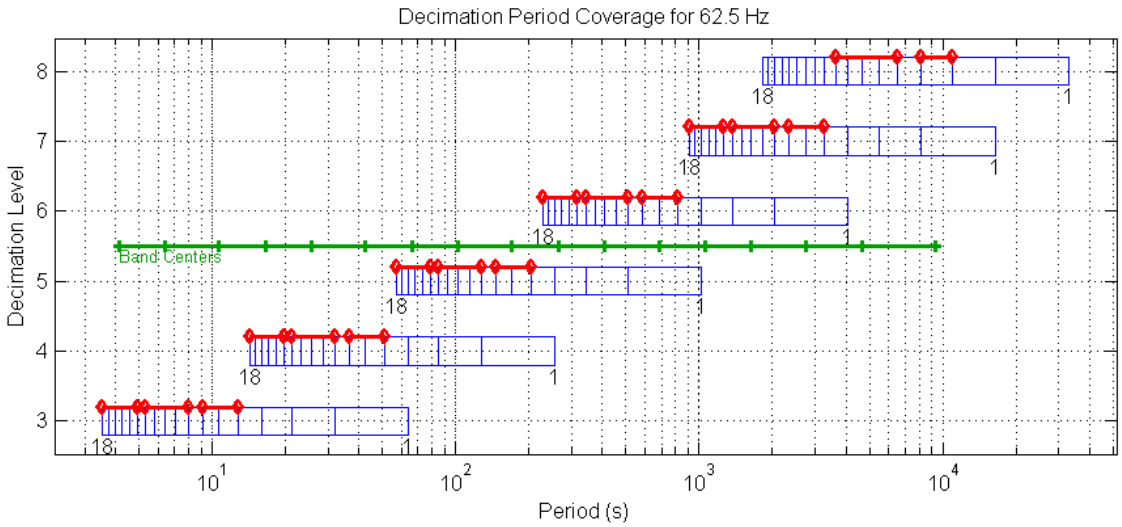

Figure 5.3. Periods per decimation level.
The blue bar at each decimation level indicates the periods derived from the Fourier transform window. Only the first 18 periods are shown. The red diamonds bracket those which are stacked together to yield one output period in the multi-station processing. The green bar shows the position in log period of the center of each averaging bands.

because they are too closely spaced in log frequency to be useful or are contaminated by the Hamming window. Also, we discarded the first two decimation levels because the frequencies were found to be too high to yield useful MT responses. Figure 5.3 shows the frequencies derived for decimation levels 3-8. To improve the signal-to-noise ratio, we configured the multi-station processing to stack bands of between 3 and 6 frequencies and produce a composite result at the average frequency of each band. The period in seconds for the center of each frequency band is spaced evenly in log period with a density of five periods per decade.

The Egbert multi-station processing does not use a single remote reference as is common in other procedures (Chave and Thomson, 1989; Jones *et al.*, 1989; Egbert and Booker, 1986; Gamble *et al.*, 1979). Instead, it takes a group of sites as input and uses robust techniques to determine both coherent and incoherent noise for each channel. While this technique is especially useful in the marine environment where all stations are

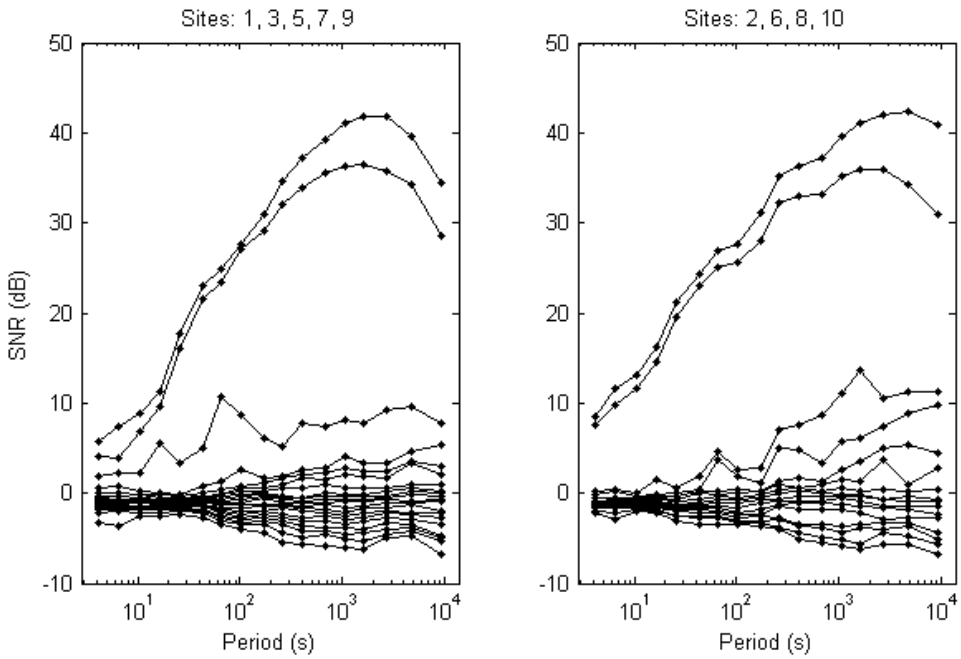

Figure 5.4. The spectral density matrix eigenvalues for the Vøring Plateau data.
The spectral density matrix eigenvalues in signal-to-noise ratio units for the signal sources determined from the Vøring plateau data by eigenvalue decomposition. Each plot is from a separate grouping of sites in the multi-station processing.

relatively closely spaced and a remote reference positioned sufficiently far away is usually not available, it can be thwarted when a majority of the sites in a processing group are especially noisy. So care must be taken in selecting groups of sites to process together. This can be a time-consuming trial-and-error process. At the Vøring Plateau, the sites were grouped by their deployment and processed without problems.

5.2.3 Data quality

One of the strengths of the Egbert multi-station processing is that it provides a quality control measure which can be used to evaluate the input data beyond the usual error estimates on apparent resistivity and phase. A central part of the processing is an eigenvalue decomposition of the spectral density matrix (SDM) which yields coherent signal source vectors. For well-behaved MT data, there should be exactly two coherent

sources well above the noise floor corresponding to the two orthogonal components of the MT plane-wave source. Figure 5.4 plots the eigenvalues for the two sets of instrument deployments, in signal-to-noise ratio units. In both cases there are two strong coherent sources and negligible noise sources, though for deployment 1, data below about 20 s must be used with care since MT data are suspect whenever there are not two primary sources at least 10 dB above the rest.

In an ideal case, the 2x2 MT impedance tensor (*Z*) has specific structure which can be examined to determine the dimensionality of MT data. When the data are 1D, the on-diagonal elements (*Zxx* and *Zyy*) are zero and the off-diagonal elements (*Zxy* and *Zyx*) are equal and opposite in sign. When the data are 2D, the off-diagonal elements are no longer equal; for 3D data, the on-diagonal elements are no longer zero. In practice, because of imperfect data and an inhomogeneous Earth, the on-diagonal elements are never zero and the off-diagonal elements are never equal. It is customary, then, to examine the dimensionality of the impedance tensor using two different tools: polarization ellipses and the Swift skew (Swift, 1967).

Figure 5.5 shows the impedance polarization diagrams for each site and period calculated from one off-diagonal member of the impedance tensor and one on-diagonal member. The on-diagonal term is small except for the longest periods, indicating that the dimensionality of the data is low and they are generally not distorted. Circular polarization is an indicator data for which a 1D interpretation is valid. The dimensionality begins to climb above ~2000 s for the southern end of the line (sites 1-3) and 700 s for the northern end of the line. Consequently we expect there to be some difference in the deep structure between the two ends as determined by inversion.

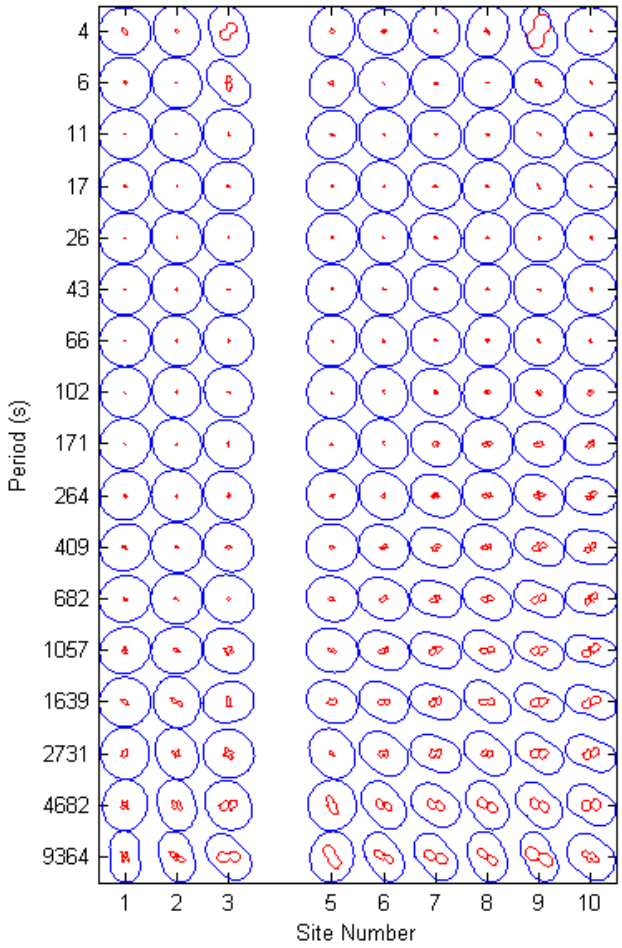

Figure 5.5. Impedance polarization diagrams for all sites, all periods.
The off-diagonal term *Zxy* is in blue and the on-diagonal *Zxx* is in red. Ellipses are formed from the real and imaginary parts of the complex values. Small on-diagonal terms and nearly circular off-diagonal terms indicate low dimensionality in the data.

The Swift skew is a measure of the 3D-ness of an MT impedance tensor based on its diagonality, and is calculated from

$$S = \frac{|Z_{xx} + Z_{yy}|}{|Z_{xy} - Z_{yx}|}. \tag{5.1}$$

The skew value S is large when the sum of the on-diagonal terms is large compared to the difference of the off-diagonal terms. For ideal 1D or 2D data, the on-diagonal terms are zero so the skew is zero; however, this rarely occurs with real data due to noise and

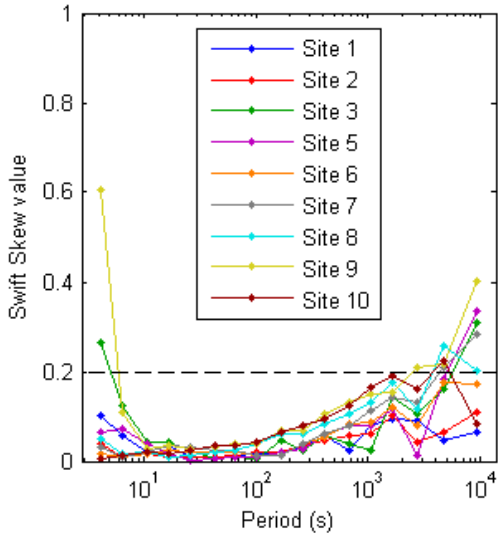

Figure 5.6. Swift skew for the Vøring data.
Skew values above an empirical limit of 0.2 are 3D or noisy. Below this limit, the dimensionality is undetermined but expected to be suitable for 2D inversion.

numerical rounding errors. Swift determined an empirical value of 0.2 as the cut-off above which data are considered to be too 3D to be valid in a 2D inversion. Below this value, the Swift skew makes no conclusion about the dimensionality of the data but asserts that it is valid for 2D interpretation. Figure 5.6 is a plot of the Swift skew values for each site and period. Aside from a few noisy data points at the highest and lowest periods, there are no obviously 3D impedances in this set.

Figure 5.7 shows the apparent resistivities and phases for the nine sites for this survey. Uncertainties for each datum are shown as 2σ. Impedances have been rotated so that the x-axis points along the strike of the survey line, 19° east of north. The declination in the survey area is less than 0.5° so no adjustment was made. The transverse electric (TE) mode, which represents electric current flow induced along geologic strike, is *Zyx* and the transverse magnetic (TM) mode, which represents current flow induced along the survey line, is *Zxy*. The uncertainties are small due to the high data quality. Deriving high

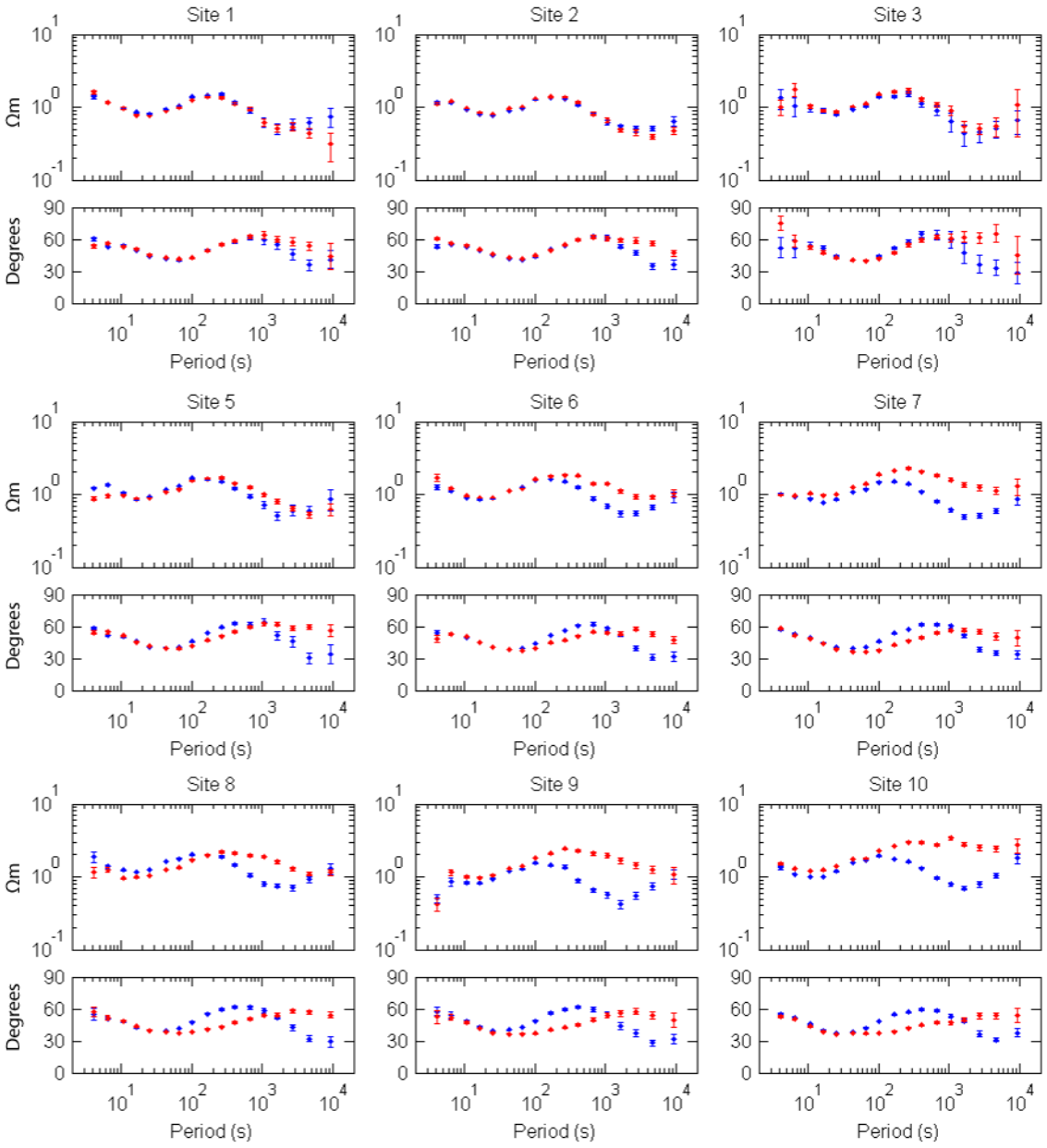

Figure 5.7. Apparent resistivities and phases of the Vøring Plateau data. Each site is rotated so that the X axis is along the survey line; therefore Zxy (blue) is the TM mode and Zyx (red) the TE mode. Error bars are plotted at 2σ size.

quality MT impedance estimates out to 10,000 s in > 1 km of water is not trivial, usually requiring many weeks of deployment time or significant geomagnetic storms. No geomagnetic storms were recorded for the deployment period according to DST estimates calculated by the World Data Center for Geomagnetism, Kyoto (http://wdc.kugi.kyoto-

u.ac.jp/dst_realtime/index.html). The high quality is probably due to the strong auroral signal at the high latitudes (>66° N) of this survey. Though the complexity of the aurora can confound subaerial MT, marine MT has the benefit of the overlying conductive ocean. The high angle of incidence of the air-water interface reduces the 3D distortions of the source field, leaving the 2D plane wave dominant.

The shape of the apparent resistivity curves is similar for all sites, rising to a high at around 200 s. This is typical of marine geology in which conductive sediments overlie a resistive basement. However, a significant feature of this dataset is a steep drop in apparent resistivity above 200 s indicating the presence of a highly conductive body at depth.

At the southern end of the line, the TE and TM mode apparent resistivities are nearly identical and a significant difference does not develop until site 6. Similarity of the two modes can indicate a substantially 1D environment, as indicated by the polarization ellipses. The phases, however, show a difference at long periods for all sites. Since phase leads apparent resistivity in the sensing of deeper structure, this may indicate that whatever is causing the difference in the modes in the north end of the line is also present in the south end, but at greater depth.

5.2.4 2D inversion

We used the Occam 2D MT inversion code of deGroot-Hedlin and Constable (1990) to invert the apparent resistivities and phases from the nine sites in this survey. This code uses a dual mesh approach (Wannamaker *et al.*, 1987): a triangular finite-element mesh for the forward solver and a rectangular model space for the inversion. The

forward mesh is much finer than the model space to allow for suppression of numerical noise. For this survey, we used a forward mesh with 101,920 triangular elements and an inversion mesh with 9,332 model blocks (6,613 of which are free parameters). We used simplified bathymetry from Smith and Sandwell (1997) for the plateau and the abyssal depths to the north and south. The model blocks are especially fine near the sites (< $1/6^{th}$ of the skin depth of the shortest period), growing larger with depth and lateral distance from the sites. The sensitivity of the MT method to fine-scale structure decreases with distance from the observation sites, so there is no need to mesh finely at depth. Figure 5.8 shows a subset of the inversion mesh around the sites to illustrate the increase in model block size.

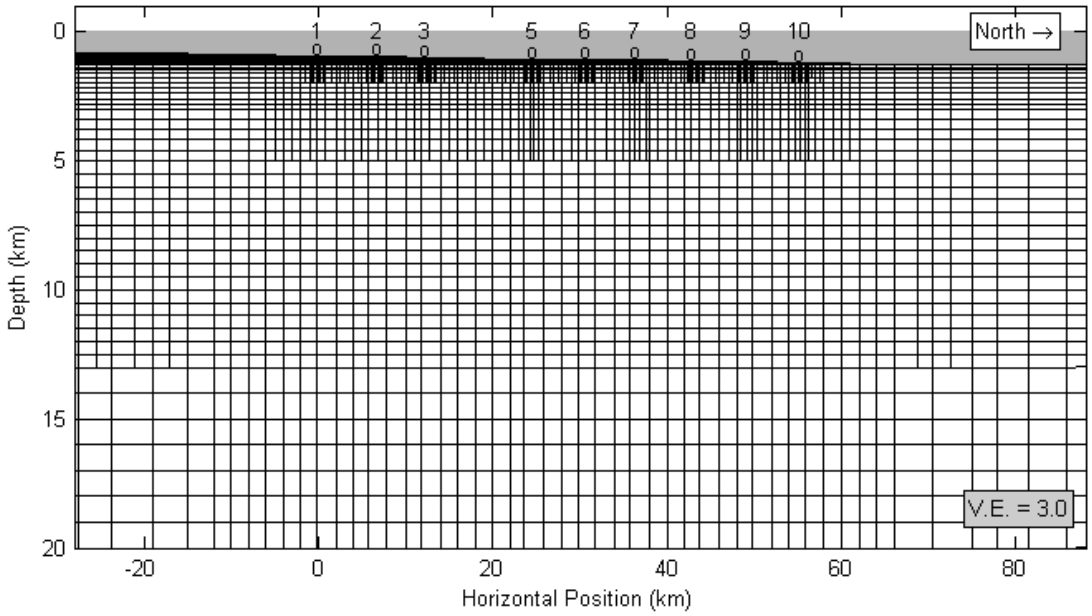

Figure 5.8. A subset of the model space used for the Vøring 2D MT inversions. Model blocks increase in size with depth. Near the sites, the block size is a fraction of the skin depth of the shortest period. The model extends to over 100 km deep and several 1000 km to each side to allow the forward solver to meet the condition that the fields go to zero at the boundaries.

We ran a variety of 2D inversions to examine the properties of the data. Apparent resistivities and phases were inverted with a minimum error floor of 10%. For site 3, the two shortest periods and the longest period were eliminated. For site 9, the shortest period was eliminated. In every case discussed below, the inversion ran to a target misfit of RMS 1.0 within a few iterations, then proceeded for a few further iterations to minimize the roughness of the model.

In Figure 5.9a, we show the result of inverting both the TM and TE data. The conductive sediments extend to between 1-2 km below the seafloor and the resistive basement is 5-7 km thick with resistivity values ranging between 2 and 100 Ωm, though this is uncertain since MT is not as sensitive to resistors as it is to conductors. The shallow sediments appear disconnected because of the large site spacing (~6 km) compared with the layer thickness. The resistive plug at ~20 km horizontal range and the deeper concentration of conductivity are most likely due to the inversion taking advantage of the lack of constraint caused by the missing site. The difference between the south (left) and north (right) sides of the model reflects the split in the TM and TE modes observed in sites 6-10. It is difficult to determine with 2D inversion of only a single line of sites whether or not this difference is due to off-line structure. Since the TE mode represents current flow along geologic strike, it is, in general, much more sensitive to off-line structure than the TM mode. Though the polarization ellipses and Swift skews do not indicate any large 3D effects, they do not preclude 3D structure. It is unlikely that the difference in modes is caused by the coast effect (e.g. Heinson and Constable, 1992) because attenuation from the mid-crustal conductor limits the periods at which the coast is sensed here to above longer than 4000 seconds.

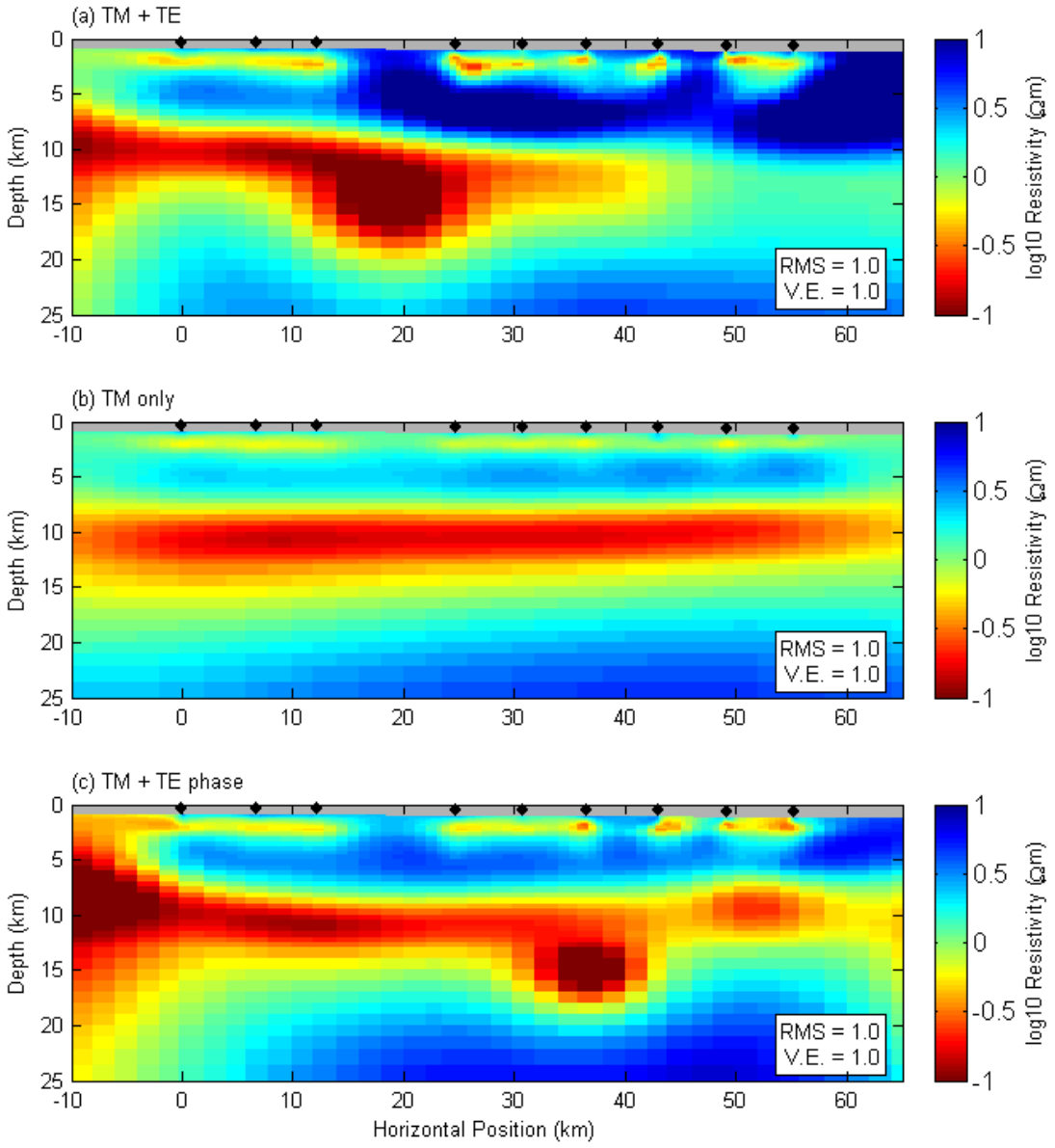

Figure 5.9. 2D smooth inversion results for the Vøring plateau data.
Smooth inversion results for (a) TM + TE data, (b) TM only, and (c) TE phase + TM. Data were inverted with 10% error floor and each inversion converged to an RMS misfit of 1.0. There is no vertical exaggeration. North is to the right.

Figure 5.9b is the result of inverting only the TM data. The TM mode represents induced current flow along the survey line and is consequently more sensitive to along-line structure and less sensitive to 3D effects. This inversion converges quite

rapidly to what is essentially a 4 layer model: 1-2 km thick conductive sediments, 5-7 km thick resistive basement, 6-8 km thick deep conductor, and a resistive half-space. The discontinuous bodies of the full inversion are gone, but so are almost all of the higher resistivity values. In a TM-only inversion, the resistivity contrasts are less pronounced, so the smoothness constraint of the Occam inversion takes a more prominent role in defining the final model.

The TM mode data do not require a break in the mid-crustal conductor, so it is most likely structurally continuous since a break would create a galvanic distortion easily sensed by the TM mode. The TE data sense a difference in the conductivity values of the northern and southern portion of the conductor as evident in the apparent resistivities in Figure 5.7. The full inversion (Figure 5.9a) must balance the two modes with the result that the mid-crustal conductor is concentrated in the southern half of the model compared to the TM-only inversion (Figure 5.9b).

These are 2D isotropic inversions, so there is the possibility that the difference between the TM and TE modes is due to 3D structure or anisotropy. However, as has been previously noted, there is no evidence for 3D structure in the Swift skew or polarization ellipses. While the uniformity of these indicators does not preclude 3D structure, it makes it unlikely. Also, there is no evidence for anisotropy, which would normally appear as a split in the modes in the short period data. It seems likely, therefore, that the mid-crustal conductor is continuous across the model space as indicated by the TM mode, but that there are large lateral variations in its resistivity-thickness product, as indicated by the TE mode, that cannot be accommodated by a smooth inversion of data from both modes.

It is sometimes possible to combine the sensitivity to inline structure of the TM mode with the sensitivity to resistivity values of the TE mode by inverting the TE mode phases along with the TM mode data. Though we do not believe the local structure to be very 3D, eliminating the TE mode apparent resistivities lessens the influence of galvanic effects from off-line structure – galvanic effects influence apparent resistivity, but not phase. Also, by removing the TE apparent resistivities, we are halving the number of TE data involved in the misfit calculations, effectively placing emphasis on the TM mode while still requiring that differences in the modes be accommodated. In Figure 5.9c we show that this technique recovers essentially the 4 layer model of the TM-only inversion with enhanced values for the resistivities. Layer 1 (the surface sediment) is still discontinuous and a conductive "bulls-eye" has appeared below site 7, but layers 2 and 3 remain continuous across the model.

MT inversions are not very sensitive to resistors, especially when sandwiched between conductors, so the smoothing constraint in the inversion in Figure 5.9c is likely lowering the resistivity value of layer 2 more than it is raising the values of layers 1 and 3. It is possible to derive a better estimate of the resistivities of these layers by placing breaks in the roughness penalty at various depths. If the breaks are placed at the appropriate depths, the smoothing constraint will not "bleed" the conductor into the resistive layer. This should provide reasonable estimates of the resistivity values of the conductive layers and minimum estimates for the resistive layers.

We ran several new inversions in which we allowed for breaks in the vertical roughness penalty at 8, 10, and 12 km below sea level and at either 2.5 or 3 km below sea level. As above, these inversions included only the TE mode phases with the TM mode

data. Figure 5.10a shows the inversion result with breaks in the roughness penalty at 2.5, 8, 10, and 12 km depth below sea level. The mid-crustal conductor concentrates between 8 and 12 km depth with little leakage of low resistivity values outside these boundaries. The break at 10 km is required to keep the inversion from creating a "bulls-eye" conductor below the northern sites. It allows the inversion to accommodate the difference in the TE and TM modes in this area. When only TM data are inverted, this cut is not necessary. The cut at 2.5 km appears, in this inversion, to be too shallow because lower resistivities leak across it, especially in the southern portion of the line.

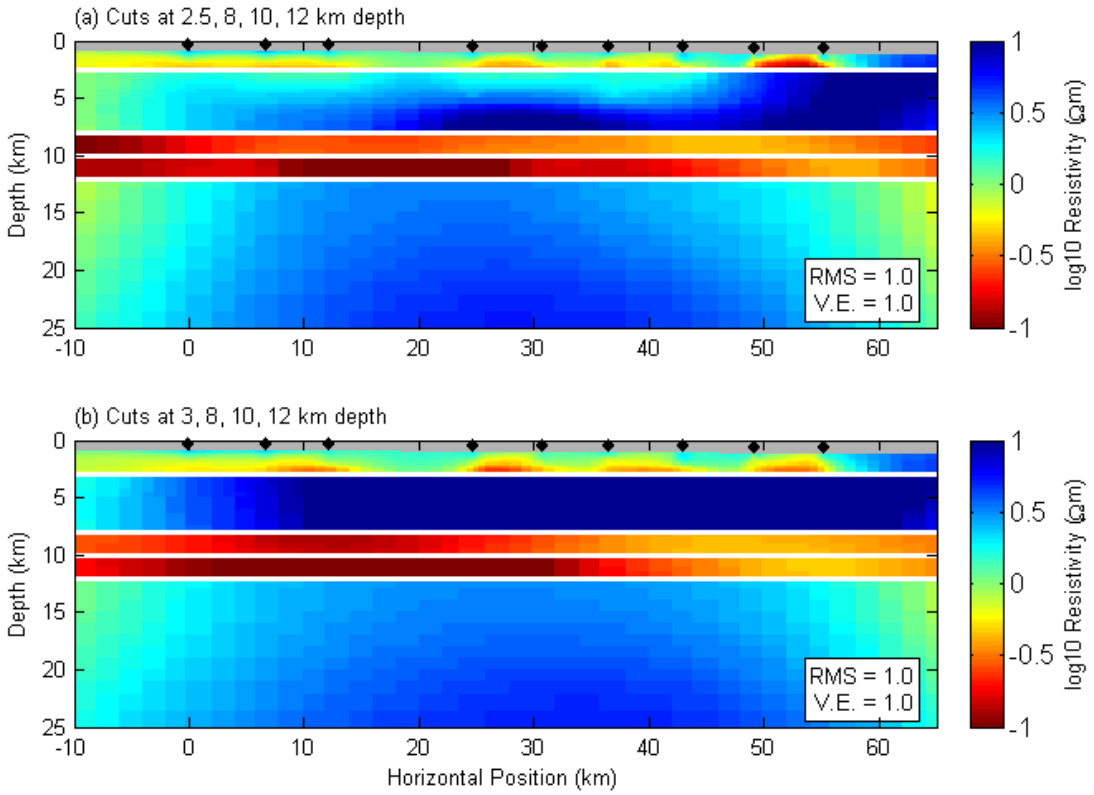

Figure 5.10. 2D inversion results with vertical penalty breaks.
Models resulting from 2D inversion of TE phase + TM data with breaks in the vertical roughness penalty at (a) 2.5, 8, 10, and 12 km, and (b) 3, 8, 10, and 12 km. The break at 2.5 km depth is too shallow, as evidenced by the leakage of conductivities from the overlying sediments into the resistive basement layer.

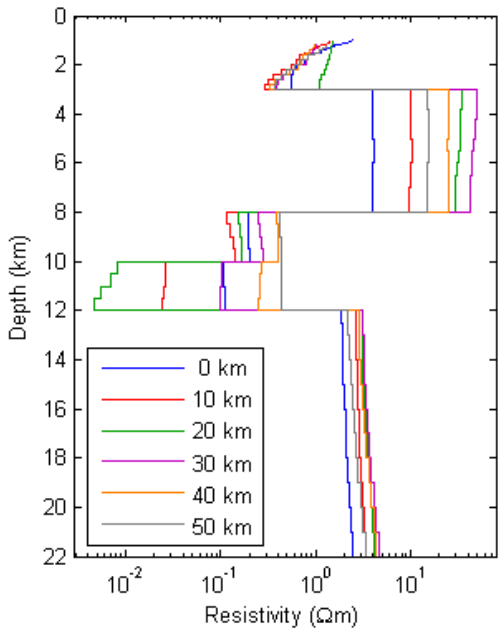

Figure 5.11. Profiles extracted from 2D inversion of the Vøring plateau. Depth versus resistivity profiles extracted from the inversion shown in Figure 5.10b at 10 km intervals between positions from 0 to 50 km along the inversion line.

Figure 5.10b shows the result from the 2D inversion in which the shallow penalty break has been moved down from 2.5 km to 3 km. The resistivity leakage across this boundary that is evident in the previous inversion is gone, indicating that this is a better depth to the bottom of the conductive sediments. Lateral variations in the sediment layer between sites 5 and 10 are not interpretable due to the 6 km site spacing. With site spacing on the order of the layer thickness (~2 km), we could probably image variations in the basement depth along the line as well as more structure in the sediments.

In Figure 5.11, we show five depth profiles extracted from the inversion in Figure 5.10b at 10 km intervals from 10 to 50 km distance along the inversion line. The profiles are very similar, due in large part to the cuts in the roughness penalty allowing large resistivity contrasts. From these profiles and the previous inversions, we postulate a simplified geologic model for this area as outlined in Table 5.1.

Table 5.1. Simple geologic description of the Vøring plateau from 2D MT inversion.

Layer	Resistivity	Top Depth (km bsl)	Description
1	~1 Ωm	-	Conductive sediments.
2	≥ 20 Ωm	2.5 – 3	Resistive upper basement. The depth to the basement varies from 3 km in the south to 2.5 km in the north. The resistivity value is a lower bound because of the conductive layers above and below.
3	~0.1 Ωm	8	Mid-crustal conductor.
4	≥ 2-5 Ωm	12	Lower crustal basement. The resistivity value for this layer is quite uncertain because, as the apparent resistivity data in Figure 5.7 show, the resistivity increase is only captured by the last one or two TE data points and the last decade of TM data points.

The anomalously conductive layer varies across the line, with resistivities reaching extremely low values of 0.01 Ωm in the south and very low values of 0.4 Ωm in the north. To a certain extent, MT inversions may trade between conductivity and thickness to achieve substantially similar resulting apparent resistivity and phase values. Anomalies are often characterized by their conductance (conductivity time thickness). The conductance of this layer varies from ~10^5 S in the south to ~10^4 S in the north. In comparison, the conductance of the overlying ocean is only ~3000 S.

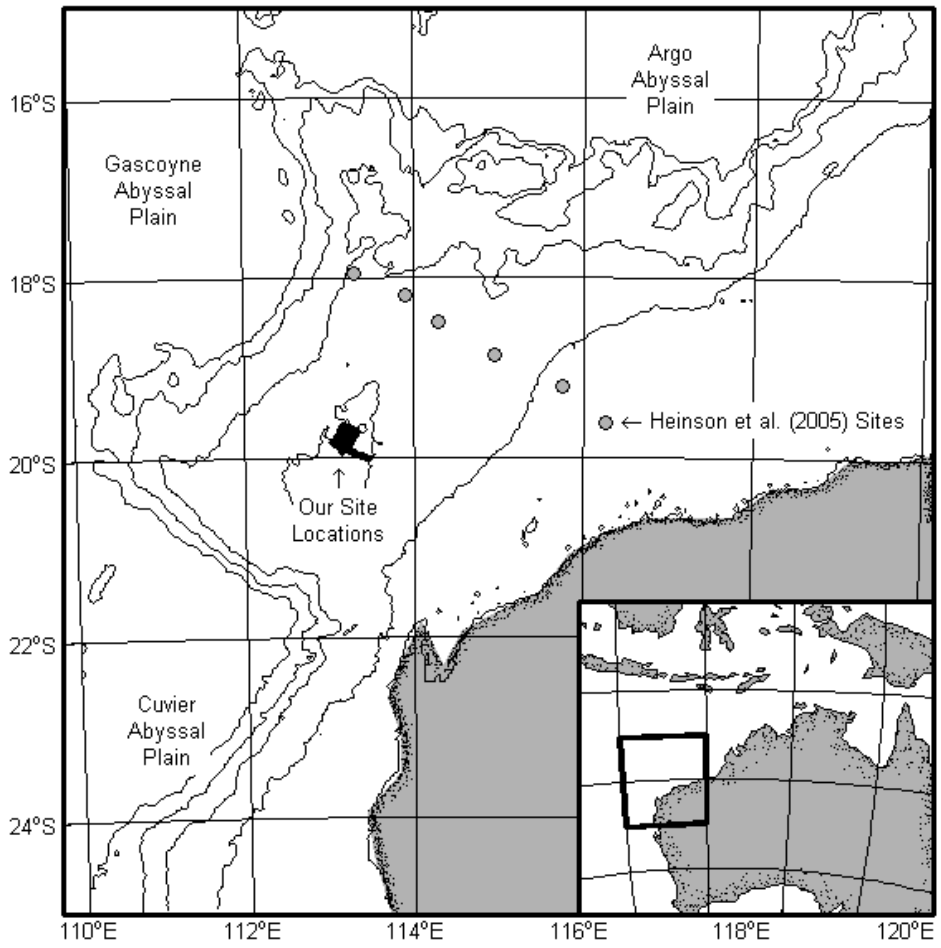

Figure 5.12. The Exmouth Plateau.

A map of the Exmouth plateau with bathymetry contours every 1000 m in depth. Our sites are located on the Exmouth Arch, the high point of the plateau, at a depth of ~950 m. For reference, the site locations from the earlier study of Heinson *et al.* (2005) are shown as filled circles across the northern portion of the plateau.

5.3 Exmouth Plateau

5.3.1 Description of the plateau and survey

The Exmouth Plateau is a large block of thinned continental crust off the northwest Australian margin remaining from the breakup of Gondwanaland, and is surrounded on three sides by abyssal depths (Figure 5.12). Several periods of extension occurred in the Triassic and Jurassic before the final rift formation in the Early Cretaceous (Veevers and Johnstone, 1974). Rifting that formed the Argo Abyssal Plain

north of the plateau occurred in the late Jurassic and at an oblique angle to the final rifting along the western and southern edges of the Exmouth, such that while the southern transform boundary is linear and relatively sharp, the northern boundary is comprised of rotated blocks and voluminous volcanic output (Boyd *et al.*, 1992; Exon *et al.*, 1992; Exon *et al.*, 1982; Larson *et al.*, 1979). The early periods of extension led to large scale normal faulting roughly perpendicular to the eventual spreading direction, and to the formation of numerous near-shore sub-basins now buried beneath sediment fill. These sub-basins may be the expression of an early failed rift arm of a triple junction which has since moved off and been subducted (Direen *et al.*, 2008; Larson *et al.*, 1979).

The Exmouth plateau crust is approximately 20 km thick (Mutter and Larson, 1989), the top 3-5 km of which are Cretaceous and younger sediments overlying Triassic and Paleozoic rock. The plateau was uplifted and truncated during the Jurassic, forming a major unconformity in seismic sections. The layers above this unconformity are generally not cut by faulting. Older layers are cut by steeply dipping faults which become listric or sole out at mid-crustal depths between 8-15 km (Driscoll and Karner, 1998; Boyd and Bent, 1992; Boyd *et al.*, 1992; Exon *et al.*, 1982).

The plateau has undergone thinning by at least a factor of 2, which Driscoll and Karner (1998) model using depth-dependent extension having brittle deformation in the upper crust layered over ductile deformation in the lower crust. They propose that the change in deformation style is accommodated by a sub-horizontal detachment zone at ~15 km depth. A magnetotelluric and geomagnetic depth sounding survey by Heinson *et al.* (2005) identified a highly conductive body (< 0.1 Ωm) in the mid-crust at

approximately this depth. They interpreted the conductivity as being due to well-connected carbon accumulated along the fault fractures.

In a more recent study, Direen *et al.* (2008) jointly interpret seismic reflection, seismic refraction, gravity, and magnetic data, confirming that the seismically transparent lower crust has irregular top and bottom surfaces indicative of the "pinch and swell" structures of ductile thinning. Additionally, they note that the remnant magnetic field across the plateau, which has relatively small variations compared to oceanic crust, has on average a strong negative value which is more likely to be of mafic igneous origin than crustal. Accordingly, they reinterpret a high velocity body below the outboard 150 km of the plateau lower crust and above the Moho as being peridotite that is 30% serpentinized and find that it is similar in character to bodies seen in the Browse and Bonaparte Basins (Goncharov, 2004) and the Vøring Plateau (Gernigon *et al.*, 2003). Most authors have identified this body to be igneous underplating (c.f. Planke *et al.*, 2000; Lorenzo *et al.*, 1991; Mutter and Larson, 1989), but Direen *et al.* (2008) propose that the locus of rifting is >100 km further west of the plateau edge than previously thought, across a broad area of heavily extended continental crust in-filled with rift related magmatism. They speculate that the peridotite body is unrelated to final breakup and is likely from an earlier, failed rifting event in which the crust was not yet sufficiently weak to be breached.

Volcanic sills intrude extensively throughout the mid-crust at 8-12 km (Stagg *et al.*, 2004). Direen *et al.* (2008) attribute these sills to providing a long wavelength, low amplitude positive component to the magnetic field measurements. The density of these

sills are modeled as only slightly higher than that of the surrounding Paleozoic material so contribute very little to gravity measurements.

The surface heat flow measured on the Exmouth Plateau is generally unremarkable except for two features: a low, centered ~20-30 km north of our survey, and a high 230 km to the ESE over the Barrow sub-basin near Barrow Island (Swift *et al.*, 1992; Swift, 1991). It has been proposed that this high-low pair is connected by a hydrothermal convective cell driven by lateral variations in thermal conductivity from variable thicknesses of sediment cover. However, the high aspect ratio of the convective cell (230 x 12 km) makes this interpretation speculative.

Our survey involved the deployment of broadband electromagnetic receivers in a 144 site grid over the Scarborough gas field to collect both controlled-source electromagnetic (all sites) and MT data (122 sites). The experimental design, data quality, and controlled-source inversion results are reported in separate publications (Myer *et al.*, 2011a submitted; Myer *et al.*, 2011b submitted). Briefly, there were four phases of deployment, the first three of which apply to MT: the deployment of (1) a long E-W trending line with site spacing between 500 and 2000 m, (2) a grid of five N-S trending lines with 2 km site spacing along the lines and variable spacing between them, and (3) a long N-S trending line with site spacing between 1 and 2 km. The Exmouth Plateau is periodically swept by especially strong, tide-related deep currents (Van Gastel *et al.*, 2009; Lim *et al.*, 2008) which caused considerable shaking of some instruments, but MT impedances were successfully derived from 112 sites. The orientation of the survey is such that lines are close to either parallel or perpendicular to the fossil spreading direction.

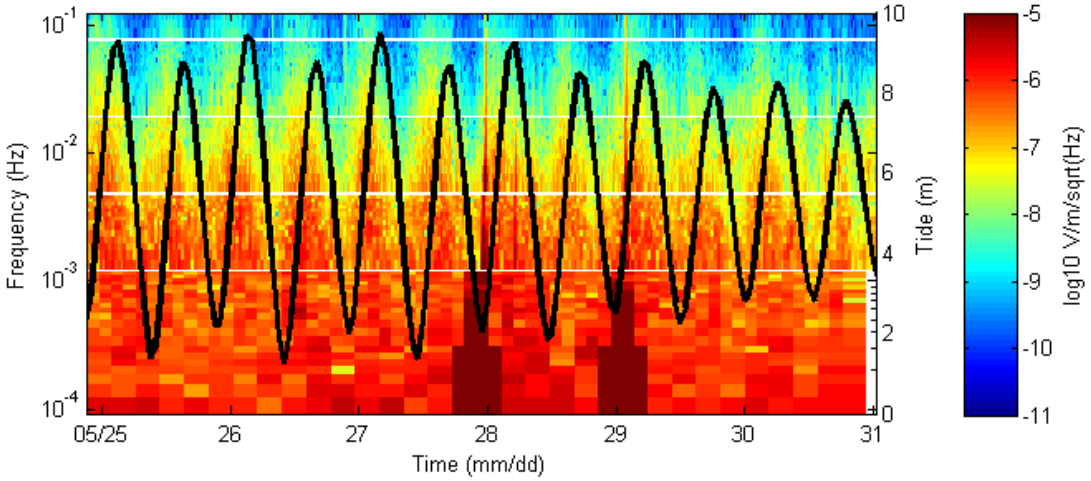

Figure 5.13. Spectrogram and tides for Exmouth site 17.
Spectrogram of the Ex channel from site 17 in phase 1, overlain with the tides measured at the official tide station in Broome, WA ~1000 km away. There is a strong correlation between the broad spectrum noise (10-1000 s) and the tidal surge which declines as the tide amplitude declines. Tide data from the Australian Baseline Sea Level Monitoring Project at http://www.bom.gov.au/oceanography/projects/abslmp/data.

5.3.2 Calculation of impedances

Calculation of impedances for the Exmouth plateau data follows the same procedure as that used for the Vøring plateau with a few additions to account for the lower signal-to-noise ratio found in this environment. During the first phase of deployments, there was a period of especially strong currents which shook the instruments strongly enough to create noise across the spectrum from a few seconds to 1000 s period. Figure 5.13 shows the spectrogram of an electric field channel from site 17 overlaid with the tide data obtained from the Australian Baseline Sea Level Monitoring Project as measured in Broome, WA. The noise is pervasive enough in the data that our usual processing procedure as described for Vøring was unable to derive useful impedances.

Since the tidal noise only occupies a portion of each day, decreases in amplitude as the tides abate over time, and there are many days of deployment available, we

implemented a procedure to clip these noisy data. Figure 5.14 shows the available time from the sites in line 1. The times of heavy tidal noise that were eliminated correspond to the horizontal black bands from site 6 to site 32. The blacked out areas in the figure, which progress forward in time from site 40 to site 1 then back down to site 40 again, are from the CSEM tow and were also clipped.

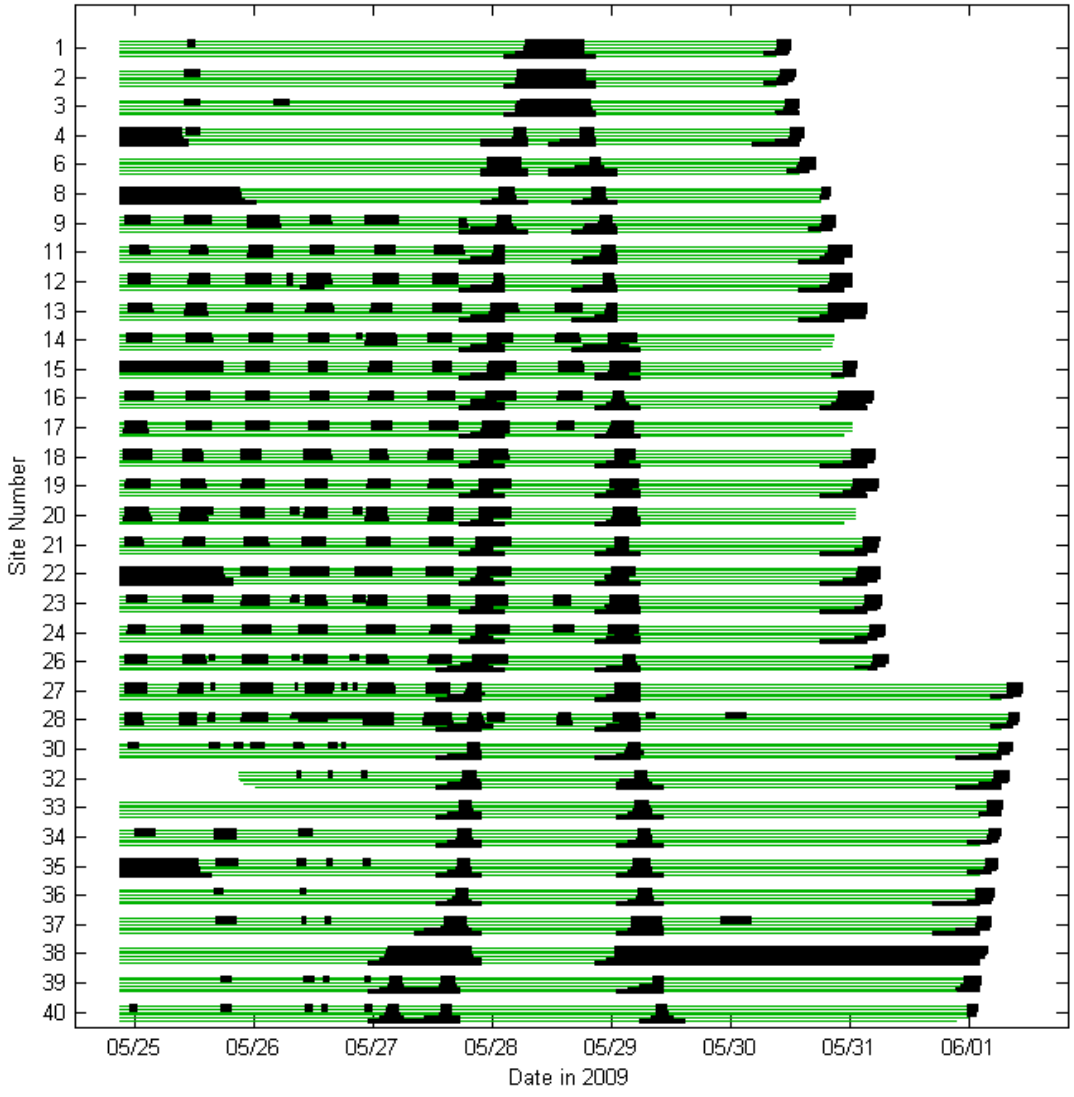

Figure 5.14. Time available for line 1 of the Exmouth survey.
Green lines indicate Fourier coefficients that are available from each of the eight cascade decimation levels applied to the time series. Black regions indicate data that have been excluded by eye from subsequent processing.

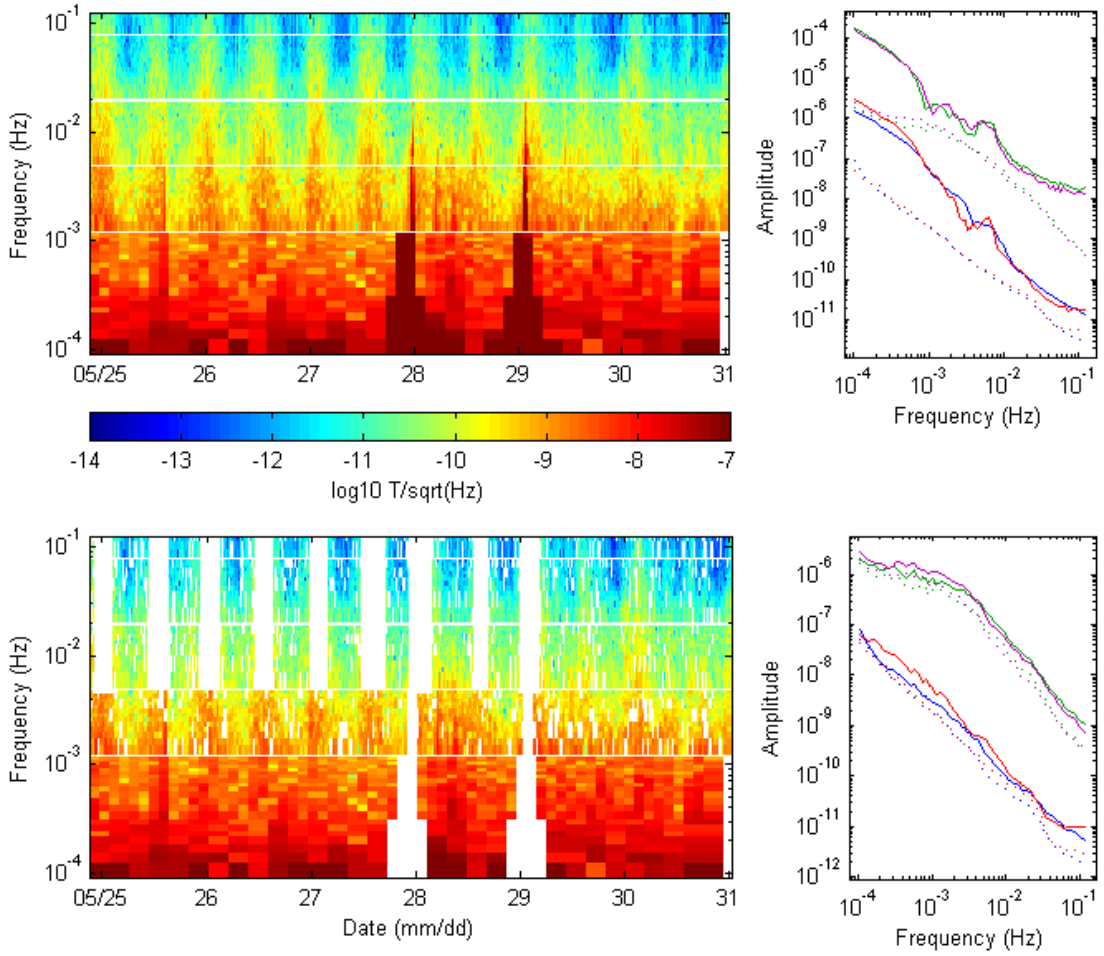

Figure 5.15. Sample Exmouth data before and after noise clipping.
Data from the Hx channel of site 17 before (top panels) and after (bottom panels) data clipping. The large white rectangles are from data that were clipped by eye whereas the miscellaneous speckling of white throughout were eliminated by the coherence measure. The right hand panels show the mean (solid lines) and medians (dotted lines) of all four channels: Hx, Hy, Ex, and Ey in blue, red, green, and magenta, respectively. Clipping noisy data barely affects the median, but shifts the mean towards the median.

To eliminate the noisy data, we examined a spectrogram produced from the Fourier coefficients derived by the first stage of the data processing and then blocked out sections of data manually. As a guide, we used calculations of the mean and median at each frequency. The mean will deviate widely from the median when there are strong noise sources, such as tidal motion, and strong spikes, such as from the receiver's acoustic transponder. When these noisy data have been blocked out, the mean

approximately equals the median and the remaining Fourier coefficients are saved. A second, automated process is then run on the remaining coefficients to eliminate those whose coherence between Hx and Ey or Hy and Ex is below a threshold. For phases 1 and 2, this threshold was 0.4; for phase 3, it was 0.2. Figure 5.15 shows an example of a spectrogram from before and after the data elimination process along with the difference between the mean and median values across frequencies.

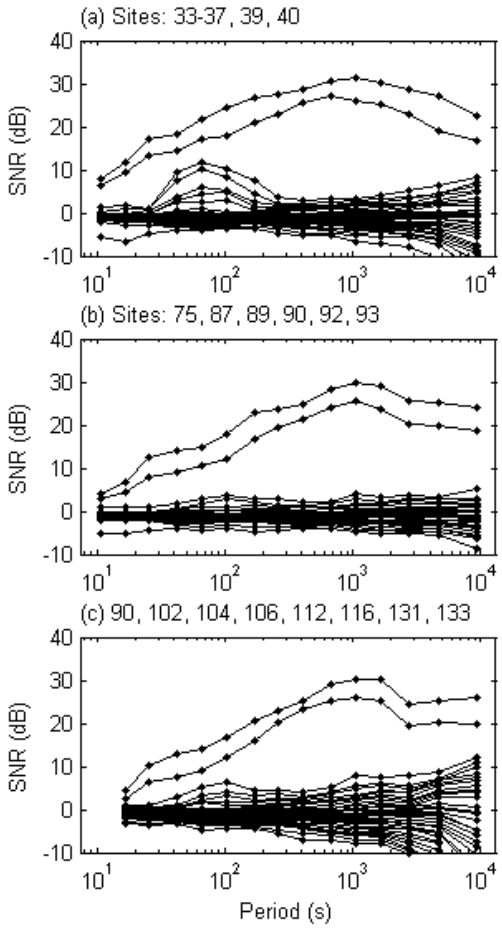

Figure 5.16. Spectral density matrix eigenvalues for the Exmouth data.
Plot of the eigenvalues for phases 1-3 (a-c) for the multi-station groupings containing the sites used as a reference for all other groupings in each phase. Because common reference sites are used, the spectral density matrix plots are nearly identical throughout each phase. Note that the 10 s data were too noisy to be used in phase 3.

5.3.3 Data quality

The strong tidal noise during phase 1 made it necessary to group many of the sites with the same few low noise sites. Though the noise in phases 2 and 3 was lighter, a similar approach was used on those site groupings as well. This in effect created a common, virtual remote reference from a group of three to six sites for each phase. Because of this, the spectral density matrix values are similar across each phase of the survey. Figure 5.16 shows a group of sites from each phase. Some of the sites in these groups form the reference sites for the rest of the Exmouth data. The tidal noise in phase 1 shows up as increased power in the noise eigenvalues between 20 and 300 s. However, this does not appear to have had an adverse effect on the source signal as seen in the impedance polarization ellipses (Figure 5.17) which are nearly circular at all but the longest periods where the data are very noisy. The Swift skew (Figure 5.18) is generally high above 1000 s period because most long period data in this survey are very noisy.

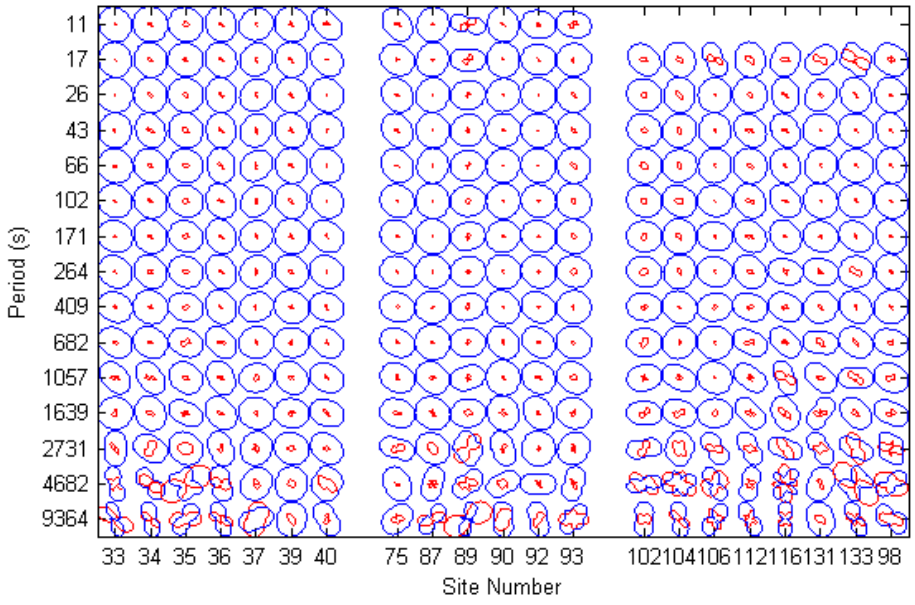

Figure 5.17. Impedance polarization ellipses for the Exmouth reference sites. The circular nature of the polarization ellipses indicates the measured fields are not seriously distorted. The randomness at the longest periods is due to noisy data.

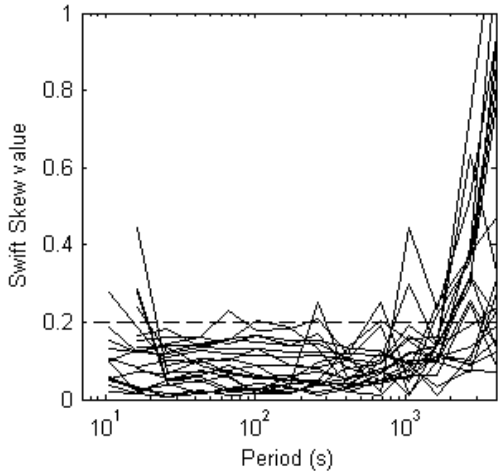

Figure 5.18. Swift skew for the Exmouth reference sites.
Skew values are plotted for the reference sites shown in Figure 5.16 and Figure 5.17. The skew values above 1000 s are high due to very noisy data.

Though the above figures show data from the reference sites for Exmouth and thus represent the best data, the remaining ~100 sites are generally good. The spectral density matrix and impedance polarization ellipse values for the additional sites show very little variation from those shown here. Skew values are generally the same or slightly higher. The largest difference between the sites is in the error estimates for the apparent resistivities and phases. To demonstrate the wide range of quality in the data, Figure 5.19 shows a selection of examples of the good, the bad, and the ugly (Leone, 1966). Site 12 was exceptionally noisy and represents the poorest quality data. The data in periods above 1000 s mostly have error estimates greater than 100% and are excluded from inversion. The data above a few hundred seconds period are also very noisy and many are excluded from inversion. Site 20 is an average site, with usable data out to ~1000 s period. Most of the Exmouth plateau MT impedances are similar in quality to this. Site 54 is a high quality site and extends usable data out to 10^4 s as well as achieving

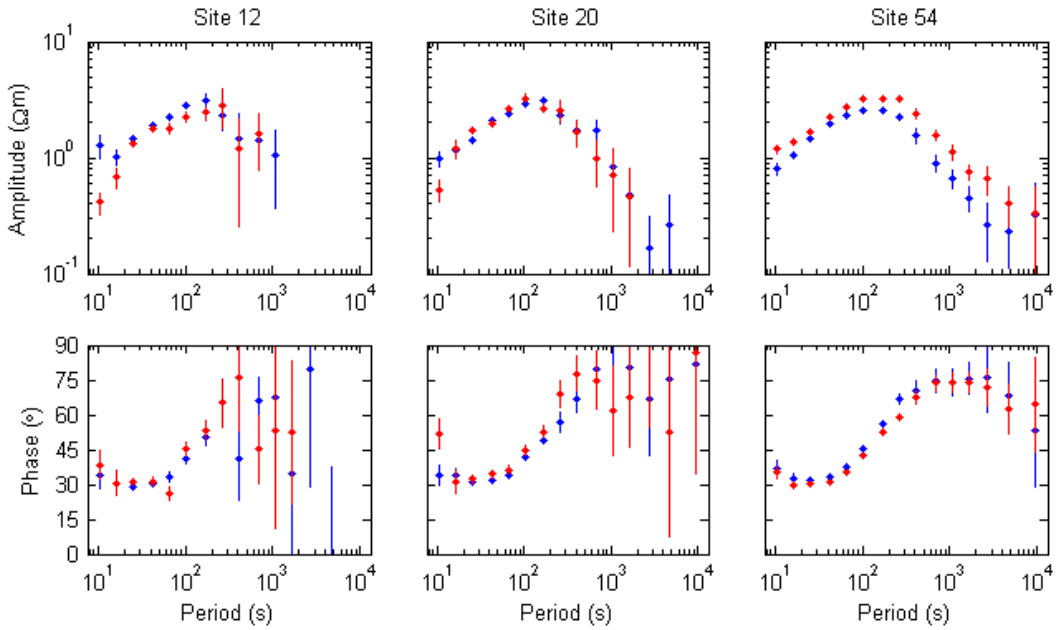

Figure 5.19. Examples of varied data quality in the Exmouth data.
Apparent resistivities and phases for three sites from line 1 of the Exmouth plateau data which illustrate the wide range of data quality. Data with error estimates ≥ 100% have been excluded. Most sites are similar to site 20.

less noisy short period values. Because of the tide-related noise, fewer than ten sites have data of this quality.

In many sites, the TE and TM modes at the shortest two periods (11 and 17 s) appear to split but are so widely varied site-to-site that we suspect that they are just noisy and that the error bars do not reflect the true level of noise. The SNR of the eigenvalues at these periods is generally quite low (< 5 dB). Uncertainties for these two periods are probably underestimated because of the large number of Fourier coefficients which are stacked together in the processing (~10^4 values). In higher quality sites, the two modes do not diverge at these periods. For most sites, data below 20 s period were excluded from inversion.

A common feature of all of the Exmouth sites is the absence of a difference between the TE and TM modes, regardless of the data rotations. The Vøring data show a

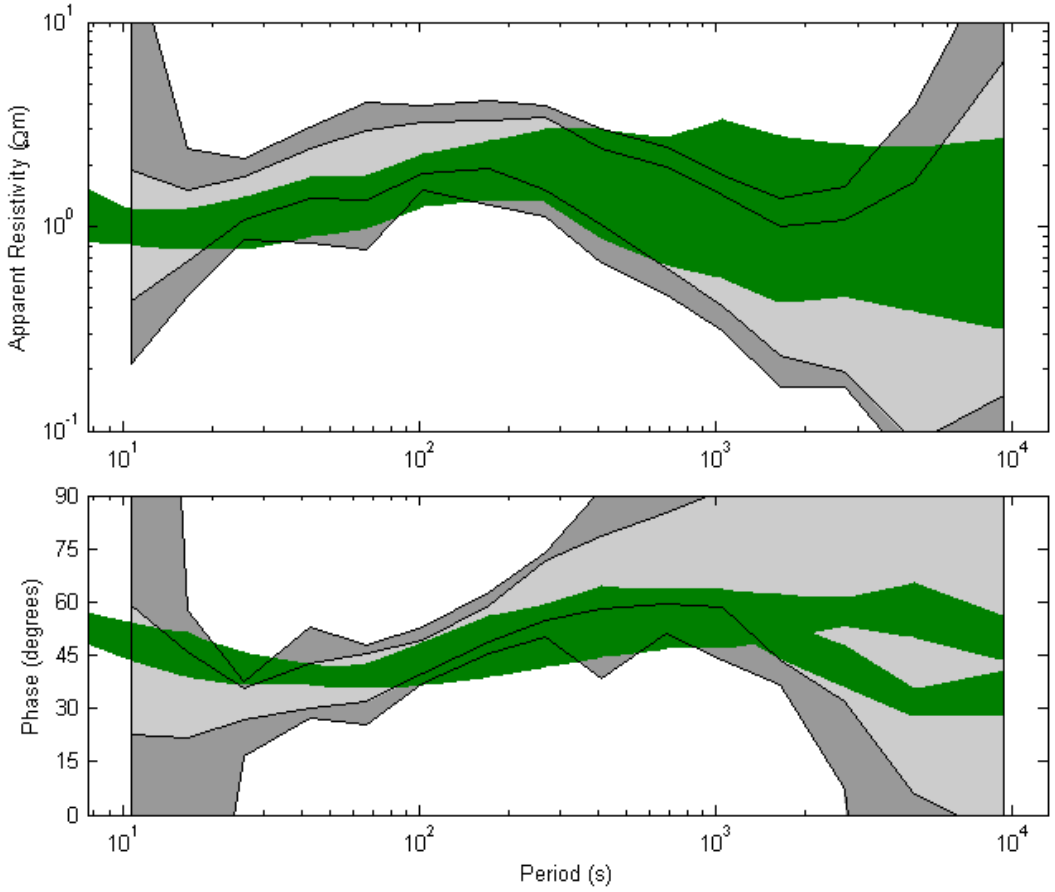

Figure 5.20. Apparent resistivity and phase for all MT data.
Apparent resistivity and phase for MT data from both surveys. The dark grey zone defines the extent of all of the data from the Exmouth plateau survey. 95% of the Exmouth data lie within the light grey region. The green region defines the extent 100% of the Vøring plateau data. The gap in the Vøring phase data is from the split in the TE and TM modes. Data whose error estimates are ≥ 100% are excluded.

split in the modes at the longest periods indicating some complex sub-surface structure. The Exmouth data, on the other hand, are essentially homogeneous in TE and TM and this accounts for the nearly circular polarization ellipses. In Figure 5.20 we show the bounds on all the Exmouth apparent resistivity and phase values for both TM and TE. The Vøring data are overlaid on the figure for comparison. The downward turn of apparent resistivities toward a conductive lower crust is sharper and steeper than for the Vøring data which suggests that inversion of Exmouth will resolve an even more conductive body. The similarity across all sites makes it easy to estimate that the basic

geologic structure is a conductive sediment package underlain by a resistive basement which rests on top of a massively conductive body.

The wide band in the Vøring distribution at longer periods obscures the fact that there is a distinct turn upward in the TE mode at about 2000 s. The Exmouth data may also turn upwards, but data at these long periods have large enough uncertainties that it is not strictly required.

5.3.4 2D inversion of line 1

We inverted the Exmouth line 1 data using the same code as for Vøring. Line 1 is coast perpendicular, so the model space includes both the shallowing continental slope and coast in the east as well as the distal plateau slope and abyssal plain in the west. The forward mesh has ~152,000 finite element triangles and the inversion uses 8695 model bricks, 7816 of which are free parameters. As before, the model bricks near the seafloor are less than $1/6^{th}$ of a skin depth in size for the shortest period and grow in size with depth and lateral distance from the survey line. We inverted apparent resistivities and phases for both TE and TM modes (1328 data points) with a minimum 10% error floor. Data with Swift skew above 0.2 or low eigenvalue SNR were not included. The inversion converged to RMS 1.0 and produced the model in Figure 5.21. As predicted by the data analysis, the model is primarily three layered: shallow 1 Ωm conductive sediments over 10 Ωm crustal basement, both underlain by a conductor whose resistivity values vary between 0.1 and 0.01 Ωm. Also as predicted, our data do not resolve the bottom of the conductive body, which extends in all directions to the edges of the model space. Surprisingly, the top surface of the conductive body contains large amplitude “ripples”

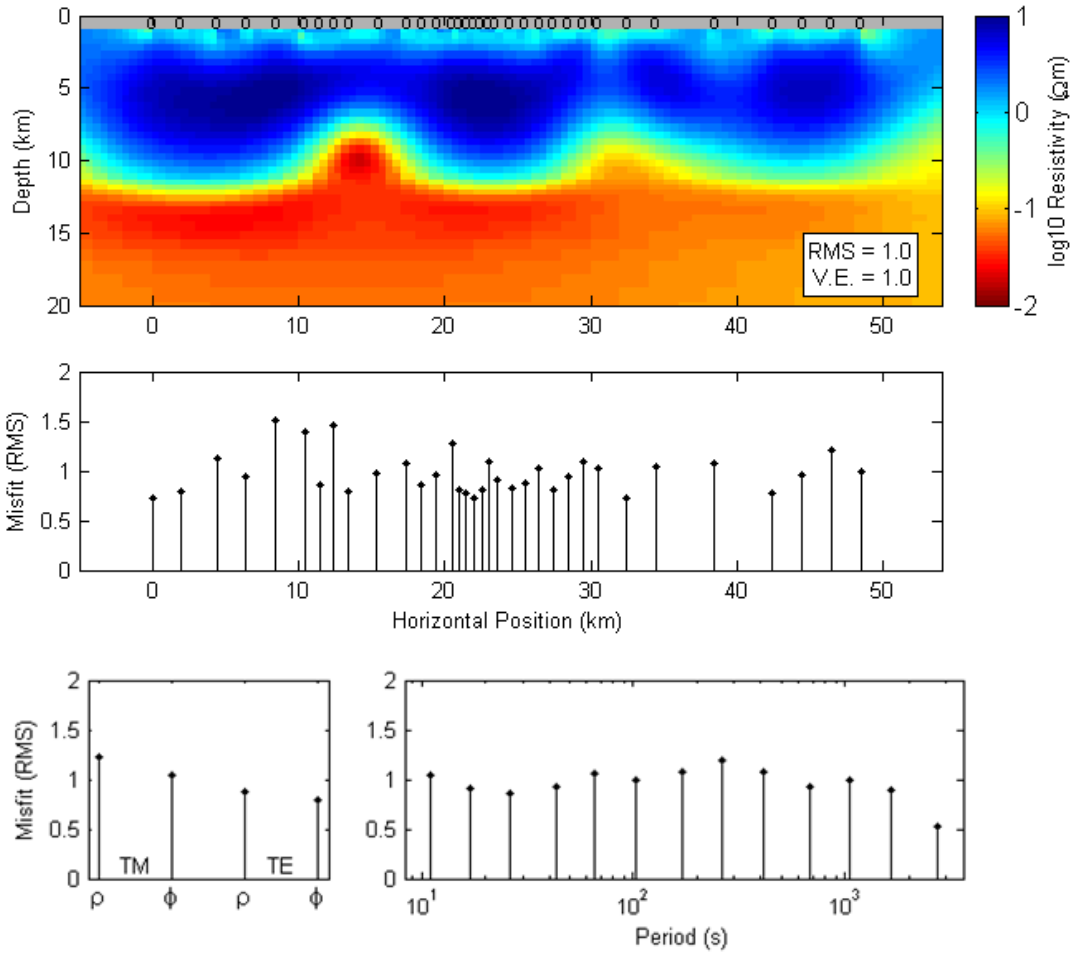

Figure 5.21. 2D inversion results for Exmouth Line 1.
Model of resistivities resulting from the inversion of TE and TM mode apparent resistivity and phase data. The model extends much farther than is shown here in order to satisfy the boundary conditions of the forward code. The bottom panel shows the RMS misfit calculated separately for the data of each site. The overall RMS is 1.0. Sites locations are denoted by the circles across the seafloor. East is to the right.

(3-5 km high x 10-15 km wide) which a casual examination of apparent resistivities and phases from site to site does not reveal.

The deep conductive body under the Exmouth plateau was first reported by Heinson *et al.* (2005) from a survey near the northern end of the plateau. Their site spacings were approximately 50-100 km and stretched across the plateau from the outer edge to the shallow continental shelf with data from ~100 s to 30000 s period. Because of the wide site spacing and dearth of high frequency data, they were unable to resolve the

shape of the conductor, but showed that it is approximately 0.1 Ωm, runs across the entire plateau, and has a very slight dip down towards the continent. They theorized that the conductor represented the accumulation of graphite on a sub-horizontal detachment fault posited by Driscoll and Karner (1998) to be at a depth of approximately 15 km.

Our data find the same amplitude conductive body more than 200 km south of the Heinson *et al.* study, indicating that it possibly exists under the entire plateau. The ripples which we resolve are of particular interest because of the impact they may have on the interpretation of this conductive body. If, for example, the conductivity is from the accumulation of graphite on a fault surface, then that fault must have later been highly deformed to produce these ripples. Yet seismic stratigraphy studies show no such deformation in the layers above it which were extant at the time of extension (Boyd *et al.*, 1992). This may lead to alternative explanations such as the diapiric rise of a less dense conductive body like the massively serpentinized peridotite found at the Iberian and south Australian passive margins (Direen *et al.*, 2011; Henning *et al.*, 2004) or conductive mineralization in ultra-mafic sills injected into the plateau.

To determine whether the ripples are an artifact of a poor fit to a few data, we examined the misfit for each site separately. The middle panel in Figure 5.21 shows that though there are a few scattered sites with higher misfit, there is no correlation between the misfit and the ripples; data from sites over the ripples are fit just as well as data from other sites. A similar examination of misfit by data type (i.e. TE and TM apparent resistivity and phase) and by period shows no dominant source of misfit skewing the resulting model.

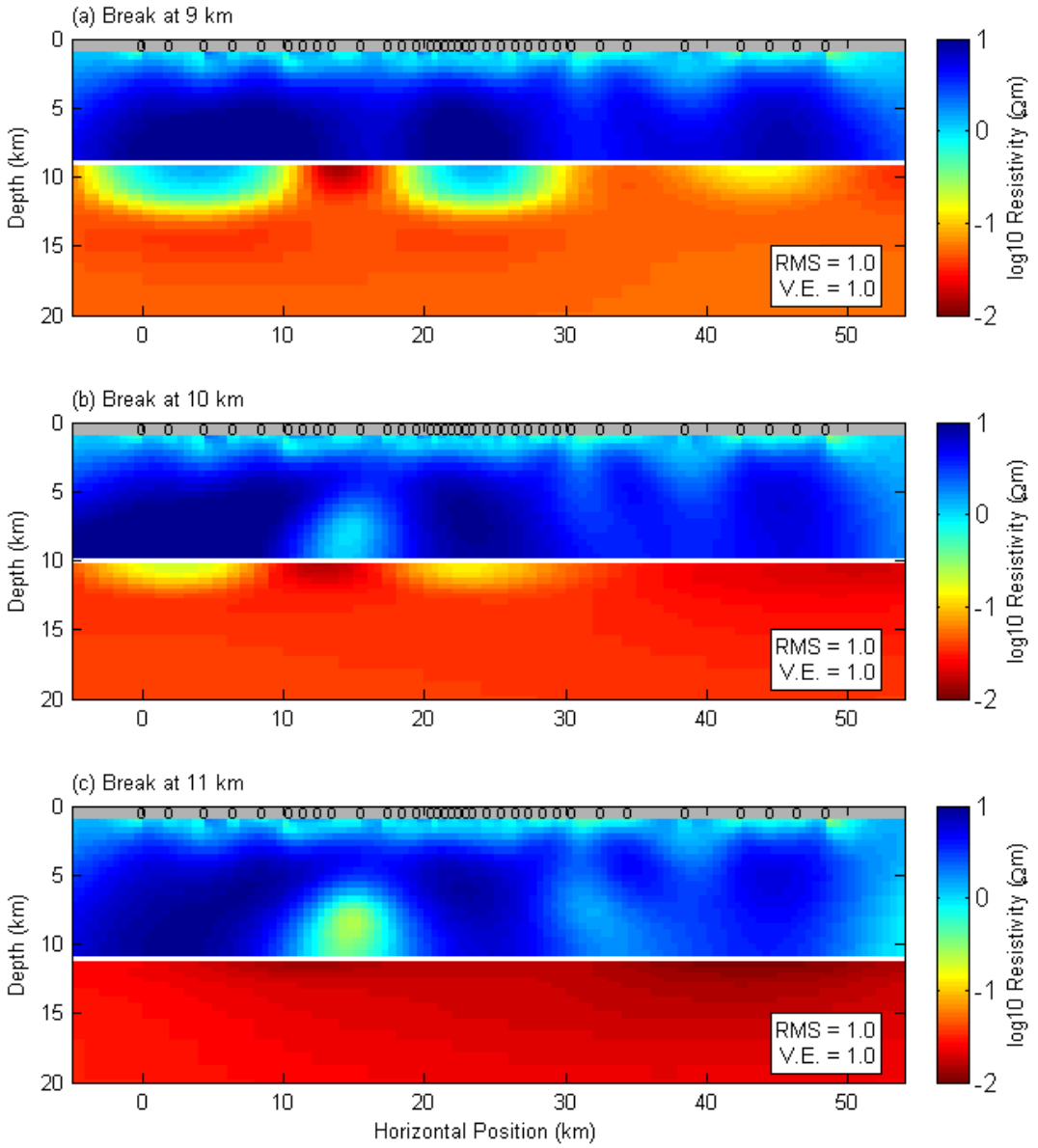

Figure 5.22. 2D inversion of line 1 with breaks in the vertical roughness.
Inversion of the same data as in Figure 5.21, but with a break in the vertical roughness penalty at (a) 9 km, (b) 10 km, or (c) 11 km. The ripple feature between 10-20 km horizontal position is always present, even when there is a horizontal roughness penalty and no vertical penalty. The eastern ripple is not as robustly required.

We examined whether the ripples are required by the data by placing a "break" in the vertical roughness penalties at a particular depth then re-inverting. Allowing the inversion to develop a high contrast in resistivity across a vertical boundary without penalty, while still enforcing horizontal smoothness, should eliminate the ripple

structures if they are not a dominant feature of the data. In Figure 5.22 we show the models resulting from three such inversions where the vertical break has been placed at 9, 10, and 11 km, respectively. All inversions converged to an RMS misfit of 1.0. The cuts show that the ripple feature between 10-20 km is more robust than the one further east, which may not necessarily be required by the data as shown when the break is at 10 km. When the break is deep (e.g. 11 km), the top of the western ripple "bleeds" upward across the boundary indicating that its top is above this depth. When the break is shallow (e.g. 9 km), the resistive crust on either side of the ripple bleeds downward, indicating that the

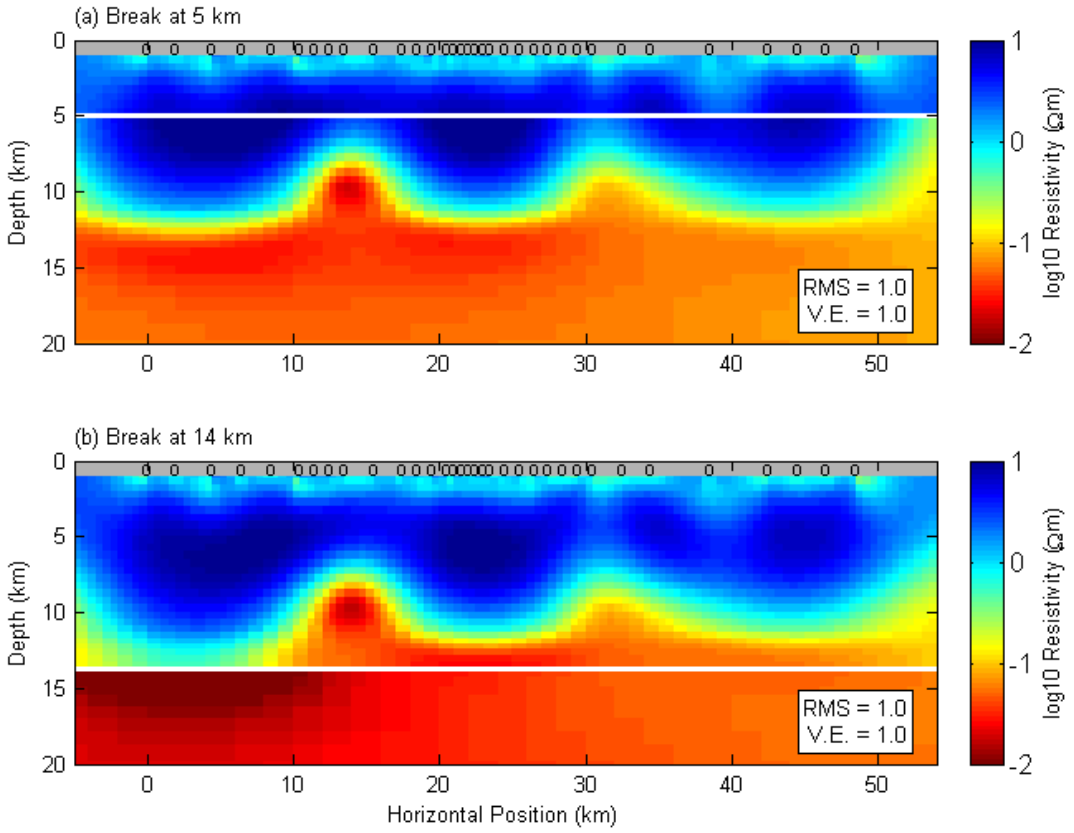

Figure 5.23. 2D inversion with vertical breaks, constraining the maximum amplitude of the ripples.

2D inversion with breaks in the vertical roughness penalties at 5 and 14 km, top and bottom panels respectively. The break has become irrelevant to the inversion result at these depths, indicating the maximum extent of the conductive surface.

conductive surface is deeper at this point. This latter case is especially interesting because MT is not as sensitive to resistors as to conductors. In terms of this hypothesis test, this means that the resistive body below the 9 km break is more likely to be removed by the horizontal smoothing than the conductive body above the 11 km break. That the resistive body is still present in the 9 km inversion indicates that its presence is required by the data.

Looked at another way, the three inversions in Figure 5.22 also constrain the minimum size of the conductive ripples. The top of the conductive anomaly can be mostly concentrated below 9 km depth and the resistive "valleys" can be entirely concentrated above 11 km depth. This yields a minimum amplitude of 2 km for the ripple.

The maximum amplitude can be constrained by continuing to move the break depth until it is irrelevant; i.e. it is shallow enough that a resistor appears both above and below it, or deep enough that a conductor appears both above and below it. We ran this suite of vertical-break inversions and show in Figure 5.23 that the break becomes irrelevant at 5 and 14 km yielding a maximum amplitude of 9 km for the ripple. The inversion without breaks (Figure 5.21) shows the amplitude to be 4-5 km which is an average value between these limits.

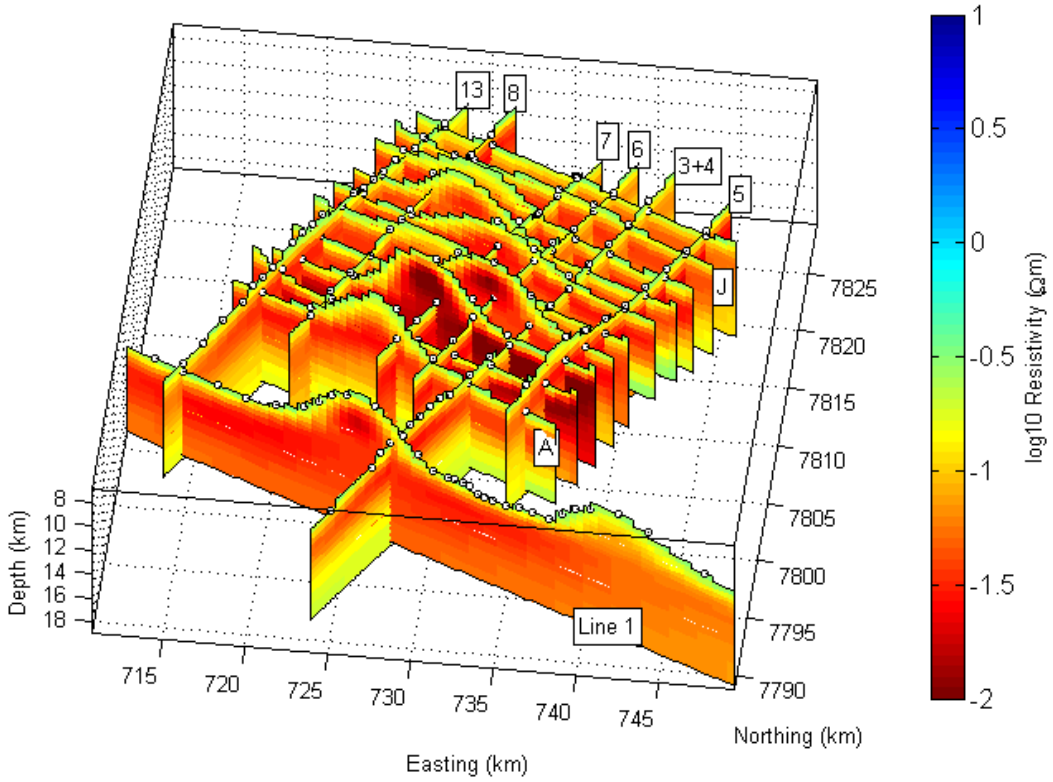

Figure 5.24. Fence plot of 2D inversion models for all Exmouth lines.
2D inversion models for all seventeen lines of the Exmouth data. Numbers and letters in boxes are the line designations. East-west lines are lettered A-J. The top of each model is stripped off down to the depth at which the resistivity drops below 0.3 Ωm. Filled circles are the site locations in each inversion, draped on the surfaces for clarity. The east-west lines consist of 6 sites each except for Line 1 which has 34. The north-south lines have 10 or more sites each. All inversions converged to a misfit between RMS 1.0 and 1.1.

5.3.5 2D inversion of all lines

We inverted the remaining sixteen lines of Exmouth data in 2D and show all the model results in a fence plot in Figure 5.24. These models all converged to an RMS misfit between 1.0 and 1.1 and in each case the misfit is distributed evenly among the various components, frequencies, and sites as discussed for line 1. In order to provide a good view of the surface of the conductive layer, the top portion of each model has been cut away to the depth at which the conductivity dips below 0.3 Ωm. The depth of the conductive surface away from the ripples is 11-12 km. The western ripple in line 1

continues in most of the east-west trending lines (A-J) but with gradually decreasing amplitude northwards.

The north-south lines generally do not show the large amplitude ripples, having instead variations in depth on the order of ~2 km and concentrations of higher conductivity where they run through 4-6 km high ripples of the east-west lines. Ordinarily one might attribute this to the rotation of the modes (i.e. the TE mode of the north-south lines has the same orientation as the TM mode of the east-west lines), however, as the modes are nearly identical in all sites, we believe this has no contribution here. With the exception of line 1, the east-west lines include only 6 sites each, positioned where they cross the north-south trending lines. Therefore, the lateral position and amplitude of the conductive ripple is not well constrained in these lines. It is striking, however, that the amplitude of the ripple matches that of the more densely spaced line 1.

From the fence diagram, it appears that the conductive anomaly contains an elevated feature like a ridge line which strikes north-east, approximately parallel to the distal edge of the plateau. It is at least 25 km long and dissipates to the north.

5.3.6 Prejudiced Inversions

Because the Exmouth survey does not contain long enough period data, we cannot resolve the thickness of the conductive body directly. The roughness penalty smooths the conductor outward to the edges of the model space because beyond some range there is minimal or no cost in data misfit to do so. However, by adding a prejudice to the inversion model parameters, we can get an estimate of the minimum thickness of conductor necessary to produce the measured responses by forcing the inversion to return

to a predetermined value when model parameters fall outside the resolution of the data. The result will not be a true minimum thickness because the roughness penalty which is still in place will tend to smooth out any sharp contrast. However, it will be a good indicator of whether a thin or massive body is required.

To each converged 2D inversion line, we added a penalty for deviation of model resistivities from 1 Ωm, then continued the inversions. Since they were already converged, each new iteration remained at the RMS misfit reached in the smooth inversion (e.g. 1.0-1.1) while attempting to move all resistivity values toward the prejudice value. This resulted in small changes in the model blocks to which the data are most sensitive (i.e. those representing near surface conductive sediments, upper crustal resistive basement, and the surface of the conductive anomaly) and larger changes to the blocks below and around the edges of the conductive body.

Figure 5.25a shows the resulting model for line 1. The ripple structure in the surface of the conductive anomaly has not substantially changed, though the peaks are somewhat sharper. The thickness of the body has been trimmed down to 2-5 km and the body appears to dissipate to the east. The conductance of the body ranges between $2\text{-}8\text{x}10^4$ S which is similar to the Vøring Plateau values of $10^4\text{-}10^5$ S.

MT data are especially sensitive to conductive bodies and consequently we have observed that once these form in an inversion, they tend not to move to a new location. Tests of synthetic data generated from a model in which a conductive prism is embedded in a resistive background show that when these data are inverted with a starting model which has a conductor in the incorrect location, the inversion has a difficult time moving the conductor to the proper location. So by starting our prejudiced inversions from the

results of a smooth inversion, we have effectively fixed the location of the conductive surface.

We also inverted the data with a 1 Ωm model prejudice and a 1 Ωm half-space starting model. The result (Figure 5.25b) is a body that is approximately one model block in thickness (~400 m at 10 km depth) with extremely low resistivity of < 0.01 Ωm. The long wavelength ripples are gone, revealing an essentially tabular body. The drop in depth of the conductive body in the west is most likely an inversion artifact – the model blocks are larger deeper in the model, so when there is less sensitivity, the prejudice can be minimized by involving overall fewer blocks. These three traits (a very thin very conductive body which is tabular and deepens at the edges) are shared by all seventeen of the lines in the Exmouth survey when inverted in this manner. The conductance values are generally between $1\text{-}5 \times 10^4$ S.

Note that none of these latter inversions were able to reach an RMS misfit of 1.0. Of the seventeen, the misfit values reached varied between 1.1 and 1.8 with an average of 1.4. Since it is not usual for the Occam inversion method to converge to a misfit above 1.0, we implemented an automatic convergence criterion such that the inversion was considered converged when the misfit changed by less than 0.01 over three iterations. This allowed the inversion to continue to its second phase in which the roughness and prejudice penalties are minimized while the misfit value is held constant.

We suspect that the higher misfit values are due to the absence of vertical relief in the surface of the conductive anomaly. Calculating misfit on a per-site basis for line 1, for example, reveals higher misfit for sites west of the 20 km horizontal position than east of

it. Whether the relief need be as extreme as 5 km over 10 km distance as shown in Figure 5.25a, however, is unknown.

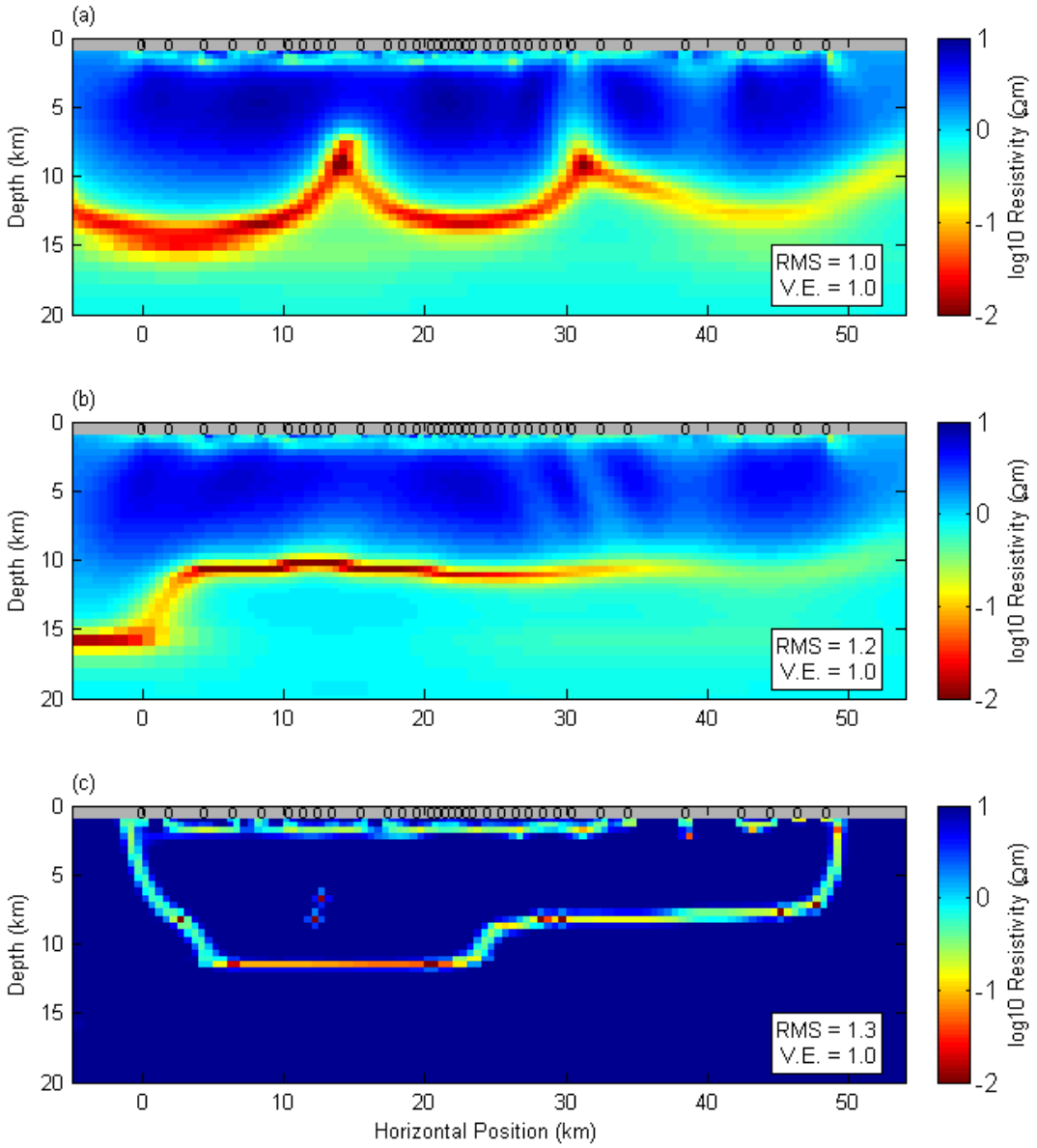

Figure 5.25. Model results for 2D inversion of Exmouth line 1 with a prejudice penalty. **2D smooth inversion of the Exmouth line 1 data with a 1 Ωm prejudice applied to all model parameters. (a) Model resulting from continuation of the inversion in Figure 5.21 with the prejudice applied after convergence. The structure of the conductive surface has sharpened and the body is much thinner. (b) Inversion started with a 1 Ωm half-space with prejudice applied from the beginning. The peaks in the conductive surface have not formed, however the inversion was unable to get below an RMS misfit of 1.2. (c) Inversion similar to (b) but with a 100 Ωm prejudice.**

We attempted to determine the conductivity structure absolutely required by the data by inverting line 1 again with an overwhelmingly resistive prejudice (100 Ωm). In Figure 5.25c, we show that this inversion, which converged to a misfit of 1.3, developed a curious conductive envelope which effectively eliminated sensitivity to any model blocks beyond it, thus minimizing the prejudice penalty. The main conductive body is again tabular, but two small single-block conductors have formed at the location of the top of the western peak. This raises the possibility that the ripple structures we have seen in the Exmouth 2D inversions are actually smaller conductive bodies which are separate from, but perhaps lightly connected to, a more extensive tabular body – analogous to a complex of sills. Why these bodies do not appear when the prejudice is only 1 Ωm is unknown but this perhaps accounts for the misfit.

5.4 Discussion

Lower crustal conductors are found in a wide variety of tectonic settings. Values of 20-30 Ωm in lower continental crust and 1-10 Ωm in lower oceanic crust are usually considered "low" (Bedrosian, 2007), so our values of 0.1 to 0.01 Ωm are unusual. We rule out problems with electronics or calibration since we have used these receivers in other areas of the world without detecting deep conductors (e.g. Constable *et al.*, 2009), and values in the same range were derived by Heinson *et al.* (2005) with a completely different equipment system. The possible causes of deep crustal conductors have been reviewed by Simpson (1999) and Bedrosian (2007) and in general are: pore fluids, melt, or mineral phases. Of this latter, some possibilities are graphite precipitated along fault

zones, well-connected serpentinization products (e.g. magnetite), and conductive minerals precipitated along mafic sills.

For these two plateaus, we can easily eliminate melt and pore fluids. To obtain the very low resistivity values modeled, 100% basaltic melt would be required (Roberts and Tyburczy, 1999; Tyburczy and Waff, 1983) and there is no evidence of an extant melt body below either plateau (e.g. high temperature vents and seamounts). Regarding pore fluids, Heinson *et al.* (2005) point out that to produce the very low resistivities modeled here either the pore fluid conductivity would need to be unreasonably low (10^{-5} Ωm) or the porosity unreasonably high (50%).

Serpentinized peridotite may produce low conductivities if magnetite is precipitated along grain boundaries in a well connected matrix (Stesky and Brace, 1973). Magnetite by itself can be much more conductive than 0.1 Ωm (Kakudate *et al.*, 1979; Lorenz and Ihle, 1975; Drabble *et al.*, 1971; Verwey and Haayman, 1941); however in a mineral assemblage with serpentinized peridotite, conductivities this low have not been observed in the lab. This is possibly due to the irreversible destruction of the magnetite matrix during exhumation of the samples studied, as suggested by Frost *et al.* (1989) in the context of graphite films. We note that a recent study claims to have definitively measured serpentinite resistivity in the 10^4 Ωm range (Reynard *et al.*, 2011), but in this case the samples were first ground up then pressed into larger samples, destroying any magnetite connectedness and making these measurements only valid for the bulk serpentinite minerals (hydrated magnesium silicates).

Even supposing that in situ serpentinized peridotite could produce low enough resistivities, seismic velocity structure does not favor it as an explanation for the

Exmouth and Vøring anomalies. The p-wave velocity structure for the Exmouth Plateau, for example, is less than 5.0 km/s down to ~10 km then 5.7-6.4 km/s for another ~10 km (Fomin *et al.*, 2000; Mutter and Larson, 1989). If the conductive anomaly at ~11 km depth represents serpentinized peridotite, then the velocity structure indicates it is part of a 10 km thick layer which is >70% serpentinized (Christensen, 2004; Horen *et al.*, 1996) – i.e. the currently supposed lower crust is actually exhumed, serpentinized mantle. Serpentinization of peridotite increases its volume which, at depth, has the effect of decreasing the porosity and sealing off further peridotite from serpentinization. In order to serpentinize a 10 km thick layer, it must be continuously extended and fractured to promote water circulation. Such fracturing would presumably break any magnetite connectivity and preclude the existence of a highly conductive body. Also, at the non-volcanic Iberian passive margin where massively serpentinized peridotite has been confirmed by scientific drilling (Seifert and Brunotte, 1996; Girardeau *et al.*, 1988), the velocity structure contains only a few km of low velocities (5-6 km/s) over a much higher velocity lightly-serpentinized basement (~7.6 km/s) (Chian *et al.*, 1999; Boillot *et al.*, 1992; Whitmarsh *et al.*, 1990). This same structure has been observed at other rifted margins such as Newfoundland (Reid, 1994) and the Great Australian Bight (Sayers *et al.*, 2001), indicating that large thicknesses of serpentinized mantle peridotite are generally in the >7 km/s range. The velocity structures of the Exmouth and Vøring Plateaus do not fit this pattern.

Heinson *et al.* (2005) prefer to explain the conductive anomaly via graphite films precipitated along the detachment zone proposed by Driscoll and Karner (1998). They suggest that the source of the carbon is either mantle carbonate which decomposes as it

shallows and is preferentially precipitated along a redox front represented by the brittle-ductile transition, or methane rich sediments which precipitate carbon along shear zones. However, there are several difficulties with this explanation. We place the conductor several kilometers shallower than the proposed detachment zone at the Exmouth Plateau making its association with the brittle-ductile transition unlikely. Because our survey is more densely spaced and contains higher frequencies, our shallower depth is more robust. Also, the surface of the conductive anomaly may contain a structural ripple which is not consistent with a detachment interface unless there was post-rifting deformation. The overlying strata contain no evidence for this deformation, which would likely break the graphite connectivity anyway. In any event, there is no continuous detachment zone identified in the Vøring Plateau where we obtained similar conductivities. If the cause of the conductive anomaly is the same at these two plateaus, which seems reasonable given their similar formation histories and conductivity structures, it is very likely not detachment related.

Of course, as both plateaus are heavily faulted down to the lower crust, one may still argue that the conductive anomaly represents graphite films precipitated along these faults (Mathez *et al.*, 2008; Frost *et al.*, 1989). However, while the dominant mode of faulting is sub-vertical listric faults, the results from both plateaus indicate that the body is horizontally oriented and relatively thin. It seems unlikely that carbon films would form in only a narrow depth range along faults which are vertically oriented. A pressure-temperature related argument would not explain the depth variations of the Exmouth data.

We prefer an explanation involving well-connected mineral phases in sills intruded into the mid-crust during continental breakup. Both plateaus have sills at the depths corresponding to our conductive anomalies. Mafic sills can form layered intrusions which precipitate conductive minerals into discrete layers which are observed to extend over distances up to 100 km (Lee, 1996; Naslund and McBirney, 1996). Layers of magnetite have been observed with thicknesses ranging up to meter scale in large layered intrusions such as the Bushveld Complex in South Africa (Eales and Cawthorn, 1996), the Bjerkreim-Sokndal Intrusion in Norway (Wilson *et al.*, 1996), the Skaergaard Intrusion in Greenland (McBirney, 1996), and the Windimurra Complex in Australia (Mathison and Ahmat, 1996).

The Heinson *et al.* (2005) study reported a conductance of $2x10^4$ S/m, which is compatible with our results. Considering that the conductivity of pure magnetite is about $2x10^4$ S (Lorenz and Ihle, 1975; Drabble *et al.*, 1971), this is equivalent to a 1 m layer or assemblage of layers in each plateau. Ferré *et al.* (2009) examined borehole cores from the Insizwa and Bushveld layered intrusions in South Africa and the Great Dyke in Zimbabwe. Their results showed that magnetite layering occurs throughout the sills, magnetite is present in most layers, and magnetic susceptibilities measure up to 4 (in SI units). This latter point may be of some importance to our study because our inversion solves for resistivity and magnetic susceptibility as a single value and the results are interpreted under the assumption that magnetic susceptibility is zero. Resistivity is inversely related to magnetic susceptibility such that one plus the susceptibility acts as a divisor on resistivity values. So, for example, with a magnetic susceptibility value of 4, our conductance estimate is lowered by 1/5, as is the equivalent thickness of magnetite

required. We regard a susceptibility value of 5 to be high since most values measured from the borehole data are less than 1.0. However it illustrates the possibility that the very low resistivities resulting from our inversion may be biased downward to some unknown extent by the unknown magnetic susceptibility.

Regarding lateral extent, we have shown in the prejudiced inversions that the conductive anomaly need not be across the entire survey area in order to produce the appearance of a regional effect in the data. At the Vøring Plateau, our survey is a few tens of kilometers from the Vøring Escarpment which marks the transition from intrusive to extrusive volcanism. It seems unlikely that the conductive anomaly would continue all the way over to the Escarpment due to the shallowing of emplacement depth creating conditions unfavorable to the formation of layered intrusions. Oceanic crust is not known to be especially conductive (Behrens, 2005; Cox, 1981) and we suspect that the continent-ocean transition region with its large, often subaerially-emplaced basalt flows intermixed with continental crust is similarly resistive.

At the Exmouth Plateau, our survey covers a 40x50 km area and obtains results comparable to the 400 km long transect of Heinson *et al.* (2005) which is >200 km further north. This leads to the reasonable assumption that the conductive anomaly covers all or a large section of the plateau. Our survey is approximately midway between the continent-ocean transition and the inner sub-basins which represent an earlier failed rifting event. The 400 km transect crosses the sub-basins up onto the shallow shelf. If the conductive anomaly does cover the entire plateau as implied, then it is reasonable to assume that sills were injected throughout the plateau probably from both the earlier failed rifting event and the terminal rifting event. White *et al.* (2008) note a ratio of

intrusive to extrusive volcanism of approximately 2:1 at two separate volcanic margins which each contain failed rifts. It is possible that the Exmouth Plateau has experienced a similar ratio.

We cannot definitively conclude that the conductive anomaly at the Vøring and Exmouth Plateaus is due to conductive minerals in layered intrusions. However, the evidence for this hypothesis is reasonable: sills are observed at the appropriate depths in seismic data, sub-aerially exposed layered intrusions around the world are observed to contain well-connected magnetite layers, and the unknown magnetic susceptibilities may be artificially lowering the very low resistivities we derive from inversion. It is unknown whether other volcanic passive margins contain such low resistivities. A campaign of MT surveys at other passive margins, both volcanic and non-volcanic, may reveal additional structural clues that lead to a definitive conclusion.

Acknowledgements

We thank BHP Billiton Petroleum for funding the Exmouth Plateau survey and BHPB, Shell, Esso Australia, and Chevron for providing ingress permissions. We also thank Fugro Development and Production Company for funding the Vøring Plateau survey. We thank the Seafloor Electromagnetic Methods Consortium for funding the data processing and inversion. We thank Nick Direen and Neal Driscoll for stimulating discussion and the captain and crew of the R/V Revelle for their hard work on our behalf.

Chapter 5, in full or in part, is currently being prepared for submission for publication, D. Myer, Constable S., and Key K. The dissertation author was the primary investigator and author of this paper.

References

Bedrosian, P., 2007. MT+, Integrating magnetotellurics to determine Earth structure, composition and processes, *Surveys in Geophysics,* 28**,** 121-167.

Behrens, J.P., 2005. The Detection of Electrical Anisotropy in 35 Ma Pacific Lithosphere, PhD Thesis, University of California, San Diego, La Jolla.

Boillot, G., Beslier, M.-O. & Comas, M.C., 1992. Seismic image of undercrusted serpentinite beneath a rifted margin, *Terra Nova,* 4**,** 25-33.

Boyd, R. & Bent, A., 1992. Triassic-Lower Cretaceous wireline log data from sites 759 through 764. *in Proceedings ODP Science Results*, pp. 377-391, eds. Von Rad, U. & Haq, B. U. Ocean Drilling Program, College Station, TX.

Boyd, R., Williamson, P.E. & Haq, B.U., 1992. Seismic stratigraphy and passive margin evolution of the southern Exmouth Plateau. *in Proceedings of the ODP, Science Results*, pp. 39-59, eds. Von Rad, U. & Haq, B. U. Ocean Drilling Program, College Station, TX.

Chave, A.D. & Thomson, D.J., 1989. Some comments on magnetotelluric response function estimation, *Journal of Geophysical Research-Solid Earth and Planets,* 94**,** 14215-14225.

Chian, D., Louden, K.E., Minshull, T.A. & Whitmarsh, R.B., 1999. Deep structure of the ocean-continent transition in the southern Iberia Abyssal Plain from seismic refraction profiles: Ocean Drilling Program (Legs 149 and 173) transect, *JGR,* 104**,** 7443-7462.

Christensen, N.I., 2004. Serpentinites, Peridotites, and Seismology, *International Geology Review,* 46**,** 795-816.

Constable, S., Key, K. & Lewis, L., 2009. Mapping offshore sedimentary structure using electromagnetic methods and terrain effects in marine magnetotelluric data, *Geophys. J. Int.,* 176**,** 431-442.

Constable, S., Orange, A.S., Hoversten, G.M. & Morrison, H.F., 1998. Marine magnetotellurics for petroleum exploration Part I: A sea-floor equipment system, *Geophysics,* 63**,** 816-825.

Cox, C.S., 1981. On the electrical conductivity of the oceanic lithosphere, *Physics of The Earth and Planetary Interiors,* 25**,** 196-201.

deGroot-Hedlin, C. & Constable, S., 1990. Occam inversion to generate smooth, 2-dimensional models from magnetotelluric data, *Geophysics,* 55**,** 1613-1624.

Direen, N.G., Stagg, H.M.J., Symonds, P.A. & Colwell, J.B., 2008. Architecture of volcanic rifted margins: new insights from the Exmouth-Gascoyne margin, Western Australia, *Aust. J. Earth Sci.,* 55**,** 341-363.

Direen, N.G., Stagg, H.M.J., Symonds, P.A. & Colwell, J.B., 2011. Dominant symmetry of a conjugate southern Australian and East Antarctic magma-poor rifted margin segment, *Geochem. Geophys. Geosyst.,* 12**,** Q02006.

Drabble, J.R., Whyte, T.D. & Hooper, R.M., 1971. Electrical conductivity of magnetite at low temperatures, *Solid State Communications,* 9**,** 275-278.

Driscoll, N.W. & Karner, G.D., 1998. Lower crustal extension across the Northern Carnarvon basin, Australia: Evidence for an eastward dipping detachment, *J. Geophys. Res.-Solid Earth,* 103**,** 4975-4991.

Eales, H.V. & Cawthorn, R.G., 1996. The Bushveld Complex. *in Layered Intrusions*, pp. 181-229, ed. Cawthorn, R. G. Elsevier.

Egbert, G.D., 1997. Robust multiple-station magnetotelluric data processing, *Geophys. J. Int.,* 130**,** 475-496.

Egbert, G.D. & Booker, J.R., 1986. Robust Estimation of Geomagnetic Transfer-Functions, *Geophysical Journal of the Royal Astronomical Society,* 87**,** 173-194.

Eldholm, O., Thiede, J. & Taylor, E., 1989a. 1 1. The Norwegian Continental Margin: Tectonic, Volcanic, and Paleoenvironmental Framework. *in Proc. ODP, Sci. Results*, pp. 5-26, eds. Eldholm, O., Thiede, J., Taylor, E. & et al. Ocean Drilling Program, College Station, TX.

Eldholm, O., Thiede, J. & Taylor, E., 1989b. 1 Evolution of the Voring volcanic margin. *in Proc. ODP, Sci. Results*, pp. 1033-1065, eds. Eldholm, O., Thiede, J., Taylor, E. & et al. Ocean Drilling Program, College Station, TX.

Exon, N.F., Haq, B.U. & von Rad, U., 1992. 1 1. Exmouth Plateau Revisited: Scientific Drilling and Geological Framework. *in Proc. ODP, Sci. Results*, pp. 3-20, eds. von Rad, U., Haq, B. U. & et al. Ocean Drilling Program, College Station, TX.

Exon, N.F., Von Rad, U. & Von Stackelberg, U., 1982. The geological development of the passive margins of the Exmouth Plateau off northwest Australia, *Marine Geology,* 47**,** 131-152.

Fernández, M., Torne, M., Garcia-Castellanos, D., Vergés, J., Wheeler, W. & Karpuz, R., 2004. Deep structure of the Vøring Margin: the transition from a continental

shield to a young oceanic lithosphere, *Earth and Planetary Science Letters,* 221**,** 131-144.

Ferré, E.C., Maes, S.M. & Butak, K.C., 2009. The magnetic stratification of layered mafic intrusions: Natural examples and numerical models, *Lithos,* 111**,** 83-94.

Fomin, T., Goncharov, A., Symonds, P. & Collins, C., 2000. Acoustic structure and seismic velocities in the Carnarvon Basin, Australian North West Shelf: towards an integrated study, *Explor. Geophys.,* 31**,** 579-583.

Frost, B.R., Fyfe, W.S., Tazaki, K. & Chan, T., 1989. Grain-boundary graphite in rocks and implications for high electrical conductivity in the lower crust, *Nature,* 340**,** 134-136.

Gamble, T.D., Clarke, J. & Goubau, W.M., 1979. Magnetotellurics with a Remote Magnetic Reference, *Geophysics,* 44**,** 53-68.

Gernigon, L., Ringenbach, J.C., Planke, S., Le Gall, B. & Jonquet-Kolstø, H., 2003. Extension, crustal structure and magmatism at the outer Vøring Basin, Norwegian margin, *Journal of the Geological Society,* 160**,** 197-208.

Girardeau, J., Evans, C.A. & Beslier, M.O., 1988. Structural analysis of plagioclase-bearing peridotites emplaced at the end of continental rifting: Hole 637A, ODP Leg 103 on the Galicia margin. *in Proc. ODP, Sci. Results*, pp. 209-223, eds. Boillot, G., Winterer, E. L. & et al. Ocean Drilling Program, College Station, TX.

Goncharov, A., 2004. Basement and crustal structure of the Bonaparte and Browse basins, Australian northwest margin. *in Timor Sea Petroleum Geoscience Symposium*, pp. 551–566, eds Ellis, G. K., Baillie, P. W. & Munson, P. J. Northern Territory Geological Survey.

Heinson, G. & Constable, S., 1992. The electrical-conductivity of the oceanic upper mantle, *Geophys. J. Int.,* 110**,** 159-179.

Heinson, G., White, A. & Lilley, F.E.M., 2005. Rifting of a passive margin and development of a lower-crustal detachment zone: Evidence from marine magnetotellurics, *Geophysical Research Letters,* 32.

Henning, A.T., Sawyer, D.S. & Templeton, D.C., 2004. Exhumed upper mantle within the ocean-continent transition on the northern West Iberia margin: Evidence from prestack depth migration and total tectonic subsidence analyses, *J. Geophys. Res.,* 109**,** B05103.

Horen, H., Zamora, M. & Dubuisson, G., 1996. Seismic waves velocities and anisotropy in serpentinized peridotites from xigaze ophiolite: Abundance of serpentine in slow spreading ridge, *Geophysical Research Letters,* 23**,** 9-12.

Jones, A.G., Chave, A.D., Egbert, G., Auld, D. & Bahr, K., 1989. A Comparison of Techniques for Magnetotelluric Response Function Estimation, *JGR,* 94**,** 14201-14213.

Kakudate, Y., Mori, N. & Kino, Y., 1979. Pressure effect on the anomalous electrical conductivity of magnetite, *Journal of Magnetism and Magnetic Materials,* 12**,** 22-25.

Larson, R.L., Mutter, J.C., Diebold, J.B., Carpenter, G.B. & Symonds, P., 1979. Cuvier Basin: A product of ocean crust formation by Early Cretaceous rifting off western Australia, *Earth and Planetary Science Letters,* 45**,** 105-114.

Lee, C.A., 1996. A Review of Mineralization in the Bushveld Complex and some other Layered Intrusions. *in Layered Intrusions*, pp. 103-145, ed. Cawthorn, R. G. Elsevier.

Leone, S., 1966. The Good, The Bad, and The Ugly, pp. 2:41MGM.

Lim, K., Ivey, G. & Nokes, R., 2008. The generation of internal waves by tidal flow over continental shelf/slope topography, *Environmental Fluid Mechanics,* 8**,** 511-526.

Lorenz, B. & Ihle, D., 1975. Calculation of the electrical conductivity above and below the Verwey transition in magnetite, *physica status solidi (b),* 69**,** 451-457.

Lorenzo, J.M., Mutter, J.C. & Larson, R.L., 1991. Development of the Continent-Ocean Transform Boundary of the Southern Exmouth Plateau, *Geology,* 19**,** 843-846.

Mathez, E.A., Roberts, J.J., Duba, A.G., Kronenberg, A.K. & Karner, S.L., 2008. Carbon deposition during brittle rock deformation: Changes in electrical properties of fault zones and potential geoelectric phenomena during earthquakes, *J. Geophys. Res.,* 113**,** B12201.

Mathison, C.I. & Ahmat, A.L., 1996. The Windimurra Complex, Western Australia. *in Layered Intrusions*, pp. 485-510, ed. Cawthorn, R. G. Elsevier.

McBirney, A.R., 1996. The Skaergaard Intrusion. *in Layered Intrusions*, pp. 147-180, ed. Cawthorn, R. G. Elsevier.

Mjelde, R., Kodaira, S., Shimamura, H., Kanazawa, T., Shiobara, H., Berg, E.W. & Riise, O., 1997. Crustal structure of the central part of the Vøring Basin, mid-Norway margin, from ocean bottom seismographs, *Tectonophysics,* 277**,** 235-257.

Mutter, J.C., 1985. Seaward dipping reflectors and the continent-ocean boundary at passive continental margins, *Tectonophysics,* 114**,** 117-131.

Mutter, J.C. & Larson, R.L., 1989. Extension of the Exmouth Plateau, offshore northwestern Australia: Deep seismic reflection/refraction evidence for simple and pure shear mechanisms, *Geology,* 17**,** 15-18.

Mutter, J.C., Talwani, M. & Stoffa, P.L., 1982. Origin of seaward-dipping reflectors in oceanic crust off the Norwegian margin by "subaerial sea-floor spreading", *Geology,* 10**,** 353-357.

Naslund, H.R. & McBirney, A.R., 1996. Mechanisms of Formation of Igneous Layering. *in Layered Intrusions*, pp. 1-43, ed. Cawthorn, R. G. Elsevier.

Planke, S., Symonds, P.A., Alvestad, E. & Skogseid, J., 2000. Seismic volcanostratigraphy of large-volume basaltic extrusive complexes on rifted margins, *JGR,* 105**,** 19335-19351.

Reid, I.D., 1994. Crustal structure of a nonvolcanic rifted margin east of Newfoundland, *JGR,* 99**,** 15161-15180.

Reynard, B., Mibe, K. & Van de Moortèle, B., 2011. Electrical conductivity of the serpentinised mantle and fluid flow in subduction zones, *Earth and Planetary Science Letters,* 307**,** 387-394.

Roberts, J.J. & Tyburczy, J.A., 1999. Partial-melt electrical conductivity: Influence of melt composition, *JGR,* 104**,** 7055-7065.

Sayers, J., Symonds, P.A., Direen, N.G. & Bernardel, G., 2001. Nature of the continent-ocean transition on the non-volcanic rifted margin of the central Great Australian Bight, *Geological Society, London, Special Publications,* 187**,** 51-76.

Seifert, K. & Brunotte, D., 1996. Geochemistry of serpentinized mantle peridotite from Site 897 in the Iberia Abyssal Plain. *in Proc. ODP, Sci. Results*, pp. 413-424, eds. Whitmarsh, R. B., Sawyer, D. S., Klaus, A. & Masson, D. G. Ocean Drilling Program, College Station, TX.

Simpson, F., 1999. Stress And Seismicity In The Lower Continental Crust: A Challenge To Simple Ductility And Implications For Electrical Conductivity Mechanisms, *Surveys in Geophysics,* 20**,** 201-227.

Skogseid, J. & Eldholm, O., 1989. 50 Voring Plateau continental margin; seismic interpretation, stratigraphy, and vertical movements. *in Proceedings of the ODP,*

Science Results, pp. 993-1030, eds. Eldholm, O., Thiede, J. & Taylor, E. Ocean Drilling Program, College Station, TX.

Skogseid, J., Pedersen, T., Eldholm, O. & Larsen, B.T., 1992. Tectonism and magmatism during NE Atlantic continental break-up: the Voring Margin, *Geological Society, London, Special Publications,* 68**,** 305-320.

Smith, W.H.F. & Sandwell, D.T., 1997. Global Sea Floor Topography from Satellite Altimetry and Ship Depth Soundings, *Science,* 277**,** 1956-1962.

Stagg, H.M.J., Alcock, M.B., Bernardel, G., Moore, A.M.G., Symonds, P.A. & Exon, N.F., 2004. Geological framework of the Outer Exmouth Plateau and adjacent ocean basinsGeoscience Australia, Canberra.

Stesky, R.M. & Brace, W.F., 1973. Electrical Conductivity of Serpentinized Rocks to 6 Kilobars, *JGR,* 78**,** 7614-7621.

Swift, C.M., 1967. A magnetotelluric investigation of electrical conductivity anomaly in the southwestern United States, PhD Thesis, Massachusetts Institute of Technology, Cambridge, MA.

Swift, M.G., 1991. Heat flow modelling: a generalized two-dimensional diffusive and convective numerical model for the Exmouth Plateau, offshore Northwest Australia, *Tectonophysics,* 194**,** 409-426.

Swift, M.G., Boyd, R., O'Brien, D.K. & Lorenzo, J.M., 1992. Heat flow and thermal history of the Exmouth Plateau. *in Proceedings of the ODP, Science Results*, pp. 363-375, eds. Von Rad, U. & Haq, B. U. Ocean Drilling Program, College Station, TX.

Tyburczy, J.A. & Waff, H.S., 1983. Electrical conductivity of molten basalt and andesite to 25 kilobars pressure: geophysical significance and implications for charge transport and melt structure, *JGR,* 88**,** 2413-2430.

Van Gastel, P., Ivey, G.N., Meuleners, M.J., Antenucci, J.P. & Fringer, O., 2009. The variability of the large-amplitude internal wave field on the Australian North West Shelf, *Continental Shelf Research,* 29**,** 1373-1383.

Veevers, J.J. & Johnstone, M.H., 1974. Comparative stratigraphy and structure of the western Australian margin and the adjacent deep ocean floor, *Init. Repts. DSDP,* 27**,** 571-585.

Verwey, E.J.W. & Haayman, P.W., 1941. Electronic conductivity and transition point of magnetite ("Fe3O4"), *Physica,* 8**,** 979-987.

Wannamaker, P.E., Stodt, J.A. & Rijo, L., 1987. A Stable finite-element solution for two-dimensional magnetotelluric modeling, *Geophysical Journal of the Royal Astronomical Society,* 88**,** 277-296.

White, R.S., 1992. Magmatism during and after continental break-up, *Geological Society, London, Special Publications,* 68**,** 1-16.

White, R.S. & McKenzie, D., 1989. Magmatism at Rift Zones: The Generation of Volcanic Continental Margins and Flood Basalts, *J. Geophys. Res.,* 94**,** 7685-7729.

White, R.S., Smith, L.K., Roberts, A.W., Christie, P.A.F. & Kusznir, N.J., 2008. Lower-crustal intrusion on the North Atlantic continental margin, *Nature,* 452**,** 460-464.

Whitmarsh, R.B., Miles, P.R. & Mauffret, A., 1990. The ocean–continent boundary off the western continental margin of Iberia—I. Crustal structure at 40°30'N, *Geophys. J. Int.,* 103**,** 509-531.

Wilson, J.R., Robins, B., Nielsen, F.M., Duchesne, J.C. & Vander Auwera, J., 1996. The Bjerkreim-Sokndal Layered Intrusion, Southwest Norway. *in Layered Intrusions*, pp. 231-255, ed. Cawthorn, R. G. Elsevier.